

Modeling and analysis for nonlinear flows due to stretched surface



By

Madiha Rashid

A DISSERTATION SUBMITTED IN THE PARTIAL FULFILLMENT OF THE
REQUIREMENT FOR THE DEGREE OF
DOCTOR OF PHILOSOPHY
IN
MATHEMATICS

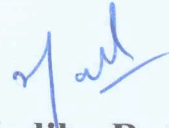
Supervised By

Prof. Dr. Tasawar Hayat

Department of Mathematics
Quaid-i-Azam University
Islamabad, Pakistan
2019

Author's Declaration

I Madiha Rashid hereby state that my PhD thesis titled Modeling and analysis for nonlinear problems involving nanofluids is my own work and has not been submitted previously by me for taking any degree from the Quaid-i-Azam University Islamabad, Pakistan or anywhere else in the country/world. At any time if my statement is found to be incorrect even after my graduate the university has the right to withdraw my PhD degree.



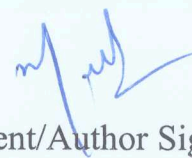
Name of Student: Madiha Rashid

Date: 06-09-2019

Plagiarism Undertaking

I solemnly declare that research work presented in the thesis titled “**Modeling and analysis for nonlinear problems involving nanofluids**” is solely my research work with no significant contribution from any other person. Small contribution/help wherever taken has been duly acknowledged and that complete thesis has been written by me. I understand the zero tolerance policy of the HEC and **Quaid-i-Azam University** towards plagiarism. Therefore, I as an Author of the above titled thesis declare that no portion of my thesis has been plagiarized and any material used as reference is properly referred/cited.

I undertake that if I am found guilty of any formal plagiarism in the above titled thesis even afterward of PhD degree, the University reserves the rights to withdraw/revoke my PhD degree and that HEC and the University has the right to publish my name on the HEC/University Website on which names of students are placed who submitted plagiarized thesis.



Student/Author Signature:

Name: **Madiha Rashid**

Modeling and analysis for nonlinear problems involving nanofluids

By

Madiha Rashid

CERTIFICATE

A DISSERTATION SUBMITTED IN THE PARTIAL FULFILLMENT OF THE
REQUIREMENTS FOR THE DEGREE OF THE DOCTOR OF
PHILOSOPHY

We accept this dissertation as conforming to the required standard

1. _____

Prof. Dr. Sohail Nadeem
(Chairman)

2. _____ 6/2/19

Prof. Dr. Tasawar Hayat
(Supervisor)

3. _____ 6/19/19

Dr. Nasir Ali

Department of Mathematics & Statistics
International Islamic University, Sector H-10
Islamabad.

4. _____

Dr. Maryam Javed

Department of Applied Mathematics
& Statistics, Institute of Space
Technology (IST), Islamabad.

Department of Mathematics
Quaid-I-Azam University
Islamabad, Pakistan
2019

Certificate of Approval

This is to certify that the research work presented in this thesis entitled **Modeling and analysis for nonlinear problems involving nanofluids** was conducted by **Ms. Madiha Rashid** under the kind supervision of **Prof. Dr. Tasawar Hayat**. No part of this thesis has been submitted anywhere else for any other degree. This thesis is submitted to the Department of Mathematics, Quaid-i-Azam University, Islamabad in partial fulfillment of the requirements for the degree of Doctor of Philosophy in field of Mathematics from Department of Mathematics, Quaid-i-Azam University Islamabad, Pakistan.

Student Name: **Madiha Rashid**

Signature: 

External committee:

a) **External Examiner 1:**

Name: **Dr. Nasir Ali**

Designation: Associate Professor

Office Address: Department of Mathematics & Statistics, Faculty of Basics Applied Sciences International Islamic University, Islamabad.

Signature: 

b) **External Examiner 2:**

Name: **Dr. Maryiam Javed**

Designation: Associate Professor

Office Address: Department of Applied Mathematics & Statistics, Institute of Space Technology (IST), Islamabad.

Signature: 

c) **Internal Examiner**

Name: **Dr. Tasawar Hayat**

Designation: Professor

Office Address: Department of Mathematics, QAU Islamabad.

Signature: 

Supervisor Name:

Prof. Dr. Tasawar Hayat

Signature: 

Name of Dean/ HOD

Prof. Dr. Sohail Nadeem

Signature: _____

DEDICATED TO

MY BELOVED PARENTS

AND

MY SUPERVISOR

Acknowledgement

All praise for Allah, the creator, the Glorious and the Merciful Lord, who guides me in darkness, helps me in difficulties and enables me to view stumbling blocks as stepping stones to the stars to reach the ultimate stage with courage. I am nothing without my Allah but I can achieve everything with His assistance. All of my veneration and devotion goes to our beloved Prophet Hazrat Muhammad ﷺ the source of humanity, kindness and guidance for the whole creatures and who declared it an obligatory duty of every Muslim to seek and acquire knowledge. My Allah shower His countless blessings upon Muhammad ﷺ, His family and companions.

I express deepest gratitude to my respected, affectionate and devoted supervisor Prof. Dr. Tasawar Hayat for his intellectual guidance, constant encouragement, suggestions and inexhaustible inspiration throughout my research work. He was the backbone of this research work with constructive criticism and extensive discussions. In short his tireless work, unique way of research and devotion to his profession cannot be expressed in words.

I wish to express my heartiest thanks and gratitude to my parents Mr. and Mrs. Rashid Mehmood Toor the one who can never ever be thanked enough for the overwhelming love, kindness and care they bestow upon me. They support me financially as well as morally and without their proper guidance it would not been possible for me to complete my higher education. I am also thankful to each and every member of my family. Special thanks to my husband Awaiz Arif Cheema and my Parents in law Mr. and Mrs. Muhammad Arif Cheema. I am also grateful to my brothers Lt. Aqib Mehmood Toor, Muhammad Wajid Toor and Abdul Basit Toor.

I would like to express my gratitude to respected teacher Prof. Dr. Muhammad Ayub, Prof. Abdul Waseem Siddique, Prof. Dr. Malik Muhammad Yousaf, Prof. Dr. Sohail Nadeem, Prof. Dr. Masood Khan, Dr. Khalid Saifullah and Dr. Muhammad Aslam. These are all those people who made me what I am today, they polished me at different stages of my life and taught me whatever I am today.

I gratefully acknowledge my Ph.D fellows Muhammad Irfan, Muhammad Waqas, Sumaira Qayyum, Sumaira Jabeen, Sadaf Nawaz, Farwa haider and Muhammad Ijaz Khan for their brilliant ideas and important contribution in refining my research work. Their professional guidance has nourished and polished my intellectual skills and I will always remain thankful to them.

I am thankful to my dearest friend Kiran Rafique for everything which she did for me. It is my pray to almighty ALLAH that please give my friend everything she desires.

I enact my heartiest and deepest thanks to all my lab fellows who were there in lab during my Ph.D session (03-03-2016 to 6-9-2019).

In the end thanks to all my research fellows and to those people who directly and indirectly helped me during my research work.

Madiha Rashid

06-09-2019

Preface

Nanofluids contain particles of size smaller than 100nm which are homogeneously and stably dispersed in base fluid. Metals (*Al*, *Cu*, *Fe* and *Au*), oxide ceramics (*CuO*, *TiO₂*, *Al₂O₃* and *Fe₃O₄*), carbides ceramics (*TiC* and *SiC*), single or multi-walled carbon nanotubes (SWCNTs and MWCNTs), semiconductors (*TiO₂* and *SiO₂*) and many composite materials act as nanoparticles. The advanced type of improving heat conductivity of base fluids like water, engine oil, toluene and ethylene glycol is to append nano sized particles. Nanofluids are a novel concept. Inclusion of nanoparticles in base fluids remarkably enhances the heat transfer performance. Cooling is the most technical challenge faced in countless industries such as manufacturing, electronics and automobiles. Nanofluids have great potentials in transportation, to improve automotive and heavy-duty engine cooling rates by reducing the complexity of thermal management systems, lowering the weight and enhancing the efficiency. Nanoparticles shows antibacterial properties or drug-delivery properties. Nanoamteial is more effective in nano/micro-electro-mechanical devices and heat exchangers. Non-Newtonian fluids deviates the Newtonian's law of viscosity. Rheological characteristics of non-Newtonian fluids give rise to highly complicated and very complex constitutive relation. In recent past several non-linear liquids models are proposed according to their physical behaviors and shear. Examples of such fluids are drilling muds, sugar solutions, blood, polymers of molecular weights, ceramics, shampoos and lubricants. Many industrial procedures such as petroleum reservoirs, polymer processing, ceramics, food production and pharmaceutical industries are the main focus of non-linear fluids. Features of heat transfer is based through involvement of various mechanism i.e., thermal radiation, Joule heating, entropy generation, convective conditions and heat source/sink.

Having all the above aspects in mind, the modeling for flows of nanofluid involving nanoparticles is made. Solutions and analysis are presented by homotopy analysis technique. The present thesis is designed as follows.

Chapter one provides literature review and expressions for basic laws of conservation of mass, momentum, energy and concentration. Mathematical formulation and boundary layer expressions of nanofluids, thixotropic and Maxwell fluids are provided. Basic concept of homotopy analysis method is also incorporated.

Chapter two addresses the two dimensional flow of nanofluid due to curved stretching surface. Modeling is based upon silver-water nanofluid. Convergent series solutions for nonlinear systems are constructed. Solutions are presented for the contributions of involved sundry variables. Discussion is made for velocity. Expressions of skin friction coefficient is calculated through numerical data. The contents of this chapter are published in **Results in Physics 8 (2018) 1104–1109**.

Chapter three extends the analysis of chapter two for magnetite nanofluid. Flow and heat transfer are discussed. Here analysis involve thermal radiation, heat generation and convective boundary conditions. The modeled non-linear systems are reduced into dimensionless expressions. Homotopic convergent solutions with appropriate domains are derived. Importance of physical parameters are narrated via plots. Computations of skin friction and Nusselt numbers are explained. Outcomes of present chapter are published in **Results in Physics 7 (2017) 3107–3115**.

The purpose of chapter four is twofold. Firstly magnetohydrodynamic flow of nanofluid due to non-linear stretching surface is developed. Transverse magnetic field is applied. Such consideration is significant in magnetic cell separation and to predict blood flow problems. Secondly to inspect entropy generation rate. Slip effects are considered at the boundary. Joule heating, thermal radiation and heat generation/absorption. Non-linear systems are solved by taking optimal homotopy analysis method. The detail of plotted graphs is discussed. The obtained results are published in **Journal of Molecular liquids 276 (2019) 441–452**.

The chapters five and six are prepared for the flow analysis with MHD and carbon nanotubes. In chapter five the nanoparticles of magnetic characteristics are considered

while in chapter six characteristics of both single and multi-walled carbon nanotubes are discussed. Porous medium is specified by modified Darcy's law. Homogeneous-heterogeneous reactions and convective boundary conditions are entertained. Solutions of various parameters are computed and analyzed. Main observations are summarized in the conclusions. Material of these two chapters are published in **Results in Physics 8 (2018) 268–275** and **International Journal of Numerical Methods for Heat and fluid flow**.

Chapter seven presents homogeneous-heterogeneous reactions in three-dimensional flow of silver-water nanofluid. Fluid flow is caused by rotating disk of variable thickness. Implementation of appropriate transformation leads to ordinary differential variables. Physical quantities are explained graphically. The obtained results are published in **International Journal of Heat and Mass transfer, 113 (2017) 96–105**.

Chapter eight is structured to show the MHD characteristics of nanofluid due to stretching cylinder. Silver (Ag), Copper (Cu), Copper oxide (CuO), Titanium oxide (TiO_2) and Aluminium-oxide (Al_2O_3) nanoparticles with water is considered. Present analysis focuses on entropy generation rate with modified Darcy's law. Non-linear radiation and non-uniform heat source/sink are also present. For heat transport phenomenon convective conditions are employed. For reduction of PDEs into ODEs transformation procedure is implemented. Non-linear problems are computed through optimal homotopy technique. Flow behavior in terms of velocity, temperature, entropy rate, Bejan number and skin friction and heat transfer rate are emphasized in the discussion. The outcomes of this chapter are published in **Applied Nanoscience DOI: org./10.1007/s13204–019–00961–2 (2019)**.

The analysis of Maxwell nanofluid is discussed in chapters nine and ten. Electrically conducting fluid is considered with combined effects heat and mass transfer. Modeling is developed via non-linear convection and heat generation/absorption. Non-linear version of thermal radiation is adopted. Activation energy is also used. The contents of chapter

nine are submitted. Material of chapter ten is published in **Journal of the Brazilian Society of Mechanical Sciences and Engineering DOI: [org./10.1007/s40430-019-1576-3](https://doi.org/10.1007/s40430-019-1576-3) (2019)**.

Chapter eleven reports the salient features of thixotropic nanofluid due to stretching sheet of variable thickness. Stagnation point flow is analyzed. The derived non-linear systems are solved. Intervals of convergence are verified. Velocity, temperature, concentration, skin friction and local Sherwood and Nusselt numbers are examined for influential parameters. The obtained results are published in **Iranian Journal of Science and Technology, Transactions A; Science DOI: [org./10.1007/s40995-00688-3](https://doi.org/10.1007/s40995-00688-3) (2019)**.

Contents

1	Literature review and basics equations	11
1.1	Background	11
1.2	Fundamental laws	16
1.2.1	Law of conservation of mass	16
1.2.2	Conservation of linear momentum	17
1.2.3	Law of conservation of energy	18
1.3	Basic laws for Buongiorno's model	19
1.3.1	Law of conservation of linear momentum	19
1.3.2	Law of conservation of energy	19
1.3.3	Conservation of concentration	21
1.4	Entropy and second law of thermodynamics	22
1.4.1	Entropy	22
1.4.2	Entropy in irreversible process	22
1.4.3	Second law of thermodynamics	22
1.5	Boundary layer expressions of non-Newtonian fluids	23
1.5.1	Maxwell fluid	23
1.5.2	Thixotropic fluid	23
1.6	Solution methodology	24
1.6.1	Homotopy analysis method	24
1.6.2	Solutions derivation by HAM	25
1.6.3	Zeroth-order deformation problems	25

1.6.4	m th order deformation problems	26
1.6.5	Solutions by OHAM	26
1.6.6	Optimal convergence control parameter	26
2	MHD flow of Ag-water nanofluid by nonlinear curved stretching sheet	27
2.1	Model development	27
2.1.1	Physical quantities	31
2.2	Solution derivation	31
2.2.1	Zero th -order system	32
2.2.2	m th -order deformation systems	32
2.3	Convergence of homotopy solutions	33
2.4	Physical results and discussion	35
2.4.1	Velocity	35
2.4.2	Pressure	38
2.4.3	Skin friction coefficient	39
2.4.4	Comparative study	40
2.5	Conclusions	40
3	MHD convective flow of Fe₃O₄-water nanofluid by non-linear curved stretching sheet	41
3.1	Mathematical formulation	41
3.1.1	Physical quantities of curiosity	44
3.2	Computations of series solutions	45
3.3	Convergence of series solutions	45
3.4	Interpretations of results	47
3.4.1	Velocity	47
3.4.2	Pressure	51
3.4.3	Temperature	52

3.4.4	Skin friction coefficient and heat transfer rate	56
3.5	Concluding remarks	57
4	Entropy generation in flow of Fe_3O_4-water nanofluid with slip effects	58
4.1	Flow model	58
4.1.1	Quantities of interest	61
4.2	Entropy generation	62
4.3	Optimal homotopy analysis method	63
4.4	Convergence analysis	63
4.5	Results and discussion	65
4.5.1	Velocity	65
4.5.2	Temperature	68
4.5.3	Local entropy generation rate $N_g(\xi)$ and Bejan number Be	73
4.5.4	Surface drag force and heat transfer rate	79
4.6	Conclusions	81
5	Three-dimensional flow of Fe_3O_4-water nanofluid with homogeneous-heterogeneous reactions	82
5.1	Flow equations	82
5.1.1	Physical quantities	86
5.2	Optimal homotopic solutions	86
5.3	Optimal convergence analysis	87
5.4	Physical interpretation	89
5.4.1	Velocity components	89
5.4.2	Temperature	92
5.4.3	Concentration	94
5.4.4	Skin friction coefficient and local Nusselt number	96
5.4.5	Comparative study	99

5.5	Conclusions	99
6	Darcy-Forchheimer bidirectional flow in (SWCNTs) and (MWCNTs) carbon nanotubes with homogeneous-heterogeneous reactions	100
6.1	Problem formulation	101
6.1.1	Quantities of interest	104
6.2	Homotopy procedure	104
6.3	Convergence	104
6.4	Results and discussion	107
6.4.1	Velocity components	108
6.4.2	Temperature	113
6.4.3	Concentration	115
6.4.4	Skin friction coefficient and heat transfer rate	118
6.5	Conclusions	120
7	Nanofluid flow due to rotating disk with variable thickness and homogeneous-heterogeneous reactions	122
7.1	Problem formulation	122
7.1.1	Physical quantities	126
7.2	Homotopy procedure	127
7.3	Convergence	128
7.4	Results and discussion	130
7.4.1	Axial velocity	130
7.4.2	Radial and Azimuthal velocity components	132
7.4.3	Temperature	136
7.4.4	Concentration	137
7.4.5	Skin friction coefficient and Nusselt number	139
7.4.6	Comparative study	141

7.4.7	Conclusions	141
8	Entropy generation in Darcy-Forchheimer flow of nanofluid due to stretching cylinder	142
8.1	Mathematical description	142
8.1.1	Physical quantities of curiosity	144
8.2	Entropy generation	144
8.3	OHAM Solutions	145
8.4	Results and discussion	152
8.4.1	Velocity	152
8.4.2	Temperature	155
8.4.3	Entropy generation and Bejan number	158
8.4.4	Skin friction coefficient and heat transfer rate	162
8.5	Concluding remarks	162
9	Chemically reactive flow of Maxwell nanofluid due to stretching cylinder with thermal radiation	164
9.1	Problem statement	164
9.1.1	Local Nusselt number	167
9.1.2	Sherwood number	167
9.2	Solution Methodology	167
9.3	Convergence analysis	168
9.4	Interpretation	171
9.4.1	Velocity	171
9.4.2	Temperature	173
9.4.3	Concentration	177
9.4.4	Heat and mass transfer rates	179
9.5	Major findings	181

10 Chemically reactive flow of Maxwell nanofluid due to stretching cylinder with activation energy	182
10.1 Modeling	182
10.1.1 Quantities of interest	184
10.2 Homotopy procedure	185
10.3 Convergence analysis	186
10.4 Discussions	187
10.4.1 Velocity	187
10.4.2 Temperature	190
10.4.3 Concentration	191
10.4.4 Heat and mass transfer rates	193
10.4.5 Comparison results	194
10.5 Conclusions	195
11 Magnetohydrdynamic flow of thixotropic nanofluid with Soret and Du- four. . .	196
11.1 Formulation	196
11.1.1 Physical quantities of curiosity	199
11.2 HAM Solutions	200
11.3 Convergence	200
11.4 Analysis	202
11.4.1 Dimensionless velocity field	202
11.4.2 Temperature	203
11.4.3 Concentration	206
11.4.4 Skin friction coefficient and local Nusselt and Sherwood numbers .	208
11.5 Closing remarks	210
Bibliography	210

Chapter 1

Literature review and basics equations

This chapter contains the motivation and survey of literature for considerations of nanofluids, rotating disk, surfaces with variable thickness, Darcy-Forchheimer porous medium, non-Newtonian materials, entropy generation and homogeneous-heterogeneous reactions. Techniques utilized for solutions development are briefly mentioned.

1.1 Background

Nanofluids are a new class of nanotechnology-based heat transfer fluids with augmented thermal properties at the smallest possible concentrations by uniform dispersion and stable suspension of nanoparticles (1-100nm) in host fluids. Nano-sized metallic particles (Copper, Silver, gold, Titanium or their oxides), carbon nanotubes and nitrides (SiN) are used in traditional heat transfer fluids to form slurries. Combinations of nanoparticles and base fluids can create several heterogeneous nanofluids. Applications of nanofluids are significant in industrial and biomedical processes such as engine cooling, drag reductions refrigeration, chillers, high-power lasers, oil engine transference, cooling of electronics, boiler, hybrid-powered engines, microwave tubes, drilling, lubrication, nanofluids in transformer cooling oil, cooling of welding, great energy savings and emissions reductions. Word "nanofluid" is credited by Choi and Eastman [1]. Xuan and Li [2] worked on heat transfer enhancement of nanofluids. Choi et al. [3] designed nanoparticles to refine

the quality of product and enhance thermal conductivity of fluids. Daungthonsuk and Wongwises [4] gave a review of convective heat transfer nanofluids. Recently literature on experimental and theoretical attempts regarding nanofluid is quite extensive. Few reviews on nanofluids are presented in refs. [5]-[13]. Apart from these Buongiorno [14] developed a mathematical model of convective transport of nanofluids. Buongiorno introduces seven slip mechanisms between nanoparticles and base fluid. He concluded that there is an abnormal enhancement in thermal conductivity due to presence of thermophoretic and Brownian diffusion of nanoparticles. Buongiorno et al. [15] shows no anomalous thermal conductivity enhancement in considered fluids. With these view points the nanofluid flow due stretching sheet with chemical reaction is discussed by Hayat et al. [16]. Pourhoseini et al. [17] worked on silver-water nanofluid due to plate exchanger. Nanofluid flow due to permeable stretching/shrinking sheet with regression and stability analyses is given by Jahan et al.[18]. Reddy et al. [19] discussed the salient aspects of thermophoresis and Brownian motion in nanofluid flow past a slandering stretching surface.

Flows due to non-Newtonian materials has gained continuous attention of several researchers. Examples of non-Newtonian fluids in geophysics and bio-engineering fields are food products, milk, apple sauce, toothpaste, ketchup, crystal growth, blood at low and oil reservoirs etc. Non-Newtonian fluids for their multiple properties are not accounted by a single relation. These fluids introduce a non-linear relationship between shear stress and strain rate. Non-Newtonian fluids are classified into differential, integral and rate types. One of them, Maxwell liquid is simplest subclass of rate type liquids. recently, Tan et al. [20] gave a Maxwell fluid flow among two plates. Thixotropic fluid model is another important fluid model. The complexity among shear thinning and thixotropic fluid is that viscosity diminishes in a shear thinning liquid with enhancement of the shear rate. However, the thixotropic fluid reveals a viscosity decay via time at the constant shear rate. Blasius flow of thixotropic fluids is presented by Sadeqi et al. [21]. Few related studies to non-Newtonian fluids can be looked through the refs. [22]-[25] and

several attempts therein.

Flow due to stretching surface expanded great interest due to its application in industrial and engineering forms. Most of the applications using flow generated in hot rolling, broadsheets manufacture, rubber sheet, liquid crystals in condensation processes, fiber spinning, glass blowing, melt-spinning, wire drawing, paper production, polymer sheet filaments, polymer extrusion and so on. Fluid flow due to linear stretching surface was initially reported by Crane [26]. Extensive information on this topic now exists. However in most cases it is assumed that velocity of stretching surface is linearly proportional to the distance from fixed origin. However realistically stretching sheet may not necessarily be linear. Gupta and Gupta [27] discussed the flow due to stretching sheet. Three-dimensional nanofluid flow due to non-linear stretching sheet is reported by Khan et al. [28]. Analytical solutions of nanofluid flow subject to nonlinear stretching velocity is analyzed by Mahanthesh et al. [29]. Besides the flow due to flat stretching sheet are mostly attended. In past fluid flow by curved stretching surface is not elaborated properly. Very less attention is given about the study fluid flow due to curved stretching surface. Sajid et al. [30] examined fluid flow subject to curved surface with linear stretching velocity. Micro polar fluid flow past curved stretching sheet is modeled and analyzed by Naveed et al. [31]. Viscous flow due to curved stretching sheet with convective conditions is addressed by Hayat et al. [32]. Recently Sanni et al. [33] developed a mathematical modeling for non-linear curved stretching sheet. Later on, Hayat et al. [34] considered nanofluid flow subject to non-linear curved stretching sheet. Soret and Dufour effects in nanofluid flow due to non-linear curved stretching surface is analyzed by Reddy et al. [35]. Flow of nanofluid by non-linear stretching velocity is addressed by Hayat et al. [36].

Practical and theoretical significance of applied sciences and engineering convince the flow analysis in rotating frame. Flow due to rotating surfaces gained much attention of engineers and researchers. Dominant applications include centrifugal filtration process,

air cleaning machines, rotating machinery, medical equipment, designs of multi-pore distributor and converter etc. Initial work on rotating disk is presented by Karman [37]. Stewartson [38] analyzed the fluid flow between two rotating coaxial disks. Fluid flow between two rotating disks is studied by Mellor et al. [39]. Ming et al. [40] elaborated power-law fluid flow due to rotating disk. Cu-water nanofluid flow due to rotating disk is given by Hayat et al. [41]. The previous papers mainly discussed the flow by a disk of negligible thickness. However due to acceleration/declaration, the thickness of stretching surface may increase/decrease with distance. This factor depends on the value of the velocity power-index. Applications regarding to surfaces of variable thickness are significant in mechanical, architectural, civil, marine and aeronautical engineering. Fang et al. [42] described flow subject to stretching sheet of variable thickness. Subhashini et al. [43] presented the fluid flow due to stretching sheet with variable thickness. Reasonable recent literature is now available for rotating disk problems (see refs. [44]-[47]).

The concept of fluid flow in porous space has great importance in geophysics, environmental and industrial systems, civil and chemical engineering, catalytic reactors, heat exchanger layouts, fibrous insulation, mechanics of nanofluid, petroleum technology, oil production, geothermal energy schemes, nuclear waste disposal, petroleum resources, blood flow via lungs or arteries, fermentation process, gas-cleaning filtration, ground water pollution and porous bearings and pipes. For the very first time Darcy's theory is used for porous space problems [48]. The classical Darcy's law is insufficient when inertia and boundary features are taken into account at high flow rate. So it's impossible to neglect the inertia and boundary features. Forchheimer [49] considered these aspects by taking additional terms through square velocity factor in Darcian velocity expression. Flow of homogeneous fluids saturating porous medium is given by Muskat [50]. Seddeek [51] discussed flow of porous media. Fluid flow with Darcy-Brinkman-Forchheimer relation is proposed by Singh et al. [52]. Pal and Mondal [53] studied fluid flow with Darcy-Forchheimer expression. Darcy-Forchheimer flow in carbon nanotubes is discussed by

Hayat et al. [54]. Ganesh et al. [55] presented Darcy-Forchheimer flow of nanofluid due to stretching sheet.

Recently, some researchers have focused on entropy of thermodynamical systems. Entropy generation refers to irreversible thermodynamical deterioration of systems. For assessment of irreversibility (entropy generation) the second law of thermodynamics has been utilized. The level of irreversibility obtaining during any thermal process is measured by entropy generation. Thermodynamic irreversibility (entropy generation) generally accompanied the processes of heat transportation. Specific factors are responsible for irreversibilities generation like fluid friction, Joule dissipation, heat transportation through fixed temperature difference and diffusion etc. Entropy generation relates the heat transportation, elementary thermodynamic principles and fluid mechanics. Entropy generation implements these sources to formulate the real structures and procedures which are categorized by constraints (finite, time). Entropy generation minimization (EGM) technique is used to optimize performance of thermal devices such as switches, electrical and motor control, temperature sensor's for power conversion and thermal science education. They are restricted by heat or mass transportation and irreversibilities regarding fluid flow. Bejan [56, 57] scrutinized idea of entropy generation minimization (system disorderedness). He observed that two diverse features i.e. liquid friction and heat transportation due to temperature gradient. These features are responsible for production of entropy in fluid flow process. He also delineated the numerous applications in which irreversibility is minimized on a multifaceted level. However for practical utilization the entropy generation rate must be minimized for thermodynamic functioning up gradation. Flow of Casson nanofluid with entropy generation is presented by Abolbashari et al. [58]. Some recent advancement in this direction can be see in the attempts [59]-[65].

Concept of chemical reactions are classified into heterogeneous and homogeneous reactions regarding to uniformity of a subject. Such reactions are utilized in chemically

reacting structures like catalysis, combustion and biochemical systems. In the presence or absence of a catalyst these reactions manifestly. There is a key difference among homogeneous and heterogeneous reactions. Homogeneous reactions contain chemical changes which are solely dependent only on nature of interaction among reactants. Such reactions are simple and have uniformity for example oxyacetylene torch burning. While reactions on the surface of catalyst of various phases are occurred in heterogeneous reactions. Such reactions are complex and have lack uniformity. Flow behavior subject to chemical reaction has significant application in metabolism of food in body, explosion of fireworks, crops damage, air and water pollution, polymer and ceramics, formation and dispersion of fog, groves of fruit trees and atmospheric flows. Chaudhary and Merkin [66] proposed a simple isothermal model for homogeneous-heterogeneous reactions in flow with different diffusivities for reactant and autocatalyst. After that Merkin [67] worked on boundary layer flow with homogeneous-heterogeneous reactions. Hayat et al. [68] described homogeneous-heterogeneous reactions in nanofluid flow due to rotating disk of variable thickness. Raees et al. [69] anticipated a homogeneous-heterogeneous reactions for nanofluid flow. Homogeneous combustion of methane-air mixture and heterogeneous reaction characteristics in micro channel is presented by Wang et al. [70]. Alzahrani [71] reported the effect of homogeneous-heterogeneous reactions in flow of carbon nanotubes. Homogeneous-heterogeneous reactions in three dimensional radiative flow of nanofluid is presented by Hayat et al. [72].

1.2 Fundamental laws

1.2.1 Law of conservation of mass

Law of conservation of mass stems from the principle that mass can neither be created nor destroyed inside the control volume. For a known velocity and no source/sinks it is sufficient to model the continuity equation (flow is continuous). Moreover in the law

of conservation of mass total inlet and outlet flux is constant. Differential form of law of conservation of mass for compressible fluid is

$$\frac{\partial \rho}{\partial t} + \nabla \cdot (\rho \mathbf{V}) = 0, \quad (1.1)$$

where ρ exhibits fluid density, t is the time and $\mathbf{V} = (u, v, w)$ the velocity of the fluid.

For incompressible fluid, law conservation of mass is

$$\nabla \cdot \mathbf{V} = 0. \quad (1.2)$$

In Cartesian coordinates the operator and continuity equation is given by

$$\nabla = \frac{\partial}{\partial x} i + \frac{\partial}{\partial y} j + \frac{\partial}{\partial z} k, \quad (1.3)$$

$$\frac{\partial u}{\partial x} + \frac{\partial v}{\partial y} + \frac{\partial w}{\partial z} = 0, \quad (1.4)$$

where as in cylindrical coordinates we have

$$\nabla = e_r \frac{\partial}{\partial r} + e_\theta \frac{\partial}{\partial \theta} + e_z \frac{\partial}{\partial z}, \quad (1.5)$$

$$\frac{1}{r} \frac{\partial}{\partial r} (r v_r) + \frac{1}{r} \frac{\partial}{\partial \theta} (v_\theta) + \frac{\partial}{\partial z} (v_z) = 0. \quad (1.6)$$

The operator and continuity equation an in terms of curvilinear coordinates is written as

$$\nabla = (r + R) \frac{\partial}{\partial r} e_r + R \frac{\partial}{\partial x} e_x, \quad (1.7)$$

$$\frac{\partial}{\partial r} [(r + R) v] + R \frac{\partial u}{\partial x} = 0. \quad (1.8)$$

1.2.2 Conservation of linear momentum

It is stated that total linear momentum of an isolated system remains conserved. Mathematically, we have

$$\rho_{nf} \frac{d\mathbf{V}}{dt} = -\nabla \cdot \boldsymbol{\tau} + \rho_{nf} \mathbf{b}. \quad (1.9)$$

This equation contained the inertial forces which is the internal force on left hand side while on the right hand side the first term is due to the surface force which is an external force and last term is body force.

The Cauchy stress tensor is defined as

$$\tau = -p\mathbf{I} + \mu_{nf}\mathbf{A}_1, \quad (1.10)$$

where $\frac{d}{dt}(= \frac{\partial}{\partial t} + \mathbf{V} \cdot \nabla)$ is the material derivative, \mathbf{I} signifies the identity tensor, p the pressure and \mathbf{A}_1 the first Rivlin Ericksen tensor given as

$$\mathbf{A}_1 = (\nabla\mathbf{V}) + (\nabla\mathbf{V})^{tr}. \quad (1.11)$$

The dynamics viscosity of nanofluid is [73]:

$$\mu_{nf} = \frac{\mu_f}{(1 - \phi)^{2.5}}, \quad (1.12)$$

where the effective nanofluid density is taken as follows [74]:

$$\rho_{nf} = \rho_f(1 - \phi) + \rho_s\phi, \quad (1.13)$$

in which ϕ is the solid volume fraction of nanoparticles, nf represents the thermophysical properties of the nanofluid, s is defined as nano solid particles and f in subscript explain base fluid. It is worth mentioning that nanofluid analysis is absent for $\phi = 0$.

1.2.3 Law of conservation of energy

Law of conservation of energy interprets that total energy of the framework is conserved. It is obtained through first law of thermodynamics. Energy equation for nanofluid in the presence of viscous dissipation and thermal radiation can be written as

$$(\rho C_p)_{nf} \frac{dT}{dt} = \tau \cdot \mathbf{L} + k_{nf} \nabla^2 T - \nabla \cdot \mathbf{q}_h, \quad (1.14)$$

where \mathbf{q}_h is the radiative heat flux. First law of thermodynamics states that the increase in the internal energy of a thermodynamical system is equal to the amount of heat

energy added to the system minus the amount of energy lost as a result of the work done by the system on the surroundings.

The effective nanofluid heat capacity $(\rho C_p)_{nf}$ is

$$(\rho C_p)_{nf} = (\rho C_p)_f (1 - \phi) + (\rho C_p)_s \phi. \quad (1.15)$$

and the effective thermal conductivity of nanofluid k_{nf} by Maxwell-Garnett Model is given by [75]:

$$\frac{k_{nf}}{k_s} = \frac{k_s + 2k_f - 2\phi(k_f - k_s)}{k_s + 2k_f + 2\phi(k_f - k_s)}. \quad (1.16)$$

1.3 Basic laws for Buongiorno's model

1.3.1 Law of conservation of linear momentum

Generalized equation of motion is

$$\rho \frac{d\mathbf{V}}{dt} = \nabla \cdot \boldsymbol{\tau} + \rho \mathbf{b}. \quad (1.17)$$

1.3.2 Law of conservation of energy

Nanofluid energy equation can be written as

$$\rho C_p \frac{dT}{dt} = -\text{div} \check{\mathbf{q}}_r + I_p \nabla \cdot \mathbf{S}_p, \quad (1.18)$$

where I_p is the specific enthalpy of nanoparticles material, \mathbf{S}_p is the nanoparticles diffusion mass flux and $\check{\mathbf{q}}_r$ is the energy flux. No radiation is present. The first term on left hand side of exhibits the combined effects of change in local energy and advection term. On the right hand side first term comes from Fourier's law of heat conduction and last term is due to nanoparticles. Energy flux is given by

$$\check{\mathbf{q}}_r = -k \nabla T + I_p \mathbf{S}_p. \quad (1.19)$$

Eq. (1.18) becomes

$$\begin{aligned}
 \rho C_p \frac{dT}{dt} &= -\nabla \cdot (-k\nabla T + I_p \mathbf{S}_p) + I_p \nabla \cdot \mathbf{S}_p, \\
 &= k\nabla^2 T - \nabla \cdot (I_p \mathbf{S}_p) + I_p \nabla \cdot \mathbf{S}_p, \\
 &= k\nabla^2 T - I_p \nabla \cdot \mathbf{S}_p - \mathbf{S}_p \cdot \nabla I_p + I_p \nabla \cdot \mathbf{S}_p, \\
 &= k\nabla^2 T - \mathbf{S}_p \cdot \nabla I_p.
 \end{aligned} \tag{1.20}$$

Considering

$$\nabla I_p = C_p \nabla T, \tag{1.21}$$

one obtains from Eq. (1.20)

$$\rho C_p \frac{dT}{dt} = k\nabla^2 T - C_p \mathbf{S}_p \cdot \nabla T. \tag{1.22}$$

Diffusion mass flux \mathbf{S}_p for the nanoparticles, given as the sum of two diffusion terms (Brownian diffusion and thermophoresis) by

$$\mathbf{S}_p = \mathbf{S}_{p,B} + \mathbf{S}_{p,T}, \tag{1.23}$$

with

$$\mathbf{S}_{p,B} = -\rho_p D_B \nabla C. \tag{1.24}$$

Here Brownian diffusion coefficient D_B can be defined by the Einstein-Stokes equation

$$D_B = \frac{k_B T}{3\pi\mu d_p}, \tag{1.25}$$

in which k_B is the Boltzmann's constant and d_p the nanoparticles diameter. Further

$$\mathbf{S}_{p,T} = \rho_p C \mathbf{V}_\tau, \tag{1.26}$$

$$\mathbf{V}_\tau = -\tilde{\gamma} \frac{\mu}{\rho} \frac{\nabla T}{T}, \tag{1.27}$$

for the thermophoresis velocity \mathbf{V} . In above equation the proportionality factor $\tilde{\gamma}$ (while ρ_p and ρ are the densities of nanoparticles and base fluid respectively) can be expressed as follows:

$$\tilde{\gamma} = 0.26 \frac{k}{2k + k_p}, \quad (1.28)$$

in which k_p and k are the thermal conductivities of the particle material respectively and fluid. Hence thermophoresis diffusion flux is given by

$$\mathbf{S}_{p,T} = -\rho_p D_T \frac{\nabla T}{T}, \quad (1.29)$$

where

$$D_T = \frac{\tilde{\gamma} \mu C}{\rho}, \quad (1.30)$$

which is the thermophoresis diffusion coefficient. From Eqs. (1.24) and (1.29), diffusion mass flux is given by

$$\mathbf{S}_p = -\rho_p D_B \nabla C - \rho_p D_T \frac{\nabla T}{T}. \quad (1.31)$$

Thus Eq. (1.22) becomes

$$\rho C_p \frac{dT}{dt} = k \nabla^2 T + \rho_p C_p \left[D_B \nabla C \cdot \nabla T + D_T \frac{\nabla T \cdot \nabla T}{T} \right]. \quad (1.32)$$

1.3.3 Conservation of concentration

For the nanoparticles the concentration equation is

$$\frac{\partial C}{\partial t} + \mathbf{V} \cdot \nabla C = -\frac{1}{\rho_p} \nabla \cdot \mathbf{S}_p, \quad (1.33)$$

where ρ_p is the mass density of the nanoparticles, C is nanoparticles volume fraction and \mathbf{S}_p is the diffusion mass flux. Now

$$\frac{\partial C}{\partial t} + \mathbf{V} \cdot \nabla C = \nabla \cdot \left[D_B \nabla C + D_T \frac{\nabla T}{T} \right], \quad (1.34)$$

which is the concentration equation for nanofluids.

1.4 Entropy and second law of thermodynamics

1.4.1 Entropy

Entropy is a measure of disorder or randomness of molecular motion of the system. Entropy of a system increases if heat flows into the system at constant temperature and it decreases if heat leaves the system at constant temperature. It is a state function which depends on the state of system. The absolute value of entropy can't be determined however change in entropy can be determined by the relation:

$$dS = \frac{dQ}{dt}. \quad (1.35)$$

This expression shows that entropy of a system increases if heat flows into the system at constant temperature and it decreases if heat leaves the system a constant temperature.

1.4.2 Entropy in irreversible process

In nature there is no reversible process due to friction and heat transfer. Thus every thermodynamic process is irreversible. To find the entropy change for an irreversible process, we choose a path by connecting the initial and final states and calculate the entropy change by the equation:

$$S = \int_i^f \frac{dQ}{dt}. \quad (1.36)$$

1.4.3 Second law of thermodynamics

The second law of thermodynamics in terms of entropy stated as in any thermodynamic process, that proceeds from one equilibrium state to another, the entropy of the system + environment either remains unchanged or increases. For reversible process, the entropy does not change. For irreversible processes i.e., for all natural processes, the total entropy of the system must increase. It is possible that the entropy of system might decrease, but entropy of environment shows increase of magnitude. Therefore the total

change in entropy is always positive. Entropy generation consists of three sources i.e. entropy generation due to heat transfer, viscous dissipation and mass diffusion. Entropy equation is expressed as

$$N_g = \frac{k_f}{T_\infty} (\nabla T)^2 + \mu_f \Phi, \quad (1.37)$$

where

$$\Phi = \frac{1}{\mu_f} : \nabla \mathbf{u}. \quad (1.38)$$

1.5 Boundary layer expressions of non-Newtonian fluids

1.5.1 Maxwell fluid

Extra stress tensor \mathbf{S} for Maxwell fluid is

$$\left(1 + \lambda_1 \frac{D}{Dt}\right) \mathbf{S} = \mathbf{S} + \lambda \frac{D\mathbf{S}}{Dt} = \mu A_1, \quad (1.39)$$

where λ_1 signifies relaxation time, $\frac{D}{Dt}$ for covariant tensor, μ for dynamic viscosity and A_1 for first Rivlin-Erickson tensor.

For tensor rank two, vector \mathbf{b}_1 and scalar φ , we have

$$\frac{D\mathbf{S}}{Dt} = \frac{\partial \mathbf{S}}{\partial t} + (\mathbf{V} \cdot \nabla) \mathbf{S} - \mathbf{S} (\nabla \mathbf{V})^{tr} - (\nabla \mathbf{V}) \mathbf{S}, \quad (1.40)$$

$$\frac{D\mathbf{b}_1}{Dt} = \frac{\partial \mathbf{b}_1}{\partial t} + (\mathbf{V} \cdot \nabla) \mathbf{b}_1 - \mathbf{S} (\nabla \mathbf{V})^{tr} - (\nabla \mathbf{V}) \mathbf{b}_1, \quad (1.41)$$

$$\frac{D\varphi}{Dt} = \frac{\partial \varphi}{\partial t} + (\mathbf{V} \cdot \nabla) \varphi. \quad (1.42)$$

Momentum equation after boundary layer approximations leads to

$$\rho \left(1 + \lambda_1 \frac{D}{Dt}\right) \frac{d\mathbf{V}}{dt} = - \left(1 + \lambda_1 \frac{D}{Dt}\right) \nabla p + \left(1 + \lambda_1 \frac{D}{Dt}\right) (\nabla \cdot \mathbf{S}). \quad (1.43)$$

1.5.2 Thixotropic fluid

Extra stress tensor τ_{ij} for this fluid is

$$\tau_{ij} = 2\mu (\Lambda_{2d}(t)) d_{ij}. \quad (1.44)$$

Here viscosity is time-dependent through allowing the second invariant of deformation rate tensor to be time-dependent and Λ_{2d} denote the second invariant of deformation rate tensor. It is defined as

$$\Lambda_{2d} = \frac{\partial u_i}{\partial x_j} + \frac{\partial u_j}{\partial x_i}. \quad (1.45)$$

Here

$$\Lambda_{2d} = (2d_{ij})^2 = 4 \left(\left(\frac{\partial u}{\partial x} \right)^2 + \frac{1}{2} \left(\frac{\partial v}{\partial x} + \frac{\partial u}{\partial y} \right)^2 + \left(\frac{\partial v}{\partial y} \right)^2 \right) > 0. \quad (1.46)$$

For viscosity function we have

$$\mu = \mu_0 - 2R_a^* \left(\frac{\partial u}{\partial y} \right)^2 + 4R_b^* \left(u \frac{\partial u}{\partial y} \frac{\partial^2 u}{\partial x \partial y} + v \frac{\partial u}{\partial y} \frac{\partial^2 u}{\partial y^2} \right). \quad (1.47)$$

1.6 Solution methodology

It is very difficult and some times even impossible to compute the exact solutions of non-linear problems in science and engineering. Usually perturbation, Adomian decomposition and homotopy perturbation methods are used to find solutions of nonlinear equations. Besides, the homotopy analysis method (HAM) is also employed for the convergent solutions development.

1.6.1 Homotopy analysis method

The concept of homotopy was first formulated by Poincare around 1900 (Collins 2004). In topology, two functions are called homotopic if one can be "continuously deformed" into the other. Homotopy is a combination of two Greek words homos means identical and topos means place. If there exists two continuous mapping g_1 and g_2 from the topological space S into the topological space Z resulting g_1 is homotopic to g_2 . A continuous mapping G exists then

$$G : S \times [0, 1] \rightarrow Z, \quad (1.48)$$

such that for each $s \in S$

$$G(s, 0) = g_1(s), \quad G(s, 1) = g_2(s). \quad (1.49)$$

The mapping G is called the homotopy between g_1 and g_2 .

1.6.2 Solutions derivation by HAM

Homotopy analysis method (HAM)[77]-[84] is independent of large/small parameter. It also provides exemption to choose multiple ways of base functions. This method is convenient to adjust and control convergence region. For the fundamental concept of homotopy analysis technique, we assume a non-linear differential equations.

$$\mathcal{N}[u(\xi)] = 0, \quad (1.50)$$

in which \mathcal{N} stands for nonlinear operator, $u(\xi)$ for unknown function and ξ for independent parameter.

1.6.3 Zeroth-order deformation problems

$$(1 - q)\mathcal{L}[u(\xi, q) - u_0(\xi)] = q\hbar\mathcal{N}[u(\xi, q)], \quad (1.51)$$

in which q is homotopic variable i.e., $0 \leq q \leq 1$, $\hbar \neq 0$ for auxiliary variable, \mathcal{L} for linear operator and $u_0(\xi)$ for initial guess satisfying the boundary conditions. When $q = 0$ and $q = 1$ then

$$u(\xi, 0) - u_0(\xi) = 0 \quad \text{and} \quad u(\xi, 1) - u_0(\xi) = 0, \quad (1.52)$$

respectively. When q increases from 0 to 1 then $u(\xi, q)$ vary from initial solution $u_0(\xi)$ to desired solution $u(\xi)$. According to Taylor series we have

$$u(\xi, q) = u_0(\xi) + \sum_{m=1}^{\infty} u_m(\xi)q^m, \quad u_m(\xi) = \frac{1}{m!} \left. \frac{\partial^m u(\xi, q)}{\partial q^m} \right|_{q=0}. \quad (1.53)$$

1.6.4 mth order deformation problems

The resulting problems at this order are given by

$$\mathcal{L} [u_m(\xi) - \chi_m u_{m-1}(\xi)] = \hbar \mathcal{R}_m(u_{m-1}), \quad (1.54)$$

$$\mathcal{R}_m(u_{m-1}) = \frac{1}{(m-1)!} \left. \frac{\partial^{m-1} u(\xi, q)}{\partial q^{m-1}} \right|_{q=0}. \quad (1.55)$$

$$\chi_m = \begin{cases} 0, & m \leq 1 \\ 1, & m > 1 \end{cases}, \quad (1.56)$$

The solution of system can be acquired utilizing a suitable software like MATHEMATICA. If the auxiliary variable, initial guess and the auxiliary linear operator is selected accurately, the series will converge at $q = 1$. Thus

$$u(\xi) = u_0(\xi) - \sum_{m=1}^{\infty} u_m(\xi). \quad (1.57)$$

1.6.5 Solutions by OHAM

1.6.6 Optimal convergence control parameter

The non-zero auxiliary variables \hbar defines convergence portion. We can compute the minimum estimations of such variables by taking small error. In the frame of HAM, the \hbar plays a pivot role. That is why such variables refer to as convergence control parameter which differs HAM from other analytical approximation methods. In order to reduce CPU time we have applied concept of minimization by considering averaged squared residual errors [77]. It is given by

$$\varrho_m = \frac{1}{k+1} \sum_{l=0}^k \left[\mathcal{N} \left(\sum_{i=0}^m u_m(\xi) \right)_{\xi=l\delta^*\xi} \right]^2, \quad (1.58)$$

where ϱ_m is the total residual squares error.

Chapter 2

MHD flow of Ag-water nanofluid by nonlinear curved stretching sheet

The present chapter concentrates on two-dimensional flow of viscous nanofluid due to nonlinear curved stretching surface. Nanofluid is suspension of Silver(Ag) nanoparticles and water(H_2O). Magnetic field of strength (B_0^*) is applied. Apposite transformations are utilized in obtaining dimensionless expressions. Homotopy analysis method (HAM) is implemented for computations of convergent series solutions at zeroth and mth order deformations. Pressure inside the boundary layer flow induced by curved stretching surface cannot be ignored. The characteristics of volume fraction of silver nanoparticles, dimensionless radius of curvature, power-law index and magnetic parameter are discussed on pressure, velocity and skin friction coefficient. Our findings indicate that the magnitude of velocity reduces for higher silver nanoparticles volume fraction. Clearly magnitude of pressure and velocity distributions are inversely related to the dimensionless radius of curvature.

2.1 Model development

Here steady two-dimensional flow of an incompressible viscous nanofluid bounded by non-linear curved stretching sheet coiled in a circle of radius (R) is formulated. Silver nanoparticles with water as a regular base fluid is considered. Nanofluid is electrically conducted due to magnetic field of constant strength (B_0^*) applied in the r -direction.

Induced magnetic field for low magnetic Reynolds number is not entertained. We adopted curvilinear coordinates (r, x) to construct relevant equations (see Figure (2.1)). We have taken x and r -axes along and transverse direction to surface respectively. Surface has stretching velocity $u_w(x) = u_0 x^n$ where u_0 is the positive constant and n the power-law index.

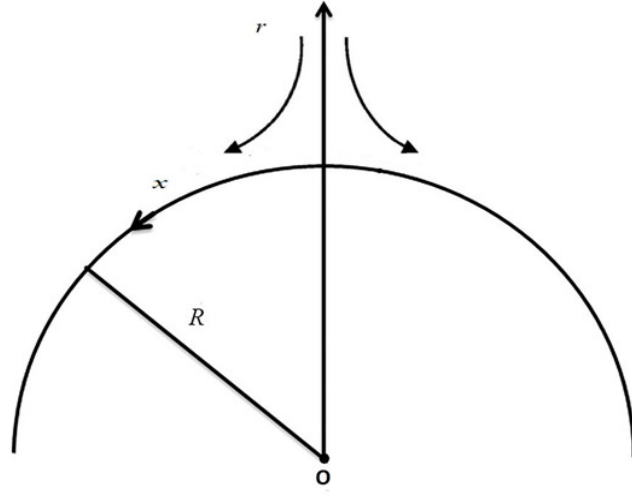


Figure 2.1: Geometry of the flow.

The boundary layer flow equations are given as:

$$\frac{\partial}{\partial r} [(r + R)v] + R \frac{\partial u}{\partial x} = 0, \quad (2.1)$$

$$\frac{u^2}{r + R} = -\frac{1}{\rho_{nf}} \frac{\partial p}{\partial r}, \quad (2.2)$$

$$\rho_{nf} \left(v \frac{\partial \tilde{u}}{\partial r} + \frac{Ru}{r + R} \frac{\partial u}{\partial x} + \frac{uv}{r + R} \right) = \mu_{nf} \left(\frac{\partial^2 u}{\partial r^2} - \frac{u}{(r + R)^2} + \frac{1}{r + R} \frac{\partial u}{\partial r} \right) - \frac{R}{r + R} \frac{\partial p}{\partial x} - \sigma_{nf} B_0^{*2} u, \quad (2.3)$$

subjected boundary conditions are [33]:

$$\begin{aligned} u &= u_0 x^n, \quad v = 0 \text{ at } r = 0, \\ u, \frac{\partial u}{\partial r} &\rightarrow 0 \text{ as } r \rightarrow \infty. \end{aligned} \quad (2.4)$$

In the above expressions velocity components along (r, x) directions are specified by (u, v) and p the pressure.

Effective dynamic viscosity of the nanofluid by Brinkman is given as [73]:

$$\mu_{nf} = \frac{\mu_f}{(1 - \phi)^{2.5}}, \quad (2.5)$$

and the density of nanofluid is

$$\rho_{nf} = (1 - \phi)\rho_f + \phi\rho_s. \quad (2.6)$$

Electrical conductivity of nanofluid is [76]:

$$\frac{\sigma_{nf}}{\sigma_f} = 1 + \frac{3 \left(\frac{\sigma_s}{\sigma_f} - 1 \right) \phi}{\left(\frac{\sigma_s}{\sigma_f} + 2 \right) - \left(\frac{\sigma_s}{\sigma_f} - 1 \right) \phi}, \quad (2.7)$$

where ϕ signifies solid volume fraction of nanoparticles, s in subscript is for nano solid particles and f in subscript for base fluid.

The thermal diffusivity of nanofluid is given by

$$\alpha_{nf} = \frac{k_{nf}}{(\rho C_p)_{nf}}, \quad (2.8)$$

where the heat capacitance of nanofluid is

$$(\rho C_p)_{nf} = (1 - \phi)(\rho C_p)_f + \phi(\rho C_p)_s. \quad (2.9)$$

Effective thermal conductivity of nanofluid for spherical nanoparticles is approximated by Maxwell Garnett Model as

$$\frac{k_{nf}}{k_f} = \frac{(k_s + 2k_f) - 2\phi(k_f - k_s)}{(k_s + 2k_f) + 2\phi(k_f - k_s)}. \quad (2.10)$$

Here μ_f indicates dynamic viscosity, ρ_f and ρ_s density of fluid and solid particles and k_s and k_f thermal conductivities of solid nanoparticles and base fluid respectively.

In order to get the solution, appropriate variables are defined as

$$\begin{aligned} u &= u_0 x^n \tilde{f}'(\xi), \quad v = -\frac{R}{r+R} \sqrt{\tilde{u}_0 \nu_f x^{n-1}} \left[\left(\frac{n+1}{2} \right) \tilde{f}(\xi) + \left(\frac{n-1}{2} \right) \xi \tilde{f}'(\xi) \right], \\ p &= \rho_f u_0^2 x^{2n} \tilde{P}(\xi), \quad \xi = \sqrt{\frac{u_0 x^{n-1}}{\nu_f}} r. \end{aligned} \quad (2.11)$$

Prime denotes differentiation with respect to ξ . Mass conservation law is automatically satisfied. After using Eq. (2.11), Eqs. (2.2) and (2.3) can be reduced as follows:

$$\frac{\partial \tilde{P}}{\partial \xi} = (1 - \phi + \phi \frac{\rho_s}{\rho_f}) \frac{\tilde{f}'^2}{\xi + K^*}, \quad (2.12)$$

$$\begin{aligned} \frac{1}{(1-\phi+\phi\frac{\rho_s}{\rho_f})} \left(\frac{2nK^*}{(\xi+K^*)} \tilde{P} + \frac{(n-1)\xi K^*}{2(\xi+K^*)} \frac{\partial \tilde{P}}{\partial \xi} \right) &= \frac{1}{(1-\phi)^{2.5}(1-\phi+\phi\frac{\rho_s}{\rho_f})} \left(\begin{aligned} &\tilde{f}''' + \frac{\tilde{f}''}{(\xi+K^*)} \\ &-\frac{\tilde{f}'}{(\xi+K^*)^2} \end{aligned} \right) \\ &- \left(\frac{(1+n)\xi+2nK^*}{2(\xi+K^*)^2} \right) K^* \tilde{f}'^2 + \frac{(n+1)K^*}{2(\xi+K^*)^2} \tilde{f} \tilde{f}' + \frac{(n+1)K^*}{2(\xi+K^*)} \tilde{f} \tilde{f}'' \\ &- M \left(\frac{\sigma_{nf}}{\sigma_f} \right) \left(\frac{1}{1-\phi+\phi\frac{\rho_s}{\rho_f}} \right) \tilde{f}', \end{aligned} \quad (2.13)$$

with

$$\begin{aligned} \tilde{f}'(0) &= 1, \quad \tilde{f}(0) = 0, \\ \tilde{f}'(\infty) &\rightarrow 0, \quad \tilde{f}''(\infty) \rightarrow 0. \end{aligned} \quad (2.14)$$

In above expressions $K^* = R\sqrt{\frac{u_0 x^{n-1}}{\nu_f}}$ denotes the dimensionless radius of curvature parameter, $M = \frac{\sigma_f B_0^{*2}}{\rho_f u_0 x^{n-1}}$ the magnetic parameter and $\text{Pr} = \frac{\nu_f (\rho C_p)_f}{k_f}$ the Prandtl number. For velocity of fluid, the pressure can be eliminated from Eqs. (2.12) and (2.13) and we get

$$\begin{aligned} &\left(\frac{1}{(1-\phi)^{2.5}(1-\phi+\phi\frac{\rho_s}{\rho_f})} \right) \left(\tilde{f}^{(iv)} + \frac{2}{(\xi+K^*)} \tilde{f}''' - \frac{\tilde{f}''}{(\xi+K^*)^2} + \frac{\tilde{f}'}{(\xi+K^*)^3} \right) \\ &+ \frac{(n+1)K^*}{2(\xi+K^*)} \tilde{f} \tilde{f}''' + \frac{(n+1)K^*}{2(\xi+K^*)^2} \tilde{f} \tilde{f}'' - \frac{(n+1)K^*}{2(\xi+K^*)^3} \tilde{f} \tilde{f}' - \frac{(3n-1)}{2(\xi+K^*)} K^* \tilde{f}' \tilde{f}'' \\ &- \frac{(3n-1)K^*}{2(\xi+K^*)^2} \tilde{f}'^2 - M \left(\frac{\sigma_{nf}}{\sigma_f} \right) \left(\frac{1}{(1-\phi+\phi\frac{\rho_s}{\rho_f})} \right) \left(\frac{\tilde{f}'}{(\xi+K^*)} + \tilde{f}'' \right) = 0. \end{aligned} \quad (2.15)$$

Through Eq. (2.13) the pressure is

$$\left(\frac{1}{(1-\phi + \phi \frac{\rho_s}{\rho_f})} \right) \frac{2nK^*}{(\xi + K^*)} \tilde{P} = \left[\begin{array}{l} \left(\frac{1}{(1-\phi)^{2.5}(1-\phi + \phi \frac{\rho_s}{\rho_f})} \right) \left(\tilde{f}''' + \frac{\tilde{f}''}{(\xi + K^*)} - \frac{\tilde{f}'}{(\xi + K^*)^2} \right) \\ + \frac{(n+1)K^*}{2(\xi + K^*)} \tilde{f} \tilde{f}'' + \frac{(n+1)K^*}{2(\xi + K^*)^2} \tilde{f} \tilde{f}' \\ - \frac{nK^*}{2(\xi + K^*)^2} \tilde{f}'^2 - M \left(\frac{\sigma_{nf}}{\sigma_f} \right) \left(\frac{1}{(1-\phi + \phi \frac{\rho_s}{\rho_f})} \right) \tilde{f}' \end{array} \right]. \quad (2.16)$$

2.1.1 Physical quantities

Skin friction coefficient characterizes the surface drag. Mathematical expression for velocity gradient in x -direction is

$$\tilde{C}_{sf} = \frac{\tau_{rx}|_{r=0}}{\rho_f u_0^2 x^{2n}}, \quad (2.17)$$

where shear stress τ_{rx} is

$$\tau_{rx} = \mu_{nf} \left(\frac{\partial u}{\partial r} - \frac{u}{r + R} \Big|_{r=0} \right). \quad (2.18)$$

Final form of skin friction coefficient can be written as follows:

$$(\text{Re}_x)^{0.5} \tilde{C}_{sf} = \frac{1}{(1-\phi)^{2.5}} \left(\tilde{f}''(0) - \frac{\tilde{f}'(0)}{K^*} \right), \quad (2.19)$$

in which $\text{Re}_x = u_0 x^{n+1} / \nu_f$ shows the local Reynolds number.

2.2 Solution derivation

Here we employed homotopic scheme initiated by Liao [77] for the computations of problem comprising Eqs. (2.12)-(2.15). For HAM solutions, we have auxiliary function ($\mathcal{H}_{\tilde{f}}$) and initial approximations ($\tilde{f}_0(\xi)$) with auxiliary linear operator ($\mathcal{L}_{\tilde{f}}$) as follows:

$$\mathcal{H}_{\tilde{f}} = \exp(-2\xi), \quad (2.20)$$

$$\tilde{f}_0(\xi) = \exp(-\xi) - \exp(-2\xi), \quad (2.21)$$

$$\mathcal{L}_{\tilde{f}} = \tilde{f}^{(iv)} - 5\tilde{f}'' + 4\tilde{f}, \quad (2.22)$$

subject to the properties

$$\mathcal{L}_{\tilde{f}} [C_1 e^\xi + C_2 e^{-\xi} + C_3 e^{2\xi} + C_4 e^{-2\xi}] = 0, \quad (2.23)$$

in which C_i ($i = 1 - 4$) indicate the constants.

2.2.1 Zeroth-order system

We write

$$(1 - q)\mathcal{L}_{\tilde{f}} [\tilde{F}(\xi; q) - \tilde{f}_0(\xi)] = q\tilde{h}_{\tilde{f}}\mathcal{H}_{\tilde{f}}\mathcal{N}_{\tilde{f}}[\tilde{F}(\xi; q)], \quad (2.24)$$

$$\tilde{F}(0; q) = 0, \quad \tilde{F}'(0; q) = 1, \quad \tilde{F}'(\infty; q) \rightarrow 0, \quad \tilde{F}''(\infty; q) \rightarrow 0, \quad (2.25)$$

Nonlinear operators are

$$\begin{aligned} \mathcal{N}_{\tilde{f}} [\tilde{F}(\xi; q)] = & \left(\frac{1}{(1 - \phi)^{2.5}(1 - \phi + \phi \frac{\rho_s}{\rho_f})} \right) \left(-\frac{\frac{\partial^4 \tilde{F}(\xi; q)}{\partial \xi^4} + \frac{2}{(\xi + K^*)} \frac{\partial^3 \tilde{F}(\xi; q)}{\partial \xi^3}}{(\xi + K^*)^2} + \frac{1}{(\xi + K^*)^3} \frac{\partial \tilde{F}(\xi; q)}{\partial \xi} \right) \\ & - M \left(\frac{\sigma_{nf}}{\sigma_f} \right) \left(\frac{1}{(1 - \phi + \phi \frac{\rho_s}{\rho_f})} \right) \left(\frac{1}{(\xi + K^*)} \frac{\partial \tilde{F}(\xi; q)}{\partial \xi} + \frac{\partial^2 \tilde{F}(\xi; q)}{\partial \xi^2} \right) \\ & + \frac{(n + 1)K^*}{2(\xi + K^*)} \tilde{F}(\xi; q) \frac{\partial^3 \tilde{F}(\xi; q)}{\partial \xi^3} + \frac{(n + 1)K^*}{2(\xi + K^*)^2} \tilde{F}(\xi; q) \frac{\partial^2 \tilde{F}(\xi; q)}{\partial \xi^2} \\ & - \frac{(n + 1)K^*}{2(\xi + K^*)^3} \tilde{F}(\xi; q) \frac{\partial \tilde{F}(\xi; q)}{\partial \xi} - \frac{(3n - 1)}{2(\xi + K^*)} K^* \frac{\partial \tilde{F}(\xi; q)}{\partial \xi} \frac{\partial^2 \tilde{F}(\xi; q)}{\partial \xi^2} \\ & - \frac{(3n - 1)\tilde{K}}{2(\xi + K^*)^2} \left(\frac{\partial \tilde{F}(\xi; q)}{\partial \xi} \right)^2 = 0, \quad (2.26) \end{aligned}$$

2.2.2 mth-order deformation systems

Here we write

$$\mathcal{L}_{\tilde{f}} [\tilde{f}_m(\xi) - \chi_m \tilde{f}_{m-1}(\xi)] = \tilde{h}_{\tilde{f}} \mathcal{R}_m^{\tilde{f}}(\xi), \quad (2.27)$$

$$\tilde{f}_m(0) = \tilde{f}'_m(0) = \tilde{f}_m(\infty) = \tilde{f}''_m(\infty) = 0, \quad (2.28)$$

$$\begin{aligned}
\mathcal{R}_{f,m}(\xi) &= \left(\frac{1}{(1-\phi)^{2.5}(1-\phi+\phi\frac{\rho_s}{\rho_f})} \right) \left(f_{m-1}^{(iv)} + \frac{2}{(\xi+K^*)} f_{m-1}''' - \frac{f_{m-1}''}{(\xi+K^*)^2} + \frac{f_{m-1}'}{(\xi+K^*)^3} \right) \\
&+ \frac{K^*}{(\xi+K^*)} \sum_{k=0}^{m-1} \left[\left(\frac{n+1}{2} \right) f_{m-1-k} f_k''' - \left(\frac{3n-1}{2} \right) f_{m-1-k}' f_k'' \right] - \frac{(n+1)K^*}{2(\xi+K^*)^3} \sum_{k=0}^{m-1} f_{m-1-k} f_k' \\
&+ \frac{K^*}{(\xi+K^*)^2} \sum_{k=0}^{m-1} \left[\left(\frac{n+1}{2} \right) f_{m-1-k} f_k'' - \left(\frac{3n-1}{2} \right) f_{m-1-k}' f_k' \right] \\
&- M \left(\frac{\sigma_{nf}}{\sigma_f} \right) \left(\frac{1}{(1-\phi+\phi\frac{\rho_s}{\rho_f})} \right) \left(\frac{f_{m-1}'}{(\xi+K^*)} + f_{m-1}'' \right), \tag{2.29}
\end{aligned}$$

$$\chi_m = \begin{cases} 0, & m \leq 1 \\ 1, & m > 1 \end{cases}, \tag{2.30}$$

The general solutions (\tilde{f}_m) comprising special solutions (\tilde{f}_m^*) are

$$\tilde{f}_m(\xi) = \tilde{f}_m^*(\xi) + C_1 e^\xi + C_2 e^{-\xi} + C_3 e^{2\xi} + C_4 e^{-2\xi}, \tag{2.31}$$

where the constants are

$$C_1 = C_3 = 0, C_2 = -C_4 - \tilde{f}_m^*(0), C_4 = \frac{\partial \tilde{f}_m^*(\xi)}{\partial \xi} \Big|_{\xi=0} + \tilde{f}_m^*(0). \tag{2.32}$$

2.3 Convergence of homotopy solutions

We have used the concept of homotopy analysis method to construct series solutions. In this method we have chance to adjust the convergence of solutions by letting favorable values of auxiliary variable $\hbar_{\tilde{f}}$. For acceptable estimations of such variable the \hbar -curve is drawn in Figure (2.2). Noted range of convergence parameter is $-0.23 \leq \hbar_{\tilde{f}} \leq -0.0$. Domain of convergence for obtained solution is ξ ($0 \leq \xi \leq \infty$) when $\hbar_{\tilde{f}} = -0.18$. Table (2.1) shows some physical properties of nanofluids. Table (2.2) is prepared to compute the convergence of $\tilde{f}''(0)$. Clearly $\tilde{f}''(0)$ converges at 13th order of approximations.

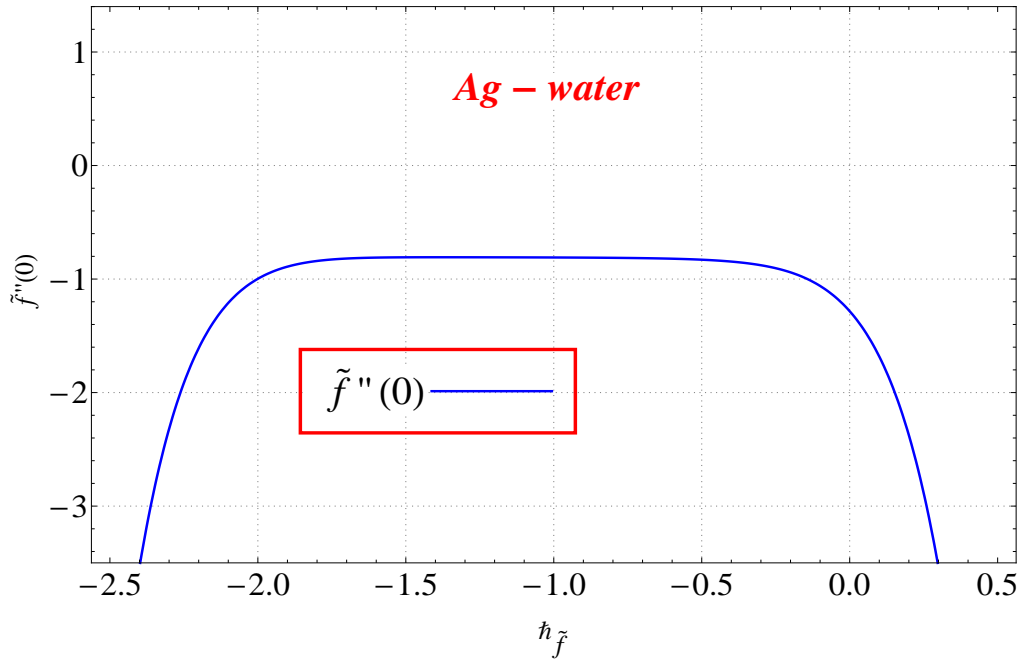


Figure 2.2: h -curve for velocity .

Table 2.1: Thermophysical properties of silver nanoparticles and water [17].

—	$k(W/m.K)$	$\rho(kg/m^3)$	$\sigma(Um)^{-1}$	$C_p(J/kgK)$
Ag(Silver)	429	10500	3.6×10^7	235
H ₂ O(Pure Water)	0.613	997.1	0.05	4179

Table 2.2: HAM solutions convergence when $\phi = 0.01, n = 0.1, K^* = 0.2, M = 0.2$ and $Pr = 6.2$.

Order of approximations	$-\tilde{f}''(0)$
1	2.9642
5	0.9403
8	0.9098
13	0.8971
17	0.8971
21	0.8971
30	0.8971
40	0.8971
50	0.8971
60	0.8971
70	0.8971

2.4 Physical results and discussion

In this section we will argue the detailed description of involved sundry variables ($0.1 \leq n \leq 0.9$), ($0.1 \leq K^* \leq 0.4$), ($0.01 \leq \phi \leq 0.05$), ($0.2 \leq M \leq 0.8$) on pressure and velocity distributions. Estimations of surface drag force is also carried out.

2.4.1 Velocity

Figure (2.3) illustrates behavior of power-law index ($n = 0.1, 0.3, 0.5, 0.9$) for velocity $\tilde{f}'(\xi)$. Velocity of the fluid declines for larger (n). It is due to the fact that positive values of (n) makes an enhancement in flatness of curved sheet and consequently the velocity decays. Behavior of dimensionless radius of curvature ($K^* = 0.1, 0.2, 0.3, 0.4$) on velocity $\tilde{f}'(\xi)$ is given in Figure (2.4). For higher values of dimensionless radius of curvature (K^*), the radius of sheet become enlarges which shows flow enhancement. This is due to the fact that curvature of the sheet significantly favors the secondary flow due to curvilinear nature of fluid flow. A secondary flow is thus superimposed on primary flow caused an increment in velocity field. Figure (2.5) depicted the effect of volume fraction of nanoparticles ($\phi = 0.01, 0.02, 0.04, 0.05$) on velocity $\tilde{f}'(\xi)$. A reduction in velocity of silver-water nanofluid is observed for positive values of (ϕ). Physically resistance between fluid particles enhances for larger (ϕ) which give rise to decreasing trend in velocity $\tilde{f}'(\xi)$. Figure (2.6) is plotted to show the impact of magnetic parameter (M) for fluid velocity $\tilde{f}'(\xi)$. A reduction in velocity is subject to higher values of ($M = 0.2, 0.4, 0.6, 0.8$). Drag force (which is known as Lorentz force) is produced due to application of magnetic field. Such force has ability to retard the fluid flow.

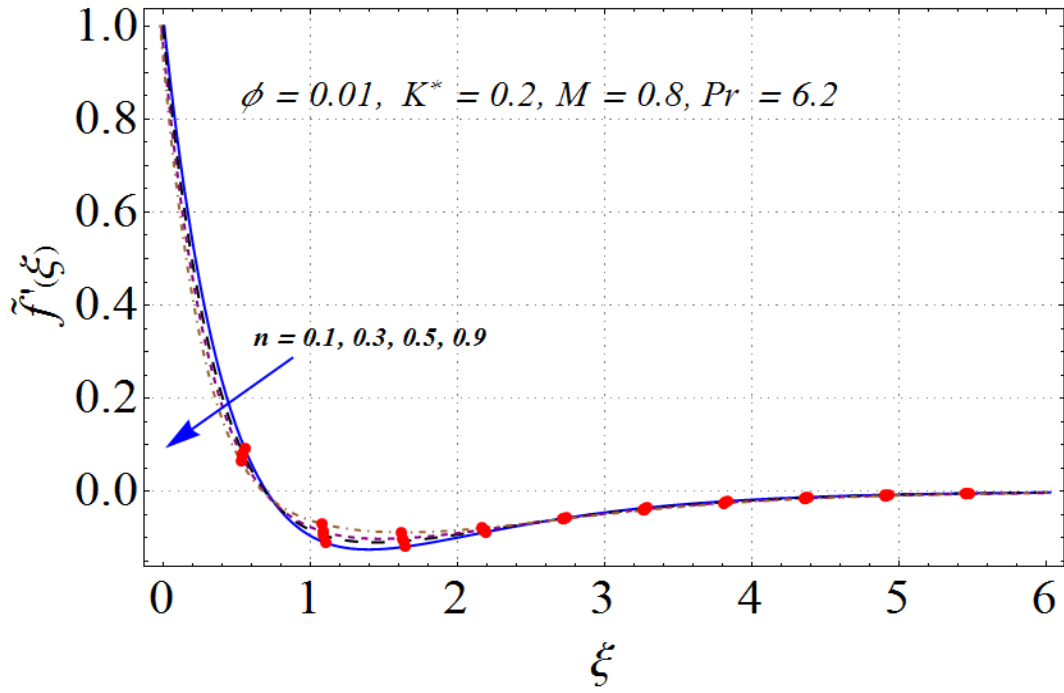


Figure 2.3: Variation of n on $\tilde{f}'(\xi)$.

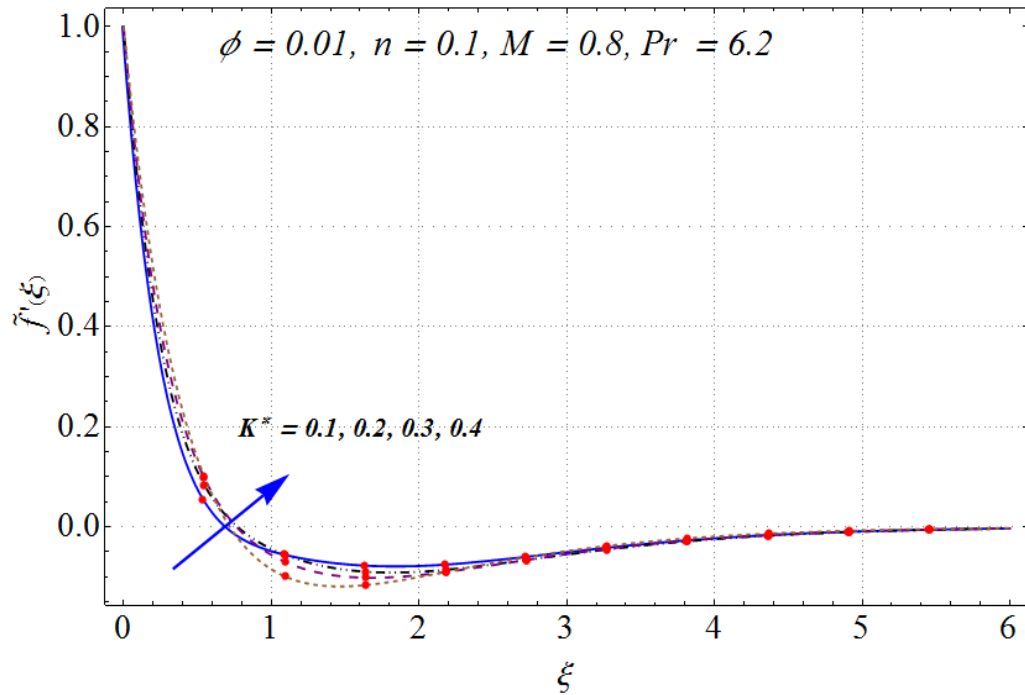


Figure 2.4: Variation of K^* on $\tilde{f}'(\xi)$

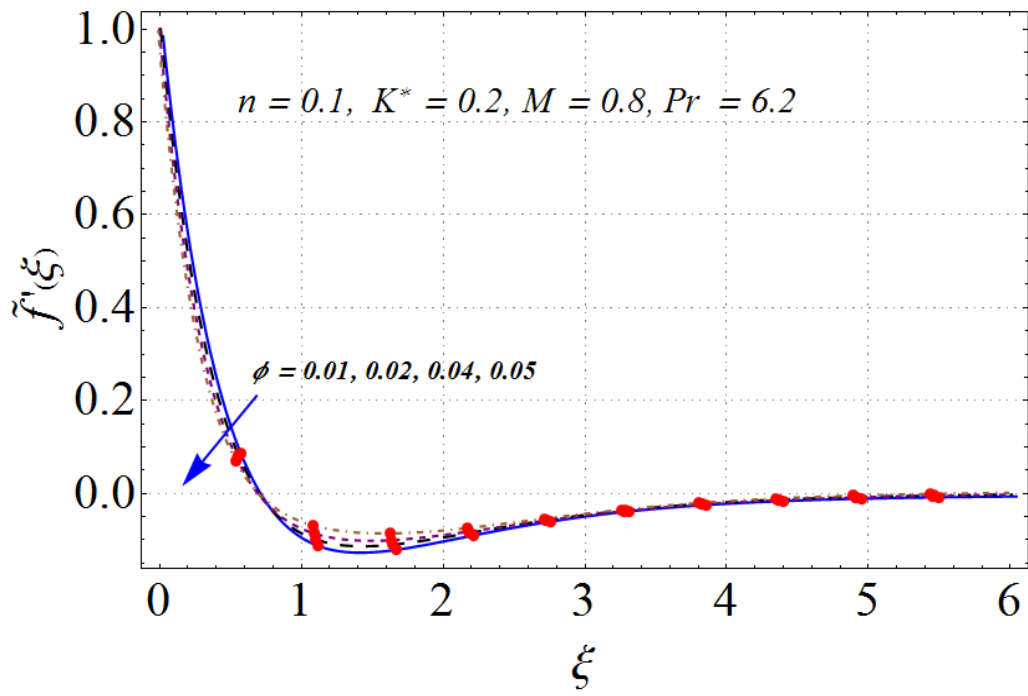


Figure 2.5: Variation of ϕ on $\tilde{f}'(\xi)$.

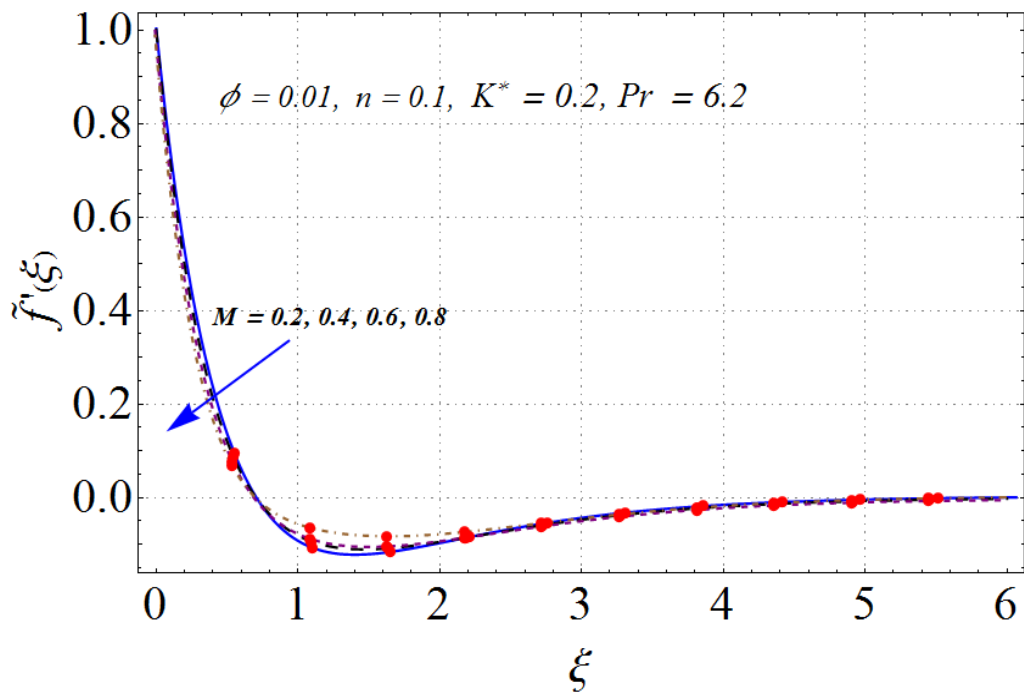


Figure 2.6: Variation of M on $\tilde{f}'(\xi)$.

2.4.2 Pressure

Figure (2.7) interprets the features of power-law index ($n = 0.1, 0.3, 0.6, 0.9$) on pressure $\tilde{P}(\xi)$ when $K^* = 0.1$, $M = 0.8$ and $\phi = 0.01$ are fixed. A dual behavior is noticed for pressure $\tilde{P}(\xi)$. Pressure $\tilde{P}(\xi)$ reduces near the boundary while increasing trend is noticed away from the surface for higher (n). In fact higher values of stretching index (n) expanded the radius of curvature that in turns enlarges the flatness of curved surface. Moreover pressure gradually approaches to zero. Figure (2.8) is prepared to examine pressure $\tilde{P}(\xi)$ for varying dimensionless radius of curvature ($K^* = 0.1, 0.2, 0.3, 0.4$) and fixed power-law index. As expected the magnitude of pressure $\tilde{P}(\xi)$ reduces for higher (K^*). It can be explained on the basis that far away from the boundary, the pressure approaches a constant value. This is because of when we move away from surface the streamlines of the flow behave in same manner as in flow over a flat stretching sheet. Notably in this case the variation of pressure inside the boundary layer cannot be neglected like a flat stretching.

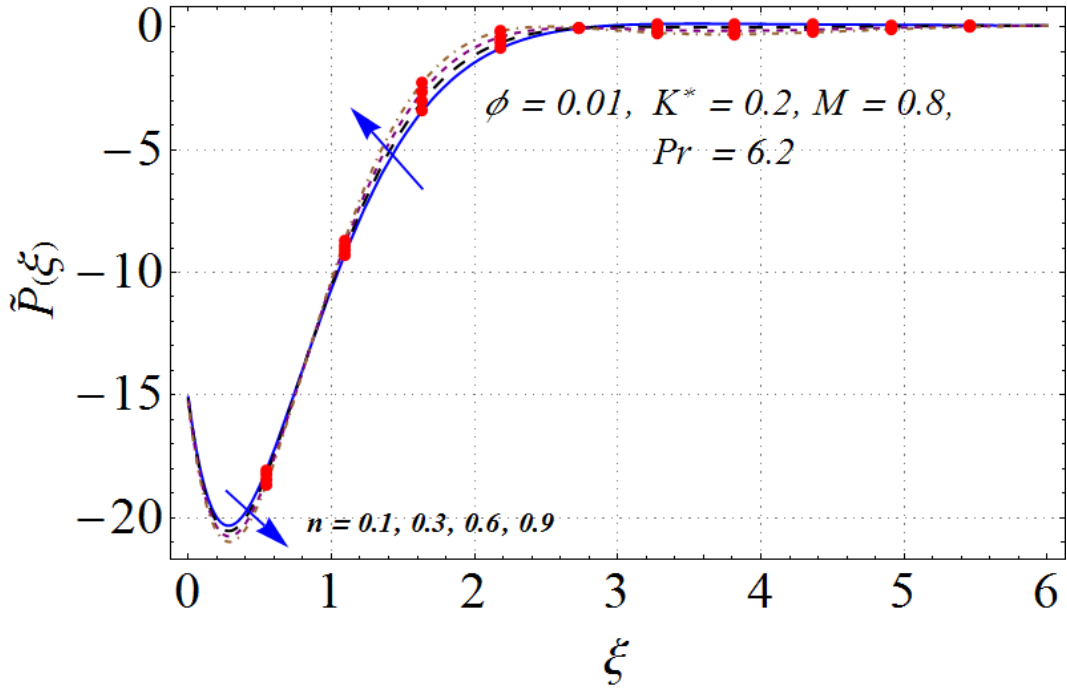
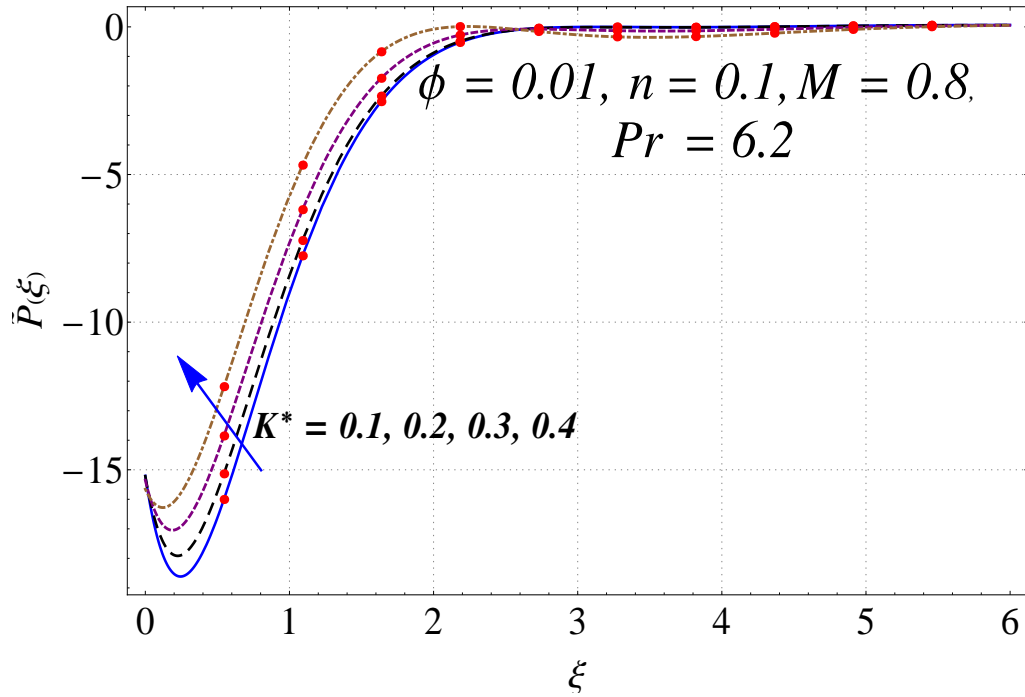


Figure 2.7: Variation of n on $\tilde{P}(\xi)$.

Figure 2.8: Variation of K^* on $\tilde{P}(\xi)$.

2.4.3 Skin friction coefficient

Skin friction coefficient $(Re_x)^{0.5} \tilde{C}_{sf}$ is computed in Table (2.3). It is noted that surface drag force enhances for power-law index and magnetic parameter while it reduces for dimensionless radius of curvature.

Table 2.3: Behaviors of n, K^* and M on skin friction coefficient for Ag-water nanofluid.

n	K^*	M	$(Re_x)^{0.5} \tilde{C}_{sf}$
0.1	0.2	0.8	0.105
0.2	—	—	0.128
0.3	—	—	0.143
0.5	—	—	0.204
—	0.1	—	0.105
—	0.2	—	0.085
—	0.4	—	0.074
—	0.6	—	0.033
—	—	0.2	0.105
—	—	0.4	0.255
—	—	0.6	0.474
—	—	0.9	0.749

2.4.4 Comparative study

Table (2.4) is constructed to verify the present results with the help of previous literature. The results are found in good agreement.

Table 2.4: Comparative values of skin friction coefficient when $n = 0.1$.

K^*	Sajid et al. [30]	Sanni et al. [33]	Present study
5	0.7576	1.1576	1.1578
10	0.8375	1.0734	1.0734
20	0.9356	1.0355	1.0351
50	0.9741	1.0414	1.0411
100	0.9870	1.0070	1.0069
1000	0.9988	1.0009	1.0011
∞	1	1	1

2.5 Conclusions

Hydromagnetic flow of silver-water nanofluid due to non-linear curved stretching surface is reported in this chapter. The important points are highlighted below.

- Pressure has dual behavior across power-law index.
- Higher values of dimensionless radius of curvature correspond to flat stretching surface.
- Velocity $\tilde{f}'(\xi)$ is decreasing function of volume fraction of nanoparticles and magnetic parameter.
- Dimensionless radius of curvature reduce the surface drag force while opposite scenario is noticed for power-law index and magnetic parameter.

Chapter 3

MHD convective flow of Fe_3O_4 -water nanofluid by non-linear curved stretching sheet

This chapter is devoted to analyze magnetohydrodynamic flow of ferrofluid due to non-linear curved stretching sheet. Ferrofluid comprises water and magnetite (Fe_3O_4) nanoparticles. Flow saturates porous medium. Heat transfer characteristics are studied by thermal radiation, heat generation/absorption and convective boundary conditions. Governing problem are made dimensionless. The obtained non-linear systems are handled by means of homotopy analysis method. Convergence intervals for solution are analyzed. Behavior of different variables on velocity and temperature are studied by plotting graphs. Moreover, the velocity and temperature gradients are also calculated and analyzed.

3.1 Mathematical formulation

Here we examine two-dimensional flow of an incompressible ferrofluid by non-linear curved stretching sheet. Magnetite (Fe_3O_4) nanoparticles suspended in water are known as ferrofluid. Curvilinear coordinates (r, x) are used to model governing equations. Stretching velocity taken in x -direction is $u = u_w$. Electrically conducting fluid is considered in the presence of magnetic field. Induced magnetic field is ignored. Effects of porous medium, thermal radiation and heat generation/absorption are also accounted. Further, the sur-

face exhibits convective boundary condition. The bottom surface of sheet is heated by convection from a hot fluid at temperature T_f while ambient fluid temperature is T_∞ . We have

$$\frac{\partial}{\partial r} [(r + R)v] + R \frac{\partial u}{\partial x} = 0, \quad (3.1)$$

$$\frac{u^2}{r + R} = -\frac{1}{\rho_{nf}} \frac{\partial p}{\partial r}, \quad (3.2)$$

$$\begin{aligned} \rho_{nf} \left(v \frac{\partial u}{\partial r} + \frac{Ru}{r + R} \frac{\partial u}{\partial x} + \frac{uv}{r + R} \right) &= -\frac{R}{r + R} \frac{\partial p}{\partial x} + \mu_{nf} \left(\frac{\partial^2 u}{\partial r^2} - \frac{u}{(r + R)^2} + \frac{1}{r + R} \frac{\partial u}{\partial r} \right) \\ &\quad - \sigma_{nf} B_0^{*2} u - \frac{\mu_{nf}}{\kappa_p} u, \end{aligned} \quad (3.3)$$

$$\begin{aligned} (\rho C_p)_{nf} \left(v \frac{\partial T}{\partial r} + \frac{Ru}{r + R} \frac{\partial T}{\partial x} \right) &= k_{nf} \left[\left(\frac{\partial^2 T}{\partial r^2} + \frac{1}{r + R} \frac{\partial T}{\partial r} \right) \right] \\ &\quad - \frac{1}{r + R} \left(\frac{\partial}{\partial r} (r + R) q_h \right) + Q_0 (T - T_\infty), \end{aligned} \quad (3.4)$$

with boundary conditions

$$\begin{aligned} u &= u_0 x^n, \quad v = 0, \quad -k_{nf} \frac{\partial T}{\partial r} = h_f (T_f - T) \quad \text{at } r = 0, \\ u, \frac{\partial u}{\partial r} &\rightarrow 0, \quad T \rightarrow T_\infty \quad \text{as } r \rightarrow \infty. \end{aligned} \quad (3.5)$$

Here (u, v) are velocity components in the radial r and transverse x directions, $u_0 > 0$ the stretching constant, p the pressure and h_f the heat transfer coefficient. According to Rosseland's approximation, the radiative heat flux q_h is

$$q_h = -\frac{4\sigma^* \partial T^4}{3k^* \partial r}, \quad (3.6)$$

in which k^* denotes mean absorption coefficient and σ^* the Stefan-Boltzmann constant. Expanding the term T^4 as a linear function of temperature in Taylor series about \tilde{T}_∞ . We have

$$T^4 \cong 4T_\infty^3 T - 3T_\infty^4. \quad (3.7)$$

After using Eqs. (3.6) and (3.7). Eq. (3.4) takes the form

$$\left(v \frac{\partial T}{\partial r} + \frac{Ru}{r+R} \frac{\partial T}{\partial x} \right) = \frac{1}{r+R} \left(\alpha_{nf} + \frac{1}{(\rho C_p)_{nf}} \frac{16\sigma^* T_\infty^3}{3k_f k^*} \right) \left[\left(\frac{\partial T}{\partial r} + (r+R) \frac{\partial^2 T}{\partial r^2} \right) \right]. \quad (3.8)$$

Considering

$$\begin{aligned} u &= u_0 x^n \tilde{f}'(\xi), \quad v = -\frac{R}{r+R} \sqrt{u_0 \nu_f x^{n-1}} \left[\left(\frac{n+1}{2} \right) \tilde{f}(\xi) + \left(\frac{n-1}{2} \right) \xi \tilde{f}'(\xi) \right], \\ p &= \rho_f u_0^2 x^{2n} \tilde{P}(\xi), \quad \tilde{\theta} = \frac{T - T_\infty}{T_f - T_\infty}, \quad \xi = \sqrt{\frac{u_0 x^{n-1}}{\nu_f}} r, \end{aligned} \quad (3.9)$$

continuity equation is automatically satisfied and Eqs. (3.2)-(3.3) and (3.8) can be reduced as follows:

$$\frac{\partial \tilde{P}}{\partial \xi} = (1 - \phi + \phi \frac{\rho_s}{\rho_f}) \frac{\tilde{f}'^2}{\xi + K^*}. \quad (3.10)$$

$$\begin{aligned} \frac{1}{(1 - \phi + \phi \frac{\rho_s}{\rho_f})} \left(\frac{2nK^*}{(\xi + K^*)} \tilde{P} + \frac{(n-1)\xi K^*}{2(\xi + K^*)} \frac{\partial \tilde{P}}{\partial \xi} \right) &= \frac{1}{(1-\phi)^{2.5} (1-\phi + \phi \frac{\rho_s}{\rho_f})} \left(\frac{\tilde{f}'''}{(\xi + K^*)} + \frac{\tilde{f}''}{(\xi + K^*)} \right) \\ &\quad - \frac{(1+n)\xi + 2nK^*}{2(\xi + K^*)^2} K^* \tilde{f}'^2 + \frac{(n+1)K^*}{2(\xi + K^*)^2} \tilde{f} \tilde{f}' \\ &\quad + \frac{(n+1)K^*}{2(\xi + K^*)} \tilde{f} \tilde{f}'' - M \frac{\left(\frac{\sigma_{nf}}{\sigma_f} \right)}{(1-\phi + \phi \frac{\rho_s}{\rho_f})} \tilde{f}', \end{aligned} \quad (3.11)$$

$$\frac{1}{(1 - \phi + \phi \frac{(\rho C_p)_s}{(\rho C_p)_f})} \left[\frac{1}{\text{Pr}} \left(\frac{k_{nf}}{k_f} + R_D \right) \left(\tilde{\theta}'' + \frac{\tilde{\theta}'}{\xi + K^*} \right) + Q \tilde{\theta} \right] + \left(\frac{(n+1)K^*}{2(\xi + K^*)} \tilde{f} \tilde{\theta}' \right) = 0, \quad (3.12)$$

with

$$\begin{aligned} \tilde{f}'(0) = 1, \quad \tilde{f}(0) = 0, \quad \tilde{\theta}'(0) &= -\frac{k_f}{k_{nf}} B_T \left(1 - \tilde{\theta}(0) \right), \\ \tilde{f}'(\infty) \rightarrow 0, \quad \tilde{f}''(\infty) \rightarrow 0, \quad \tilde{\theta}(\infty) &\rightarrow 0. \end{aligned} \quad (3.13)$$

The dimensionless variables in above equations are defined as $\lambda = \frac{\nu_f}{\kappa_p u_0 x^{n+1}}$ which signifies the permeability parameter, $M = \frac{\sigma_f B_0^2}{\rho_f u_0 x^{n+1}}$ the magnetic parameter, $\text{Pr} = \frac{\nu_f (\rho C_p)_f}{k_f}$ the Prandtl number, $R_D = \frac{16\sigma^* T_\infty^3}{3k_f k^*}$ the radiation parameter, $B_T = \frac{h_f}{k_f} \sqrt{\frac{\nu_f}{u_0 x^{n-1}}}$ the thermal

Biot number, $Q = \frac{Q_0}{u_0 x^{n+1} (\rho C_p)_f}$ the heat generation /absorption coefficient and $K^* = \sqrt{\frac{u_0 x^{n-1}}{\nu_f}} R$ the dimensionless radius of curvature. Now eliminating pressure between Eqs. (3.10) and (3.11) we obtain

$$\begin{aligned} & \left(\frac{1}{(1-\phi)^{2.5}(1-\phi+\phi\frac{\rho_s}{\rho_f})} \right) \left(\frac{\tilde{f}^{(iv)} + \frac{2}{(\xi+K^*)}\tilde{f}''' - \frac{\tilde{f}''}{(\xi+K^*)^2}}{+\frac{\tilde{f}'}{(\xi+K^*)^3} - \lambda \left(\frac{\tilde{f}'}{(\xi+K^*)} + \tilde{f}'' \right)} \right) \\ & + \frac{(n+1)K^*}{2(\xi+K^*)}\tilde{f}\tilde{f}''' + \frac{(n+1)K^*}{2(\xi+K^*)^2}\tilde{f}\tilde{f}'' - \frac{(n+1)K^*}{2(\xi+K^*)^3}\tilde{f}\tilde{f}' \\ & - \frac{(3n-1)K^*}{2(\xi+K^*)^2}\tilde{f}'^2 - \frac{(3n-1)}{2(\xi+K^*)}K^*\tilde{f}'\tilde{f}'' \\ & - M \left(\frac{\left(\frac{\sigma_{nf}}{\sigma_f} \right)}{(1-\phi+\phi\frac{\rho_s}{\rho_f})} \right) \left(\frac{\tilde{f}'}{(\xi+K^*)} + \tilde{f}'' \right) = 0, \end{aligned} \quad (3.14)$$

$$\left(\frac{1}{(1-\phi+\phi\frac{\rho_s}{\rho_f})} \right) \frac{2nK^*}{(\xi+K^*)} \tilde{P} = \left[\begin{array}{l} \left(\frac{1}{(1-\phi)^{2.5}(1-\phi+\phi\frac{\rho_s}{\rho_f})} \right) \left(\frac{\tilde{f}''' + \frac{\tilde{f}''}{(\xi+K^*)}}{-\frac{\tilde{f}'}{(\xi+K^*)^2} - \lambda\tilde{f}'} \right) \\ + \frac{(n+1)K^*}{2(\xi+K^*)}\tilde{f}\tilde{f}'' + \frac{(n+1)K^*}{2(\xi+K^*)^2}\tilde{f}\tilde{f}' \\ - \frac{nK^*}{2(\xi+K^*)^2}\tilde{f}'^2 - M \left(\frac{\left(\frac{\sigma_{nf}}{\sigma_f} \right)}{(1-\phi+\phi\frac{\rho_s}{\rho_f})} \right) \tilde{f}' \end{array} \right]. \quad (3.15)$$

3.1.1 Physical quantities of curiosity

Mathematically coefficient of skin friction is defined as

$$\tilde{C}_{sf} = \frac{\tau_{rs}|_{r=0}}{\rho_f u_0^2 x^{2n}}, \quad (3.16)$$

where wall shear stress τ_{rs} is given by

$$\tau_{rx} = \mu_{nf} \left(\frac{\partial u}{\partial r} - \frac{u}{r+R} \right) \Big|_{r=0}. \quad (3.17)$$

In dimensionless form

$$(\text{Re}_x)^{0.5} \tilde{C}_{sf} = \frac{1}{(1-\phi)^{2.5}} \left(\tilde{f}''(0) - \frac{\tilde{f}'(0)}{K^*} \right). \quad (3.18)$$

It is the ratio of heat transferred through convection (fluid motion) to the heat transferred through conduction (if the fluid is stagnant). Mathematically

$$\tilde{N}_u = \frac{xq_w}{k_f(T_f - T_\infty)}, \quad (3.19)$$

here heat flux q_w is given as

$$q_w = - \left(k_{nf} + \frac{16\sigma^* T_\infty^3}{3k^*} \right) \frac{\partial T}{\partial r} \Big|_{r=0}. \quad (3.20)$$

In dimensionless form

$$(\text{Re}_x)^{-0.5} \tilde{N}_u = - \left(\frac{k_{nf}}{k_f} + R_D \right) \tilde{\theta}'(0), \quad (3.21)$$

in which $(\text{Re}_x) = u_0 x^{n+1} / \nu_f$ denotes the Reynolds number.

3.2 Computations of series solutions

To compute solutions of given problem, we have employed homotopic scheme. For that purpose auxiliary functions $(\mathcal{H}_{\tilde{f}}, \mathcal{H}_{\tilde{\theta}})$, initial approximation $(\tilde{f}_0(\xi), \tilde{\theta}_0(\xi))$ and Linear operator $(\mathcal{L}_{\tilde{f}}, \mathcal{L}_{\tilde{\theta}})$ are given as:

$$\mathcal{H}_{\tilde{f}} = \exp(-2\xi), \mathcal{H}_{\tilde{\theta}} = \exp(-2\xi), \quad (3.22)$$

$$\tilde{f}_0(\xi) = \exp(-\xi) - \exp(-2\xi), \tilde{\theta}_0(\exp(-\xi)) = \frac{B_T}{1 + B_T} \exp(-\xi), \quad (3.23)$$

$$\mathcal{L}_{\tilde{f}} = \tilde{f}^{(iv)} - 5\tilde{f}'' + 4\tilde{f}, \mathcal{L}_{\tilde{\theta}} = \tilde{\theta}'' - \tilde{\theta}, \quad (3.24)$$

with the properties

$$\begin{aligned} \mathcal{L}_{\tilde{f}} [C_1 \exp(\xi) + C_2 \exp(-\xi)] + C_3 \exp(2\xi) + C_4 \exp(-2\xi) &= 0, \\ \mathcal{L}_{\tilde{\theta}} [C_5 \exp(\xi) + C_6 \exp(-\xi)] &= 0, \end{aligned} \quad (3.25)$$

and C_i ($i = 1 - 6$) represents the constants.

3.3 Convergence of series solutions

The concept of Liao [77] is employed to express series solutions. No doubt the auxiliary variables $\hbar_{\tilde{f}}$ and $\hbar_{\tilde{\theta}}$ have significant role to control and adjust convergence domain for

$\tilde{f}''(0)$ and $\tilde{\theta}'(0)$ in homotopy analysis method (HAM). For this purpose the \hbar curves have been organized (see Figure (3.1)). Allowed ranges for $\hbar_{\tilde{f}}$ and $\hbar_{\tilde{\theta}}$ are $-1.20 \leq \hbar_{\tilde{f}} \leq -0.85$ and $-1.5 \leq \hbar_{\tilde{\theta}} \leq -0.5$. HAM solutions converge when $\hbar_{\tilde{f}} = -1.0$ and $\hbar_{\tilde{\theta}} = -1.1$. Specific heat, density and thermal conductivity of Fe_3O_4 -water nanofluid are given in Table (3.1). Table (3.2) demonstrates the convergence of series solutions of momentum and energy constraints for Fe_3O_4 -water nanofluid. It is clear that $\tilde{f}''(0)$ and $\tilde{\theta}'(0)$ coverage at 11th and 8th order of approximations respectively.

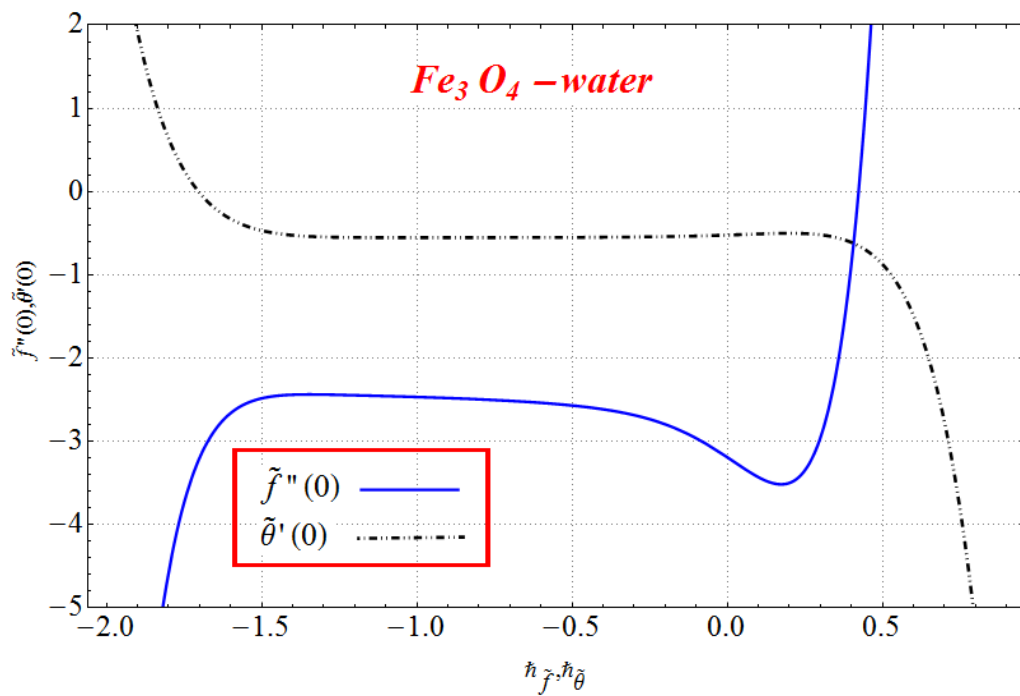


Figure 3.1: \hbar -curves for velocity and temperature fields.

Table 3.1: Thermo-physical properties of magnetite nanoparticles and water.

—	$k(W/mk)$	$\rho(kg/m^3)$	$\sigma(Um)^{-1}$	$C_p(j/m^3)$
Fe ₃ O ₄ (Iron oxide)	9.7	5180	2500	670
H ₂ O(Pure Water)	0.613	997.1	0.05	4179

Table 3.2: HAM solutions convergence when $\phi = 0.01, Q = 0.1, R_D = 0.4, \lambda = 0.5, n = M = B_T = 0.9, K^* = 1.2$ and $Pr = 6.2$.

Order of approximations	$-\tilde{f}''(0)$	$-\tilde{\theta}'(0)$
1	2.709	0.382
5	2.545	0.364
8	2.448	0.358
11	2.442	0.358
17	2.442	0.358
21	2.442	0.358
30	2.442	0.358
35	2.442	0.358
40	2.442	0.358
45	2.442	0.358
50	2.442	0.358
60	2.442	0.358

3.4 Interpretations of results

Main emphasis in this section is given to the physical illustration of emerging variables with suitable ranges ($0.1 \leq n \leq 0.9$), ($0.1 \leq K^* \leq 1.2$), ($0.01 \leq \phi \leq 0.05$), ($0.2 \leq M \leq 0.9$), ($0.1 \leq \lambda \leq 0.5$), ($0.4 \leq R_D \leq 1.0$), ($-0.4 \leq Q \leq 0.4$) and ($0.1 \leq B_T \leq 0.9$) on pressure, velocity and temperature (see Figures (3.2)-(3.13)).

3.4.1 Velocity

Figure (3.2) shows the impact of power-law index ($n = 0.1, 0.3, 0.5, 0.9$) on velocity $\tilde{f}'(\xi)$. Velocity and associated momentum layer thickness are reduced for higher (n). Influence of dimensionless radius of curvature ($K^* = 0.1, 0.3, 0.9, 1.2$) on velocity $\tilde{f}'(\xi)$ is

highlighted in Figure (3.3). Here magnitude of fluid velocity enhances when (K^*) is increased. Since for higher values of dimensionless radius of curvature (K^*), the radius of sheet enlarges which increases fluid flow. Figure (3.4) shows the consequences of volume fraction of magnetic nanoparticles ($\phi = 0.01, 0.02, 0.04, 0.05$) for velocity $\tilde{f}'(\xi)$. Velocity of fluid retards for higher (ϕ). Due to higher concentration of nanoparticles the resistance offered by fluid rises. Therefore the velocity of fluid decays. Impact of magnetite parameter ($M = 0.2, 0.4, 0.6, 0.9$) on velocity $\tilde{f}'(\xi)$ is displayed in Figure (3.5). Velocity of fluid diminishes when (M) is increased. Lorentz force is in direct relation with application of magnetic field. Higher (M) give rise to more Lorentz force so it produces resistance for fluid particles. Thus velocity $\tilde{f}'(\xi)$ reduces. Larger values of permeability parameter ($\lambda = 0.1, 0.2, 0.3, 0.5$) correspond to low velocity $\tilde{f}'(\xi)$ (see Figure (3.6)). It is noted that (λ) has inverse relation with $\tilde{f}'(\xi)$. It is concluded that medium permeability plays vital role regarding reduction of momentum layer thickness.

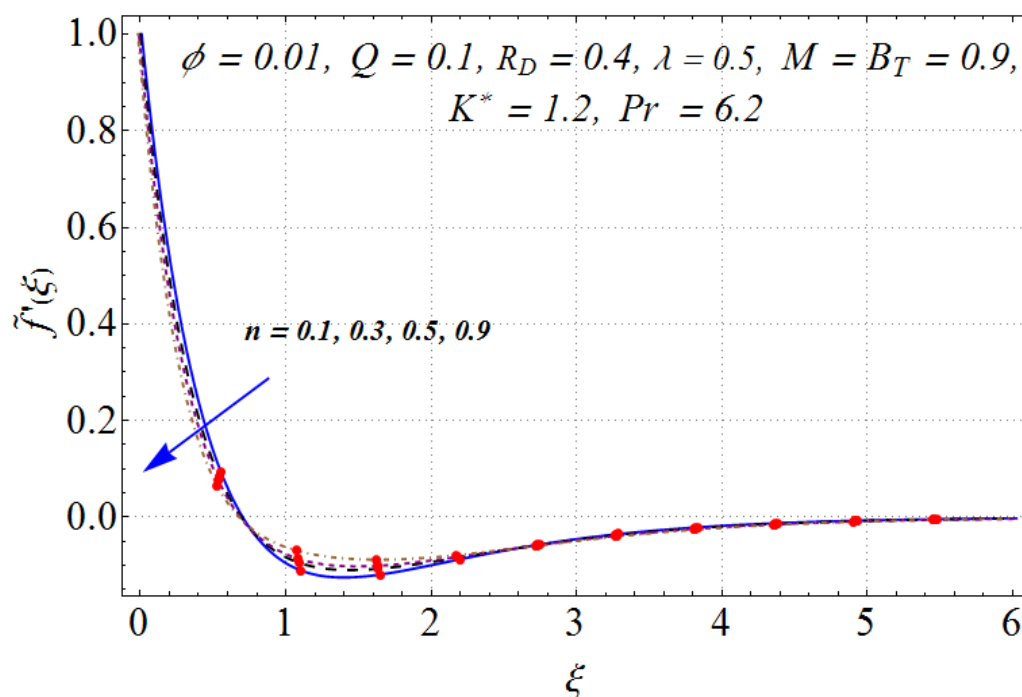


Figure 3.2: Variation of n on $\tilde{f}'(\xi)$.

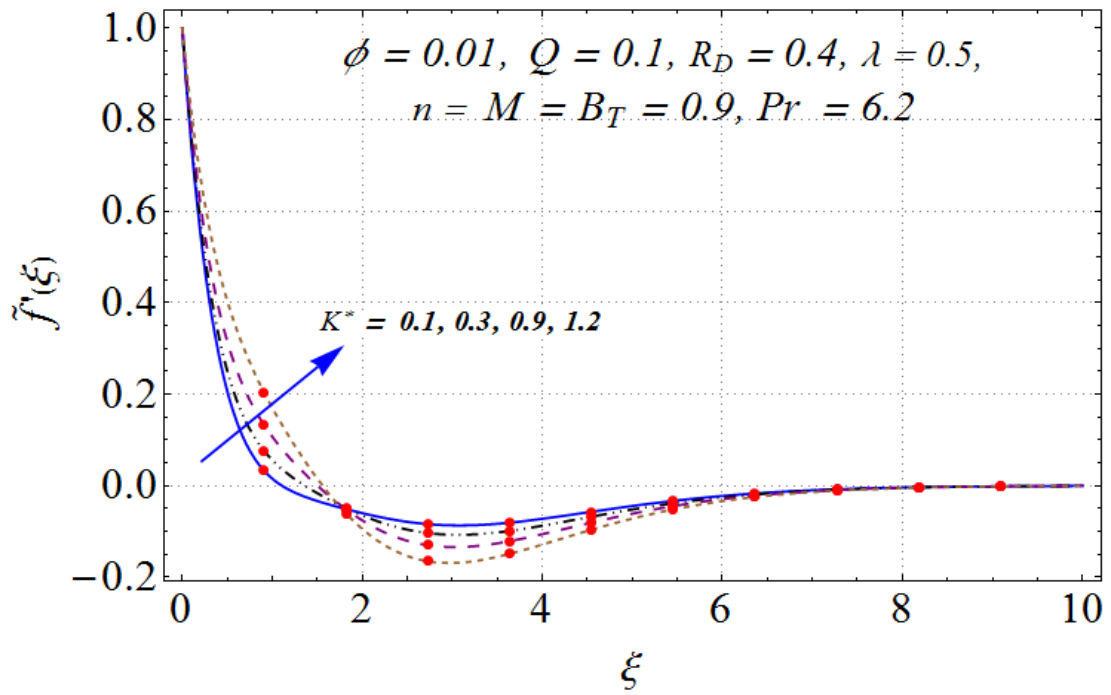


Figure 3.3: Variation of K^* on $\tilde{f}'(\xi)$.

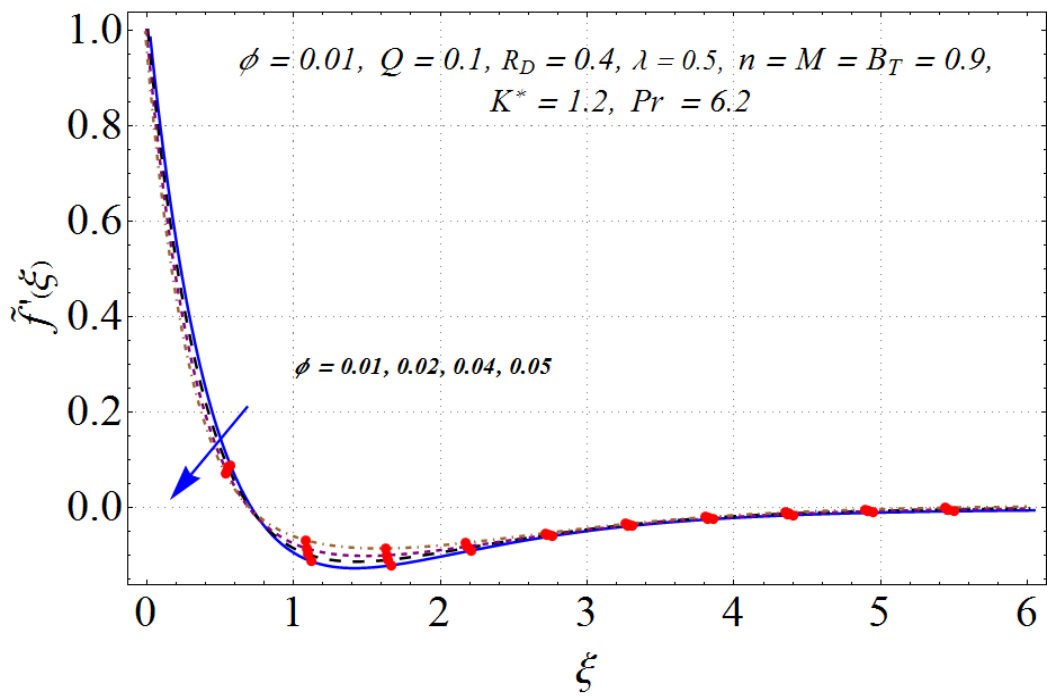


Figure 3.4: Variation of ϕ on $\tilde{f}'(\xi)$.

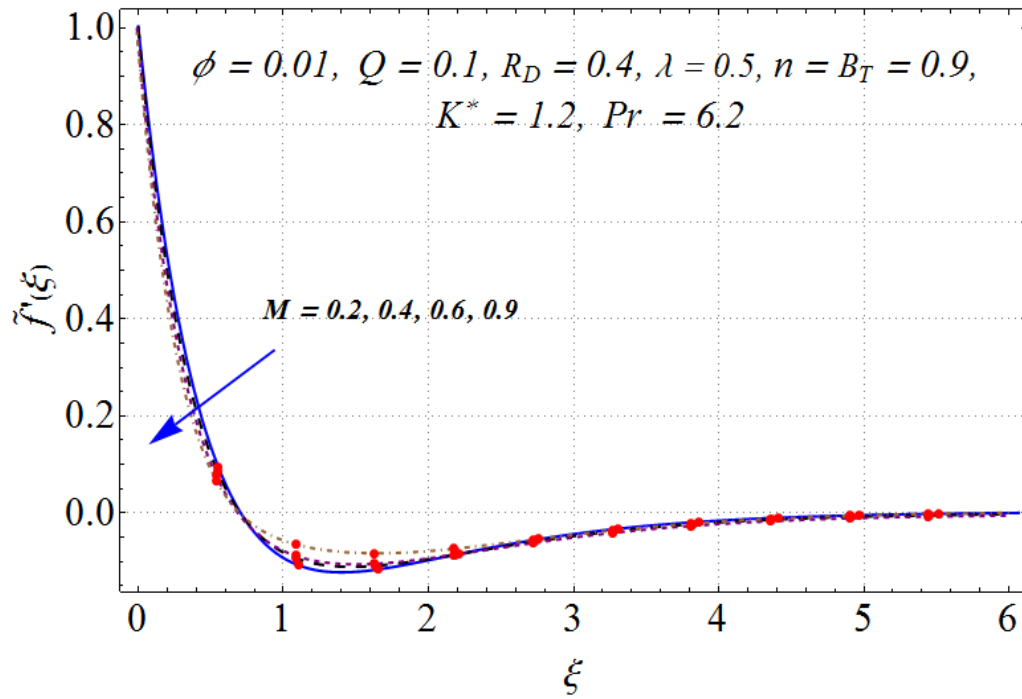


Figure 3.5: Variation of M on $\tilde{f}'(\xi)$.

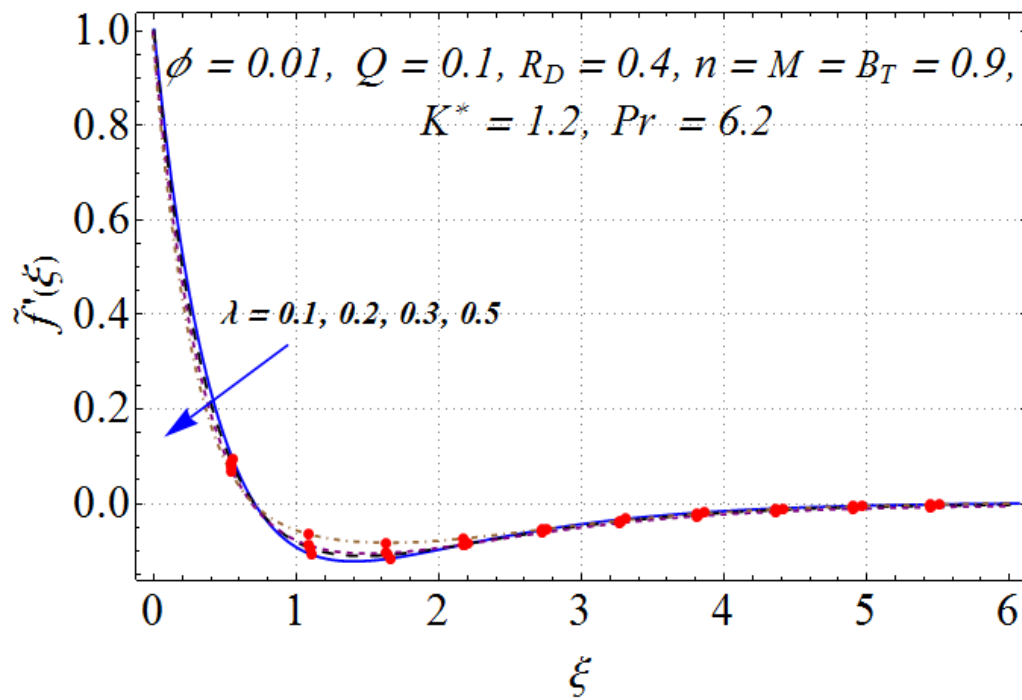


Figure 3.6: Variation of λ on $\tilde{f}'(\xi)$.

3.4.2 Pressure

Figure (3.7) is sketched to show the behavior of power-law index ($n = 0.1, 0.5, 0.6, 0.9$) on pressure $\tilde{P}(\xi)$. Here the magnitude of pressure enhances for higher (n). In fact the higher values of stretching index (increasing stretching velocity) enlarge the radius of curvature that in turns expand the flatness of curved surface. Moreover, the pressure gradually approaches to zero. Effect of larger dimensionless radius of curvature ($K^* = 0.1, 0.6, 0.9, 1.2$) on pressure $\tilde{P}(\xi)$ is scrutinized through Figure (3.8). Magnitude of pressure reduces for greater values of dimensionless radius of curvature (K^*). It is noted that pressure has constant values away from the boundary. It can be explained on the basis that when we move away from surface then the streamlines of flow behave in same manner as in case of flow past a flat stretching sheet. No variation is observed in pressure for flat stretching case i.e. $K^* \rightarrow \infty$. However, the variation of pressure inside the boundary layer cannot be ignored as in the case of flat stretching sheet.

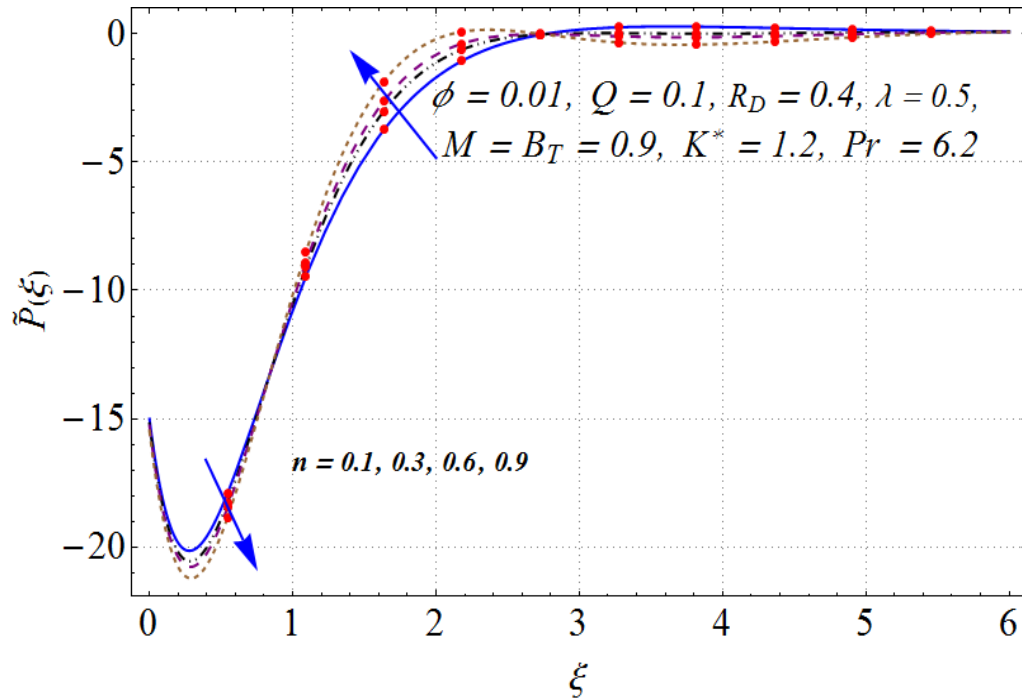


Figure 3.7: Variation of n on $\tilde{P}(\xi)$.

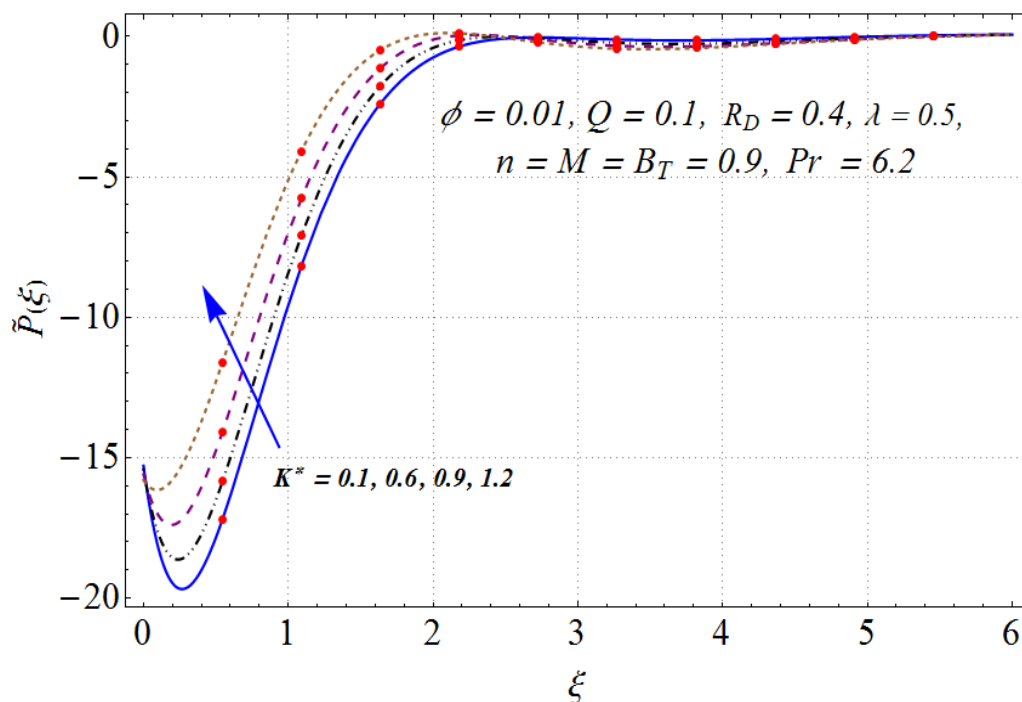


Figure 3.8: Impact of K^* on $\tilde{P}(\xi)$.

3.4.3 Temperature

Figure (3.9) provides the influence of dimensionless radius of curvature ($K^* = 0.1, 0.3, 0.9, 1.2$) on temperature $\tilde{\theta}(\xi)$. It is noted that (K^*) plays notable role regarding enhancement of thermal layer thickness. In fact for higher radius of curvature, the maximum amount of heat is transferred from sheet. As a result temperature inside the fluid rises. Contribution of volume fraction of nanoparticles (ϕ) on temperature $\tilde{\theta}(\xi)$ is captured in Figure (3.10). It predicts that the temperature $\tilde{\theta}(\xi)$ rises for larger (ϕ). The sensitivity of thermal layer thickness to volume fraction of nanoparticles (ϕ) is related with an enhancement of thermal conductivity of nanofluid. Figure (3.11) depicted the influence of radiation ($R_D = 0.4, 0.6, 0.8, 1.0$) on temperature $\tilde{\theta}(\xi)$. Temperature of fluid enhances for larger estimation of (R_D). For higher (R_D) the surface heat flux rises which is responsible of temperature $\tilde{\theta}(\xi)$ enhancement. Figure (3.12) elaborated the influence of ($Q \leq 0$) on temperature $\tilde{\theta}(\xi)$. It reveals that presence of heat generation (positive values) in thermal layer gives energy which is a responsible of temperature enhancement.

As noted the temperature of fluid decays for heat absorption parameter (negative values). Moreover ($Q = 0$) corresponds to absence of heat generation/absorption. Outcome of thermal Biot number ($B_T = 0.1, 0.3, 0.6, 0.9$) on temperature is shown in Figure (3.13). Here $\tilde{\theta}(\xi)$ has significant improvement with a small variation in (B_T). Biot number (B_T) has direct relation with heat transfer coefficient (h_f). The convective heat transfer coefficient enhances for higher (B_T). As a result temperature rises. It is also found that there is no heat transfer when $B_T = 0$.

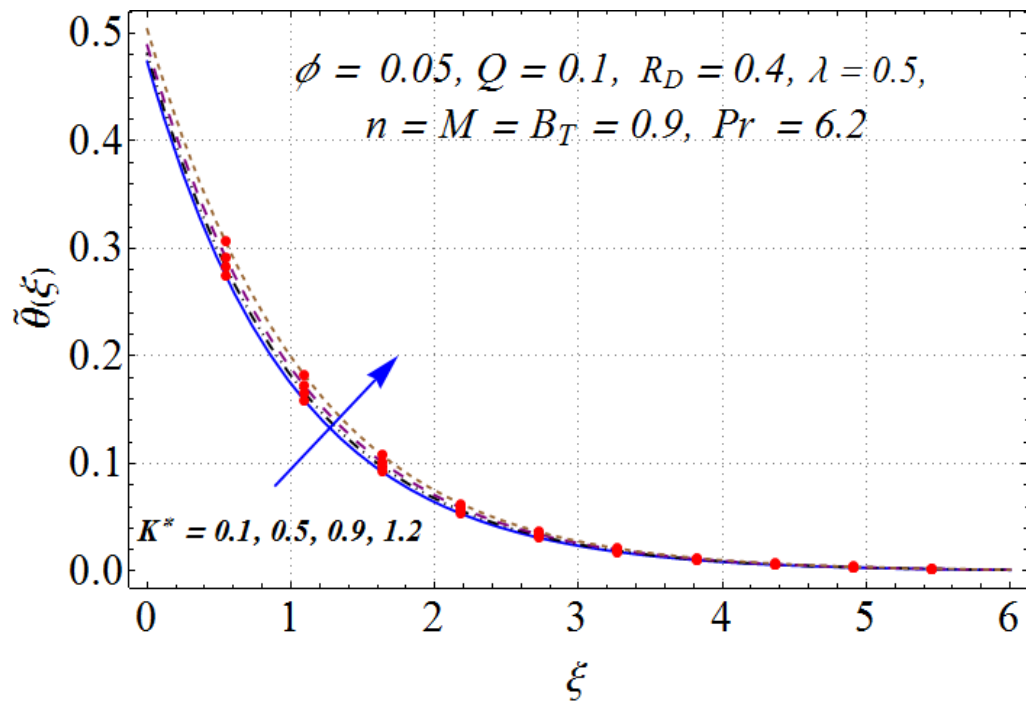


Figure 3.9: Variation of K^* on $\tilde{\theta}(\xi)$.

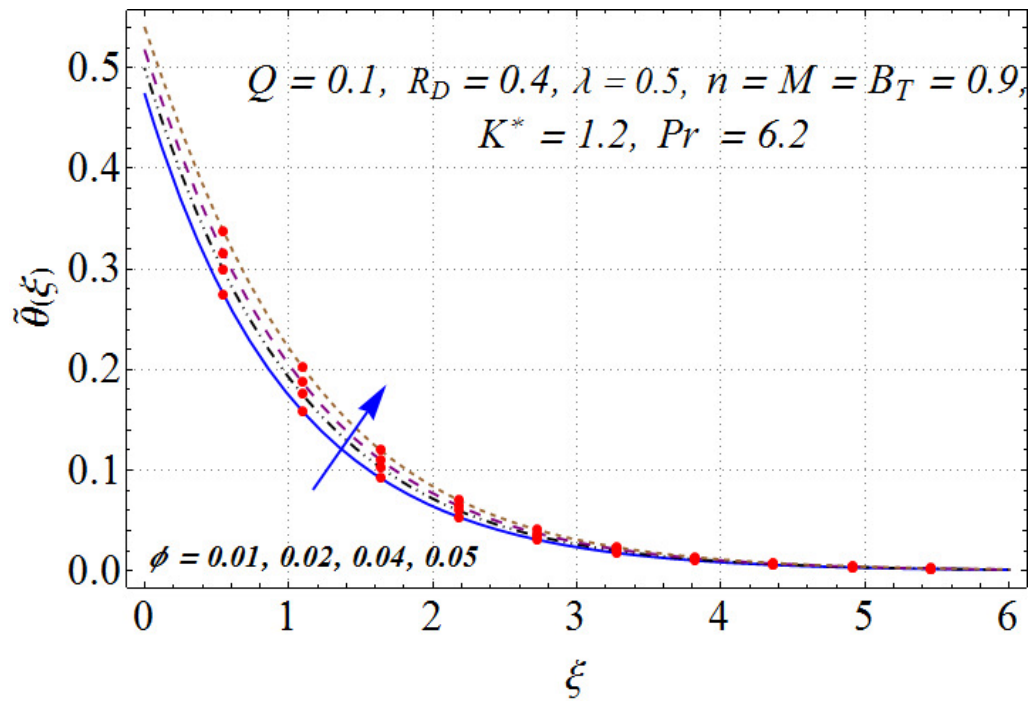


Figure 3.10: Variation of ϕ on $\tilde{\theta}(\xi)$.

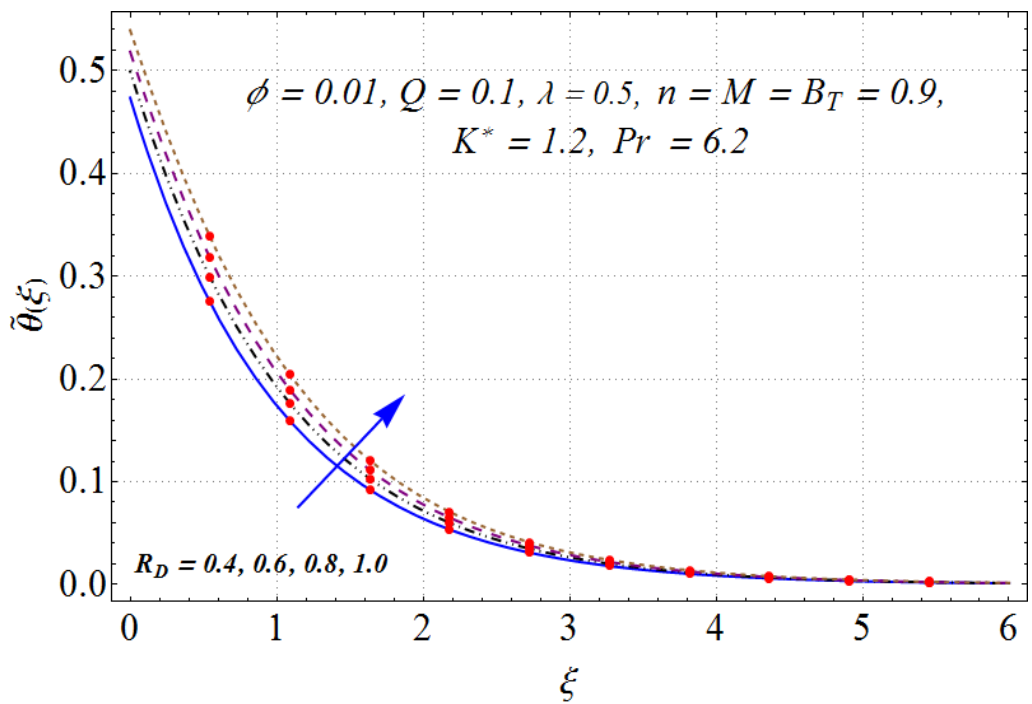


Figure 3.11: Variation of R_D on $\tilde{\theta}(\xi)$.

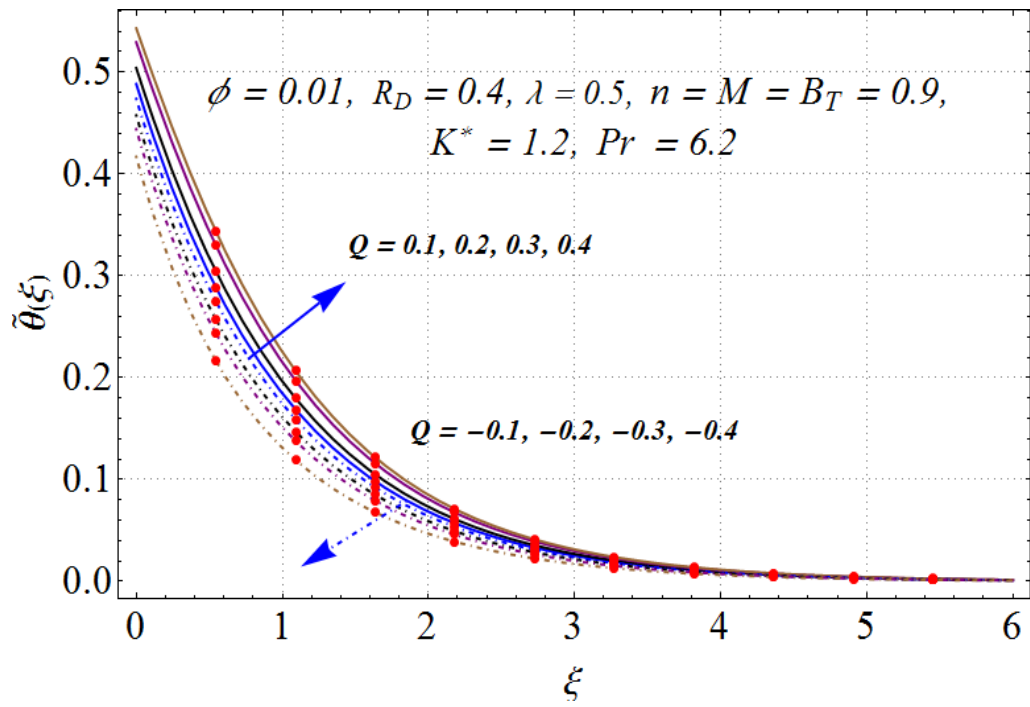


Figure 3.12: Variation of ($Q \geq 0$) on $\tilde{\theta}(\xi)$.

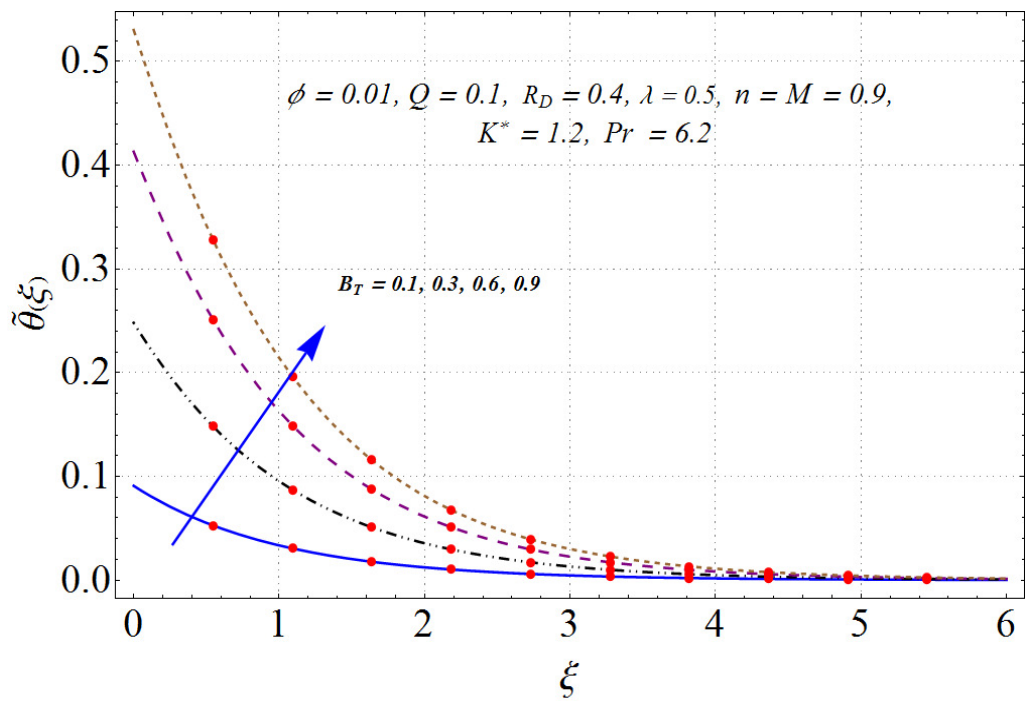


Figure 3.13: Variation of B_T on $\tilde{\theta}(\xi)$.

3.4.4 Skin friction coefficient and heat transfer rate

Magnitude of skin friction coefficient $(Re_x)^{0.5} \tilde{C}_{sf}$ decreases for higher curvature parameter K^* (see Figure (3.14)). Figure (3.15)) gives the change in magnitude of local Nusselt number for multiple values of radiation parameter (R_D). Greater radiation parameter enhances the magnitude of heat transfer coefficient.

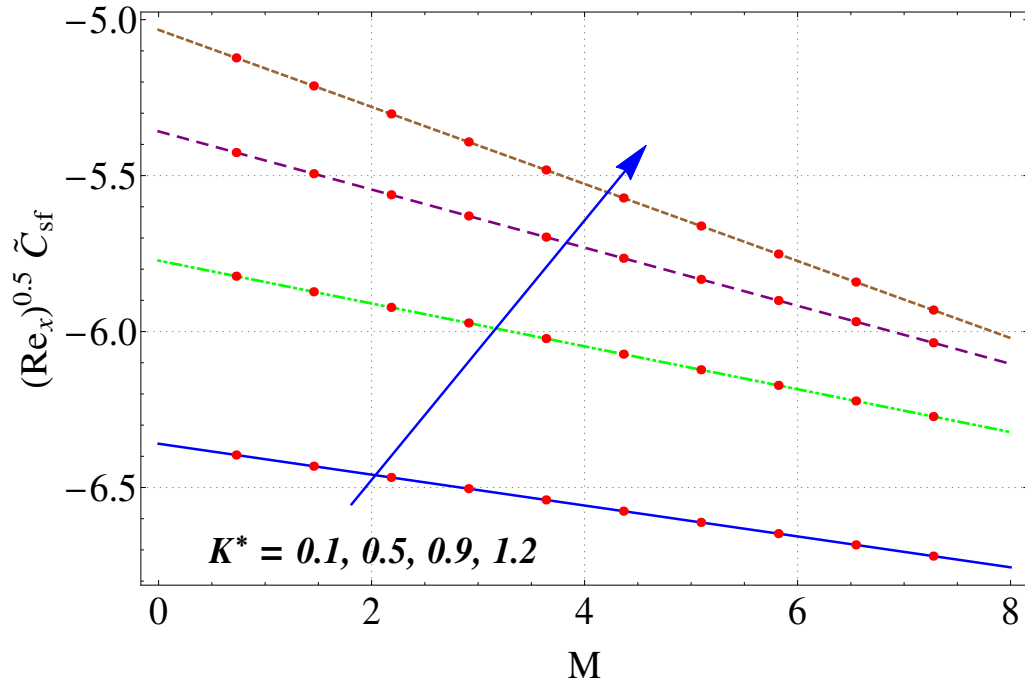


Figure 3.14: Variation of K^* on $(Re_x)^{0.5} \tilde{C}_{sf}$.

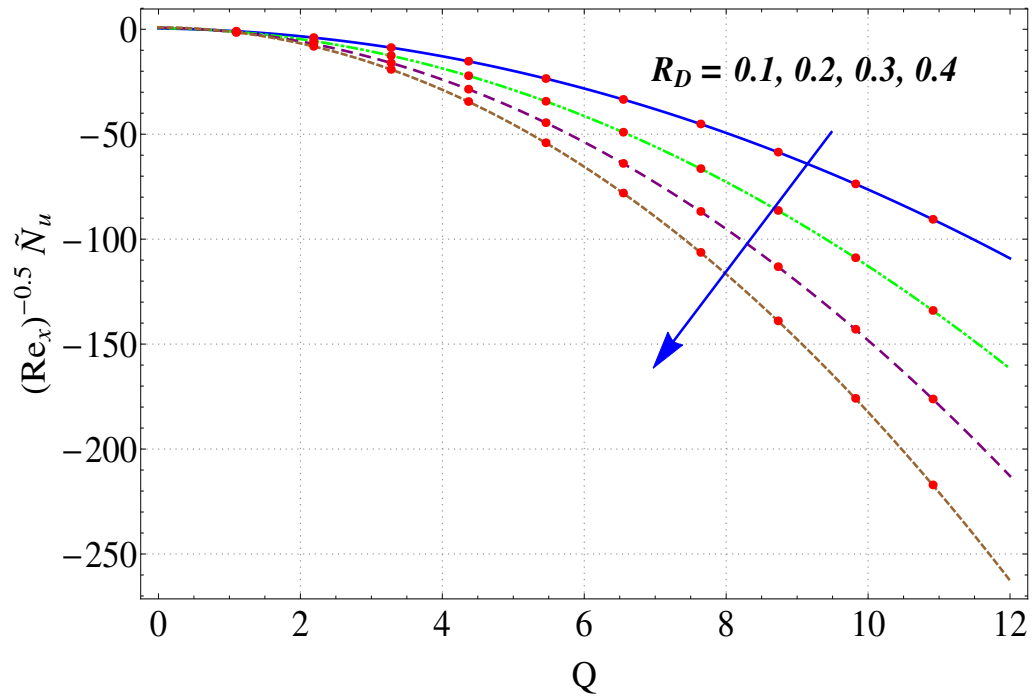


Figure 3.15: Variation of R_D on $(Re_x)^{-0.5} \tilde{N}_u$.

3.5 Concluding remarks

Magnetite nanofluid flow subject to thermal radiation and convective transport phenomena is worked out. The important points are listed below:

- Velocity of fluid declined for permeability parameter, volume fraction of nanoparticles and magnetic parameter, however conflicting trend is observed for curvature parameter.
- Quite similar behavior are being remarked for curvature parameter and radiation parameter on temperature.
- Magnitude of skin friction coefficient reduces for dimensionless radius of curvature.
- Magnitude of heat transfer rate rises for radiation parameter.

Chapter 4

Entropy generation in flow of Fe_3O_4 -water nanofluid with slip effects

The purpose of present chapter is to study the flow of nanofluid due to non-linear stretching sheet. Nanofluid is suspension of iron oxide (Fe_3O_4) nanoparticles and water (H_2O). Modeling is arranged for viscous dissipation, nonlinear radiation and Joule heating irreversibilities. Thermal and velocity slip aspects are accounted. Entropy generation analysis is a major concern of present study. Thermodynamic irreversibilities is computed by rate of entropy generation. Boundary-layer formulation of related consideration yields non-linear system. Optimal homotopy scheme is adopted to derive and scrutinize the convergent solutions subject to non-linear formulation. The plots for velocity, temperature, entropy generation and Bejan number are shown through graphs. Further skin friction and local Nusselt number are calculated and graphed.

4.1 Flow model

We examine two-dimensional flow of water-based nanofluid containing magnetite nanoparticles. Fluid flow is generated by non-linear stretching sheet with velocity u_w . Magnetic field of strength B_0^* is applied in transverse direction to flow. Effects of electric and induced magnetic fields are ignored. Entropy generation analysis is developed. Energy expression is considered by involvement of Joule heating, viscous dissipation and non-linear

thermal radiation. Heat generation/absorption aspects are also accounted. Further the surface manifests velocity and thermal slip conditions (see Figure (4.1)). Let T_f and T_∞ be fluid and ambient temperatures respectively.

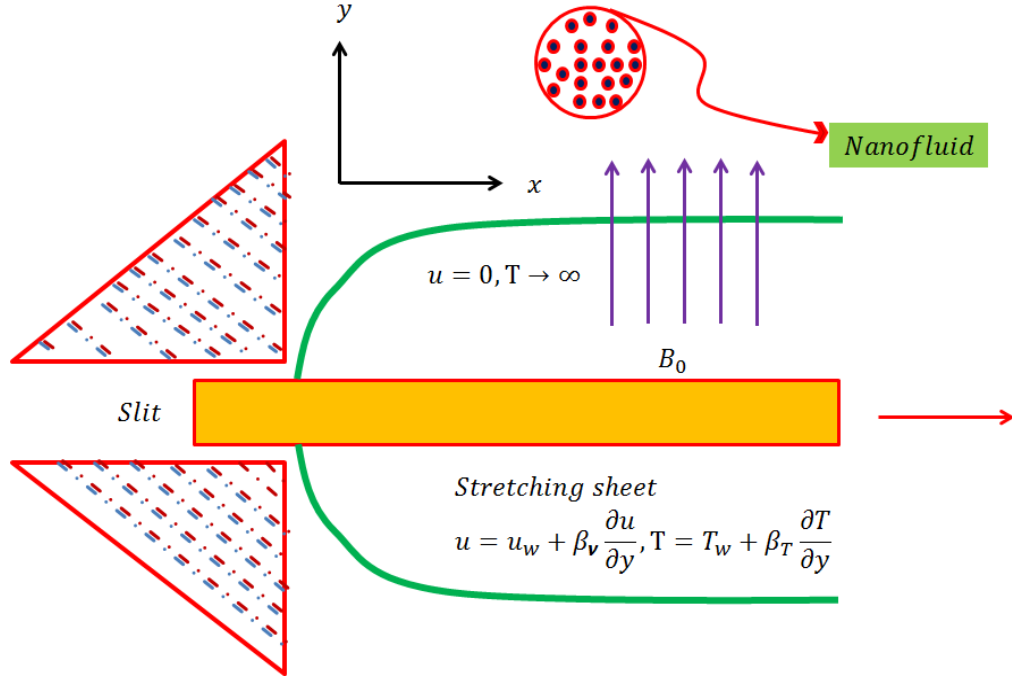


Figure 4.1: Flow geometry.

The dimensional expressions are:

$$\frac{\partial u}{\partial x} + \frac{\partial v}{\partial y} = 0, \quad (4.1)$$

$$\rho_{nf} \left(u \frac{\partial u}{\partial x} + v \frac{\partial u}{\partial y} \right) = \mu_{nf} \left(\frac{\partial^2 u}{\partial y^2} \right) - \sigma_{nf} B_0^2 u, \quad (4.2)$$

$$\begin{aligned} (\rho C_p)_{nf} \left(u \frac{\partial T}{\partial x} + v \frac{\partial T}{\partial y} \right) &= k_{nf} \frac{\partial^2 T}{\partial y^2} + \mu_{nf} \left(\frac{\partial \dot{u}}{\partial y} \right)^2 \\ &\quad - \left(\frac{\partial q_h}{\partial y} \right) + \sigma_{nf} B_0^2 u^2 + Q_0 (T - T_\infty), \end{aligned} \quad (4.3)$$

with

$$\begin{aligned} u &= u_w + \beta_v \frac{\partial u}{\partial y}, \quad v = 0, \quad T = T_w + \beta_T \frac{\partial T}{\partial y} \quad \text{at } y = 0, \\ u &\rightarrow 0, \quad T \rightarrow T_\infty \quad \text{as } y \rightarrow \infty. \end{aligned} \quad (4.4)$$

In above expressions (x, y) denote the cartesian coordinates, $u_w = u_0 x^n$ (n the power-law index), (u, v) the velocity components, β_v the velocity slip factor, β_T the thermal slip factor and Q_0 the heat source/sink coefficient.

Heat flux through Rosseland's concept $q_{\tilde{h}}$ is

$$q_{\tilde{h}} = -\frac{4\sigma^* \partial T^4}{3k^* \partial y} = -\frac{16\sigma^* T^3}{3k^*} \frac{\partial T}{\partial y}, \quad (4.5)$$

in which k^* denotes mean absorption coefficient and σ^* the Stefan-Boltzmann constant.

After using Eqs. (4.5) one has

$$\begin{aligned} \left(u \frac{\partial T}{\partial x} + v \frac{\partial T}{\partial y} \right) &= \alpha_{nf} \frac{\partial^2 T}{\partial y^2} + \frac{16\sigma^*}{3k^*} \frac{\partial}{\partial y} \left(T^3 \frac{\partial T}{\partial y} \right) + \mu_{nf} \left(\frac{\partial \ddot{u}}{\partial y} \right)^2 \\ &+ \sigma_{nf} B_0^2 u^2 + Q_0 (T - T_\infty). \end{aligned} \quad (4.6)$$

We consider

$$u = u_0 x^n \tilde{f}'(\xi), \quad v = -\sqrt{\left(\frac{n+1}{2} \right) \nu_f u_0 x^{n-1}} \left[\tilde{f}(\xi) + \frac{n-1}{n+1} \xi \tilde{f}'(\xi) \right], \quad (4.7)$$

$$\tilde{\theta}(\xi) = \frac{T - T_\infty}{T_w - T_\infty}, \quad \xi = y \sqrt{\left(\frac{n+1}{2} \right) \frac{u_0}{\nu_f} x^{n-1}}. \quad (4.8)$$

Expression (4.1) is satisfied trivially while Eqs. (4.2) and (4.6) become

$$\left(\frac{1}{(1-\phi)^{2.5} (1-\phi + \phi \frac{\rho_s}{\rho_f})} \right) \tilde{f}''' - \frac{2n}{n+1} \tilde{f}''^2 + f f'' - M \frac{\left(\frac{\sigma_{nf}}{\sigma_f} \right)}{(1-\phi + \phi \frac{\rho_s}{\rho_f})} \left(\frac{2}{n+1} \right) \tilde{f}' = 0, \quad (4.9)$$

we define

$$T = \tilde{\theta} (T_w - T_\infty) + T_\infty, \quad (4.10)$$

or

$$T = T_\infty (1 + (\theta_w - 1) \tilde{\theta}), \quad (4.11)$$

where $\theta_w = \frac{T_w}{T_\infty}$. Now we have

$$\frac{1}{\text{Pr}} \left(\frac{k_{nf}}{k_f} + R_D \right) \tilde{\theta}'' + \frac{R_D}{\text{Pr}} \begin{pmatrix} (\theta_w - 1)^3 (3\tilde{\theta}^2 \tilde{\theta}'^2 + \tilde{\theta}^3 \tilde{\theta}''') \\ + 3(\theta_w - 1)^2 (2\tilde{\theta} \tilde{\theta}'^2 + \tilde{\theta}^2 \tilde{\theta}''') \\ + 3(\theta_w - 1) (\tilde{\theta}'^2 + \tilde{\theta} \tilde{\theta}''') \end{pmatrix} \quad (4.12)$$

$$+ M E c \left(\frac{\sigma_{nf}}{\sigma_f} \right) \left(\frac{2}{n+1} \right) \tilde{f}'^2 + \frac{Ec}{(1-\phi)^{2.5}} \tilde{f}''^2 + Q \left(\frac{2}{n+1} \right) \tilde{\theta} \\ + \left(1 - \phi + \phi \frac{(\rho C_p)_s}{(\rho C_p)_f} \right) \tilde{f} \tilde{\theta}' = 0, \quad (4.13)$$

with

$$\tilde{f}(0) = 0, \quad \tilde{f}'(0) = 1 + S_v \tilde{f}''(0), \quad \tilde{\theta}(0) = 1 + S_T \tilde{\theta}'(0), \\ \tilde{f}'(\infty) \rightarrow 0, \quad \tilde{\theta}(\infty) \rightarrow 0. \quad (4.14)$$

where $M = \frac{\sigma_f B_0^2}{\rho_f u_0 x^{n-1}}$ the magnetic parameter, $S_v = \beta_v \sqrt{\left(\frac{n+1}{2}\right) \frac{u_0}{\nu_f} x^{n-1}}$ the velocity slip parameter, $R_D = \frac{16\sigma^* T_\infty^3}{3k_f k^*}$ the radiation parameter, $\text{Pr} = \frac{\nu_f (\rho C_p)_f}{k_f}$ the Prandtl number, $\theta_w = \frac{T_w}{T_\infty}$ the temperature ratio parameter, $Ec = \frac{u_0^2 x^{2n}}{\Delta T (C_p)_f}$ the Eckert number, $Q = \frac{Q_0}{(\rho C_p)_f u_0 x^{n-1}}$ the heat generation/absorption parameter and $S_T = \beta_T \sqrt{\left(\frac{n+1}{2}\right) \frac{u_0}{\nu_f} x^{n-1}}$ the thermal slip parameter.

4.1.1 Quantities of interest

The skin friction coefficient \tilde{C}_{sf} and heat transfer rate \tilde{N}_u are given by

$$\tilde{C}_{sf} = \frac{\tau_w}{\rho_f u_w^2}, \quad (4.15)$$

$$\tilde{N}_u = \frac{x q_w}{k_f (\tilde{T}_w - \tilde{T}_\infty)}, \quad (4.16)$$

where shear stress and wall heat flux are gives as

$$\tau_w = \mu_{nf} \left(\frac{\partial \tilde{u}}{\partial y} \right)_{y=0}, \quad (4.17)$$

$$q_w = -k_{nf} \frac{\partial T}{\partial y} \Big|_{y=0} + \frac{16\sigma^* T^3}{3k^*} \frac{\partial T}{\partial y} \Big|_{y=0}. \quad (4.18)$$

In dimensionless form

$$(\text{Re}_x)^{0.5} \tilde{C}_{sf} = \left(\frac{n+1}{2} \right)^{0.5} \frac{1}{(1-\phi)^{2.5}} \tilde{f}''(0). \quad (4.19)$$

$$(\text{Re}_x)^{-0.5} \tilde{N}_u = - \left(\frac{n+1}{2} \right)^{0.5} \left(\frac{k_{nf}}{k_f} + R_D(1 + (\tilde{\theta}_w - 1) \tilde{\theta}(0))^3 \right) \tilde{\theta}'(0), \quad (4.20)$$

in which local Reynolds number is $\text{Re}_x = u_0 x^{n+1} / \nu_f$.

4.2 Entropy generation

Local volumetric entropy generation rate per unit volume for MHD flow of Fe₃O₄-nanofluid over non-linearly stretching sheet with slip effects is investigated. Entropy generation is carried out through viscous dissipation, non-linear thermal radiation and Joule heating.

Here

$$S_g = \left. \begin{aligned} & \underbrace{\frac{k_f}{T_\infty^2} \left[\frac{k_{nf}}{k_f} \left(\frac{\partial T}{\partial y} \right)^2 + \frac{16\sigma^* T^3}{3k^* k_f} \left(\frac{\partial T}{\partial y} \right)^2 \right]}_{\text{Thermal irreversibility}} + \underbrace{\frac{\mu_{nf}}{T_\infty} \left(\frac{\partial u}{\partial y} \right)^2}_{\text{Fluid friction irreversibility}} \\ & + \underbrace{\frac{\sigma_{nf}}{T_\infty} B_0^{*2} (u^2)}_{\text{Joule dissipation irreversibility}}, \end{aligned} \right\} \quad (4.21)$$

where $\frac{k_f}{T_\infty^2} \left[\frac{k_{nf}}{k_f} \left(\frac{\partial T}{\partial y} \right)^2 + \frac{16\sigma^* T^3}{3k^* k_f} \left(\frac{\partial T}{\partial y} \right)^2 \right]$ signifies the entropy generation due to heat flow irreversibility through radiation effects, $\frac{\mu_{nf}}{T_\infty} \left(\frac{\partial u}{\partial y} \right)^2$ designates the irreversibility of the system owing to fluid friction irreversibility at constant density and $\frac{\sigma_{nf}}{T_\infty} B_0^{*2} (u^2)$ denotes the Joule heating irreversibility with constant magnetic flux density. Dimensionless number N_g for the entropy generation is defined as

$$N_g = \left(\frac{k_{nf}}{k_f} + R_D(\tilde{\theta}(\tilde{\theta}_w - 1) + 1)^3 \right) \alpha_T \left(\frac{n+1}{2} \right) \tilde{\theta}^{\prime 2} + Br \frac{1}{(1-\phi)^{2.5}} \left(\frac{n+1}{2} \right) \tilde{f}^{\prime 2} + M \frac{\sigma_{nf}}{\sigma_f} Br \tilde{f}^{\prime 2}, \quad (4.22)$$

where $N_g = \frac{\tilde{T}_\infty S_g \nu_f}{k_f \Delta T \dot{u}_0}$ designates the entropy generation rate, $Br = \frac{\mu_f \dot{u}_0^2 x^{2n}}{k_f \Delta T}$ the Brinkman number and $\alpha_T = \frac{\tilde{T}_w - \tilde{T}_\infty}{\tilde{T}_\infty} = \frac{\Delta \tilde{T}}{\tilde{T}_\infty}$ the dimensionless temperature difference. Bejan number

is defined as the ratio of entropy generation by virtue of heat transport irreversibility to system total entropy generation. Bejan number varies from 0 to 1. When $Be \gg 0.5$ then irreversibility subject to heat transfer dominates. The viscous effects dominant when $Be \ll 0.5$. Both effects are equal when $Be = 0.5$. Bejan number (Be) is

$$Be = \frac{\text{Entropy generation due to heat transfer}}{\text{Total entropy generation}}, \quad (4.23)$$

or

$$Be = \frac{\left(\frac{k_{nf}}{k_f} + R_D(\tilde{\theta}(\tilde{\theta}_w - 1) + 1)^3\right) \alpha_T \left(\frac{n+1}{2}\right) \tilde{\theta}'^2}{\left(\frac{k_{nf}}{k_f} + R_D(\tilde{\theta}(\tilde{\theta}_w - 1) + 1)^3\right) \alpha_T \left(\frac{n+1}{2}\right) \tilde{\theta}'^2 + Br \frac{1}{(1-\phi)^{2.5}} \left(\frac{n+1}{2}\right) \tilde{f}''^2 + M \frac{\sigma_{nf}}{\sigma_f} Br \tilde{f}''^2}, \quad (4.24)$$

4.3 Optimal homotopy analysis method

Optimal series solutions are developed for given flow system. For this purpose the initial approximations $(\tilde{f}_0(\xi), \tilde{\theta}_0(\xi))$ and linear operators $(\mathcal{L}_{\tilde{f}}, \mathcal{L}_{\tilde{\theta}})$ are given as:

$$\tilde{f}_0(\xi) = \frac{1}{1 + S_v} (1 - \exp(-\xi)), \quad \tilde{\theta}_0(\xi) = \frac{1}{1 + S_T} (\exp(-\xi)), \quad (4.25)$$

$$\mathcal{L}_{\tilde{f}} = \tilde{f}''' - \tilde{f}', \quad \mathcal{L}_{\tilde{\theta}} = \tilde{\theta}'' - \tilde{\theta}, \quad (4.26)$$

$$\mathcal{L}_{\tilde{f}} [C_1 + C_2 \exp(\xi) + C_3 \exp(-\xi)] = 0,$$

$$\mathcal{L}_{\tilde{\theta}} [C_4 \exp(\xi) + C_5 \exp(-\xi)] = 0, \quad (4.27)$$

with arbitrary constants C_i ($i = 1 - 5$).

4.4 Convergence analysis

The non-zero auxiliary variables $\hbar_{\tilde{f}}$ and $\hbar_{\tilde{\theta}}$ govern convergence portion and also homotopic solutions rate. For optimal data of $\hbar_{\tilde{f}}$ and $\hbar_{\tilde{\theta}}$ minimization concept is utilized by taking averaged squared residual errors [77]:

$$Q_m^{\tilde{f}} = \frac{1}{k+1} \sum_{l=0}^k \left[\mathcal{N}_{\tilde{f}} \left(\sum_{i=0}^m \tilde{f}^{(i)}(\xi), \sum_{i=0}^m \tilde{\theta}^{(i)}(\xi) \right)_{\xi=l\delta^* \xi} \right]^2, \quad (4.28)$$

$$\varrho_m^{\tilde{\theta}} = \frac{1}{k+1} \sum_{l=0}^k \left[\mathcal{N}_{\tilde{\theta}} \left(\sum_{i=0}^m \check{f}(\xi), \sum_{i=0}^m \tilde{\theta}(\xi) \right)_{\xi=l\delta^*\xi} \right]^2, \quad (4.29)$$

where ϱ_m^t represents total squared residual error, $\delta\xi = 0.5$ and $k = 20$. The ideal optimal values of convergence control parameters are $h_{\check{f}} = -0.604206$ and $h_{\tilde{\theta}} = -0.621623$. We write

$$\varrho_m^t = \varrho_m^{\check{f}} + \varrho_m^{\tilde{\theta}}, \quad (4.30)$$

Total average squared residual error is $\varrho_m^t = 0.0460441$. Plot for total residual error for magnetite nanofluid is depicted in Figure (4.2). Physical properties of density, specific heat and thermal conductivity is specified in Table (4.1). Table (4.2) presents the averaged residual errors with optimal values. Decay is observed for higher order of approximations.

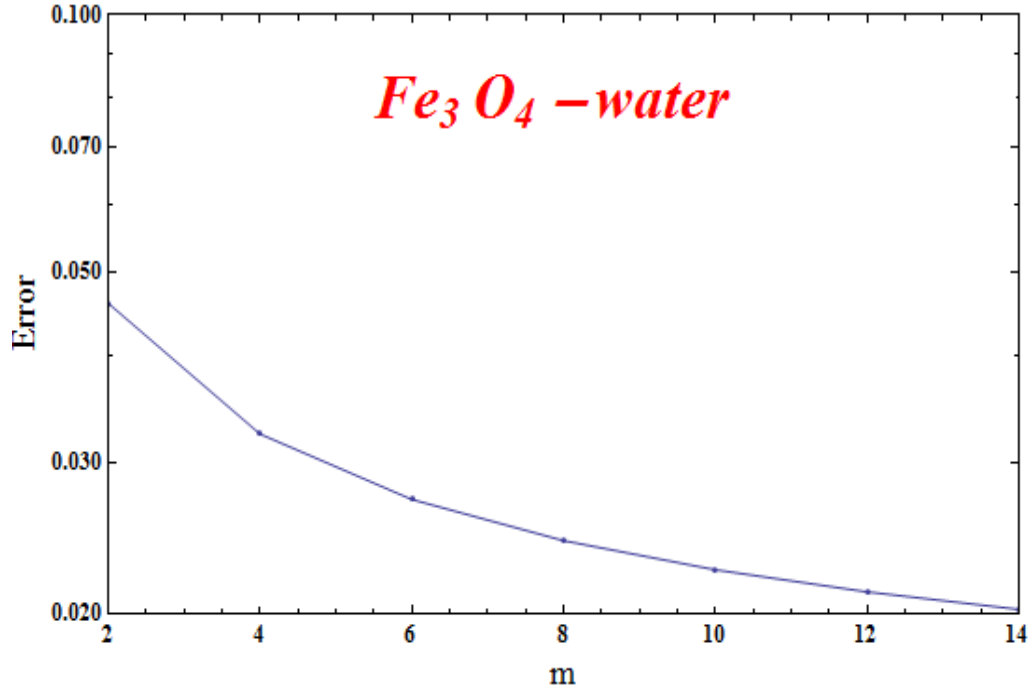


Figure 4.2: Residual error for Fe_3O_4 -water nanofluid.

Table 4.1: Thermo-physical properties of magnetite nanoparticles and water [32].

—	$k(W/mk)$	$\rho(kg/m^3)$	$\sigma(Um)^{-1}$	$C_p(j/m^3)$
Fe ₃ O ₄ (Iron oxide)	9.7	5180	2500	670
H ₂ O(Pure Water)	0.613	997.1	0.05	4179

Table 4.2: Individual averaged squared residual errors for magnetite water nanofluid.

m	$\epsilon_m^{\tilde{f}}$	$\epsilon_m^{\tilde{g}}$
2	6.40585×10^{-3}	4.35807×10^{-2}
4	2.88705×10^{-3}	3.27522×10^{-2}
6	1.81595×10^{-3}	2.82566×10^{-2}
8	1.30355×10^{-3}	2.57135×10^{-2}
10	1.00570×10^{-3}	2.40389×10^{-2}
12	8.12689×10^{-4}	2.28336×10^{-2}
14	6.78328×10^{-4}	2.19146×10^{-2}
16	5.79881×10^{-4}	2.11851×10^{-2}
18	5.04915×10^{-4}	2.05877×10^{-2}
20	4.46608×10^{-4}	2.00897×10^{-2}

4.5 Results and discussion

Effect of various flow variables satisfying ($0.02 \leq \phi \leq 0.05$), ($0.1 \leq M \leq 0.4$), ($0.2 \leq R_D \leq 0.5$), ($1.1 \leq \theta_w \leq 1.5$), ($0.1 \leq Q \leq 0.5$), ($0.01 \leq Ec \leq 0.1$), ($0.6 \leq S_v \leq 0.9$), ($1.1 \leq n \leq 1.5$) and ($0.8 \leq S_T \leq 1.2$) for velocity $\tilde{f}'(\xi)$, temperature $\tilde{\theta}(\xi)$, entropy rate and Bejan number are presented in Figures (4.3)-(4.23).

4.5.1 Velocity

Figure (4.3) elaborates influence of volume fraction of nanoparticles ($\phi = 0.02, 0.03, 0.04, 0.05$) against velocity $\tilde{f}'(\xi)$. Larger values nanoparticles volume fraction gradually reduces velocity of nanofluid. Physically fluid particles experience and offer high resistance due to incremental values of ϕ and as a result the velocity decays. Characteristics of power-law index ($n = 1.1, 1.3, 1.4, 1.5$) on velocity is depicted in Figure (4.4). For higher values of power-law index (n) the velocity of fluid enhances. Figure (4.5) exhibits influence of

magnetic parameter ($M = 0.1, 0.2, 0.3, 0.4$) on $\tilde{f}'(\xi)$. Velocity of fluid declines for higher (M). Physically the Lorentz force appeared through magnetic parameter and becomes stronger due to an increment in (M). In fact the stronger Lorentz force has ability to reduce the fluid velocity. Figure (4.6) elucidates the influence of velocity slip parameter ($S_v = 0.6, 0.7, 0.8, 0.9$) on $\tilde{f}'(\xi)$. It is noted that higher (S_v) reduce the velocity. Physically with an increment in (S_v) the stretching velocity is partially transferred to the fluid and consequently the velocity reduces.

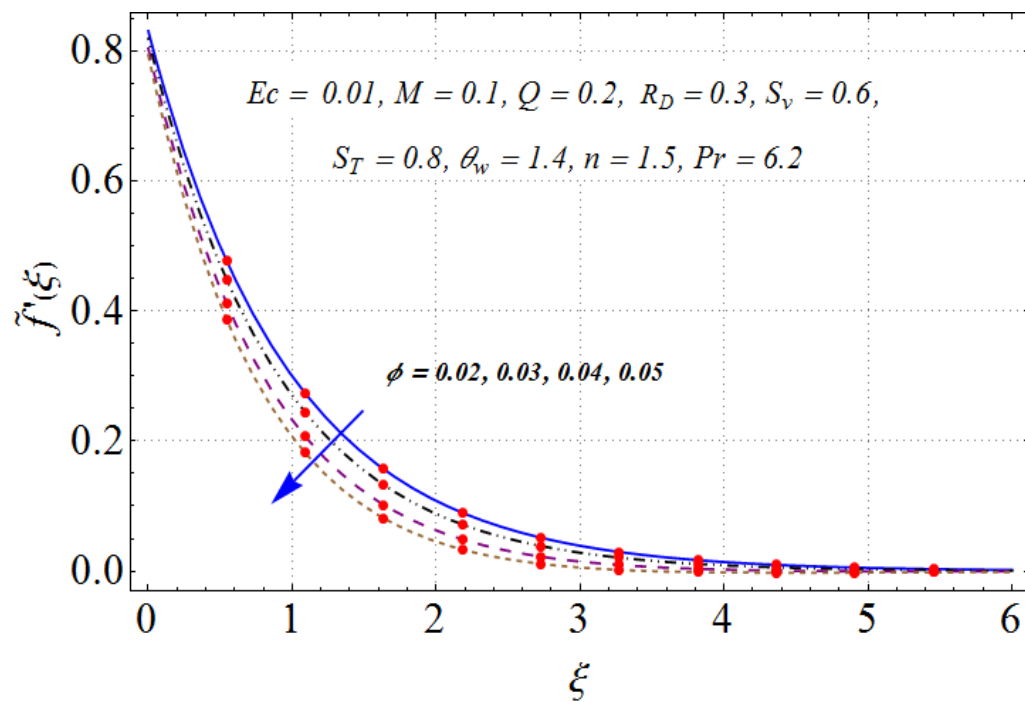


Figure 4.3: Variation of ϕ on $\tilde{f}'(\xi)$.

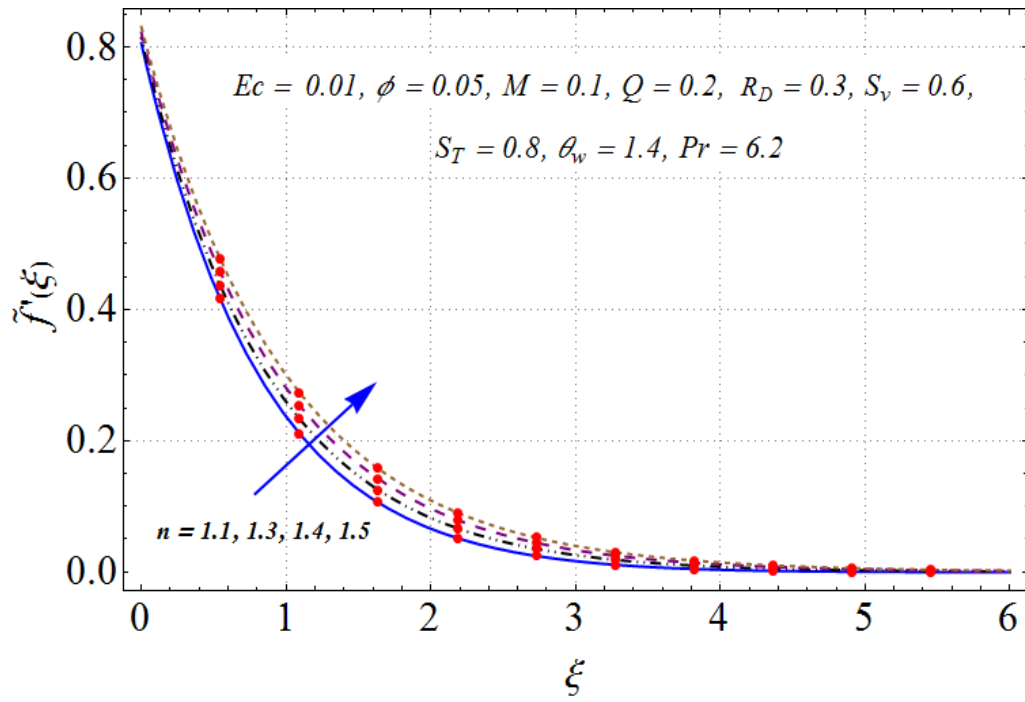


Figure 4.4: Variation of n on $\tilde{f}'(\xi)$.

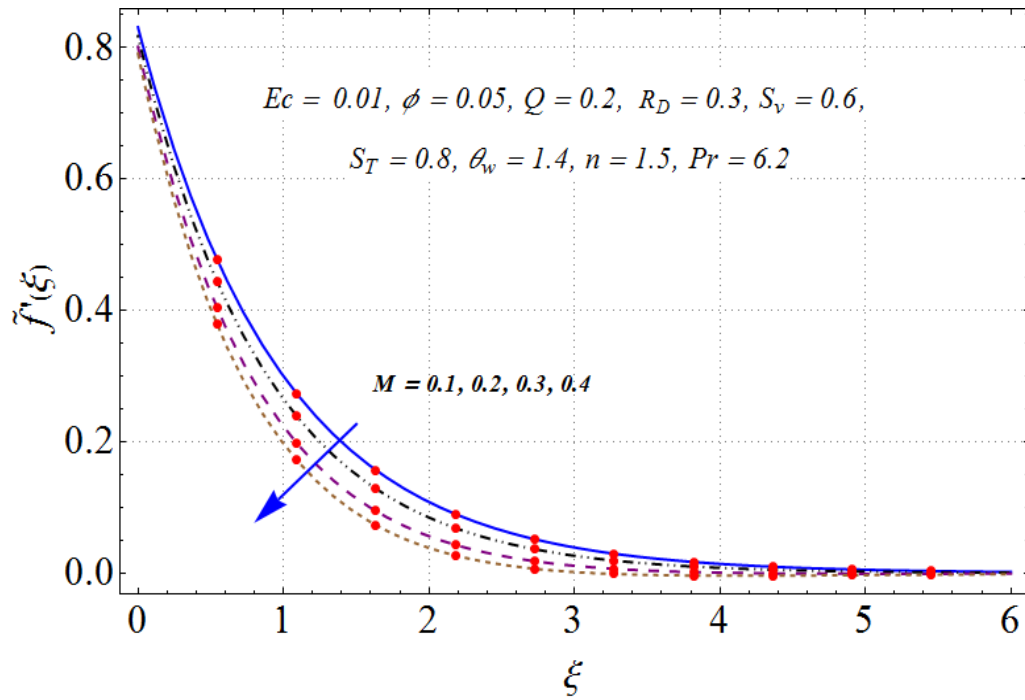
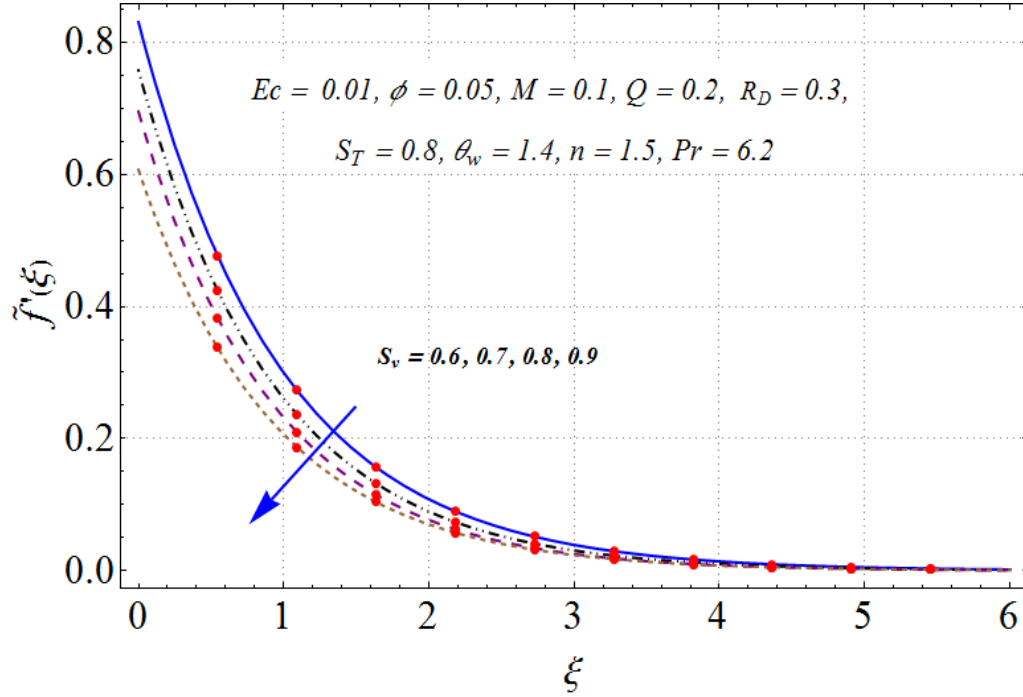


Figure 4.5: Variation of M on $\tilde{f}'(\xi)$.


 Figure 4.6: Variation of S_v on $\tilde{f}'(\xi)$.

4.5.2 Temperature

Figure (4.7) delineates the the influence of magnetite nanoparticles volume fraction ($\phi = 0.02, 0.03, 0.04, 0.05$) on temperature for Fe_3O_4 -water nanofluid. For higher (ϕ) the temperature of fluid enhances. Physically an enhancement in thermal conductivity of nanofluid leads to rise the temperature of fluid. Variation of ($n = 1.1, 1.3, 1.4, 1.5$) on fluid's temperature $\tilde{\theta}(\xi)$ is plotted in Figure (4.8). Power-law index (n) has direct relation with temperature $\tilde{\theta}(\xi)$. Influence of radiation parameter ($R_D = 0.2, 0.4, 0.5$) against temperature $\tilde{\theta}(\xi)$ is determined in Figure (4.9). It is observed that radiative heat transfer rate enhances with an increment in (R_D). This is because of larger (R_D) the coefficient of mean absorption decreases. Thus temperature enhances. Impact of Eckert number ($Ec = 0.01, 0.03, 0.7, 0.1$) on temperature $\tilde{\theta}(\xi)$ is displayed in Figure (4.10). Physically mechanical energy is converted into heat energy. It is because of internal friction of molecules. Hence temperature rises. Figure (4.11) revealed the behavior of temperature ratio parameter (θ_w) on $\tilde{\theta}(\xi)$. Clearly temperature enhances through (θ_w). It is noted that

temperature of sheet is higher in comparison with ambient temperature for higher (θ_w). Figure (4.12) displayed effect of ($Q = 0.1, 0.2, 0.4, 0.5$) on $\tilde{\theta}(\xi)$. Temperature of fluid enhances for ($Q > 0$). Physically internal energy of liquid particles rises by higher values of (Q) and so temperature increases. Moreover reverse trend is observed for ($Q < 0$). Figure (4.13) illustrates the variation of thermal slip parameter ($S_T = 0.8, 1.0, 1.1, 1.2$) on $\tilde{\theta}(\xi)$. Temperature of fluid declines via higher (S_T). Heat transfer from surface towards adjacent layers of fluid trough larger(S_T). Hence temperature declines.

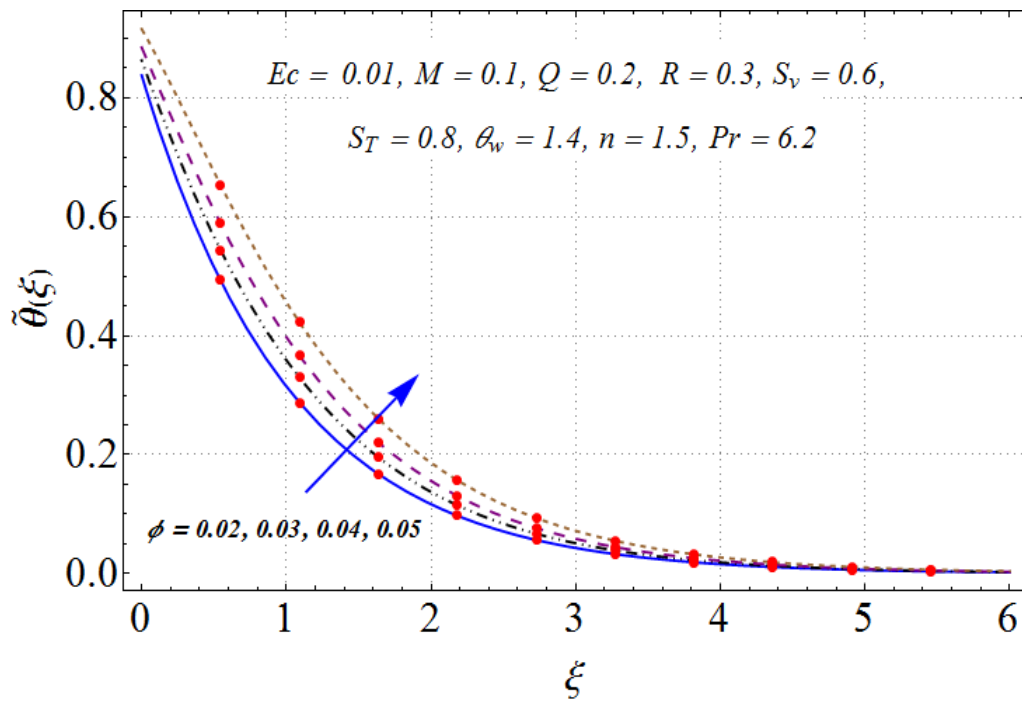


Figure 4.7: Variation of ϕ on $\tilde{\theta}(\xi)$

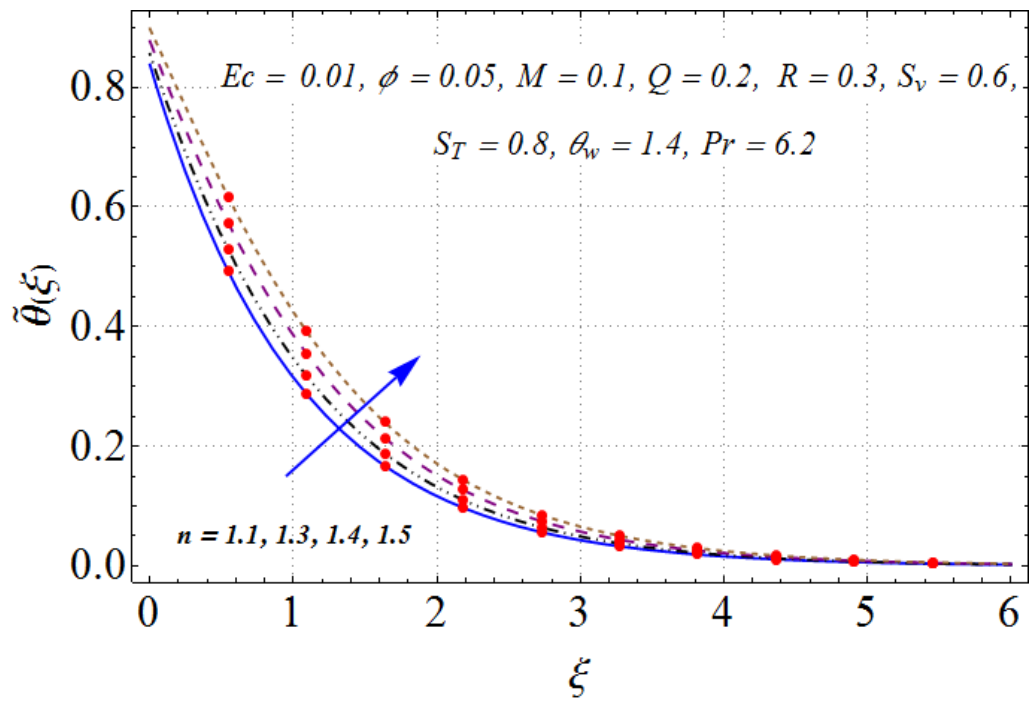


Figure 4.8: Variation of n on $\tilde{\theta}(\xi)$.

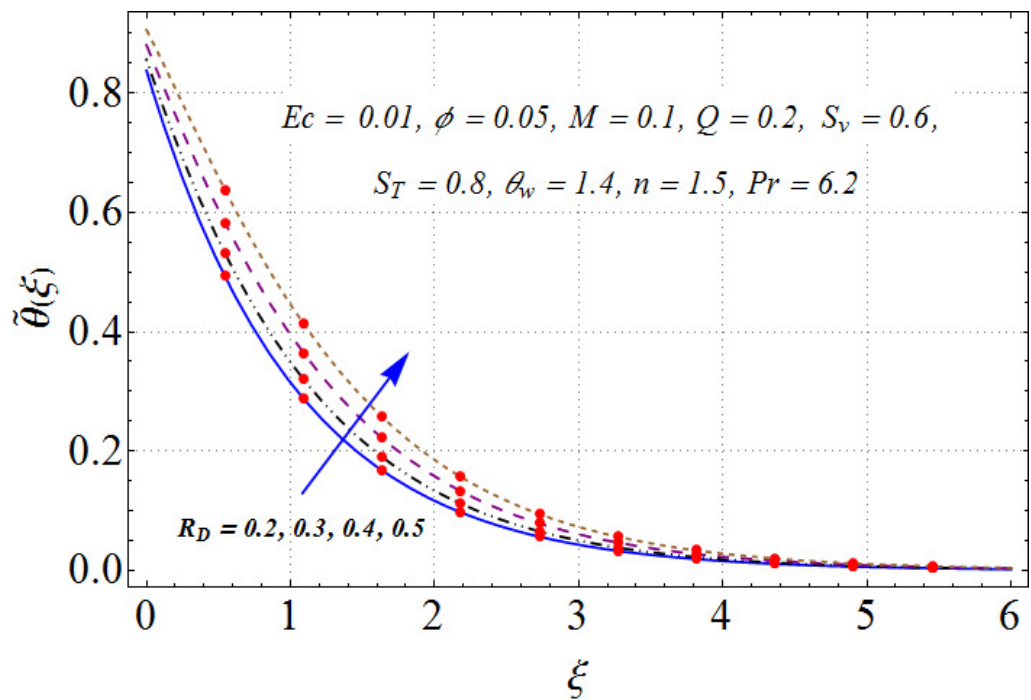


Figure 4.9: Variation of R_D on $\tilde{\theta}(\xi)$.

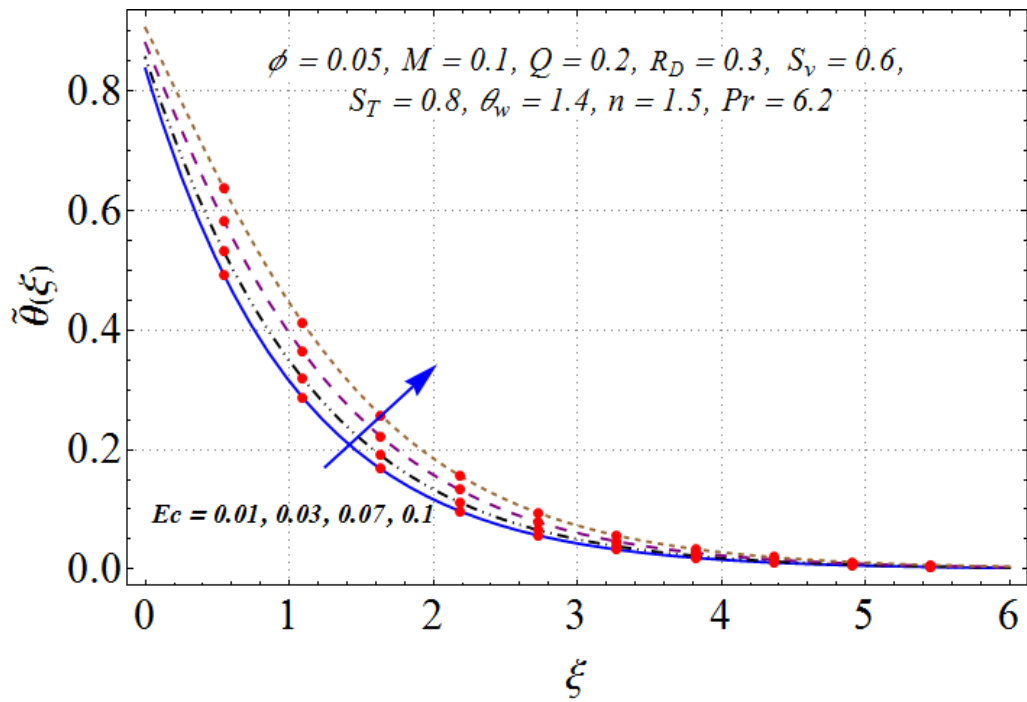


Figure 4.10: Variation of Ec on $\tilde{\theta}(\xi)$.

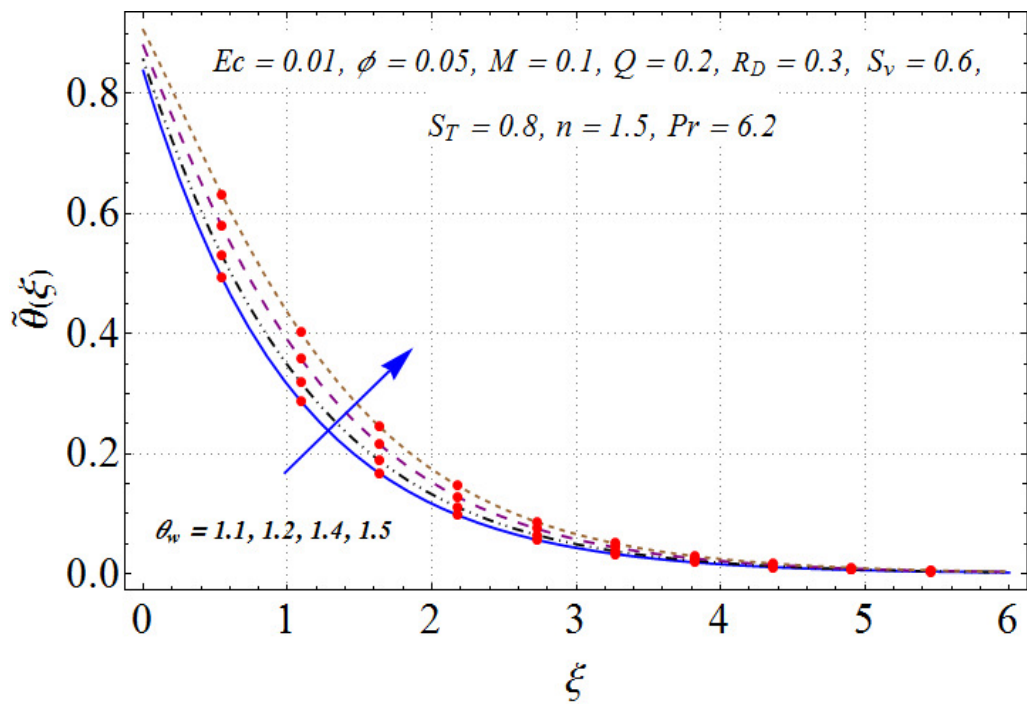


Figure 4.11: Variation of θ_w on $\tilde{\theta}(\xi)$.

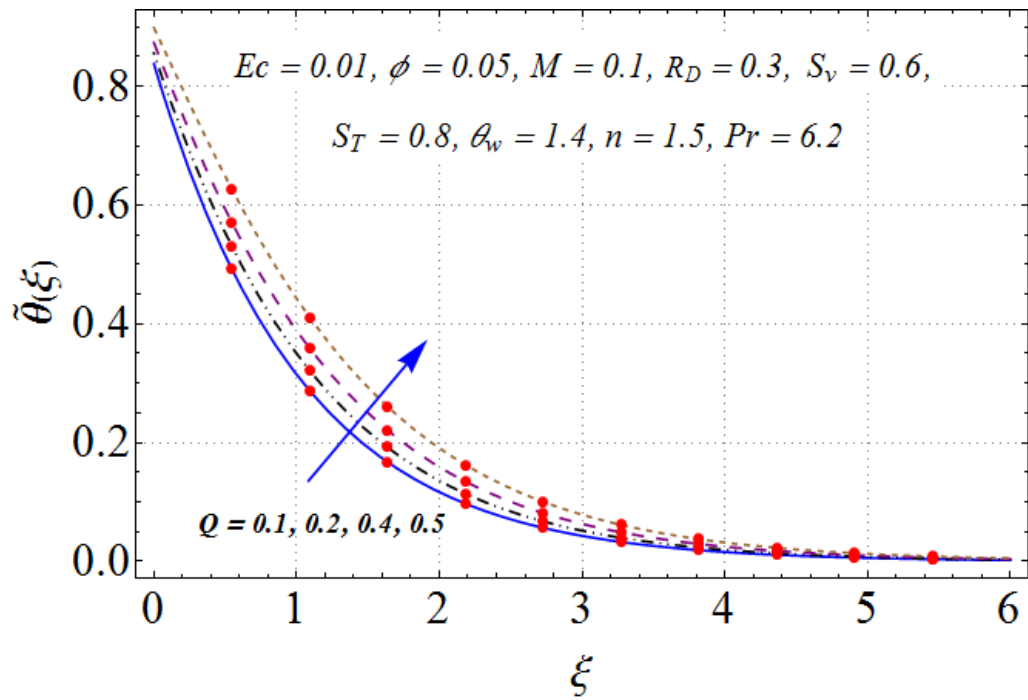


Figure 4.12: Variation of Q on $\tilde{\theta}(\xi)$.

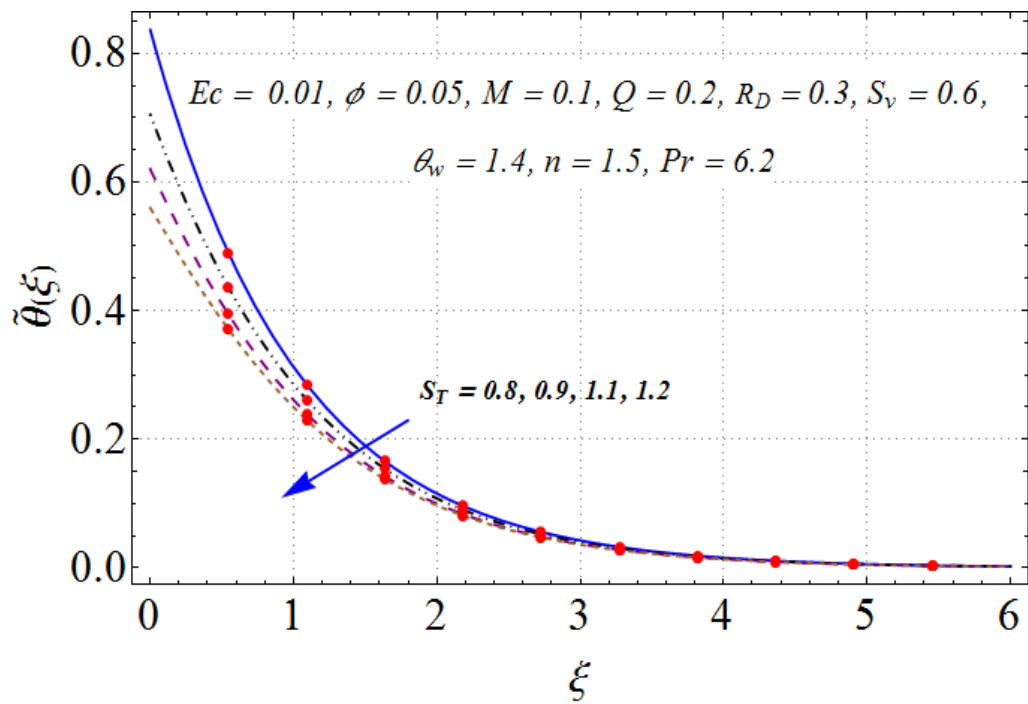


Figure 4.13: Variation of S_T on $\tilde{\theta}(\xi)$.

4.5.3 Local entropy generation rate $N_g(\xi)$ and Bejan number Be

Figures (4.14) and (4.15) are plotted to examine behavior of (ϕ) on $N_g(\xi)$ and Be . Bejan number reduces while rate of entropy generation enhances. Physically with increasing values of (ϕ) the magnetic and fluid friction effects are weaker than heat transfer. Figures (4.16) and (4.17) demonstrate the impact of (Br) on $N_g(\xi)$ and Be . Here larger (Br) reduces Bejan number (Be) and increases entropy generation rate $(N_g(\xi))$. Basically Brinkman number measures heat released by viscous heating in a relation to transfer of heat due to conduction of molecules. Near surface the viscous effects produce less amount of heat energy when compared with transfer of heat energy by molecular conduction. Large amount of heat evolved among fluid particles is a cause of entropy enhancement. As a result system disorderliness also enhances. Figures (4.18)-(4.19) demonstrate aspects of temperature difference parameter (α_T) on $N_g(\xi)$ and Be . Both quantities have increasing features for larger (α_T) . Heat transfer effects are dominant over magnetic and frictional fluid effects via higher (α_T) . Hence Be rises. It can be noticed from figure that $(N_g(\xi)) \rightarrow 0$ as we move far away from surface. Figures (4.20)-(4.21) show the radiation parameter (R_D) behavior for $(N_g(\xi))$ and (Be) . Qualitative similar behavior is noted for (Be) and $(N_g(\xi))$. Both entropy rate and Bejan number are enhanced via (R_D) . Due to enhancement of internal energy of given flow system the rate of local entropy generation $(N_g(\xi))$ and (Be) are increased. Figures (4.22) and (4.23) elucidated the behavior of (M) on $(N_g(\xi))$ and Be . Diverse behavior of (M) on $N_g(\xi)$ and Be is observed. Greater M creates an enhancement in $(N_g(\xi))$ while Be decays. Clearly (M) is very sensitive to entropy generation enhancement. For higher (M) the Lorentz force enhances due to which resistance of fluid enlarges. As a result entropy rate enhances. Bejan number fluid friction irreversibility dominates over heat and mass irreversibilities and thus (Be) decays.

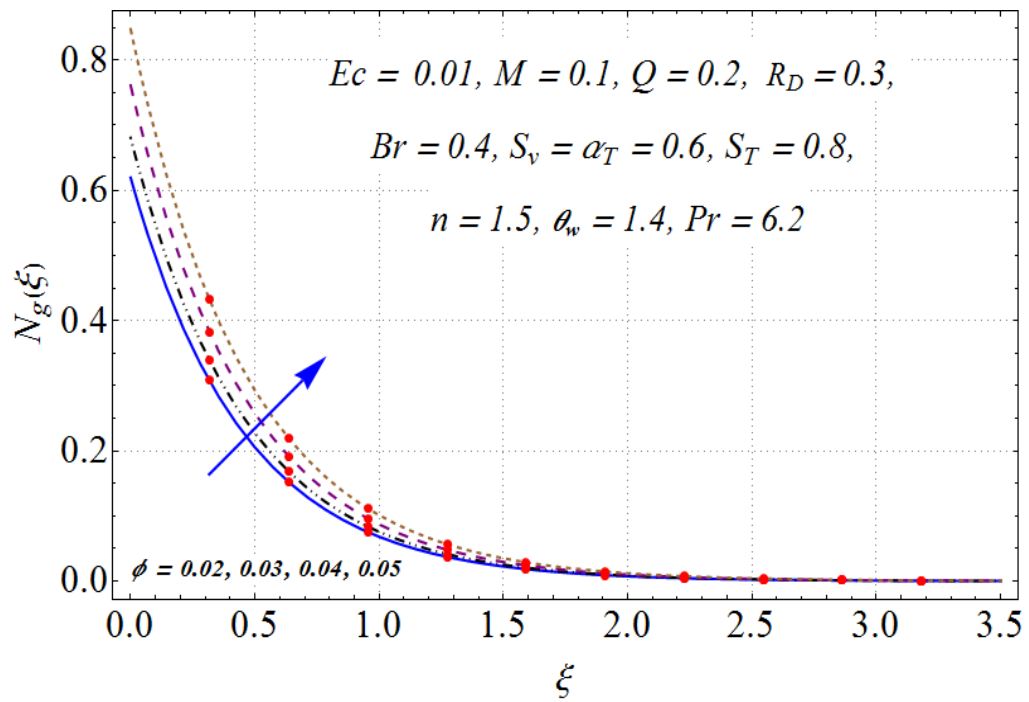


Figure 4.14: Entropy generation rate N_g via ϕ .

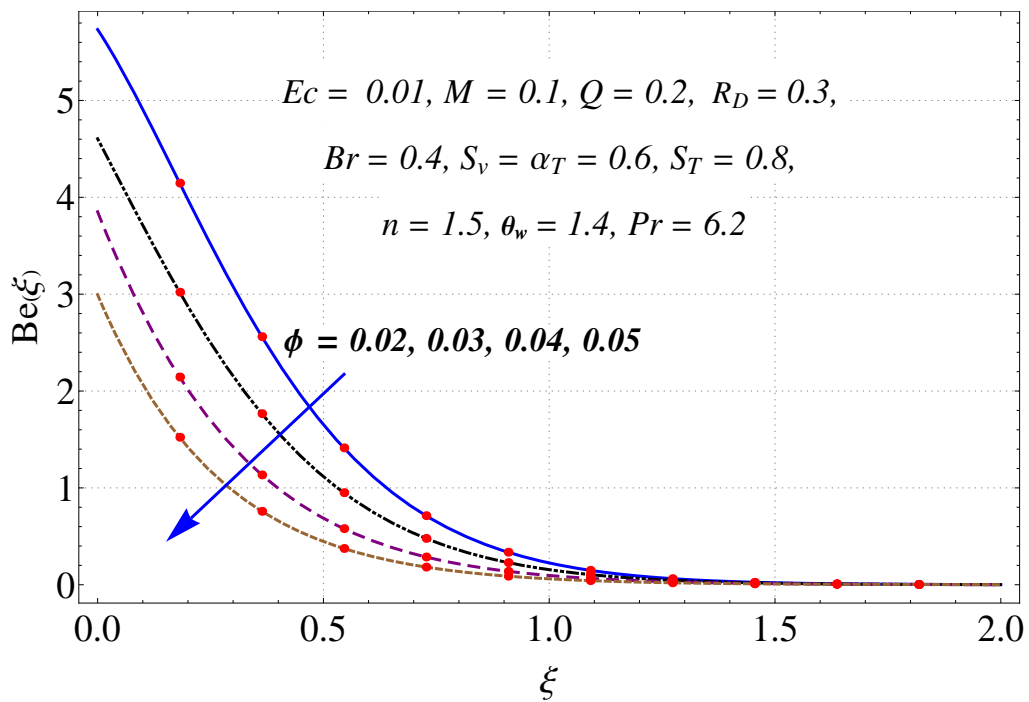


Figure 4.15: Bejan number Be via ϕ .

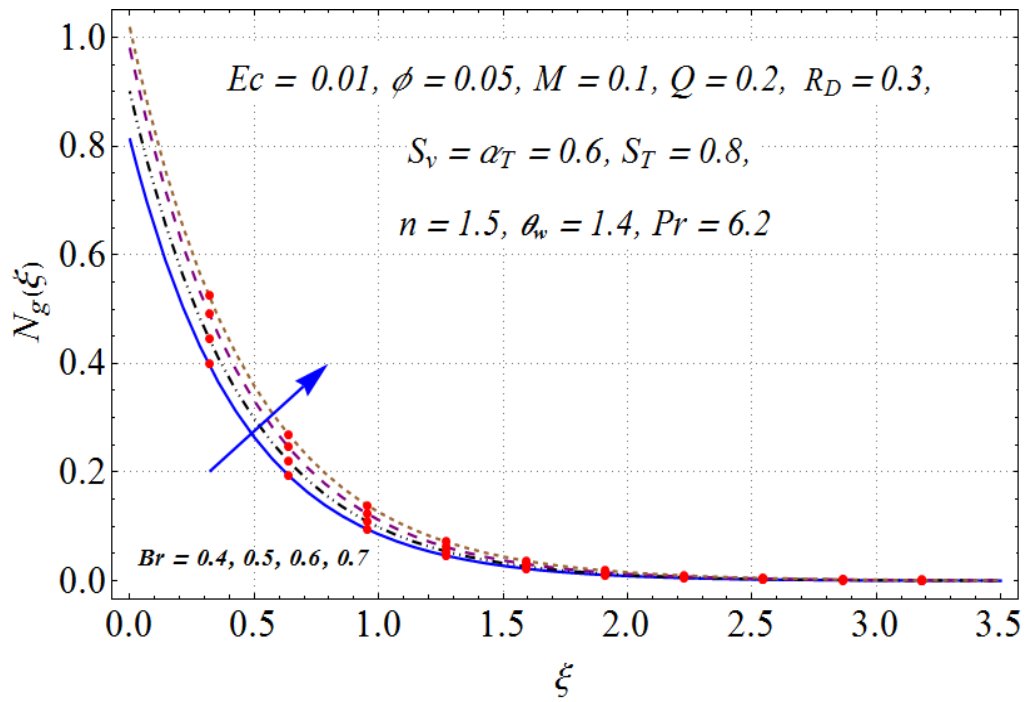


Figure 4.16: Entropy generation N_g via Br .

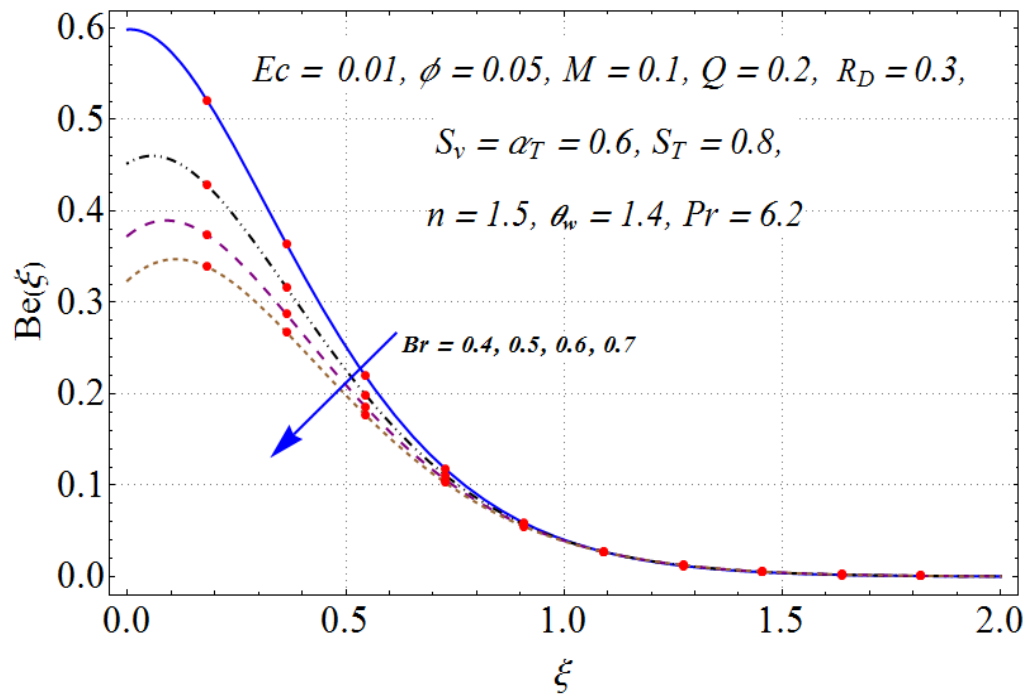


Figure 4.17: Bejan number Be via Br .

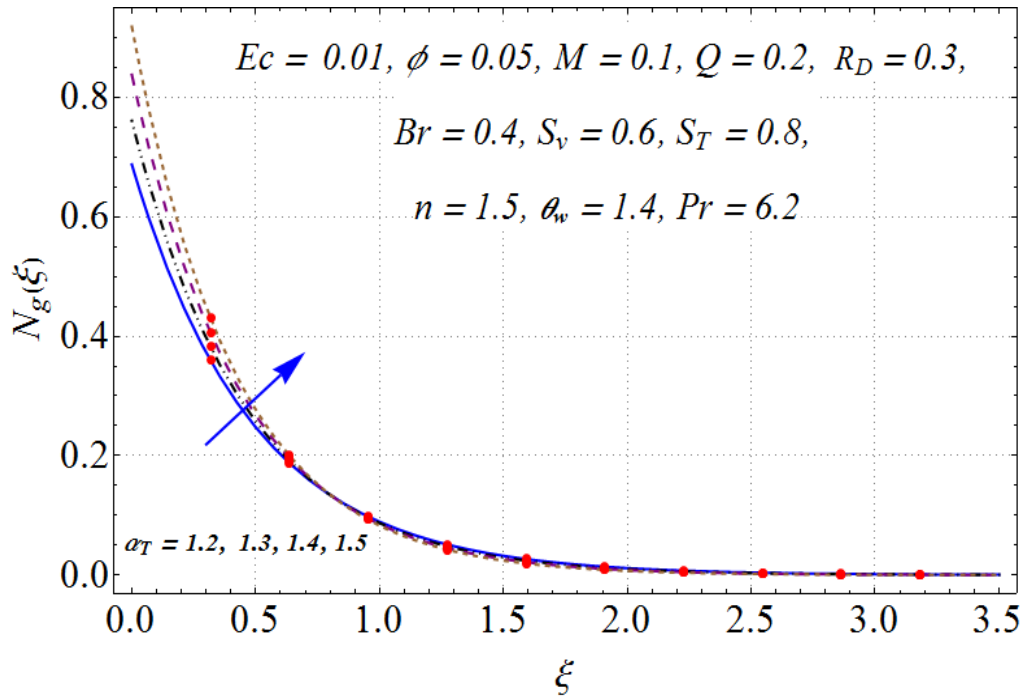


Figure 4.18: Entropy generation N_g via α_T .

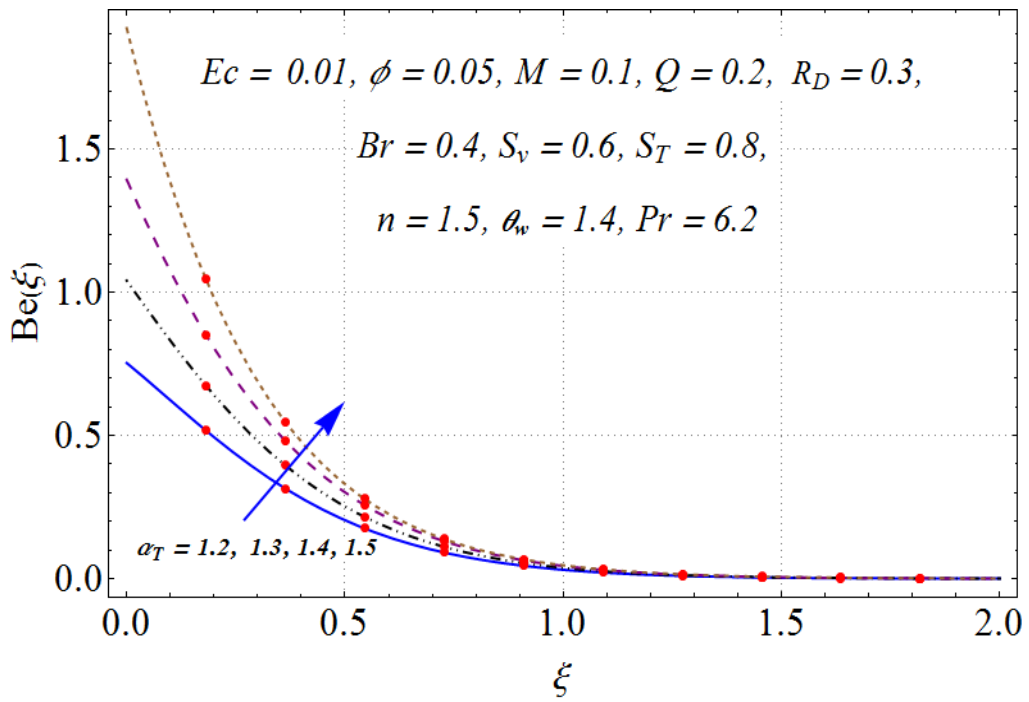


Figure 4.19: Bejan number Be via α_T .

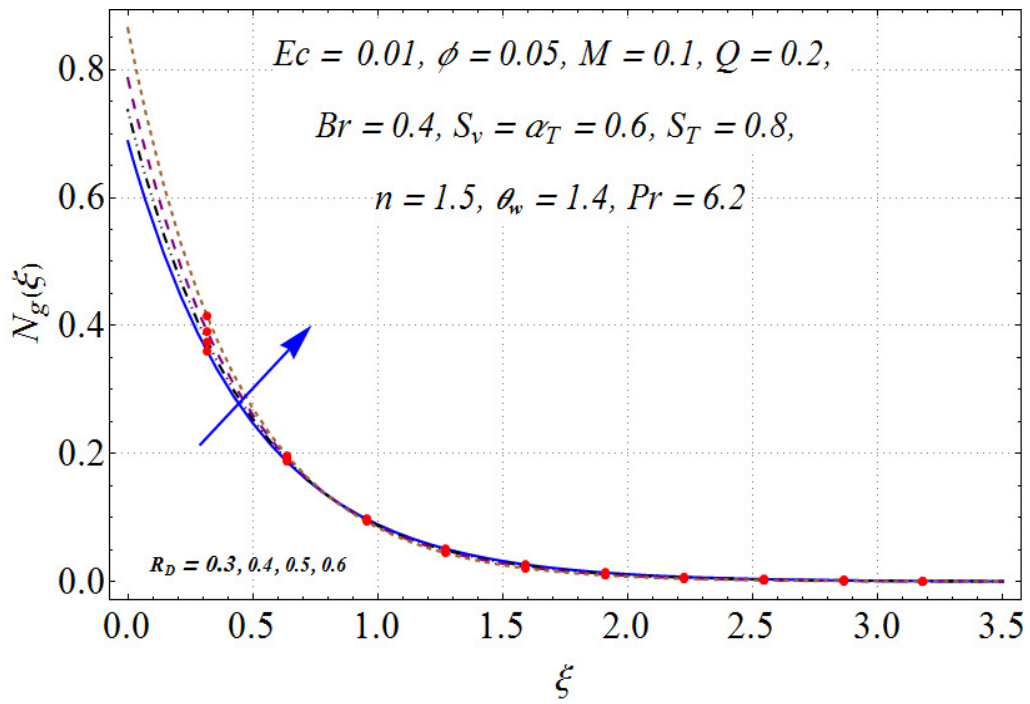


Figure 4.20: Entropy generation N_g via R_R .

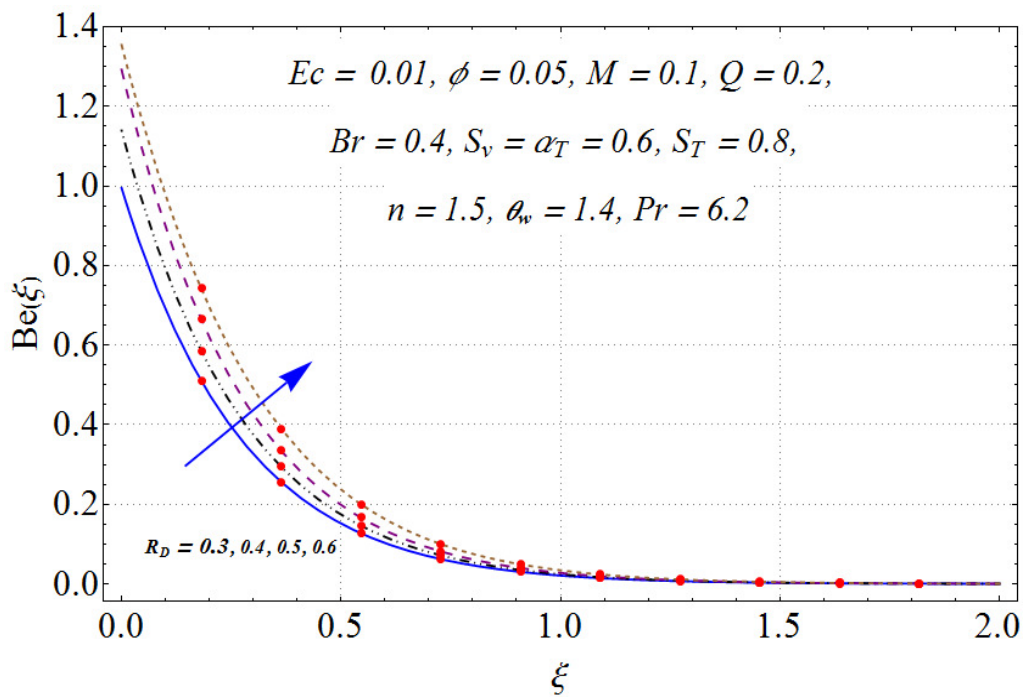


Figure 4.21: Bejan number Be via R_D .

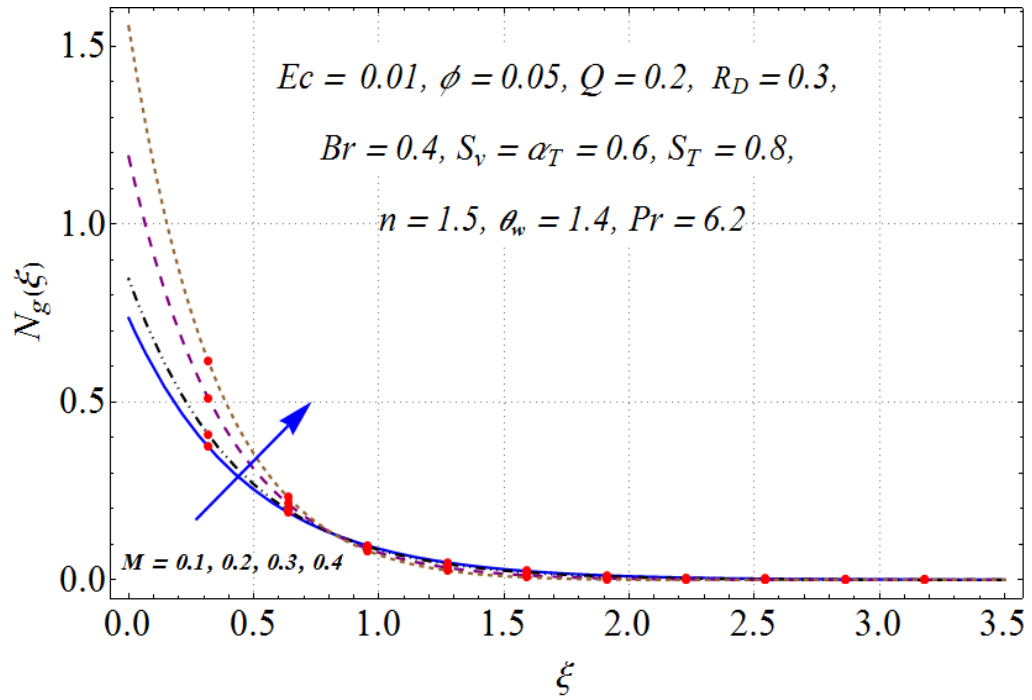


Figure 4.22: Entropy generation N_g via M .

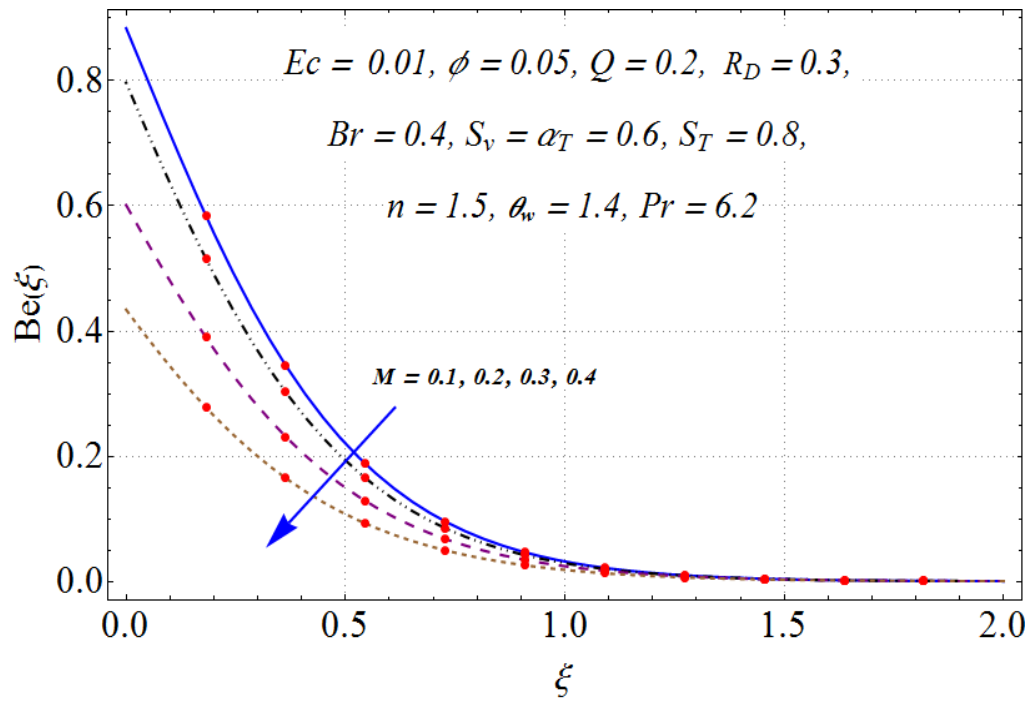


Figure 4.23: Bejan number Be via M .

4.5.4 Surface drag force and heat transfer rate

Figures (4.24)-(4.27) are sketched to show the influence of magnetic parameter (M), thermal slip (S_v), temperature ratio parameter (θ_w), Eckert number (Ec), velocity slip parameter (S_T) and nanoparticles volume fraction (ϕ) on skin friction coefficient $(Re_x)^{0.5} \tilde{C}_{sf}$ and heat transfer rate $(Re_x)^{-0.5} \tilde{N}_u$. Figure (4.24) highlights the features of magnetic parameter (M) on skin friction coefficient $(Re_x)^{0.5} \tilde{C}_{sf}$. It is reported that $(Re_x)^{0.5} \tilde{C}_{sf}$ reduces through larger (M). Skin friction coefficient $(Re_x)^{0.5} \tilde{C}_{sf}$ enhances for higher volume fraction of nanoparticles (ϕ) is shown in Figure (4.25). Figures (4.26) and (4.27) guaranteed that larger (S_T) and (θ_w) show a decay in heat transfer rate $(Re_x)^{-0.5} \tilde{N}_u$.

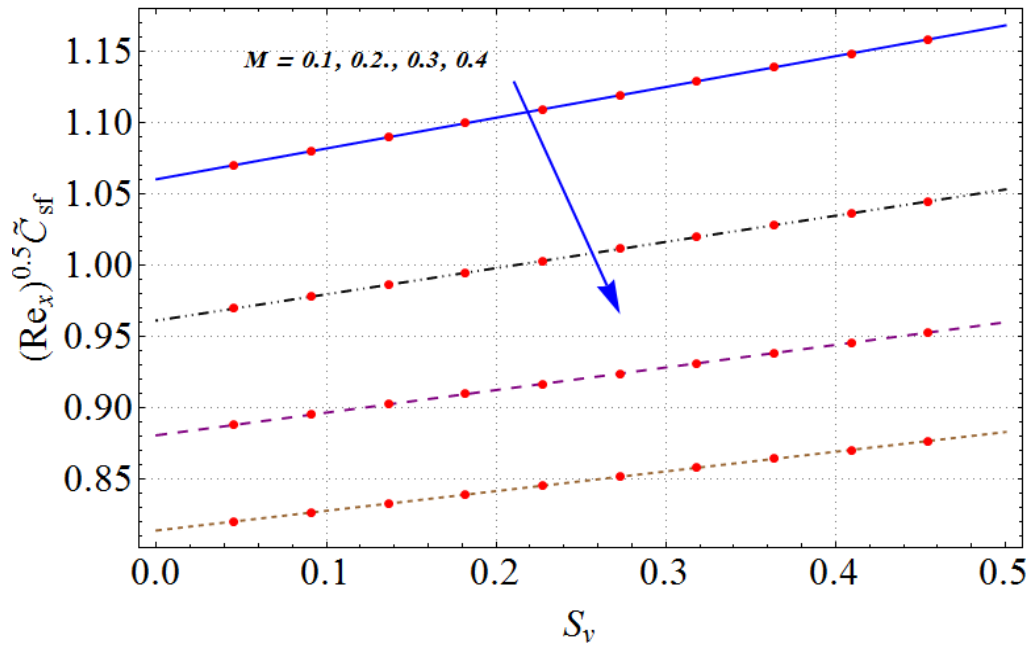


Figure 4.24: Variations of M and S_v on $(Re_x)^{0.5} \tilde{C}_{sf}$.

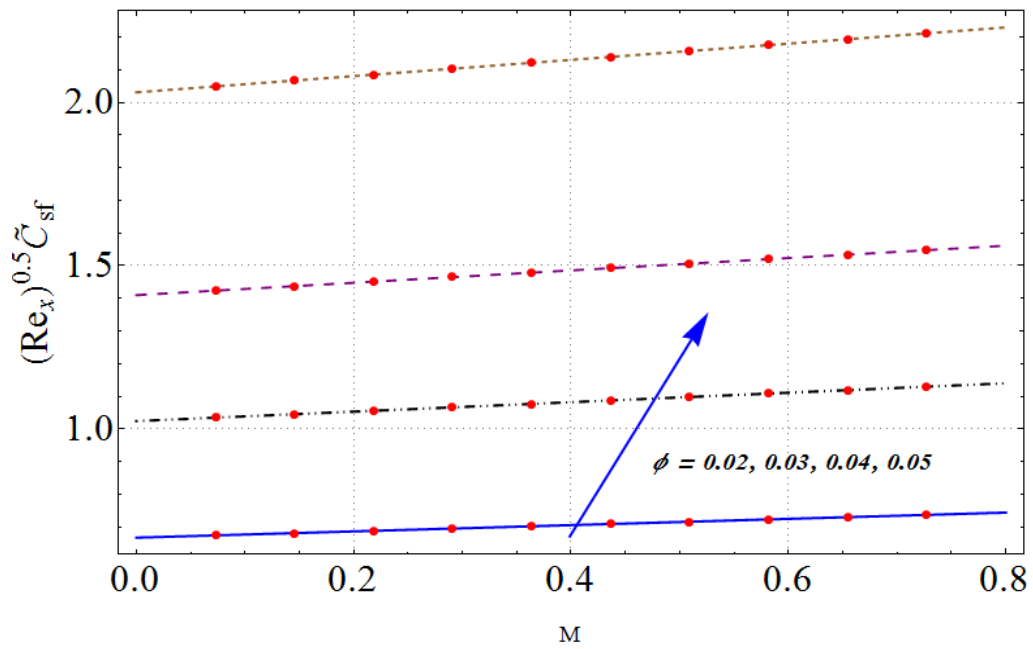


Figure 4.25: Variations of ϕ and M and on $(Re_x)^{0.5} \tilde{C}_{sf}$.

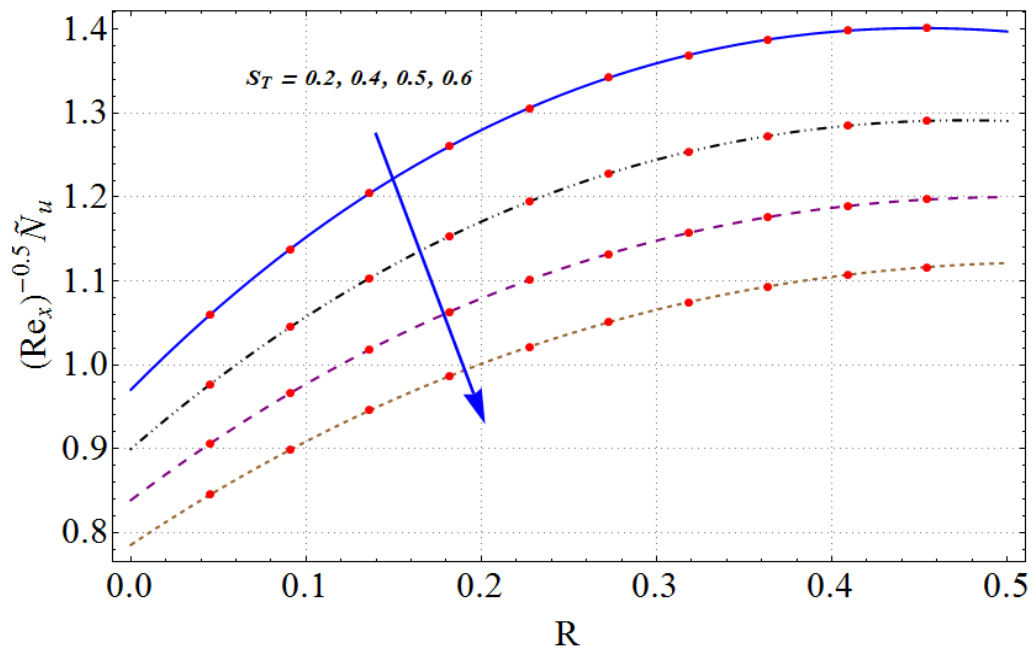


Figure 4.26: Variations of S_T and R and on $(Re_x)^{-0.5} \tilde{N}_u$.

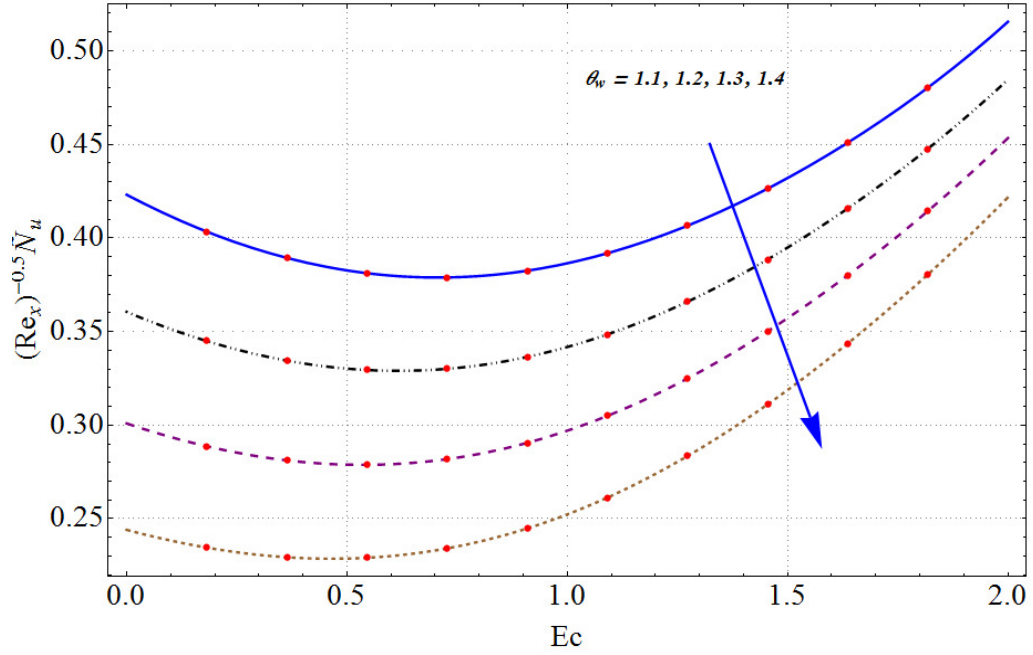


Figure 4.27: Variations of θ_w and Ec and on $(Re_x)^{-0.5} \tilde{N}_u$.

4.6 Conclusions

Here flow of magnetite nanofluid with slip effect is explored. The outcomes are mentioned below.

- Velocity declines for higher values of volume fraction of nanoparticles, magnetic parameter and velocity slip parameter.
- Temperature of fluid shows increasing behavior for volume fraction of nanoparticles, Eckert number, radiation parameter and temperature ratio parameter while decays for thermal slip parameter.
- Entropy generation rate enhances through higher volume fraction of nanoparticles, Brinkman number and radiation parameter.
- Bejan number enhances for temperature difference parameter while decays for Brinkman number.
- $(Re_x)^{0.5} \tilde{C}_{sf}$ is more for larger volume fraction of nanoparticles is observed.

Chapter 5

Three-dimensional flow of Fe_3O_4 -water nanofluid with homogeneous-heterogeneous reactions

An analysis has been carried out in this chapter for bidirectional nanofluid flow due to non-linear stretching sheet. Pure water is treated as a base fluid. Nanoparticles of magnetic characteristics are considered. Effects of non-linear radiation and non-uniform heat sink/source are examined. A simple model of homogeneous-heterogeneous reactions is used. Optimal homotopy analysis method (OHAM) is adopted for solution development of the non-linear system. Optimal estimations of auxiliary variables are obtained. Impact of several non-dimensional parameters for velocity components, temperature and concentration fields are examined. Graphs are plotted for analysis of surface drag force and heat transfer rate.

5.1 Flow equations

Three-dimensional flow of an electrically conducting viscous nanofluid is examined. Flow is caused by non-linearly stretching sheet at $z = 0$. An incompressible fluid occupies $z > 0$. Assumed that sheet is stretched with velocities $u_w = u_0(x+y)^n$ and $v_w = v_0(x+y)^n$ where u_0, v_0 are the constants (see Figure (5.1)). Contribution due to non-uniform heat

source/sink and non-linear radiation are studied. Applied magnetic field of strength B_0^* acts transversely to flow. Omission of electric and induced magnetic field is ensured.

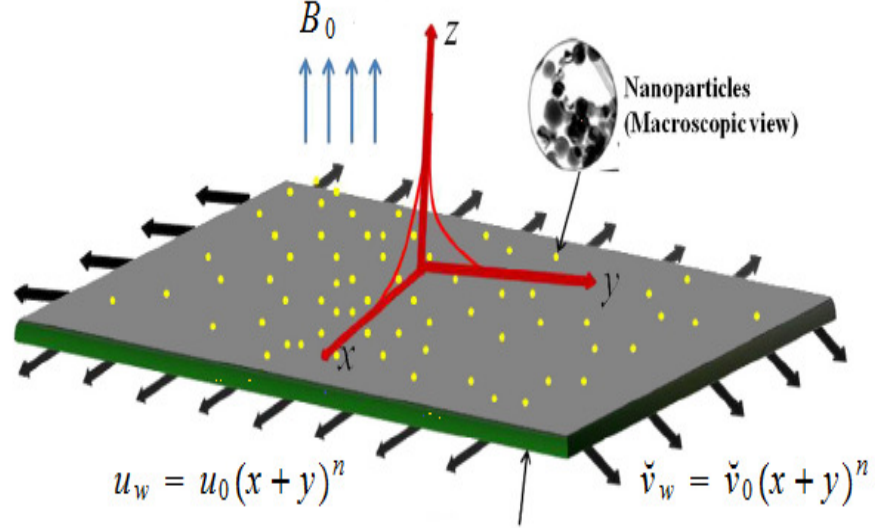
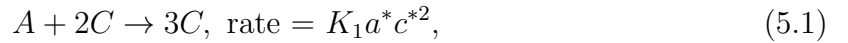


Figure 5.1: Problem sketch.

Homogeneous-heterogeneous reactions of two typical chemical species A and C have been analyzed. Homogeneous reactions for cubic auto catalysis satisfy



while on catalyst surface the required heterogeneous reactions is given by



where K_1 and K_2 are rate constants of chemical species having concentrations a^* and c^* .

Non-uniform heat source/sink) is defined by

$$Q''' = \left(\frac{k_f u_w(z)}{(x+y)\nu_f} \right) \left[I_1 (T_w - T_\infty) \tilde{f}'(\xi) + I_2 (T - T_\infty) \right], \quad (5.3)$$

where I_1 and I_2 are the heat generation/absorption coefficients respectively.

In Cartesian coordinates, the flow problems are governed by

$$\frac{\partial u}{\partial x} + \frac{\partial v}{\partial y} + \frac{\partial w}{\partial z} = 0, \quad (5.4)$$

$$\rho_{nf} \left(u \frac{\partial u}{\partial x} + v \frac{\partial u}{\partial y} + w \frac{\partial u}{\partial z} \right) = \mu_{nf} \left(\frac{\partial^2 u}{\partial z^2} \right) - \sigma_{nf} B_0^{*2} u, \quad (5.5)$$

$$\rho_{nf} \left(u \frac{\partial v}{\partial x} + v \frac{\partial v}{\partial y} + w \frac{\partial v}{\partial z} \right) = \mu_{nf} \left(\frac{\partial^2 v}{\partial z^2} \right) - \sigma_{nf} B_0^{*2} v, \quad (5.6)$$

$$(\rho C_p)_{nf} \left(u \frac{\partial T}{\partial x} + v \frac{\partial T}{\partial y} + w \frac{\partial T}{\partial z} \right) = k_{nf} \left(\frac{\partial^2 T}{\partial z^2} \right) + \frac{16\sigma^*}{3k^*} \frac{\partial}{\partial z} \left(T^3 \frac{\partial T}{\partial z} \right) - Q''', \quad (5.7)$$

$$u \frac{\partial a^*}{\partial x} + v \frac{\partial a^*}{\partial y} + w \frac{\partial a^*}{\partial z} = D_A \frac{\partial^2 a^*}{\partial z^2} - K_1 a^* c^{*2}, \quad (5.8)$$

$$u \frac{\partial c^*}{\partial x} + v \frac{\partial c^*}{\partial y} + w \frac{\partial c^*}{\partial z} = D_C \frac{\partial^2 c^*}{\partial z^2} + K_1 a^* c^{*2}, \quad (5.9)$$

$$\begin{aligned} u = u_w = u_0 (x + y)^n, \quad v = v_w = v_0 (x + y)^n, \quad w = 0, \quad T = T_w, \\ D_A \frac{\partial a^*}{\partial z} = K_2 a^*, \quad D_C \frac{\partial c^*}{\partial z} = -K_2 a^* \text{ at } z = 0, \\ u \rightarrow 0, \quad v \rightarrow 0, \quad a^* \rightarrow a_0, \quad \tilde{T} \rightarrow T_\infty, \quad c^* \rightarrow 0 \text{ as } z \rightarrow \infty, \end{aligned} \quad (5.10)$$

where (u, v, w) are the velocity components along (x, y, z) directions and D_A and D_C the diffusion coefficients respectively.

Making use of the following transformations

$$\begin{aligned} u = u_0 (x + y)^n \tilde{f}'(\xi), \quad v = v_0 (x + y)^n \tilde{g}'(\xi), \quad \xi = z \sqrt{\left(\frac{n+1}{2} \right) \frac{u_0}{\nu_f} (x + y)^{n-1}}, \\ w = -\sqrt{\left(\frac{n+1}{2} \right) \nu_f u_0 (x + y)^{n-1}} \left[(\tilde{f} + \tilde{g}) + \frac{n-1}{n+1} \xi (\tilde{f}' + \tilde{g}') \right], \\ \tilde{\theta}(\xi) = \frac{T - T_\infty}{T_w - T_\infty}, \quad a^* = \tilde{a}_0 \tilde{j}(\xi), \quad c^* = a_0 \tilde{s}(\xi). \end{aligned} \quad (5.11)$$

The continuity equation is satisfied automatically and Eqs. (5.5)-(5.10) become

$$\begin{aligned} \left(\frac{1}{(1-\phi)^{2.5} (1-\phi + \phi \frac{\rho_s}{\rho_f})} \right) \tilde{f}''' + (\tilde{f} + \tilde{g}) \tilde{f}'' - \frac{2n}{n+1} (\tilde{f}' + \tilde{g}') \tilde{f}' \\ - M \left(\frac{\sigma_{nf}}{\sigma_f} \right) \frac{1}{(1-\phi + \phi \frac{\rho_s}{\rho_f})} \tilde{f}' = 0, \end{aligned} \quad (5.12)$$

$$\begin{aligned} \left(\frac{1}{(1-\phi)^{2.5}(1-\phi+\phi\frac{\rho_s}{\rho_f})} \right) \tilde{g}''' + (\tilde{f} + \tilde{g}) \tilde{g}'' - \frac{2n}{n+1} (\tilde{f}' + \tilde{g}') \tilde{g}' \\ - M \left(\frac{\sigma_{nf}}{\sigma_f} \right) \frac{1}{(1-\phi+\phi\frac{\rho_s}{\rho_f})} \tilde{g}' = 0, \end{aligned} \quad (5.13)$$

$$\begin{aligned} \left(\frac{1}{1-\phi+\phi\frac{(\rho C_p)_s}{(\rho C_p)_f}} \right) \left[\begin{aligned} & \left(\frac{k_{nf}}{k_f} + R_D \right) \tilde{\theta}'' + \frac{2}{n+1} (I_1 \tilde{f}' + I_2 \tilde{\theta}) \\ & + R_D \begin{pmatrix} (\theta_w - 1)^3 (3\tilde{\theta}^2 \tilde{\theta}'^2 + \tilde{\theta}^3 \tilde{\theta}'') \\ + 3(\theta_w - 1)^2 (2\tilde{\theta} \tilde{\theta}'^2 + \tilde{\theta}^2 \tilde{\theta}'') \\ + 3(\theta_w - 1) (\tilde{\theta}'^2 + \tilde{\theta} \tilde{\theta}'') \end{pmatrix} \end{aligned} \right] \\ + Pr (\tilde{f} + \tilde{g}) \tilde{\theta}' = 0, \end{aligned} \quad (5.14)$$

$$\left(\frac{1}{Sc} \right) \tilde{j}'' + (\tilde{f} + \tilde{g}) \tilde{j}' - \frac{2}{n+1} K_r \tilde{j} \tilde{s}^2 = 0, \quad (5.15)$$

$$\left(\frac{\delta}{Sc} \right) \tilde{s}'' + (\tilde{f} + \tilde{g}) \tilde{s}' + \frac{2}{n+1} K_r \tilde{j} \tilde{s}^2 = 0, \quad (5.16)$$

$$\tilde{f}(0) = 0, \quad \tilde{f}'(0) = 1, \quad \tilde{g}(0) = 0, \quad \tilde{g}'(0) = \Psi, \quad \tilde{\theta}(0) = 0,$$

$$\tilde{j}'(0) = K_s \tilde{j}(0), \quad \delta \tilde{s}'(0) = -K_s \tilde{j}(0), \quad (5.17)$$

$$\tilde{f}'(\infty) \rightarrow 0, \quad \tilde{g}'(\infty) \rightarrow 0, \quad \tilde{\theta}(\infty) \rightarrow 0, \quad \tilde{j}(\infty) \rightarrow 1, \quad \tilde{s}(\infty) \rightarrow 0. \quad (5.18)$$

Here $\Psi = \frac{v_0}{u_0}$ signifies ratio variable, $M = \frac{\sigma_f B_0^2}{\rho_f u_0 x^{n-1}}$ the magnetic parameter, $R_D = \frac{16\sigma^* T_\infty^3}{3k_f k^*}$ the radiation parameter, $\theta_w = \frac{T_w}{T_\infty}$ the temperature ratio parameter, $Pr = \frac{\nu_f (\rho C_p)_f}{k_f}$ the Prandtl number, $\delta = \frac{D_C}{D_A}$ the Diffusion ratio coefficients, $Sc = \frac{\nu_f}{D_A}$ the Schmidt number, $K_r = \frac{K_1 a_0^2}{u_0 (x+y)^{n-1}}$ the homogeneous reaction strength and $K_s = \frac{K_2}{D_A} \sqrt{\frac{\nu_f}{u_0 (x+y)^{n-1}}} \sqrt{\frac{2}{n+1}}$ the heterogeneous reaction strength. Here we make an assumption that diffusion coefficients for both chemical species are same i.e. $\delta = 1$ and thus

$$\tilde{j}(\eta) + \tilde{s}(\eta) = 1 \quad (5.19)$$

Eqs. (5.15) and (5.16) yield

$$\left(\frac{1}{Sc} \right) \tilde{j}'' + (\tilde{f} + \tilde{g}) \tilde{j}' - \frac{2}{n+1} K_r \tilde{j} (1 - \tilde{j})^2 = 0, \quad (5.20)$$

with the boundary conditions

$$\tilde{j}'(0) = K_s \tilde{j}(0), \quad \tilde{j}(\infty) \rightarrow 1. \quad (5.21)$$

5.1.1 Physical quantities

Skin friction coefficient (\tilde{C}_{sfx} and \tilde{C}_{sfy}) and local Nusselt number (\tilde{N}_u) are defined as

$$\tilde{C}_{sfx} = \frac{\tau_{wx}}{\rho_f u_w^2}, \quad \tilde{C}_{sfy} = \frac{\tau_{wy}}{\rho_f v_w^2}, \quad \tilde{N}_u = \frac{(x+y) q_w}{k_f (T_w - T_\infty)}. \quad (5.22)$$

Here surface shear stress along x and y directions are given by

$$\tau_{wx} = \mu_{nf} \left(\frac{\partial u}{\partial z} \right)_{z=0}, \quad \tau_{wy} = \mu_{nf} \left(\frac{\partial v}{\partial z} \right)_{z=0}. \quad (5.23)$$

Wall heat flux is given by

$$q_w = -k_{nf} \left. \frac{\partial \tilde{T}}{\partial z} \right|_{z=0} + (q_h)_w. \quad (5.24)$$

Dimensionless expressions of (\tilde{C}_{sfx} , \tilde{C}_{sfy}) and (\tilde{N}_u) are

$$\begin{aligned} (\text{Re}_x)^{0.5} \tilde{C}_{sfx} &= \left(\frac{n+1}{2} \right)^{0.5} \frac{1}{(1-\phi)^{2.5}} \tilde{f}''(0), \\ (\text{Re}_y)^{0.5} \tilde{C}_{sfy} &= \left(\frac{n+1}{2} \right)^{0.5} \frac{1}{\Psi^{3/2} (1-\phi)^{2.5}} \tilde{g}''(0), \\ (\text{Re}_x)^{-0.5} \tilde{N}_u &= - \left(\frac{n+1}{2} \right)^{0.5} \left[\frac{k_{nf}}{k_f} + R_D (1 + (\theta_w - 1)) \tilde{\theta}(0) \right]^3 \tilde{\theta}'(0), \end{aligned} \quad (5.25)$$

in which $\text{Re}_x = \frac{u_0(x+y)^{n+1}}{v_f}$ and $\text{Re}_y = \frac{v_0(x+y)^{n+1}}{v_f}$ denote the local Reynolds numbers.

5.2 Optimal homotopic solutions

In the frame of HAM, the optimal series solutions are developed. We select suitable operators and initial guesses in the forms

$$\begin{aligned} \tilde{f}_0(\xi) &= 1 - \exp(-\xi), \quad \tilde{g}_0(\xi) = \Psi (1 - \exp(-\xi)), \\ \tilde{\theta}_0(\xi) &= \exp(-\xi), \quad \tilde{j} = 1 - \frac{1}{2} \exp\left(-\sqrt{\frac{2}{n+1}} K^s(\xi)\right), \end{aligned} \quad (5.26)$$

with

$$\mathcal{L}_{\tilde{f}} = \tilde{f}''' - \tilde{f}', \quad \mathcal{L}_{\tilde{g}} = \tilde{g}''' - \tilde{g}', \quad \mathcal{L}_{\tilde{\theta}} = \tilde{\theta}'' - \tilde{\theta}, \quad \mathcal{L}_{\tilde{j}} = \tilde{j}'' - \tilde{j}, \quad (5.27)$$

and

$$\begin{aligned} \mathcal{L}_{\tilde{f}} [C_1 + C_2 \exp(\xi) + C_3 \exp(-\xi)] &= 0, \\ \mathcal{L}_{\tilde{g}} [C_4 + C_5 \exp(\xi) + C_6 \exp(-\xi)] &= 0, \\ \mathcal{L}_{\tilde{\theta}} [C_7 \exp(\xi) + C_8 \exp(-\xi)] &= 0, \\ \mathcal{L}_{\tilde{j}} [C_9 \exp(\xi) + C_{10} \exp(-\xi)] &= 0, \end{aligned} \quad (5.28)$$

in which arbitrary constants are C_i ($i = 1 - 10$).

5.3 Optimal convergence analysis

In homotopic solutions the non-zero auxiliary variables $\tilde{h}_{\tilde{f}}$, $\tilde{h}_{\tilde{g}}$, $\tilde{h}_{\tilde{\theta}}$ and $\tilde{h}_{\tilde{j}}$ ensure convergence analysis. For optimal data of $\tilde{h}_{\tilde{f}}$, $\tilde{h}_{\tilde{g}}$, $\tilde{h}_{\tilde{\theta}}$ and $\tilde{h}_{\tilde{j}}$ we have utilized the concept given by Liao [77]. The averaged squared residual errors of the m -th order of approximations is applied to reduce the CPU-time and are given as follows:

$$\varrho_m^{\tilde{f}} = \frac{1}{k+1} \sum_{l=0}^k \left[\mathcal{N}_{\tilde{f}} \left(\sum_{i=0}^m \tilde{f}(\xi), \sum_{i=0}^m \tilde{g}(\xi) \right)_{\xi=l\delta^*\xi} \right]^2, \quad (5.29)$$

$$\varrho_m^{\tilde{g}} = \frac{1}{k+1} \sum_{l=0}^k \left[\mathcal{N}_{\tilde{g}} \left(\sum_{i=0}^m \tilde{f}(\xi), \sum_{i=0}^m \tilde{g}(\xi) \right)_{\xi=l\delta^*\xi} \right]^2, \quad (5.30)$$

$$\varrho_m^{\tilde{\theta}} = \frac{1}{k+1} \sum_{l=0}^k \left[\mathcal{N}_{\tilde{\theta}} \left(\sum_{i=0}^m \tilde{f}(\xi), \sum_{i=0}^m \tilde{g}(\xi), \sum_{i=0}^m \tilde{\theta}(\xi) \right)_{\xi=l\delta^*\xi} \right]^2, \quad (5.31)$$

$$\varrho_m^{\tilde{j}} = \frac{1}{k+1} \sum_{l=0}^k \left[\mathcal{N}_{\tilde{j}} \left(\sum_{i=0}^m \tilde{f}(\xi), \sum_{i=0}^m \tilde{g}(\xi), \sum_{i=0}^m \tilde{j}(\xi) \right)_{\xi=l\delta^*\xi} \right]^2. \quad (5.32)$$

Following

$$\varrho_m^t = \varrho_m^{\tilde{f}} + \varrho_m^{\tilde{g}} + \varrho_m^{\tilde{\theta}} + \varrho_m^{\tilde{j}}, \quad (5.33)$$

where ϱ_m^t constitute total squared residual error, $\delta^*\xi = 0.5$ and $k = 16$. For magnetite water nanofluid the convergence control parameter have optimal values like $\hbar_{\bar{f}} = -0.686258$, $\hbar_{\bar{g}} = 0.651312$, $\hbar_{\bar{h}} = -0.112385$ and $\hbar_{\bar{j}} = -1.92267$ and total average squared residual error is $\varrho_m^t = 0.384779$ taken at 2nd order of approximations. Plot for total residual error of Fe_3O_4 -water nanofluid is drawn in Figure (5.2). Thermophysical properties such as density, specific heat and thermal conductivity is shown in Table (5.1). By using optimal values of \hbar the averaged squared residual errors is computed in Table (5.2). Moreover, the averaged squared residual errors show decreasing trend for higher order deformations.

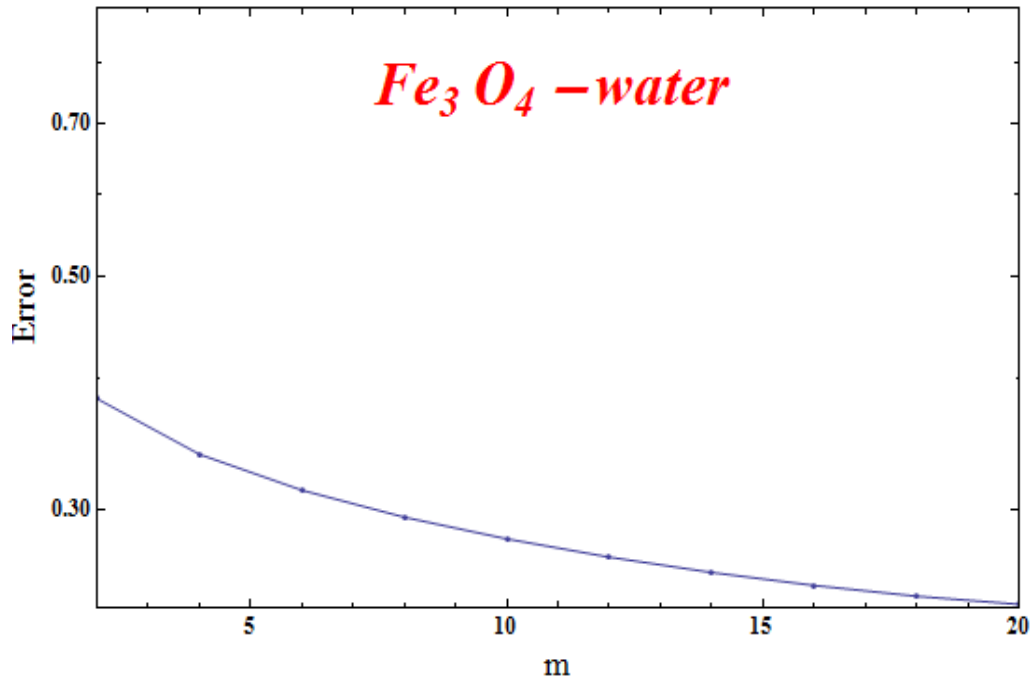


Figure 5.2: Residual error for magnetite-water nanofluid.

Table 5.1: Thermo-physical properties of magnetite nanoparticles and water.

—	$k(W/mk)$	$\rho(kg/m^3)$	$\sigma(Um)^{-1}$	$C_p(j/m^3)$
Fe ₃ O ₄ (Iron oxide)	9.7	5180	670	25000
H ₂ O(Pure Water)	0.613	997.1	0.05	4179

Table 5.2: Individual averaged squared residual errors having optimal values of auxiliary variables for magnetite water nanofluid.

m	$\epsilon_m^{\check{f}}$	$\epsilon_m^{\check{g}}$	$\epsilon_m^{\check{\theta}}$	$\epsilon_m^{\check{j}}$
2	2.97942×10^{-4}	4.38213×10^{-5}	9.50986×10^{-5}	3.84342×10^{-1}
4	6.50099×10^{-5}	8.08571×10^{-6}	5.50189×10^{-5}	3.41095×10^{-1}
6	2.97292×10^{-5}	3.26840×10^{-6}	3.85403×10^{-5}	3.15708×10^{-1}
8	1.72782×10^{-5}	1.68369×10^{-6}	2.97053×10^{-5}	2.97885×10^{-1}
10	1.13359×10^{-5}	9.92329×10^{-7}	2.42156×10^{-5}	2.84327×10^{-1}
12	8.03415×10^{-6}	6.40412×10^{-7}	2.04679×10^{-5}	2.74327×10^{-1}
14	6.00804×10^{-6}	4.41266×10^{-7}	1.77406×10^{-5}	2.65008×10^{-1}
16	4.67339×10^{-6}	3.19449×10^{-7}	1.56633×10^{-5}	2.58267×10^{-1}

5.4 Physical interpretation

This section presents the effects of $(1.0 \leq n \leq 1.3)$, $(0.2 \leq M \leq 0.8)$, $(0.1 \leq \Psi \leq 0.7)$, $(0.4 \leq R_D \leq 0.7)$, $(0.02 \leq \phi \leq 0.05)$, $(1.3 \leq \theta_w \leq 1.6)$, $(0.2 \leq K_r \leq 0.5)$ and $(0.2 \leq K_s \leq 0.5)$ for magnetite-water nanofluids on velocity components, temperature and concentration distributions. Plots for skin friction coefficient and heat transfer rate are also sketched.

5.4.1 Velocity components

Figure (5.3) illustrate the effect of $(\phi = 0.02, 0.03, 0.04, 0.05)$ on velocities $\tilde{f}'(\xi)$ and $\tilde{g}'(\xi)$. Higher (ϕ) reduces both velocities. Physically resistance between fluid particles enhances for larger (ϕ) which produce a decline in velocities $\tilde{f}'(\xi)$ and $\tilde{g}'(\xi)$. Behavior of power-law index $(n = 1.0, 1.1, 1.2, 1.3)$ on the velocities is shown in Figure (5.4). Clearly motion of fluid particles rises for higher (n) . Physically viscosity of fluid reduces due to higher values of (n) . Therefore both velocities are enhanced. Figure (5.5) is sketched to indicate the behavior of magnetic parameter $(M = 0.2, 0.4, 0.6, 0.8)$

for velocities $\tilde{f}'(\xi)$ and $\tilde{g}'(\xi)$. For larger magnetic parameter (M) both velocities of fluid decay. As expected drag force (which is known as Lorentz force) is created by application of magnetic field. This force has ability to slow down flow. Figure (5.6) is graphed to study the variation in velocities (along x and y directions) respectively for higher ratio parameter ($\Psi = 0.1, 0.3, 0.5, 0.7$). Higher values of (Ψ) constitute more velocity field along y -direction while opposite trend can be observed for velocity field along x -direction. Physically larger values of ($\Psi = \frac{v_0}{u_0}$) lead to either an increase in (v_0) or decrease in (u_0), the constant along x -direction decreased and Ψ along y -direction increases correspondingly.

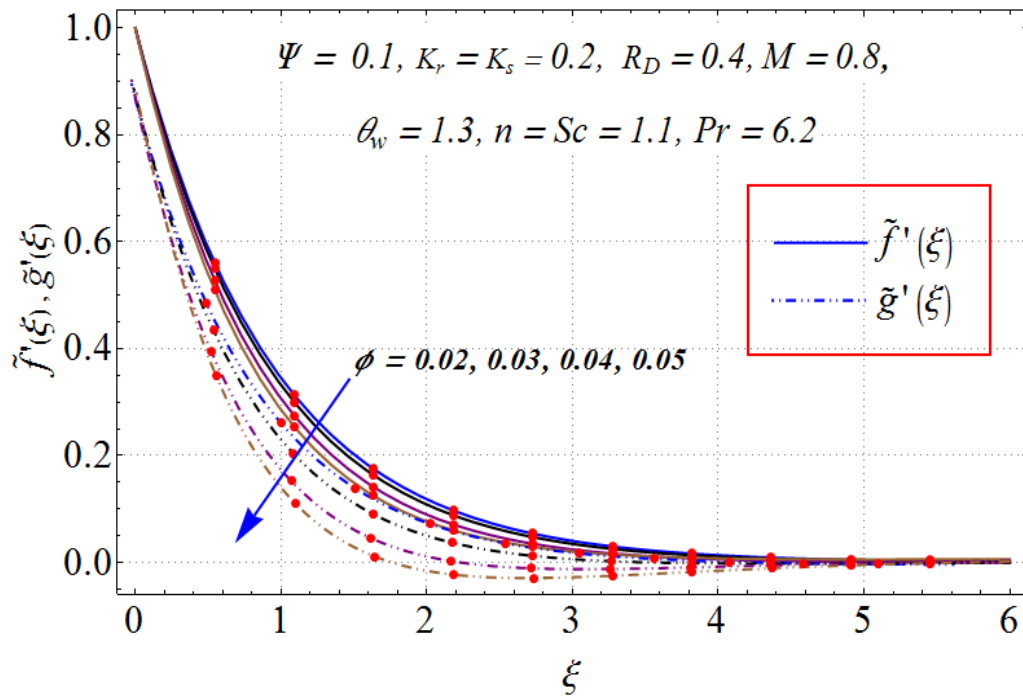


Figure 5.3: Variation of ϕ on $\tilde{f}'(\xi)$.

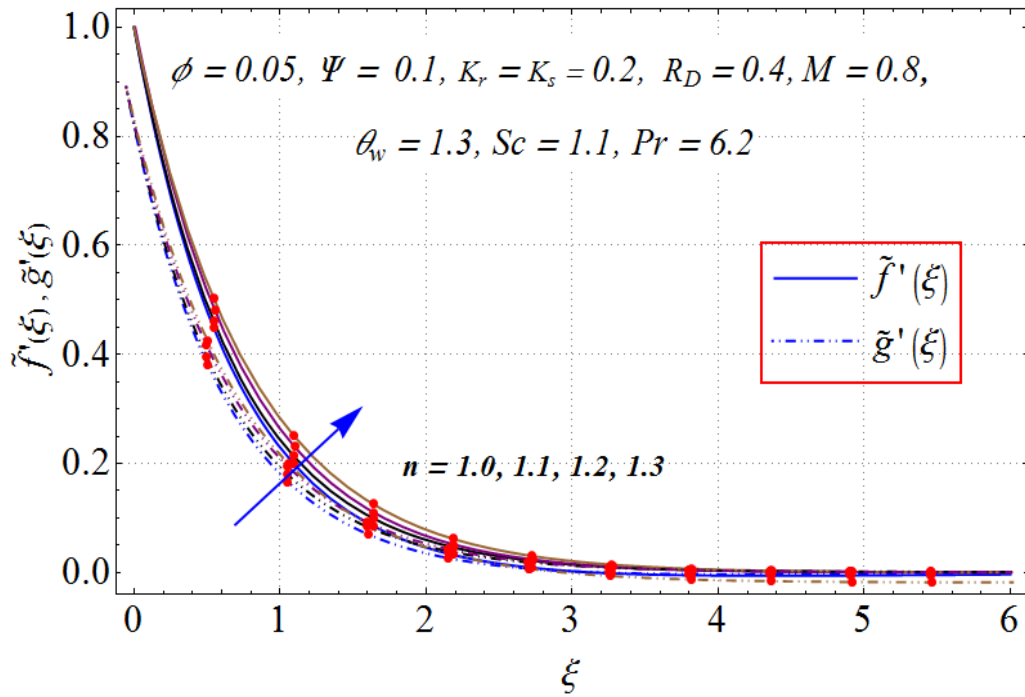


Figure 5.4: Variation of n on $\tilde{f}'(\xi)$ and $\tilde{g}'(\xi)$.

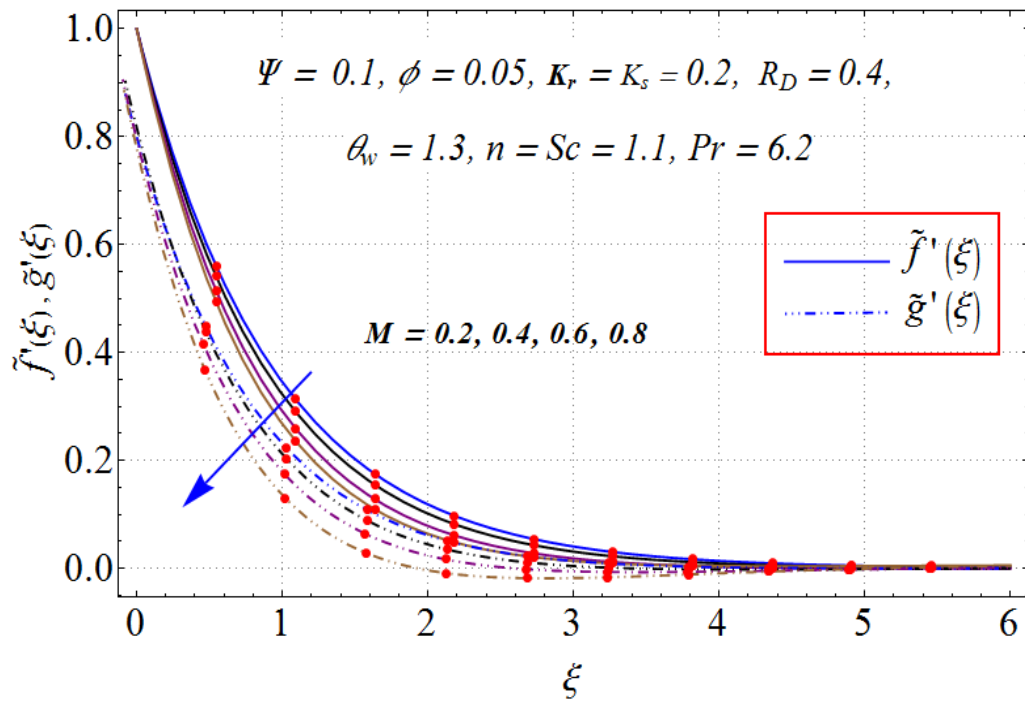
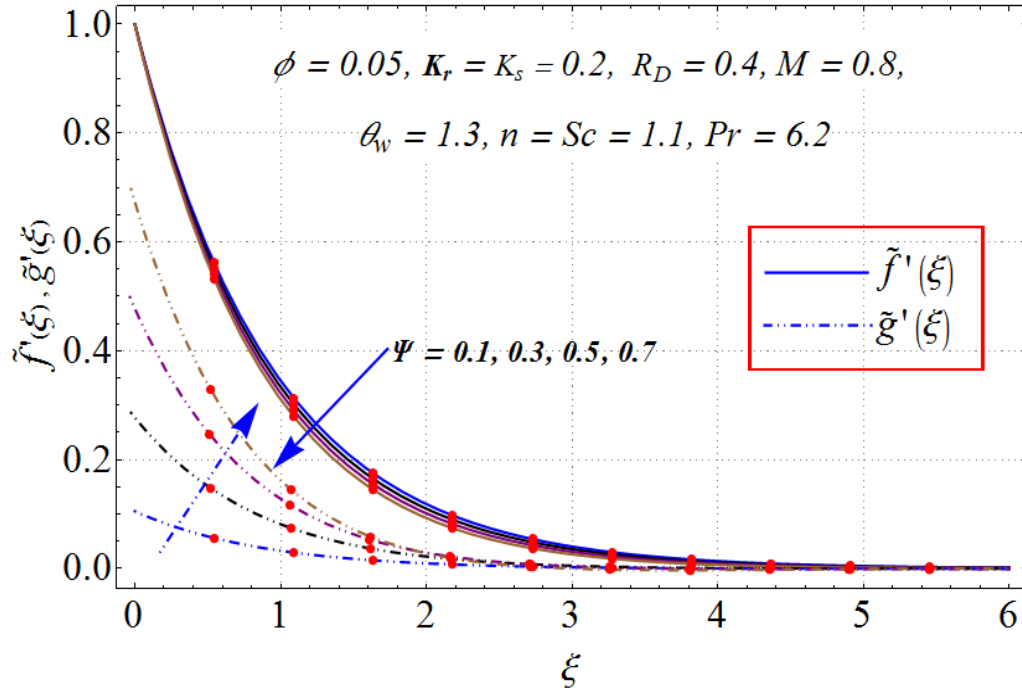


Figure 5.5: Variation of M on $\tilde{f}'(\xi)$ and $\tilde{g}'(\xi)$.


 Figure 5.6: Variation of Ψ on $\tilde{f}'(\xi)$ and $\tilde{g}'(\xi)$.

5.4.2 Temperature

Influence of nanoparticles volume fraction ($\phi = 0.02, 0.03, 0.04, 0.05$) on $\tilde{\theta}(\xi)$ is displayed in Figure (5.7). An increasing behavior of thermal field and associated layer thickness is noted via (ϕ) . It is due to the fact that higher values of (ϕ) corresponds to more thermal conductivity as well as thermal layer thickness. Figure (5.8) represents the variation in temperature for radiation parameter ($R_D = 0.4, 0.5, 0.6, 0.7$). Temperature of fluid increases for larger (R_D) . Here Rosseland radiative absorptive (k^*) reduces due to strengthening the radiation parameter. The radiative heat flux enhances and consequently the rate of radiative heat transfer enhances inside the fluid. Higher radiative heat transfer to the fluid is responsible for an increase in thermal layer growth. Impact of temperature ratio parameter ($\theta_w = 1.3, 1.4, 1.5, 1.6$) on $\tilde{\theta}(\xi)$ is illustrated in Figure (5.9). Increasing behavior is observed for temperature with an increment in $(\theta_w = \frac{T_w}{T_\infty})$. It is due to the fact that temperature of stretching sheet is higher than ambient temperature with increasing (θ_w) .

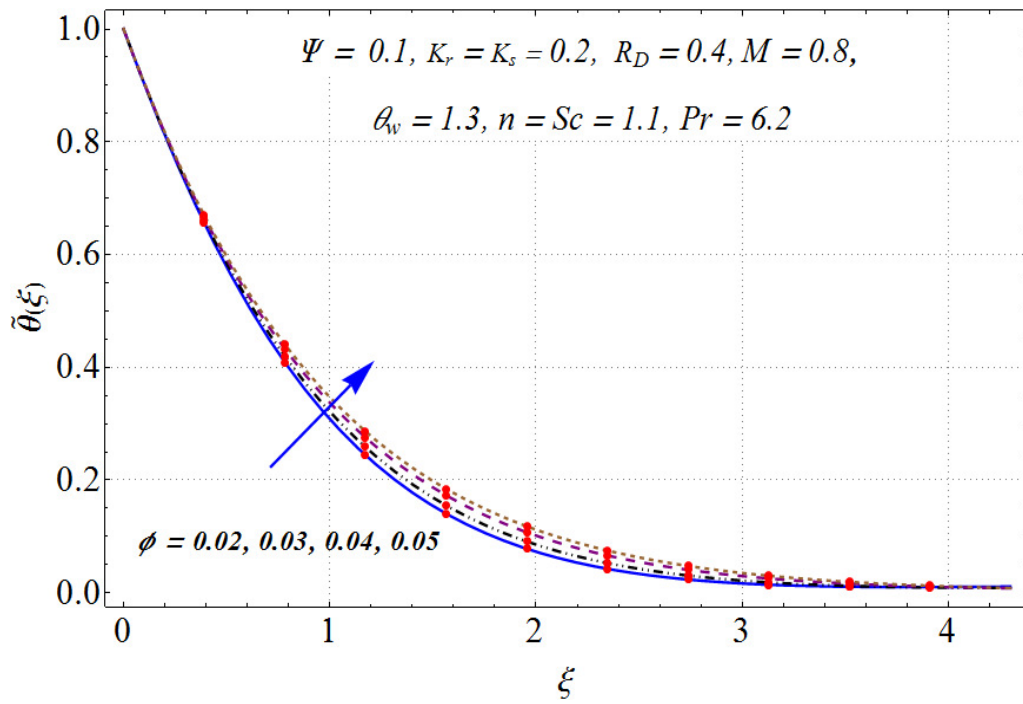


Figure 5.7: Variation of ϕ on $\tilde{\theta}(\xi)$.

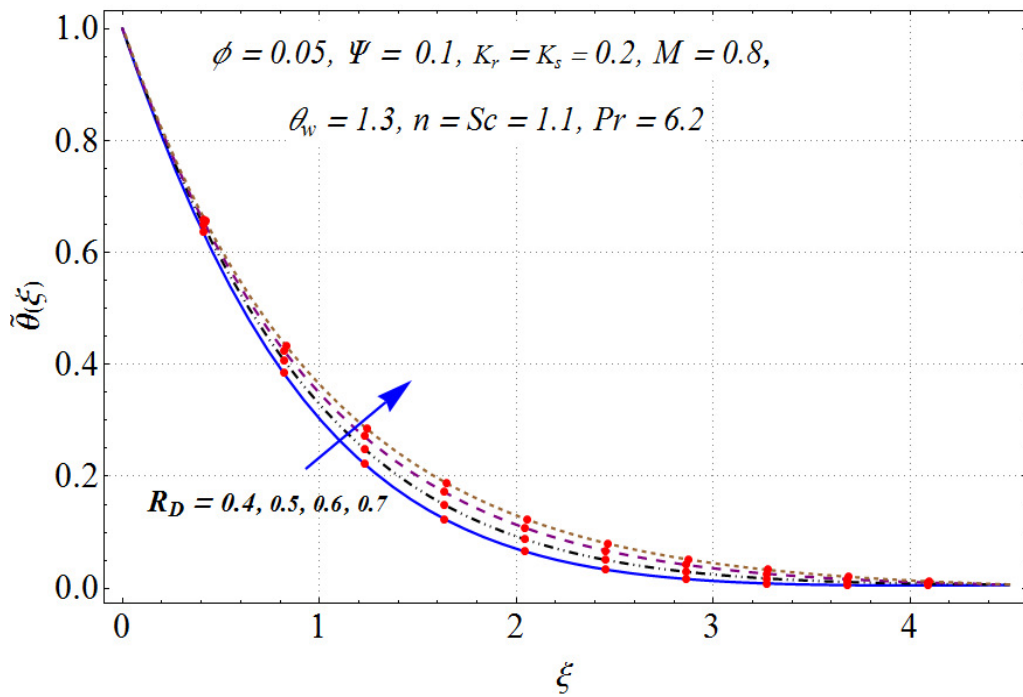
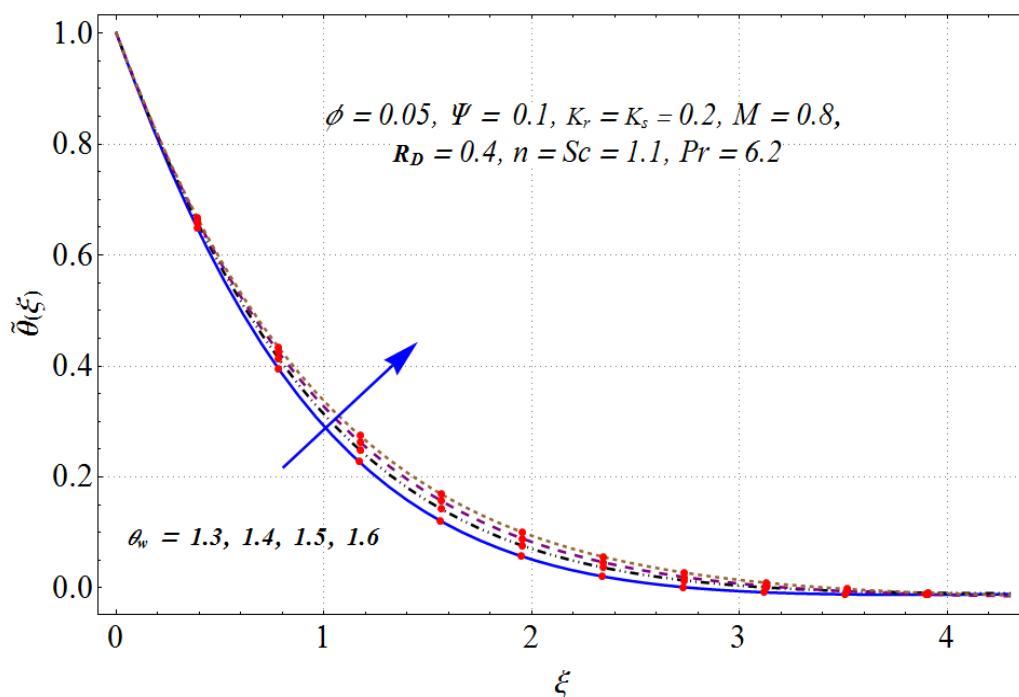


Figure 5.8: Variation of R_D on $\tilde{\theta}(\xi)$.


 Figure 5.9: Variation of θ_w on $\tilde{\theta}(\xi)$.

5.4.3 Concentration

Outcome of nanoparticles volume fraction ($\phi = 0.02, 0.03, 0.04, 0.05$) on concentration is illustrated in Figure (5.10). Here concentration of nanoparticles is an increasing function of volume fraction of nanoparticles (ϕ). Figure (5.11) is plotted to examine the impact of homogeneous reaction parameter ($K_r = 0.2, 0.3, 0.4, 0.5$) on concentration $\tilde{j}(\xi)$. Concentration reduces for higher values of homogeneous reaction parameter. It is through the fact that reactants are consumed during homogeneous reaction. Behavior of heterogeneous reaction parameter ($K_s = 0.2, 0.3, 0.4, 0.5$) on the concentration is displayed in Fig. (5.12). It has been examined that large heterogeneous parameter shows an increasing trend in concentration. For higher values of (K_s) the diffusion coefficient reduces and less diffused particles enhances the concentration.

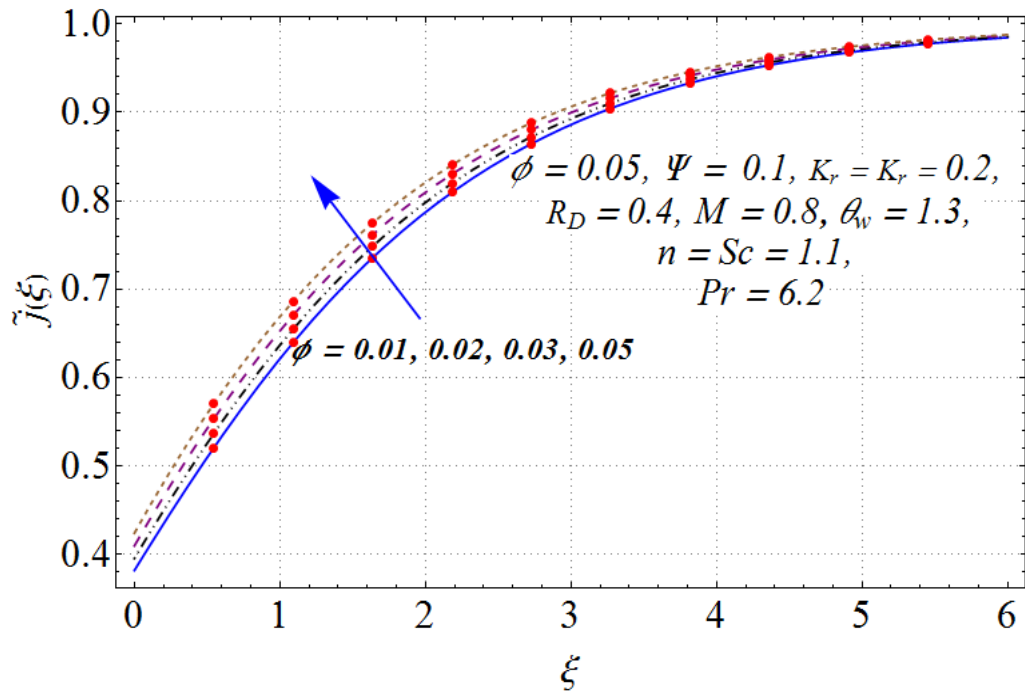


Figure 5.10: Variation of ϕ on $\tilde{j}(\xi)$.

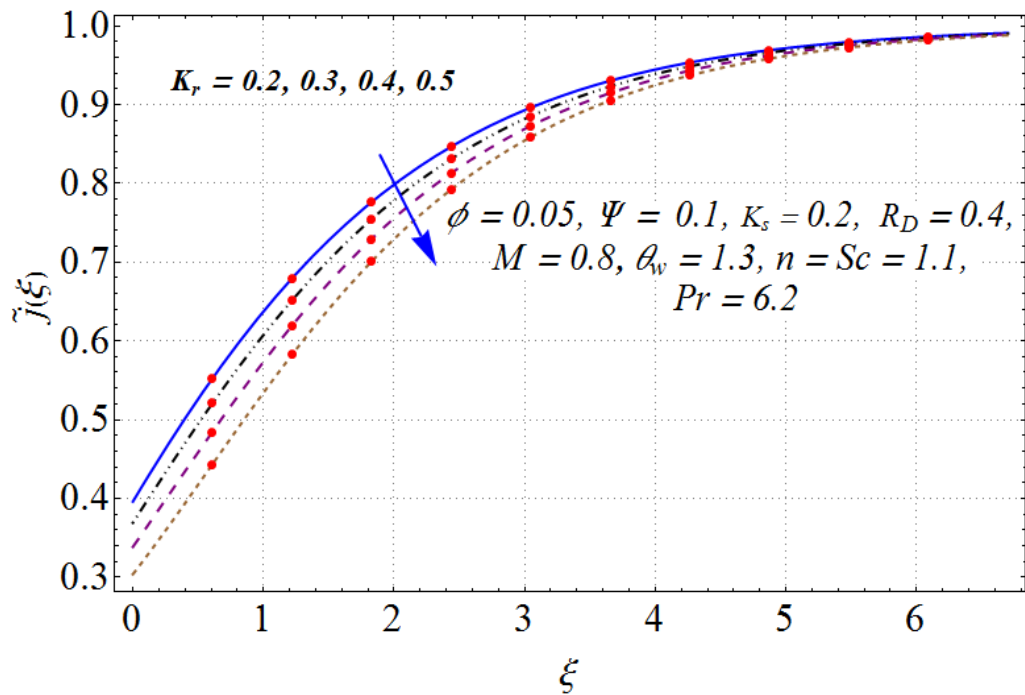
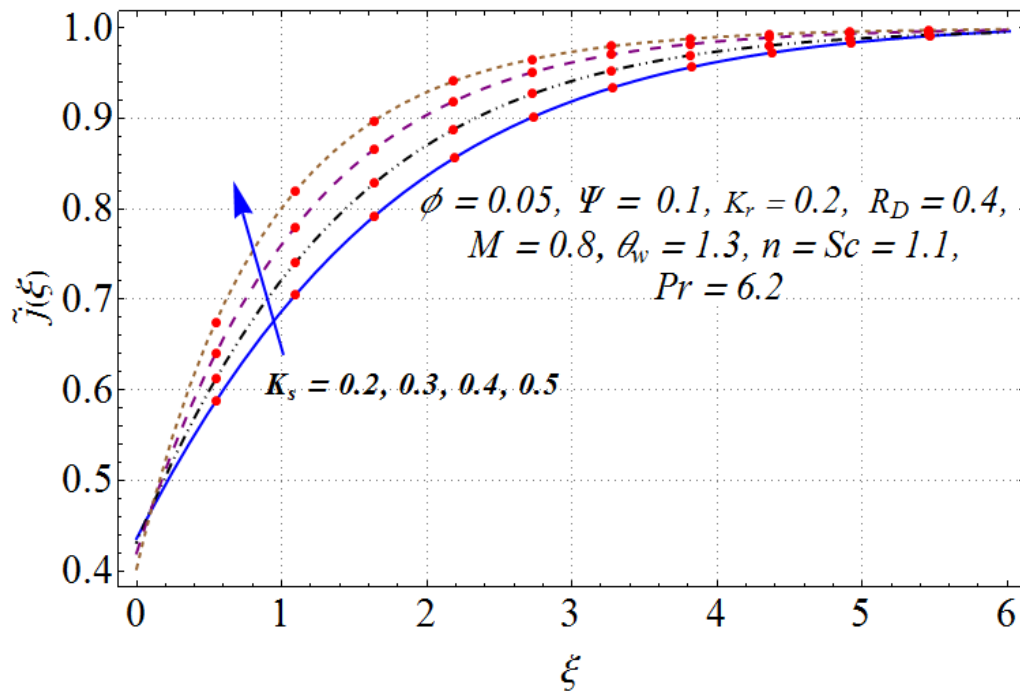


Figure 5.11: Variation of $K_r \phi$ on $\tilde{j}(\xi)$.


 Figure 5.12: Variation of K_s on $\tilde{j}(\xi)$.

5.4.4 Skin friction coefficient and local Nusselt number

Figures (5.13)-(5.16) show the skin friction coefficients (\tilde{C}_{sfx} and \tilde{C}_{sfy}) and local Nusselt number (\tilde{N}_u) for different values of volume fraction of nanomaterial, magnetic parameter, radiation parameter and temperature ratio parameter respectively. Skin friction coefficient along x-direction depicts increasing behavior via (ϕ) and (M) (see Figure (5.13)). Figure (5.14) shows that skin friction coefficient along y-direction enhances for (ϕ) and (Ψ). Figure (5.15) depicts that heat transfer rate enhances against (ϕ). Magnitude of the local Nusselt number enhances via higher (θw) (see in Figure (5.15)).

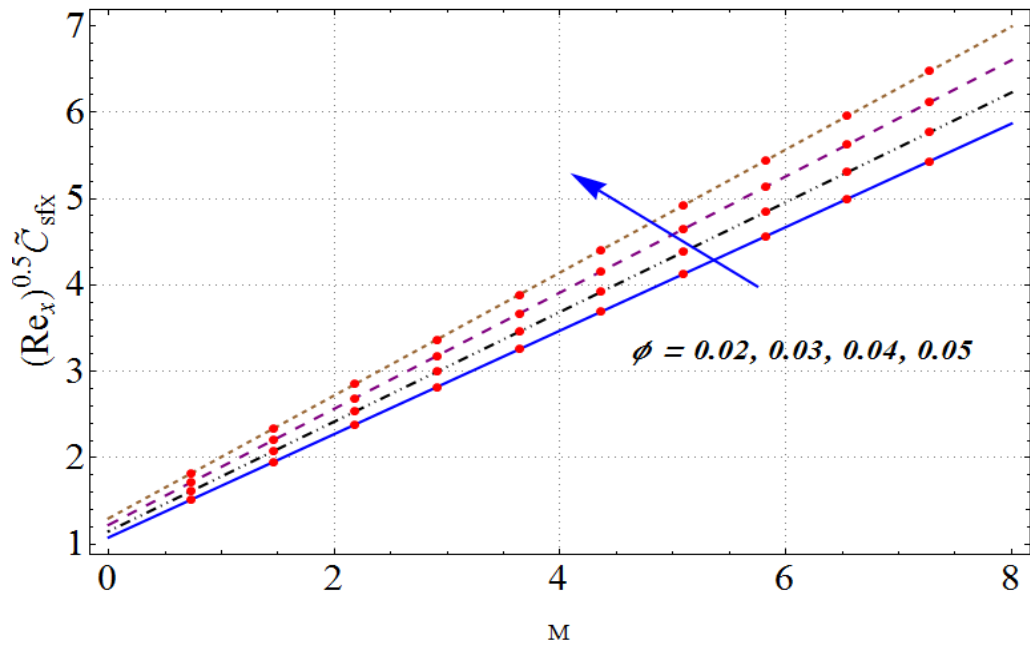


Figure 5.13: Variation of Ψ on $(\text{Re}_x)^{0.5} \tilde{C}_{sfx}$.

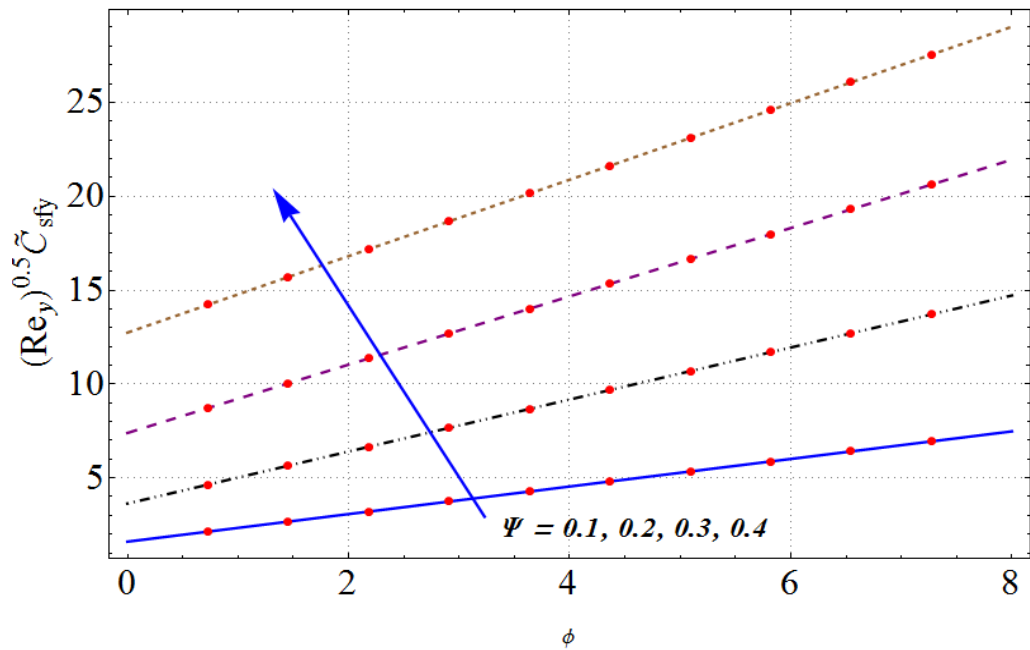


Figure 5.14: Variation of ϕ on $(\text{Re}_x)^{0.5} \tilde{C}_{sfy}$.

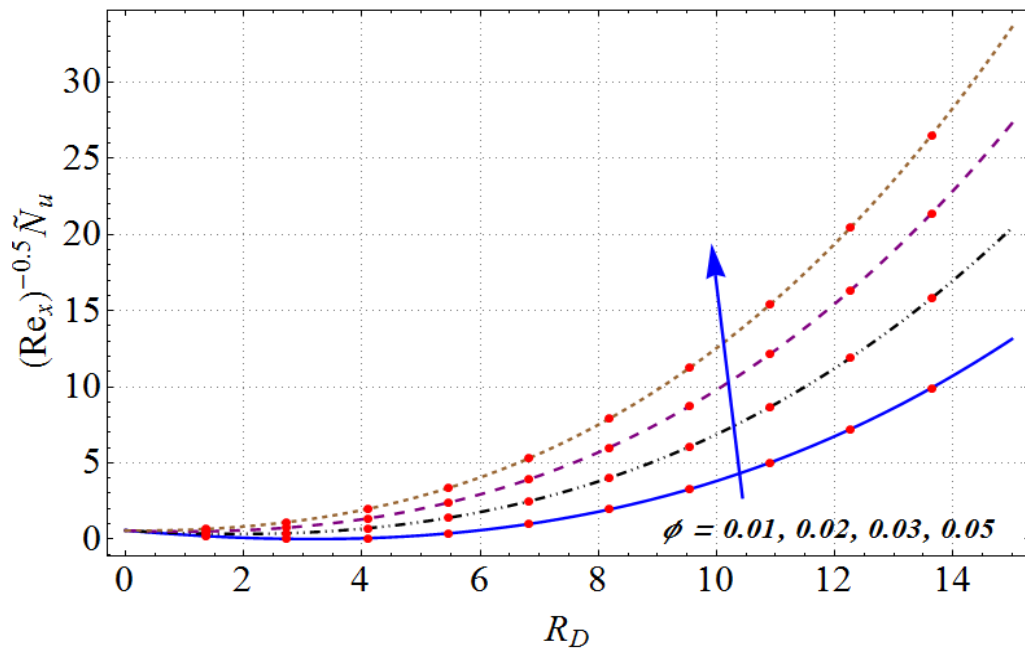


Figure 5.15: Variation of θ_w on $(\text{Re}_x)^{0.5} \tilde{N}_u$.

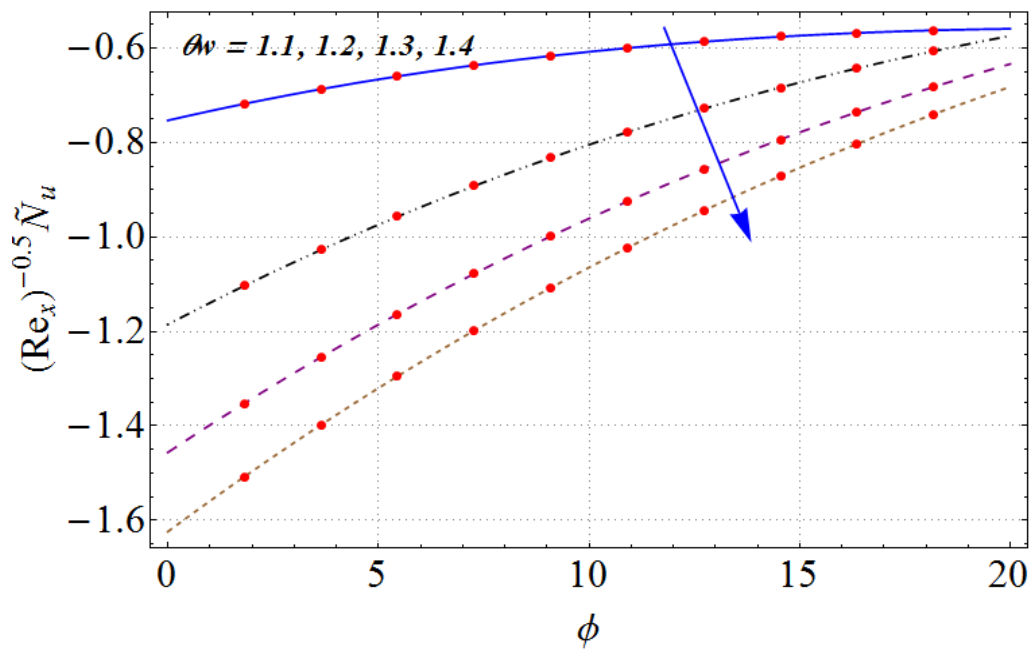


Figure 5.16: Variation of θ_w on $(\text{Re}_x)^{0.5} \tilde{N}_u$.

5.4.5 Comparative study

A comparison between analytical results of the problem and previous literature have been shown in Table (5.3). A good accuracy is obtained between two results.

Table 5.3: Comparison of the values of skin friction coefficient when $M = I_1 = I_1 = I_1 = I_1 = 0$ and variation of ϕ .

n	Ψ	ϕ	Junaid et al. [28]		Mahantesh et al. [29]		Present study	
			$\tilde{f}''(0)$	$\tilde{g}'(0)$	$\tilde{f}''(0)$	$\tilde{g}'(0)$	$\tilde{f}''(0)$	$\tilde{g}'(0)$
$n \geq 1$	0.0	0.0	1.62435	0.0000	1.62435	-0.0000	1.6243	0.00000
$n \geq 1$	0.5	0.0	1.98942	0.99471	1.98942	0.99471	1.98947	0.99477
$n \geq 1$	1.0	0.0	2.29718	2.29718	2.29718	2.29719	2.29712	2.29715
$n \geq 1$	0.1	0.05	---	---	2.20611	1.10306	2.20611	1.10306
$n \geq 1$	0.1	0.1	---	---	2.33770	1.16853	2.33711	1.16850
$n \geq 1$	0.1	0.2	---	---	2.42320	1.21160	2.42380	1.21130

5.5 Conclusions

Main points are as follows:

- For higher magnetic parameter the velocity of fluid reduces.
- Velocity components \tilde{f}' reduces while \tilde{g}' enhances for higher values of stretching rates ratio.
- Behavior of nanoparticles volume fraction for momentum and thermal layers is opposite.
- For fluid concentration the strength of heterogeneous reaction variable increases while opposite trend is noticed for homogeneous reaction case.
- Higher values of magnetic parameter and nanoparticles volume fraction enhance skin friction coefficient.

Chapter 6

Darcy-Forchheimer bidirectional flow in (SWCNTs) and (MWCNTs) carbon nanotubes with homogeneous-heterogeneous reactions

In this chapter modeling is provided for three-dimensional flow of water-based carbon nanotubes. Flow generated is due to bidirectional non-linear stretching surface. Characteristics of both single-walled carbon nanotubes (SWCNTs) and multi-walled carbon nanotubes (MWCNTs) are discussed. Darcy-Forchheimer model is used for flow saturating porous medium. Heat transfer characteristics are elaborated considering convective heating process. Homogeneous-heterogeneous reactions are also accounted. The appropriate transformations lead to strong nonlinear ordinary differential equations. Optimal homotopy analysis technique (OHAM) guided to convergent solutions. The plots are manifested and examined with respect to various variables. Skin friction coefficient and Nusselt number are computed and elaborated. The results for both SWCNTs and MWCNTs are observed and compared.

6.1 Problem formulation

Consider steady three-dimensional (3D) flow of water-based carbon nanotubes (*CNTs*) due to bidirectional non-linearly stretching of surface. Heat transfer mechanism are examined by considering Xue model [2]. An incompressible fluid saturates the porous space satisfying Darcy-Forchheimer relation. We consider cartesian coordinate system in which surface is coincident with xy -plane and fluid occupies the space $z \geq 0$. Let $u_w = u_0(x+y)^n$ and $v_w = v_0(x+y)^n$ be velocities of stretching surface along the x - and y -directions respectively. Here u_0, v_0 and $n > 0$ being the constants. The convectively heated mechanism gives surface temperature which present hot fluid temperature as T_f and heat transfer coefficient h_f . Flow analysis is developed in the presence of homogeneous-heterogeneous reactions. The resulting boundary layer expressions for present three-dimensional flow are

$$\frac{\partial u}{\partial x} + \frac{\partial v}{\partial y} + \frac{\partial w}{\partial z} = 0, \quad (6.1)$$

$$u \frac{\partial u}{\partial x} + v \frac{\partial u}{\partial y} + w \frac{\partial u}{\partial z} = \nu_{nf} \left(\frac{\partial^2 u}{\partial z^2} \right) - \frac{\nu_{nf}}{\kappa_p} u - F_e u^2, \quad (6.2)$$

$$u \frac{\partial v}{\partial x} + v \frac{\partial v}{\partial y} + w \frac{\partial v}{\partial z} = \nu_{nf} \left(\frac{\partial^2 v}{\partial z^2} \right) - \frac{\nu_{nf}}{\kappa_p} v - F_e v^2, \quad (6.3)$$

$$u \frac{\partial T}{\partial x} + v \frac{\partial T}{\partial y} + w \frac{\partial T}{\partial z} = \alpha_{nf} \left(\frac{\partial^2 T}{\partial z^2} \right), \quad (6.4)$$

$$u \frac{\partial a^*}{\partial x} + v \frac{\partial a^*}{\partial y} + w \frac{\partial a^*}{\partial z} = D_A \frac{\partial^2 a^*}{\partial z^2} - K_1 a^* c^{*2}, \quad (6.5)$$

$$u \frac{\partial c^*}{\partial x} + v \frac{\partial c^*}{\partial y} + w \frac{\partial c^*}{\partial z} = D_C \frac{\partial^2 c^*}{\partial z^2} + K_1 a^* c^{*2}. \quad (6.6)$$

The associated boundary conditions are

$$\begin{aligned} u &= u_w = u_0(x+y)^n, \quad v = v_w = v_0(x+y)^n, \quad w = 0, \\ -k_{nf} \frac{\partial T}{\partial z} &= h_f(T_f - T), \quad D_A \frac{\partial a^*}{\partial z} = K_2 a^*, \quad D_C \frac{\partial c^*}{\partial z} = -K_2 a^* \text{ at } z = 0, \\ u &\rightarrow 0, \quad v \rightarrow 0, \quad T \rightarrow T_\infty, \quad a^* \rightarrow a_0, \quad c^* \rightarrow 0 \text{ when } z \rightarrow \infty, \end{aligned} \quad (6.7)$$

Here u, v and w are flow velocities in $x-$, $y-$ and $z-$ directions respectively, $F_e = \frac{C_b}{(x+y)\sqrt{\kappa_p}}$ the Forchheimer coefficient of porous media, κ_p the porous medium permeability and C_b the drag coefficient.

Xue [2] proposed a theoretical model for which

$$\begin{aligned}\mu_{nf} &= \frac{\mu_f}{(1-\phi)^{2.5}}, \quad \rho_{nf} = \rho_f(1-\phi) + \rho_{CNT}\phi, \quad \alpha_{nf} = \frac{k_{nf}}{(\rho C_p)_{nf}}, \\ \nu_{nf} &= \frac{\mu_{nf}}{\rho_{nf}}, \quad (\rho C_p)_{nf} = (\rho C_p)_f(1-\phi) + (\rho C_p)_{CNT}\phi, \\ \frac{k_{nf}}{k_f} &= \frac{(1-\phi) + 2\phi \frac{k_{CNT}}{k_{CNT}-k_f} \ln \frac{k_{CNT}+k_f}{2k_f}}{(1-\phi) + 2\phi \frac{k_f}{k_{CNT}-k_f} \ln \frac{k_{CNT}+k_f}{2k_f}},\end{aligned}\quad (6.8)$$

where μ_{nf} stands for nanofluid effective dynamic viscosity, μ_f for dynamic viscosity of base fluid, ρ_{nf} for density of nanofluid, ρ_f for base fluid density, ϕ for volume fraction of nanoparticle, $(\rho C_p)_{nf}$ for effective heat capacity of nanofluid, ρ_{CNT} for carbon nanotubes density, k_{CNT} for thermal conductivity of carbon nanotubes and k_f for base fluid thermal conductivity.

Selecting the transformations

$$\begin{aligned}u &= u_0(x+y)^n \tilde{f}'(\zeta), \quad v = v_0(x+y)^n \tilde{g}'(\xi), \quad \xi = \left(\frac{u_0(n+1)}{2\nu_f}\right)^{1/2} (x+y)^{\frac{n-1}{2}} z, \\ w &= -\sqrt{\left(\frac{u_0\nu_f(n+1)}{2}\right)} (x+y)^{n-1} \left[(\tilde{f} + \tilde{g}) + \frac{n-1}{n+1} \xi (\tilde{f}' + \tilde{g}') \right], \\ \tilde{\theta}(\xi) &= \frac{T-T_\infty}{T_f-T_\infty}, \quad a^* = a_0 \tilde{j}(\xi), \quad c^* = a_0 \tilde{s}(\xi),\end{aligned}\quad (6.9)$$

continuity equation Eq. (6.1) is trivially verified while Eqs. (6.2)-(6.7) yield

$$\begin{aligned}\frac{1}{(1-\phi)^{2.5} \left(1-\phi + \frac{\rho_{CNT}}{\rho_f} \phi\right)} \tilde{f}''' + (\tilde{f} + \tilde{g}) \tilde{f}'' - \frac{2n}{(n+1)} (\tilde{f}' + \tilde{g}') \tilde{f}' \\ - \frac{2}{(n+1)} \frac{\lambda}{(1-\phi)^{2.5} \left(1-\phi + \frac{\rho_{CNT}}{\rho_f} \phi\right)} \tilde{f}' - \frac{2}{(n+1)} F_r \tilde{f}'^2 = 0\end{aligned}\quad (6.10)$$

$$\begin{aligned}\frac{1}{(1-\phi)^{2.5} \left(1-\phi + \frac{\rho_{CNT}}{\rho_f} \phi\right)} \tilde{g}''' + (\tilde{f} + \tilde{g}) \tilde{g}'' - \frac{2n}{(n+1)} (\tilde{f}' + \tilde{g}') \tilde{g}' \\ - \frac{2}{(n+1)} \frac{\lambda}{(1-\phi)^{2.5} \left(1-\phi + \frac{\rho_{CNT}}{\rho_f} \phi\right)} \tilde{g}' - \frac{2}{(n+1)} F_r \tilde{g}'^2 = 0\end{aligned}\quad (6.11)$$

$$\frac{1}{\text{Pr}} \frac{k_{nf}}{k_f} \tilde{\theta}'' + \left(1 - \phi + \frac{(\rho c_p)_{CNT}}{(\rho c_p)_f} \phi \right) (\tilde{f} + \tilde{g}) \tilde{\theta}' = 0, \quad (6.11)$$

$$\left(\frac{1}{Sc} \right) \tilde{j}'' + (\tilde{f} + \tilde{g}) \tilde{j}' - \frac{2}{n+1} K_r \tilde{j} \tilde{s}^2 = 0, \quad (6.12)$$

$$\left(\frac{\delta}{Sc} \right) \tilde{s}'' + (\tilde{f} + \tilde{g}) \tilde{s}' + \frac{2}{n+1} K_r \tilde{j} \tilde{s}^2 = 0, \quad (6.13)$$

$$\begin{aligned} \tilde{f}(0) &= 0, \quad \tilde{f}'(0) = 1, \quad \tilde{g}(0) = 0, \quad \tilde{g}'(0) = \Psi, \quad \theta'(0) = -\frac{k_f}{k_{nf}} B_T (1 - \theta(0)), \\ \tilde{j}'(0) &= K_s \tilde{j}(0), \quad \delta \tilde{s}'(0) = -K_s \tilde{j}(0), \end{aligned} \quad (6.14)$$

$$\tilde{f}'(\infty) \rightarrow 0, \quad g'(\infty) \rightarrow 0, \quad \theta(\infty) \rightarrow 0, \quad \tilde{j}(\infty) \rightarrow 1, \quad \tilde{s}(\infty) \rightarrow 0. \quad (6.15)$$

Here $\lambda = \frac{\nu_f}{\kappa_p u_0 (x+y)^{n-1}}$ denotes the permeability parameter, $\Psi = \frac{u_0}{u_0}$ the ratio variable, $F_r = \frac{C_b}{\sqrt{\kappa_p}}$ Forchheimer number, $B_T = \frac{h_f}{k_f} \sqrt{\frac{2}{n+1}} \sqrt{\frac{\nu_f}{u_0 (x+y)^{n-1}}}$ the Biot number, $\text{Pr} = \frac{\nu_f (\rho c_p)_f}{k_f}$ the Prandtl number, $Sc = \frac{\nu_f}{D_A}$ the Schmidt number, $\delta = \frac{D_C}{D_A}$ the ratio of diffusion coefficient, $K_r = \frac{K_1 a_0^2}{u_0 (x+y)^{n-1}}$ the homogeneous reaction strength and $K_s = \frac{K_2}{D_A} \sqrt{\frac{\nu_f}{u_0 (x+y)^{n-1}}} \sqrt{\frac{2}{n+1}}$ the heterogeneous reaction strength.

When $D_{\tilde{A}} = D_{\tilde{C}}$ then $\delta = 1$ and thus

$$\tilde{j}(\xi) + \tilde{s}(\xi) = 1. \quad (6.16)$$

Now Eqs.(6.12) and (6.13) give

$$\left(\frac{1}{Sc} \right) \tilde{j}'' + (\tilde{f} + \tilde{g}) \tilde{j}' - \frac{2}{(n+1)} K_r \tilde{j} (1 - \tilde{j})^2 = 0, \quad (6.17)$$

with the boundary conditions

$$\tilde{j}'(0) = K_s \tilde{j}(0), \quad \tilde{j}(\infty) \rightarrow 1. \quad (6.18)$$

6.1.1 Quantities of interest

The expressions for skin friction coefficients and local Nusselt number are

$$\left. \begin{aligned} (\text{Re}_x)^{0.5} \tilde{C}_{sfx} &= \left(\frac{n+1}{2}\right)^{0.5} \frac{1}{(1-\phi)^{2.5}} \tilde{f}''(0), \\ (\text{Re}_y)^{0.5} \tilde{C}_{sfy} &= \left(\frac{n+1}{2}\right)^{0.5} \frac{1}{\Psi^{3/2}(1-\phi)^{2.5}} \tilde{g}''(0), \\ (\text{Re}_x)^{-0.5} \tilde{N}_u &= -\left(\frac{n+1}{2}\right)^{0.5} \frac{k_{nf}}{k_f} \tilde{\theta}'(0), \end{aligned} \right\} \quad (6.19)$$

where $\text{Re}_x = u_w(x+y)/\nu_f$ and $\text{Re}_y = v_w(x+y)/\nu_f$ stands for local Reynolds number.

6.2 Homotopy procedure

The appropriate initial approximations and linear operators are

$$\tilde{f}_0(\xi) = 1 - \exp(-\xi), \quad \tilde{g}_0(\zeta) = \Psi(1 - \exp(-\xi)), \quad (6.20)$$

$$\tilde{\theta}_0(\xi) = \left(\frac{B_T}{B_T + \frac{k_{nf}}{k_f}} \right) \exp(-\xi), \quad \tilde{j}_0(\xi) = 1 - \frac{1}{2} \exp\left(-\sqrt{\frac{2}{n+1}} K_s \xi\right) \quad (6.21)$$

$$\mathcal{L}_{\tilde{f}} = \tilde{f}''' - \tilde{f}', \quad \mathcal{L}_{\tilde{g}} = \tilde{g}''' - \tilde{g}', \quad \mathcal{L}_{\tilde{\theta}} = \tilde{\theta}'' - \tilde{\theta}, \quad \mathcal{L}_{\tilde{j}} = \tilde{j}'' - \tilde{j}. \quad (6.22)$$

The above linear operators obey

$$\begin{aligned} \mathcal{L}_{\tilde{f}} [C_1 + C_2 \exp(\xi) + C_3 \exp(-\xi)] &= 0, \quad \mathcal{L}_{\tilde{g}} [C_4 + C_5 \exp(\xi) + C_6 \exp(-\xi)] = 0, \\ \mathcal{L}_{\tilde{\theta}} [C_7 \exp(\xi) + C_8 \exp(-\xi)] &= 0, \quad \mathcal{L}_{\tilde{j}} [C_9 \exp(\xi) + C_{10} \exp(-\xi)] = 0, \end{aligned} \quad (6.23)$$

in which C_i ($i = 1 - 10$) depict the arbitrary constants

6.3 Convergence

The averaged squared residual errors are given as

$$\varepsilon_m^{\tilde{f}} = \frac{1}{k+1} \sum_{l=0}^k \left[\mathcal{N}_{\tilde{f}} \left(\sum_{i=0}^m \tilde{f}(\xi), \sum_{i=0}^m \tilde{g}(\xi) \right)_{\xi=l\delta^*\xi} \right]^2, \quad (28)$$

$$\varepsilon_m^{\tilde{g}} = \frac{1}{k+1} \sum_{l=0}^k \left[\mathcal{N}_{\tilde{g}} \left(\sum_{i=0}^m \tilde{f}(\xi), \sum_{i=0}^m \tilde{g}(\xi) \right)_{\xi=l\delta^*\xi} \right]^2, \quad (6.24)$$

$$\varepsilon_m^{\tilde{\theta}} = \frac{1}{k+1} \sum_{l=0}^k \left[\mathcal{N}_{\tilde{\theta}} \left(\sum_{i=0}^m \tilde{f}(\xi), \sum_{i=0}^m \tilde{g}(\xi), \sum_{i=0}^m \tilde{\theta}(\xi) \right)_{\xi=l\delta^*\xi} \right]^2, \quad (6.25)$$

$$\varepsilon_m^{\tilde{j}} = \frac{1}{k+1} \sum_{l=0}^k \left[\mathcal{N}_{\tilde{j}} \left(\sum_{i=0}^m \tilde{f}(\xi), \sum_{i=0}^m \tilde{g}(\xi), \sum_{i=0}^m \tilde{j}(\zeta) \right)_{\xi=l\delta^*\xi} \right]^2. \quad (6.26)$$

Following Liao [43] :

$$\varepsilon_m^t = \varepsilon_m^{\tilde{f}} + \varepsilon_m^{\tilde{g}} + \varepsilon_m^{\tilde{\theta}} + \varepsilon_m^{\tilde{j}}, \quad (6.27)$$

where ε_m^t exhibits total squared residual error, $\delta^*\xi = 0.5$ and $k = 20$. Best optimal values of auxiliary variables for SWCNTs-Water are $\tilde{h}_{\tilde{f}} = -0.616913$, $\tilde{h}_{\tilde{g}} = -0.624129$, $\tilde{h}_{\tilde{\theta}} = -0.000163257$ and $\tilde{h}_{\tilde{j}} = -1.57895$ with total average squared residual error being $\varepsilon_m^t = 0.00230052$ whereas optimal data of convergence control parameters for MWCNTs-Water are $\tilde{h}_{\tilde{f}} = -0.610944$, $\tilde{h}_{\tilde{g}} = -0.618209$, $\tilde{h}_{\tilde{\theta}} = -0.000359268$ and $\tilde{h}_{\tilde{j}} = -1.580$ with total average squared residual error being $\varepsilon_m^t = 0.00229349$. Figures (6.1) and (6.2) are plotted for residual error of single and multi-walled carbon nanotubes. It is noted that the averaged squared residual errors show decreasing trend for higher order deformations. Table (6.1) depicts thermophysical properties of water and carbon nanotubes (CNTs). Tables (6.2) and (6.3) present the specific averaged squared residual errors by using optimal values of convergence control parameters at $m = 2$ for SWCNTs-Water and MWCNTs-Water respectively.

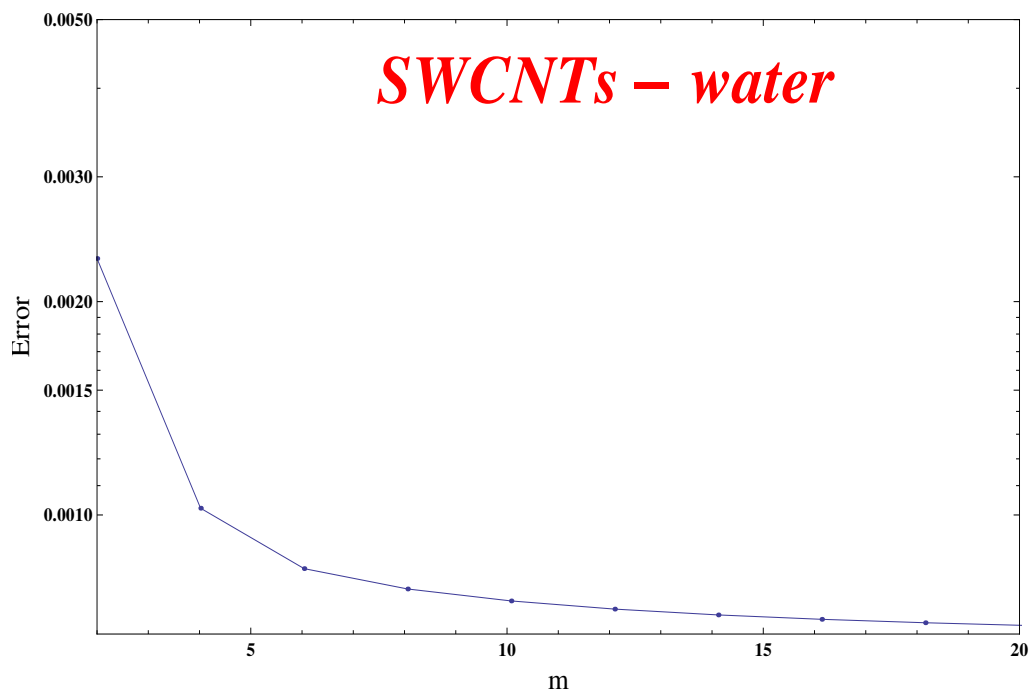


Figure 6.1: Residual error for single-walled carbon nanotubes and water.

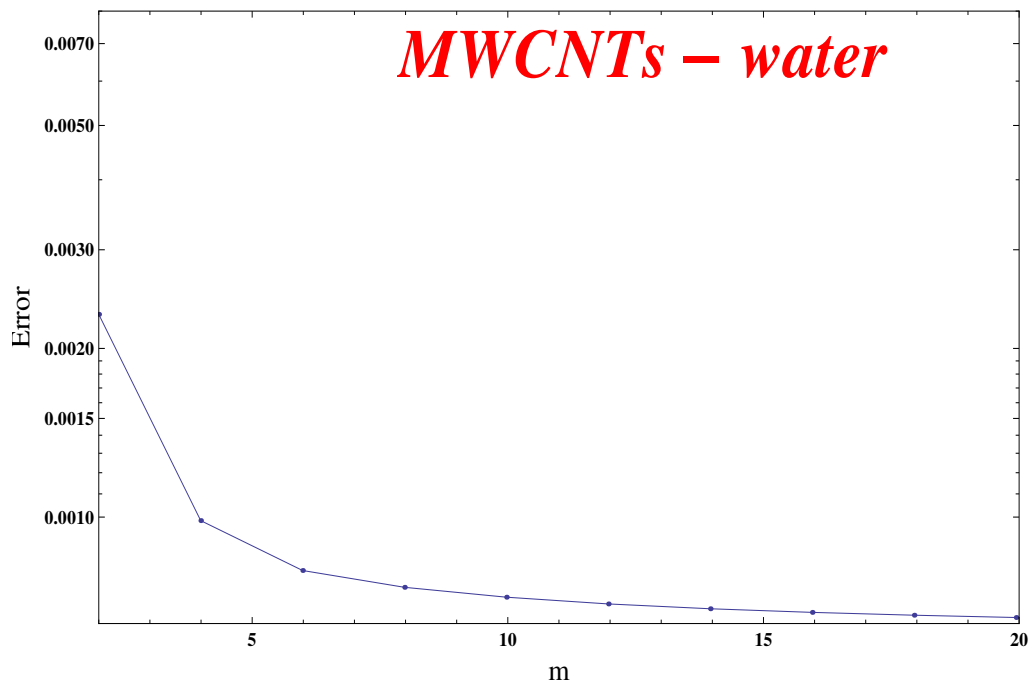


Figure 6.2: Residual error for multi-walled carbon nanotubes and water.

Table 6.1: Thermo-physical properties of single and multi-walled carbon nanotubes and water

—	$k(W/m.k)$	$\rho(kg/m^3)$	$C_p(j/kgk)$
(SWCNTs)	6600	2600	425
(MWCNTs)	3000	1600	796
H ₂ O(Pure Water)	0.613	997.1	4179

Table 6.2: Individual averaged squared residual errors for SWCNTs-water nanofluid.

m	$\varepsilon_m^{\tilde{f}}$	$\varepsilon_m^{\tilde{g}}$	$\varepsilon_m^{\tilde{\theta}}$	$\varepsilon_m^{\tilde{j}}$
2	2.97703×10^{-4}	6.42426×10^{-5}	1.11985×10^{-3}	8.18731×10^{-4}
6	3.06491×10^{-5}	7.26317×10^{-6}	9.27638×10^{-4}	6.59371×10^{-6}
10	1.07557×10^{-5}	2.6183×10^{-6}	8.73656×10^{-4}	1.64036×10^{-6}
16	4.04702×10^{-6}	1.00222×10^{-6}	8.39252×10^{-4}	1.29133×10^{-7}
20	2.53488×10^{-6}	6.31497×10^{-7}	8.26796×10^{-4}	3.53144×10^{-8}

Table 6.3: Individual averaged squared residual errors for MWCNTs-water nanofluid.

m	$\varepsilon_m^{\tilde{f}}$	$\varepsilon_m^{\tilde{g}}$	$\varepsilon_m^{\tilde{\theta}}$	$\varepsilon_m^{\tilde{\phi}}$
2	2.89912×10^{-4}	6.22793×10^{-5}	1.1175×10^{-3}	8.23794×10^{-4}
6	2.98607×10^{-5}	7.05572×10^{-6}	9.24652×10^{-4}	6.7205×10^{-6}
10	1.04900×10^{-5}	2.548×10^{-6}	8.70279×10^{-4}	1.70585×10^{-6}
16	3.95293×10^{-6}	9.77269×10^{-7}	8.35464×10^{-4}	1.30667×10^{-7}
20	2.47811×10^{-6}	6.16436×10^{-7}	8.22796×10^{-4}	3.54361×10^{-8}

6.4 Results and discussion

Here the influences of porosity parameter (λ), Forchheimer number (F_r), ratio parameter (Ψ), nanoparticle volume fraction (ϕ), thermal Biot number (B_T), homogeneous reaction variable (K_r), heterogeneous reaction variable (K_s) and Schmidt number (Sc) on the velocities $\tilde{f}'(\xi)$ and $\tilde{g}'(\xi)$, temperature $\tilde{\theta}(\xi)$ and concentration $\tilde{j}(\xi)$ fields. Figures (6.3)-(6.18) are illustrated and interpreted for such intention. Results are achieved for both single and multi-walled carbon nanotubes (*SWCNTs* and *MWCNTs*).

6.4.1 Velocity components

Figures (6.3) and (6.4) are constructed to explore the impact of volume fraction of nanoparticles ($\phi = 0.01, 0.02, 0.03, 0.4$) on velocities $\tilde{f}'(\xi)$ and $\tilde{g}'(\xi)$. It is declared that (ϕ) yields an enhancement in velocities $\tilde{f}'(\xi)$ and $\tilde{g}'(\xi)$ for both SWCNTs and MWCNTs. It is observed that velocities of fluid particles in case of MWCNTs-water base fluid is dominant than SWCNTs for higher volume fraction of nanoparticles. The role of ratio variable ($\Psi = 0.0, 0.2, 0.4, 0.5$) on velocities $\tilde{f}'(\xi)$ and $\tilde{g}'(\xi)$ for both SWCNTs and MWCNTs are addressed in Figures (6.5) and (6.6). Increasing behavior of $\tilde{g}'(\xi)$ is noted for higher (Ψ) while reverse trend is observed for $\tilde{f}'(\xi)$. Figures (6.7) and (6.8) are sketched to indicate the behavior of permeability parameter ($\lambda = 0.5, 0.6, 0.7, 0.8$) on velocities $\tilde{f}'(\xi)$ and $\tilde{g}'(\xi)$ for both SWCNTs and MWCNTs. Clearly a rise in permeability parameter (λ) corresponds to lower velocities. In fact the permeability of porous medium reduces for higher (λ). It is noted that velocity for multi-walled CNTs is lesser than single-walled CNTs. Figures (6.9) and (6.10) are constructed to examine that how the axial $\tilde{f}'(\xi)$ and transverse $\tilde{g}'(\xi)$ velocities gets affected with the variation of Forchheimer number ($F_r = 0.0, 0.1, 0.2, 0.3$). Velocities $\tilde{f}'(\xi)$ and $\tilde{g}'(\xi)$ decline via higher Forchheimer number (F_r). It is due to the fact that drag force has great association with Forchheimer number. Higher Forchheimer number increases drag force which has ability to retard the fluid velocities. It is worth mentioning that fluid velocities are more prominent in case of single-walled CNTs when compared to multi-walled CNTs.

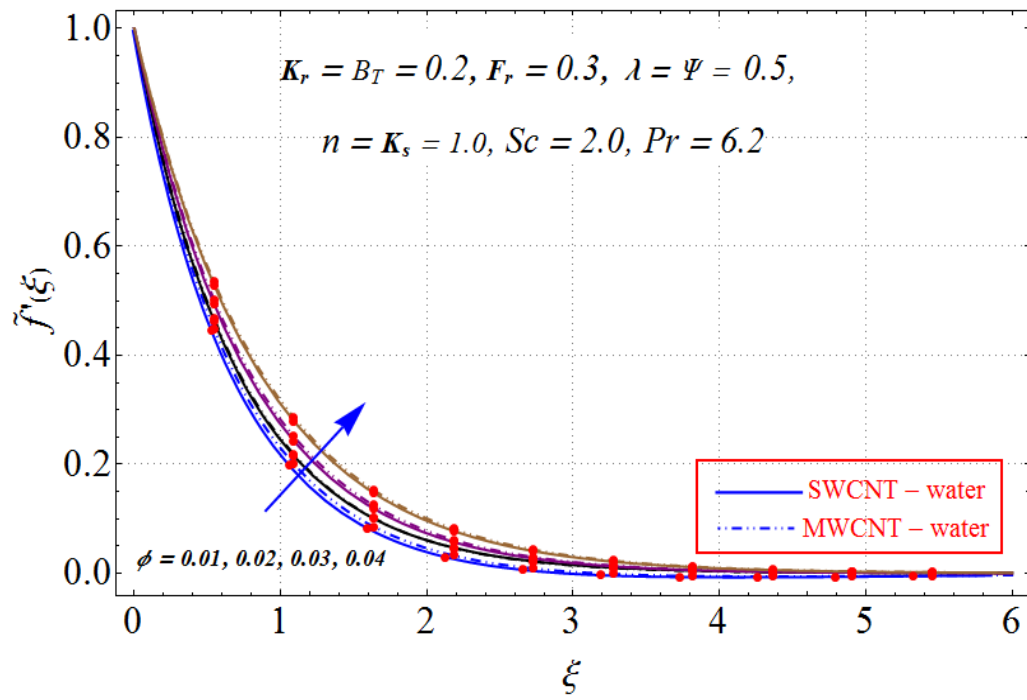


Figure 6.3: Variation of ϕ on $\tilde{f}'(\xi)$.

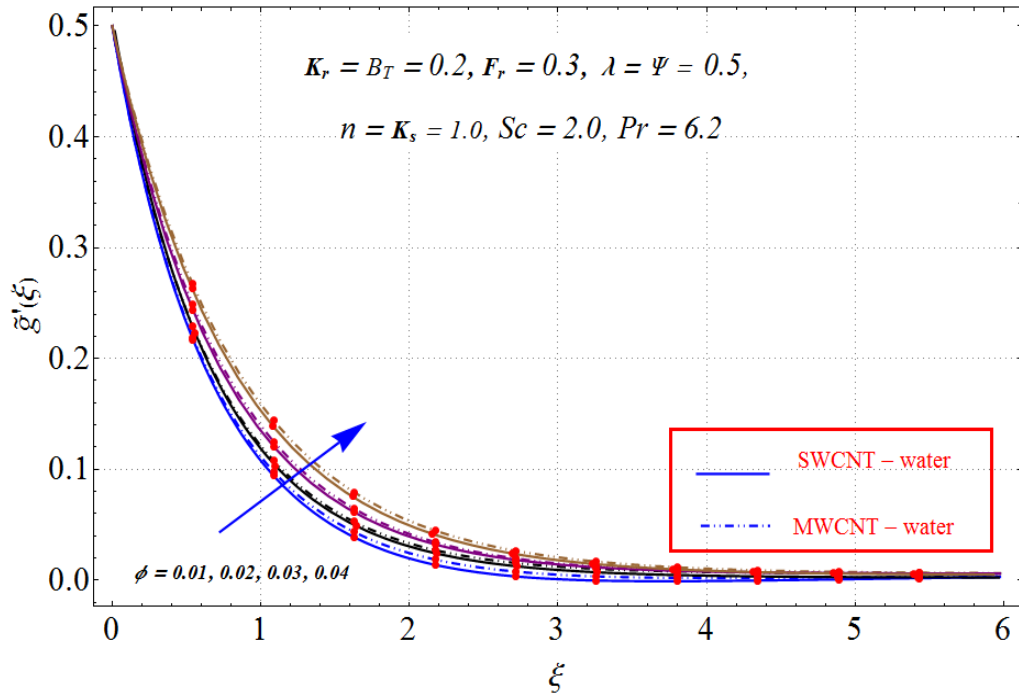


Figure 6.4: Variation of ϕ on $\tilde{g}'(\xi)$.

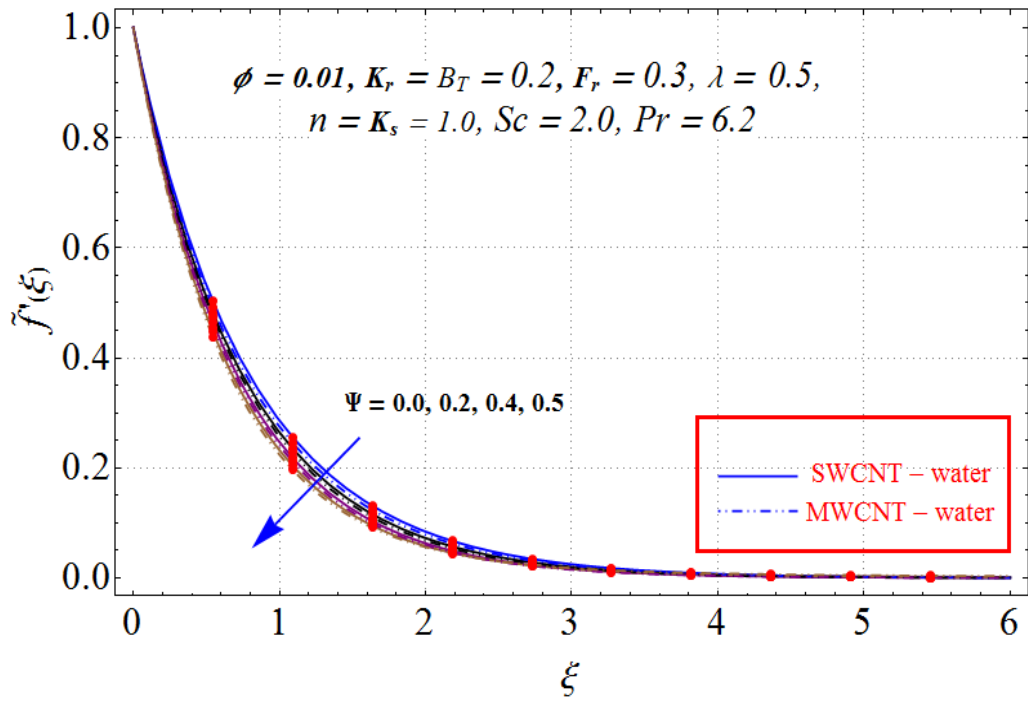


Figure 6.5: Variation of Ψ on $\tilde{f}'(\xi)$.

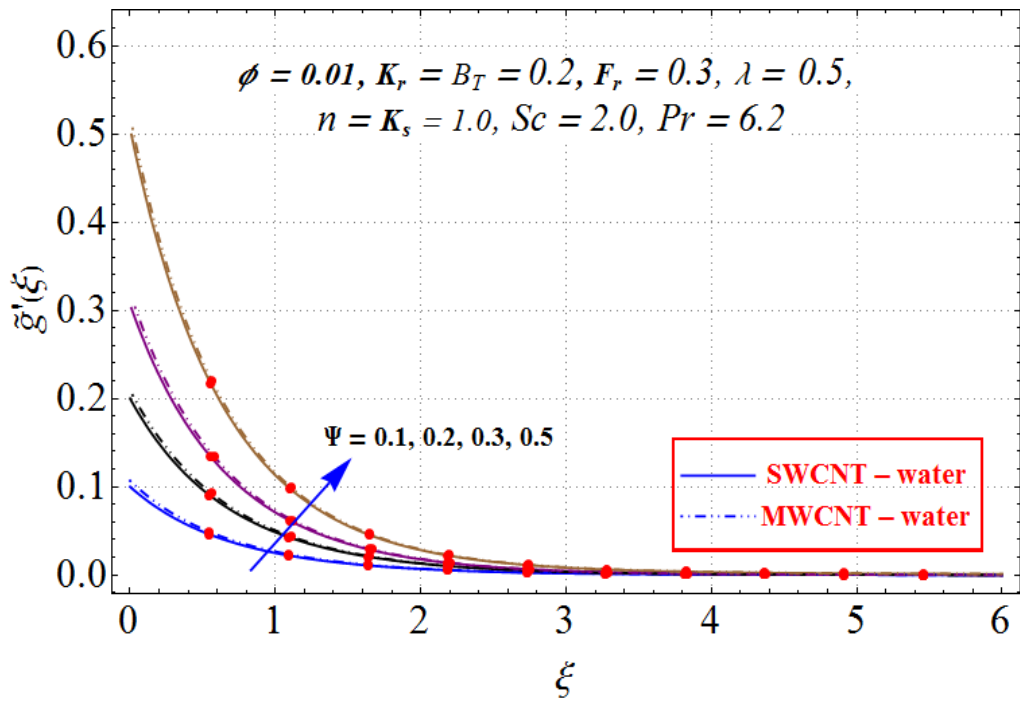


Figure 6.6: Variation of Ψ on $\tilde{g}'(\xi)$.

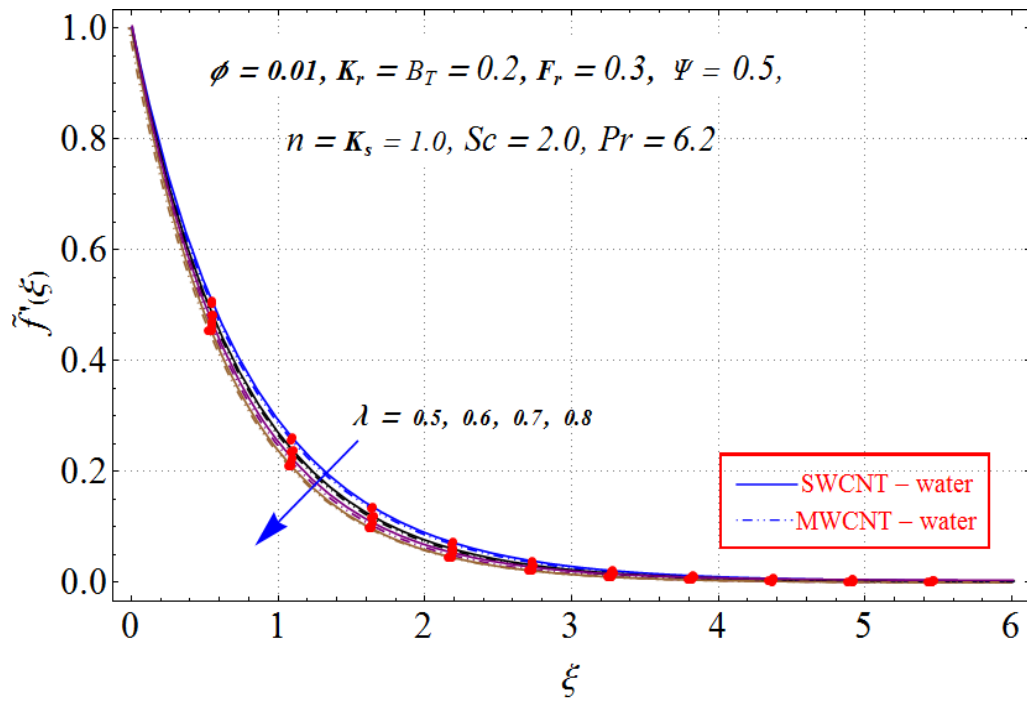


Figure 6.7: Variation of λ on $\tilde{f}'(\xi)$.

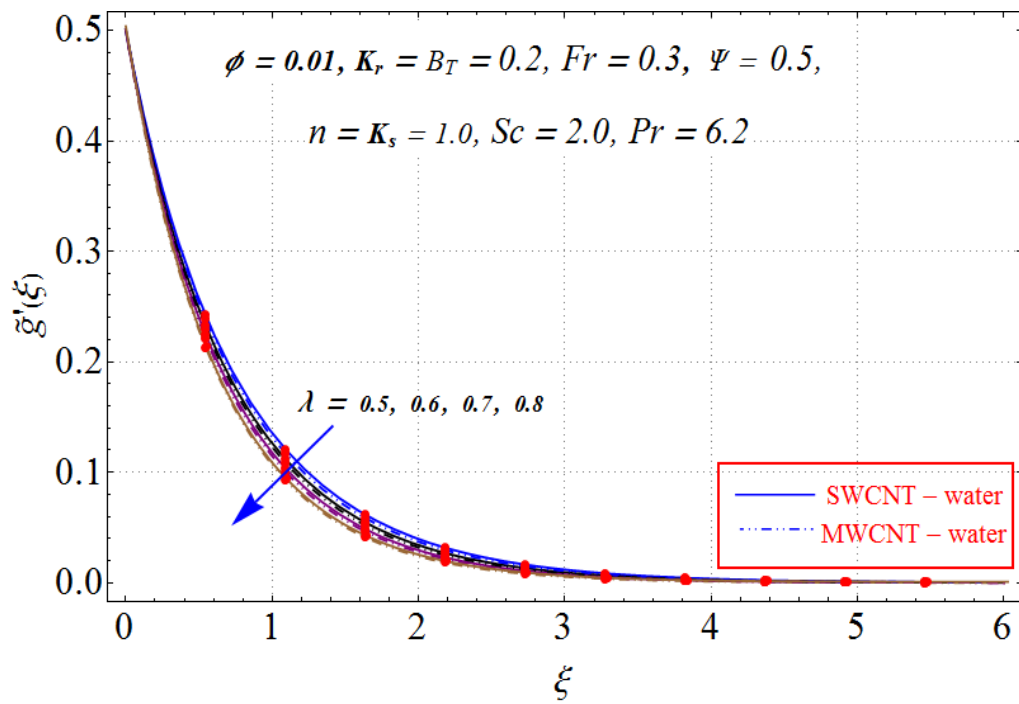


Figure 6.8: Variation of λ on $\tilde{g}'(\xi)$.

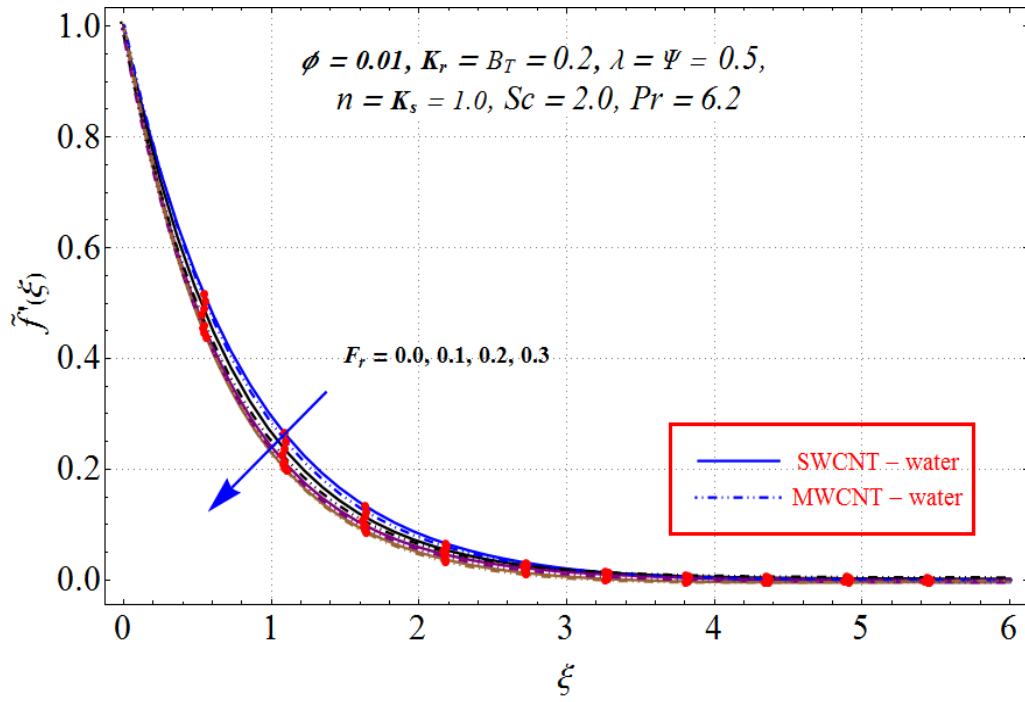


Figure 6.9: Variation of F_r on $\tilde{f}'(\xi)$.

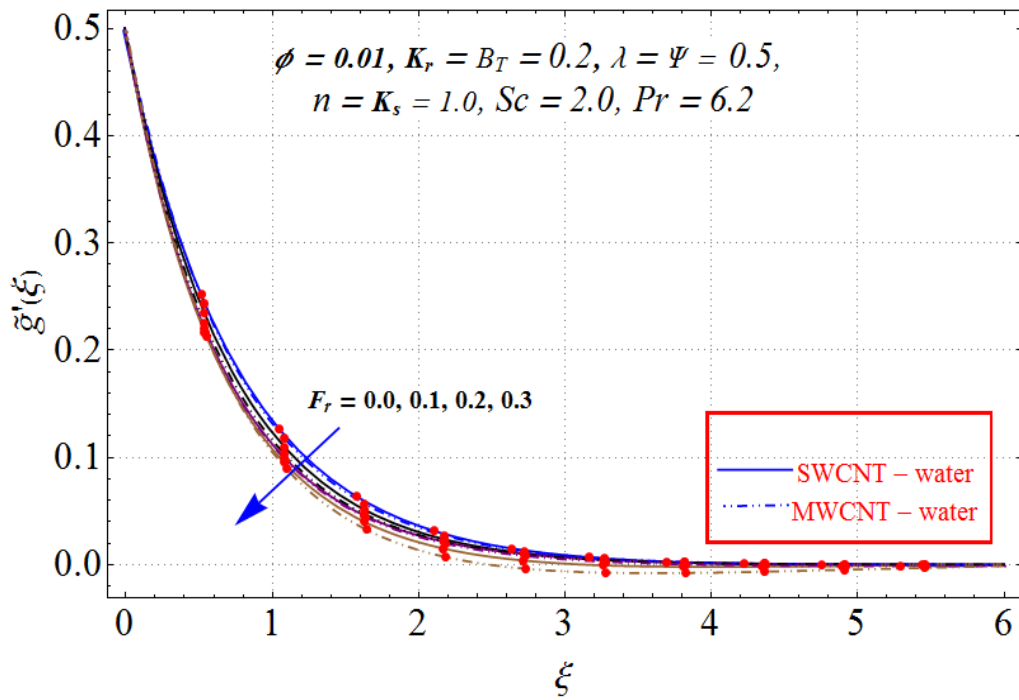


Figure 6.10: Variation of F_r on $\tilde{g}'(\xi)$.

6.4.2 Temperature

Figure (6.11) is delineated for nanoparticle volume fraction ($\phi = 0.01, 0.2, 0.03, 0.04$) variation against temperature $\tilde{\theta}(\xi)$ for both SWCNTs and MWCNTs. Clearly a rise in (ϕ) augments temperature $\tilde{\theta}(\xi)$ and thermal layer. Influence of permeability parameter ($\lambda = 0.5, 0.6, 0.7, 0.8$) against temperature $\tilde{\theta}(\xi)$ is plotted in Figure (6.12). Higher (λ) correspond to a stronger temperature for both SWCNTs and MWCNTs. In fact, the existence of the porous space enhances the resistance to the fluid flow, which rise the temperature of fluid. Figure (6.13) show the changes in temperature $\tilde{\theta}(\xi)$ for various values of Forchheimer number ($F_r = 0.0, 0.1, 0.2, 0.3$). It is clearly noticed that higher Forchheimer number (F_r) enhance the temperature for both SWCNTs and MWCNTs. Influence of thermal Biot number ($B_T = 0.2, 0.3, 0.4, 0.5$) on temperature is plotted in Figure (6.14). Larger (B_T) leads to a increasing trend in temperature for both SWCNTs and MWCNTs. Physically higher Biot number (B_T) leads to stronger convection which causes an enhancement in temperature $\tilde{\theta}(\xi)$ and related thermal layer thickness.

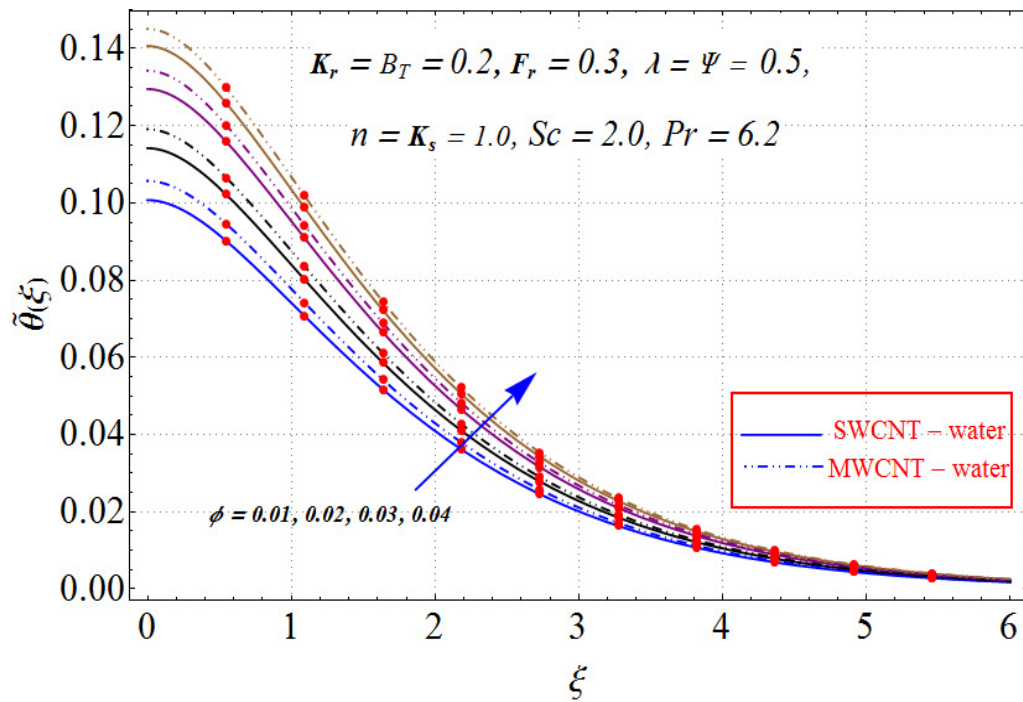


Figure 6.11: Variation of ϕ on $\tilde{\theta}(\xi)$.

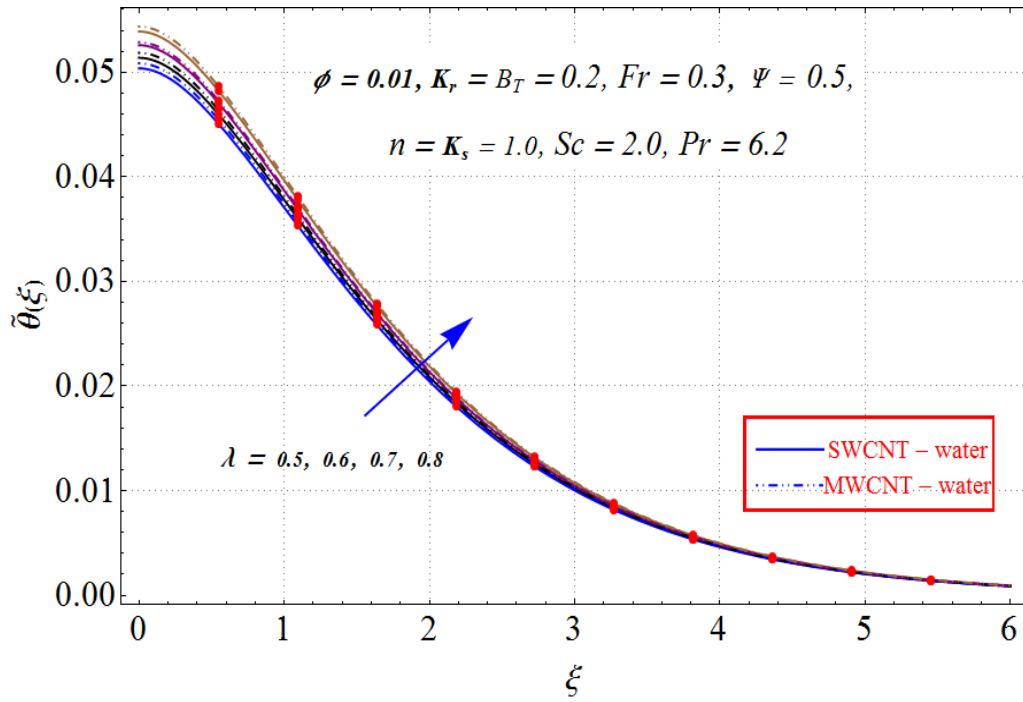


Figure 6.12: Variation of λ on $\tilde{\theta}(\xi)$.

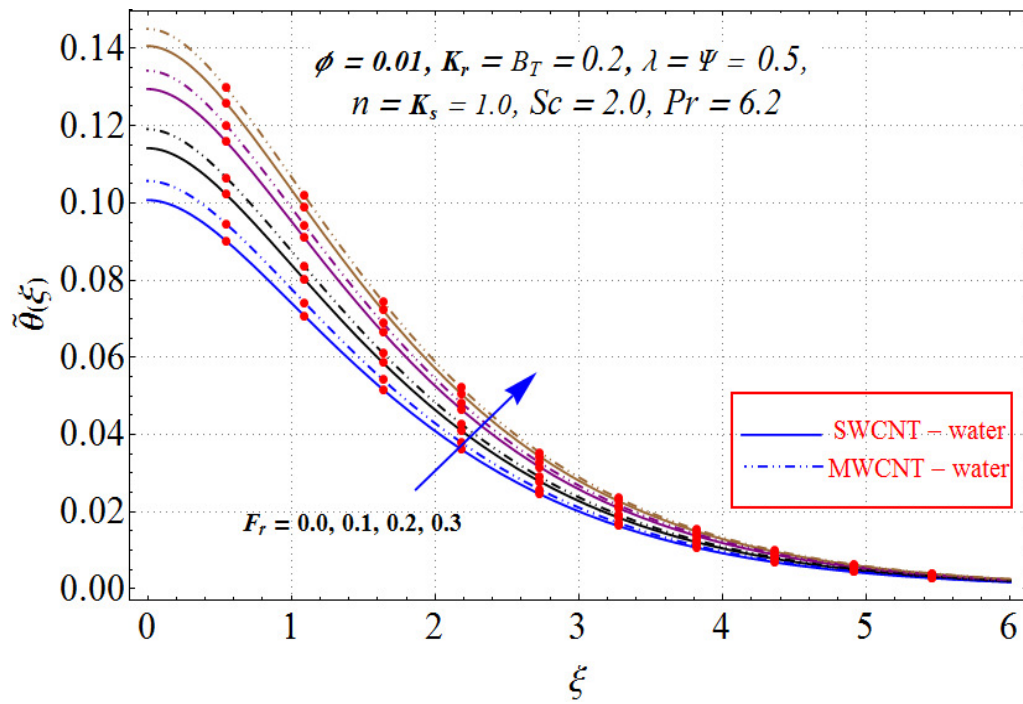


Figure 6.13: Variation of Fr on $\tilde{\theta}(\xi)$.

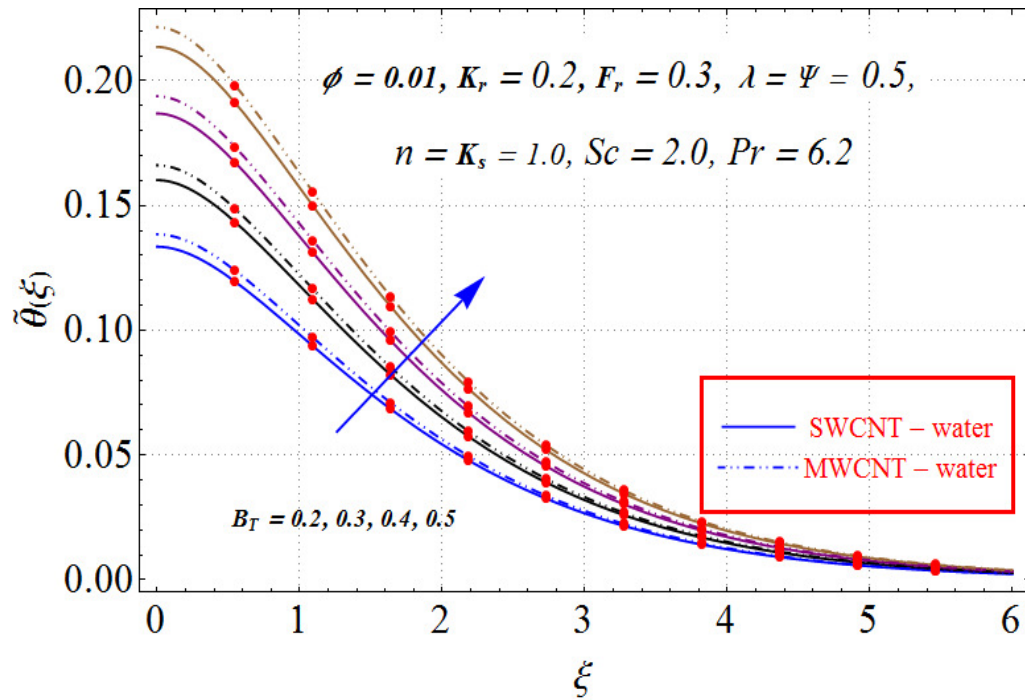


Figure 6.14: Variation of B_T on $\tilde{\theta}(\xi)$.

6.4.3 Concentration

Behavior of nanoparticle volume fraction ($\phi = 0.01, 0.02, 0.03, 0.04$) on concentration $\tilde{j}(\xi)$ for both SWCNTs and MWCNTs is depicted in Figure (6.15). It is noted that concentration of nanofluid is an increasing function of volume fraction of nanoparticles. Figures (6.16)-(6.17) represent the behavior of $\tilde{j}(\xi)$ under the variation of homogeneous reaction parameter ($K_r = 0.0, 0.1, 0.2, 0.3$) and heterogeneous reaction parameter ($K_s = 0.0, 0.3, 0.6, 1.0$) for single-walled and multi-walled CNTs. It is noted that concentration of fluid enhances for heterogeneous reaction parameter while reduces for homogeneous reaction parameter. Figure (6.18) displays the change in concentration $\tilde{j}(\xi)$ via Schmidt number ($Sc = 1.0, 1.3, 1.6, 2.0$). A rise in concentration is noted for higher values of (Sc). Physically Schmidt number is based on Brownian diffusivity. Larger (Sc) generates stronger Brownian diffusivity. Such stronger Brownian diffusivity leads to concentration enhancement.

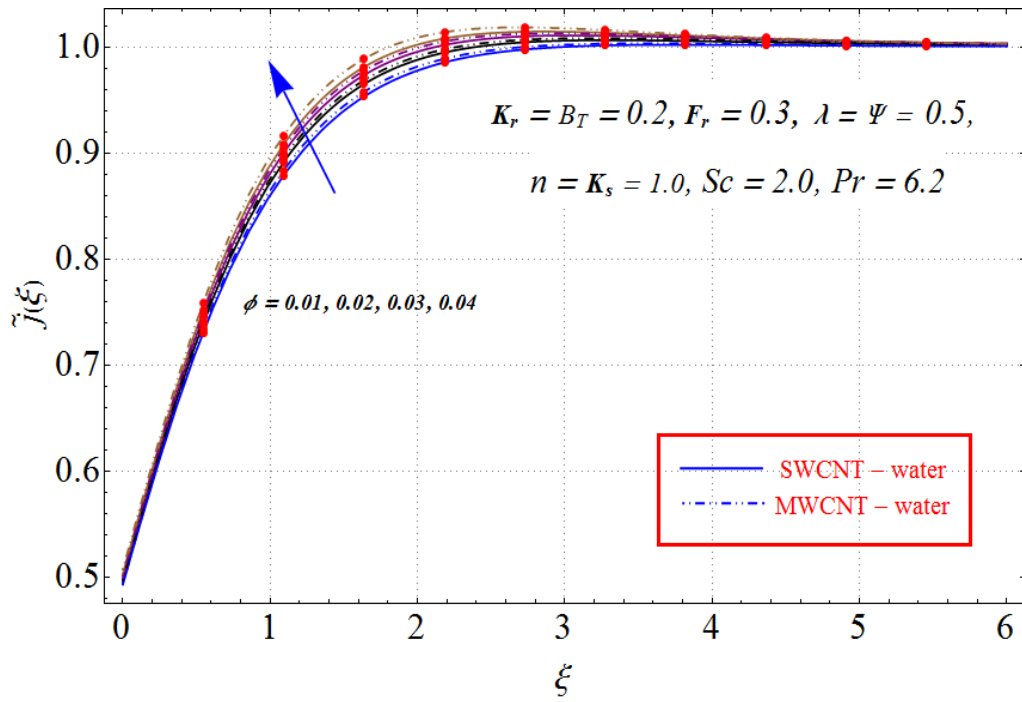


Figure 6.15: Variation of ϕ on $\tilde{j}(\xi)$.

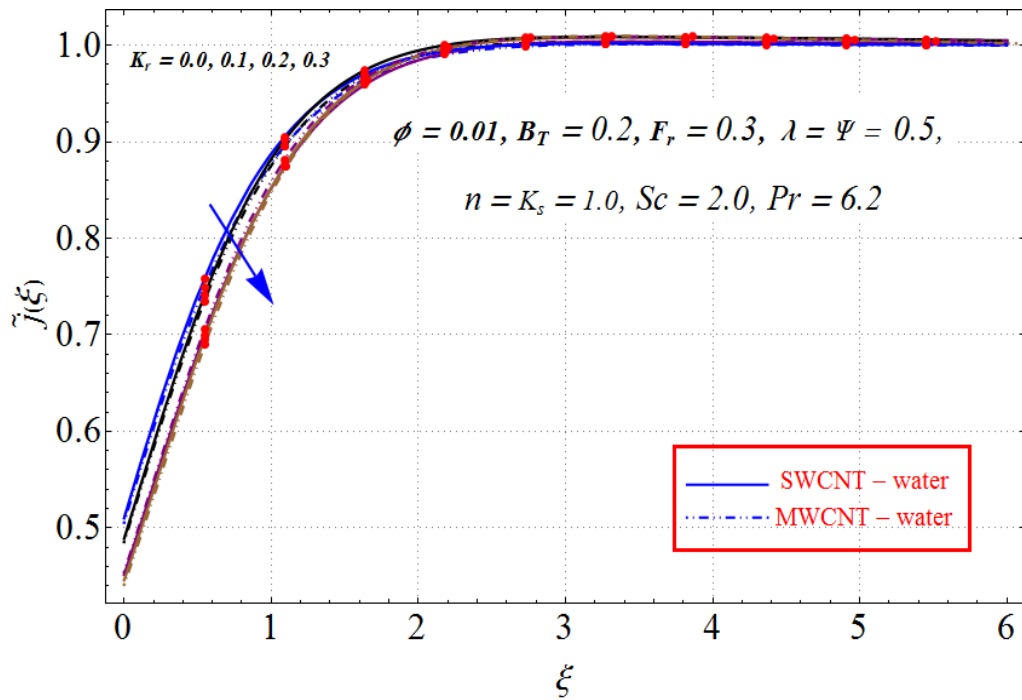


Figure 6.16: Variation of K_r on $\tilde{j}(\xi)$.

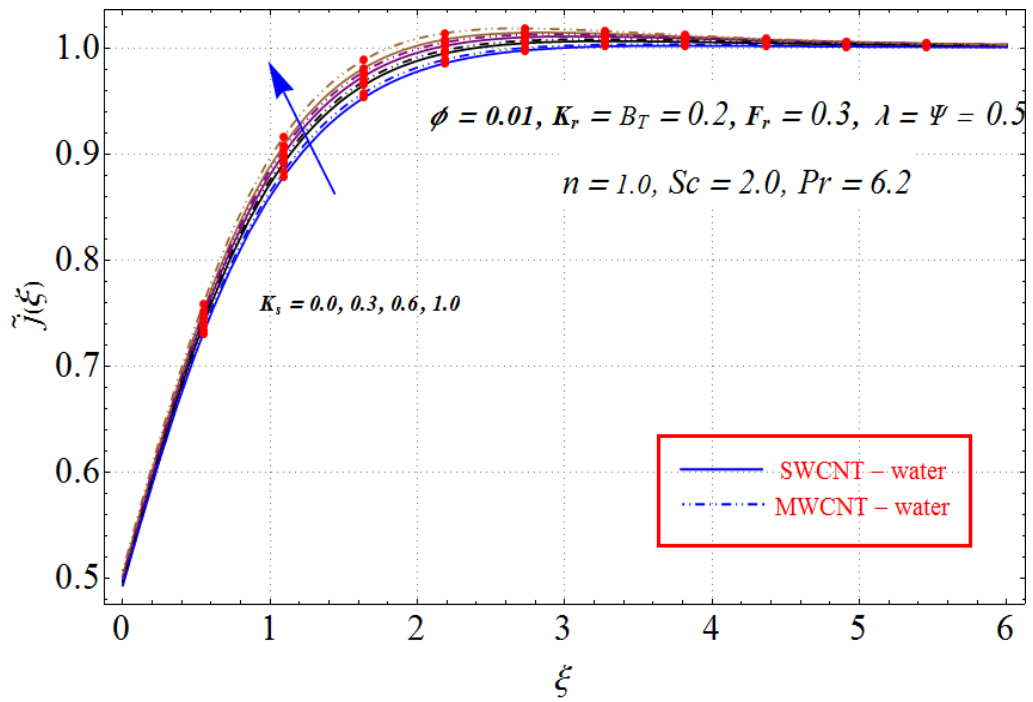


Figure 6.17: Variation of K_s on $\tilde{j}(\xi)$.

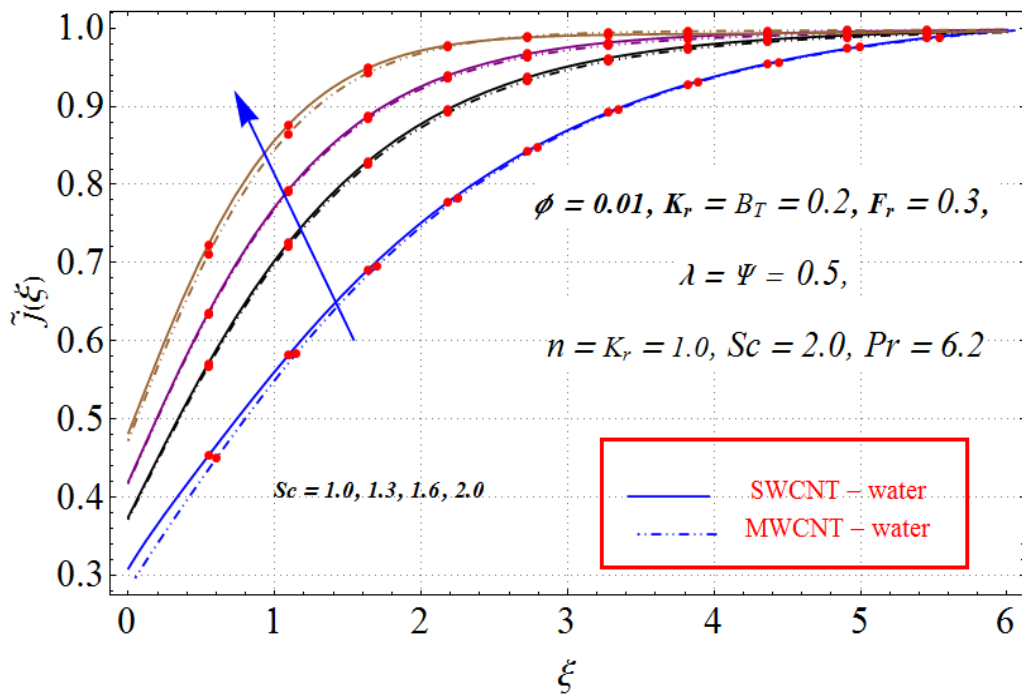


Figure 6.18: Variation of Sc on $\tilde{j}(\xi)$.

6.4.4 Skin friction coefficient and heat transfer rate

Figures (6.19) and (6.20) present the plots of skin friction coefficients $(\text{Re}_x)^{0.5} \tilde{C}_{sfx}$ and $(\text{Re}_y)^{0.5} \tilde{C}_{sfy}$ for varying nanoparticle volume fraction (ϕ) and permeability parameter (λ). Clearly the magnitude of skin friction coefficients $(\text{Re}_x)^{0.5} \tilde{C}_{sfx}$ and $(\text{Re}_y)^{0.5} \tilde{C}_{sfy}$ are enhanced for increasing values of nanoparticle volume fraction (ϕ). Figures (6.20) and (6.21) are plotted to analyze the behavior of nanoparticle volume fraction (ϕ), Biot number (B_T) and power-law index (n) on heat transfer rate $(\text{Re}_x)^{-0.5} \tilde{N}_u$. Magnitude of local Nusselt number $(\text{Re}_x)^{-0.5} \tilde{N}_u$ are enhanced for larger nanoparticle volume fraction (ϕ) and power-law index (n).

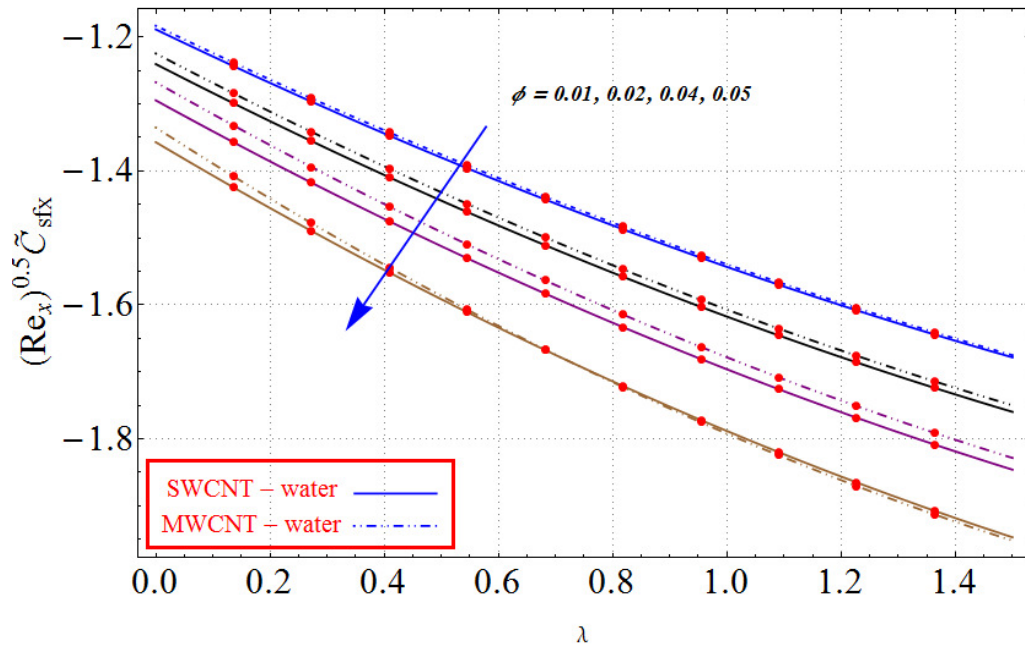


Figure 6.19: Variations of ϕ and λ on $(\text{Re}_x)^{0.5} \tilde{C}_{sfx}$.

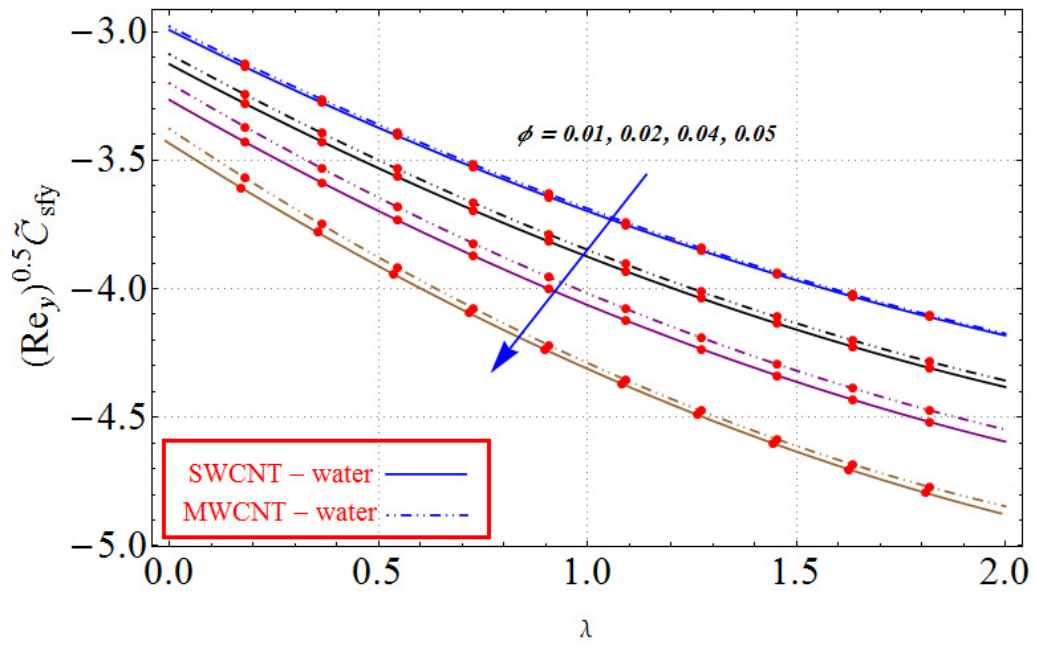


Figure 6.20: Variation of ϕ and λ on $(Re_x)^{0.5} \tilde{C}_{sfy}$.

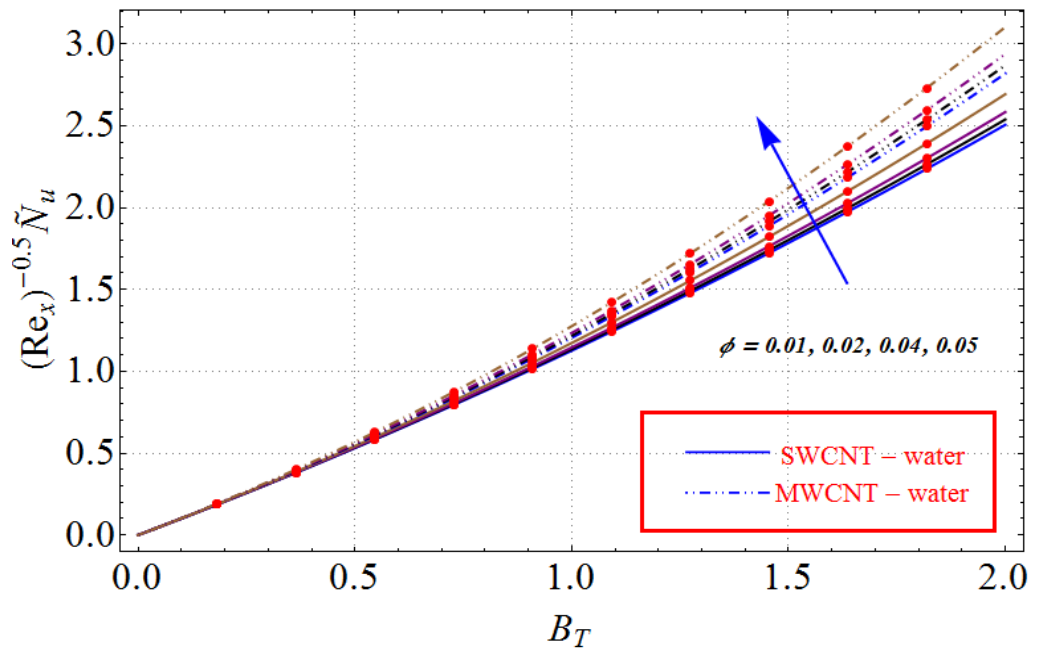


Figure 6.21: Variations of ϕ and B_T on $(Re_x)^{-0.5} \tilde{N}_u$.

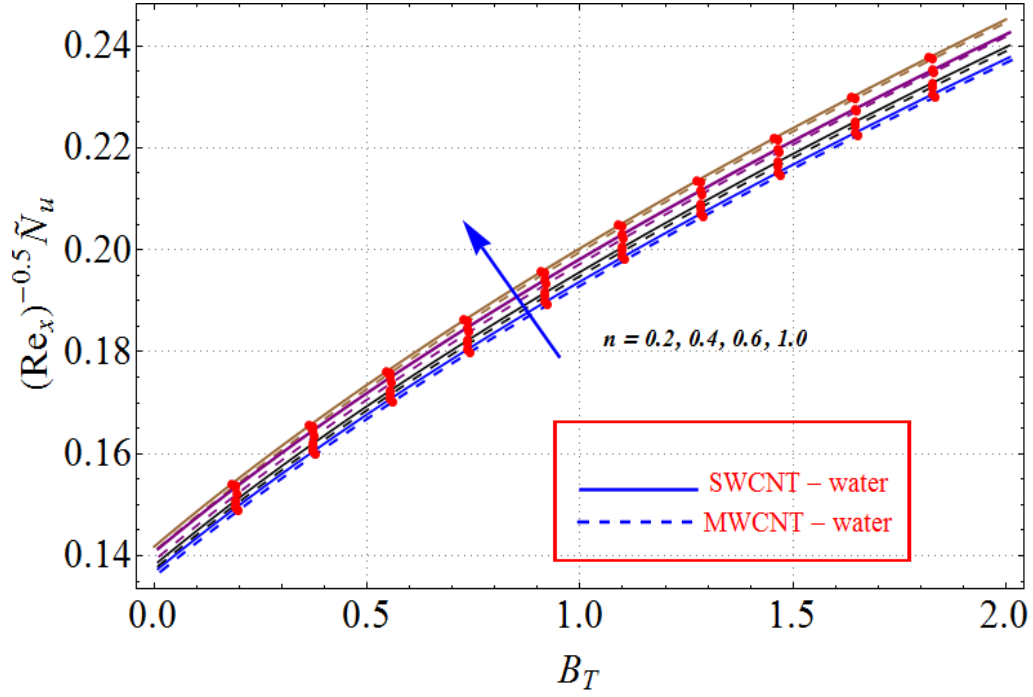


Figure 6.22: Variations of n and B_T on $(\text{Re}_x)^{-0.5} \tilde{N}_u$.

6.5 Conclusions

Three-dimensional flow of water-based carbon nanotubes induced by non-linear stretching of surface in existence of homogeneous-heterogeneous reactions has been analyzed. Main points of present analysis are described below:

- Larger ratio parameter (Ψ) correspond to lower velocity field $\tilde{f}'(\xi)$ while opposite trend is noticed for velocity field $\tilde{g}'(\xi)$.
- Increasing values of Forchheimer number (F_r) and permeability parameter (λ) show reduction in velocities $\tilde{f}'(\xi)$ and $\tilde{g}'(\xi)$.
- Velocities $\tilde{f}'(\xi)$ and $\tilde{g}'(\xi)$ and temperature $\tilde{\theta}(\xi)$ are enhances via nanoparticle volume fraction ϕ .
- Higher Biot number (B_T) enhances temperature $\tilde{\theta}(\xi)$ and more thermal layer thickness.

- ❑ Greater porosity parameter (λ) and Forchheimer number has more temperature $\tilde{\theta}(\xi)$.
- ❑ Larger Schmidt number (Sc) and heterogeneous reaction strength (K_s) present increasing trend for concentration field $\tilde{j}(\xi)$.
- ❑ Skin friction coefficients are increasing for larger nanoparticle volume fraction (ϕ).
- ❑ Local Nusselt number (Heat transfer rate) is increasing function of nanoparticle volume fraction (ϕ) and power-law index (n).

Chapter 7

Nanofluid flow due to rotating disk with variable thickness and homogeneous-heterogeneous reactions

Present chapter focuses on the steady, three-dimensional flow of water-based nanofluid. Silver is taken as nanoparticles. Flow is caused by rotating disk with variable thickness. Mass transfer subject to homogeneous-heterogeneous reactions is examined. Non-linear formulation based upon conservation laws of mass, momentum, energy and concentration is made. Homotopy concept is utilized for the development of solutions. Special attention is paid to the convergence of solutions. Plots for skin friction coefficient and Nusselt number are analyzed. Main conclusions are indicated.

7.1 Problem formulation

We consider axisymmetric nanofluid flow due to a rotating disk with constant angular frequency Ω . Assume that the disk at $z = d \left(\frac{r}{R_0} + 1 \right)^{-p}$ is not flat. Here d is the disk thickness coefficient, R_0 is the radius and p the disk thickness index. Cylindrical coordinates (r, θ, z) are employed. Geometry of problem is shown in Figure (7.1). Nanofluid is a suspension of silver (Ag) nanoparticles with water (H_2O) being a base fluid. Temperature at the surface of disk is T_w and ambient temperature is assumed to be T_∞ .

Moreover thermal radiation and Joule heating effects are not considered in the heat transfer analysis. Homogeneous–heterogeneous reactions are also considered.

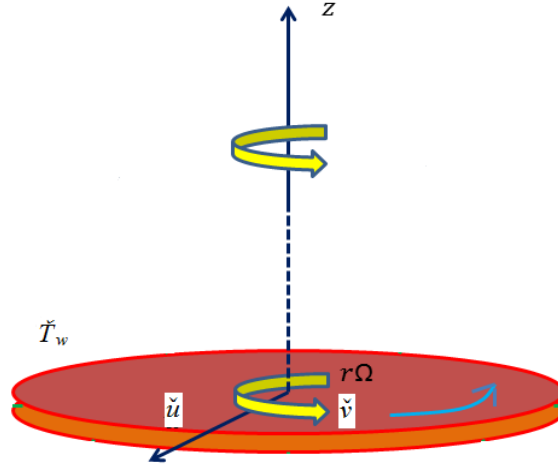


Figure 7.1: Geometry of the flow.

Under the assumptions $\frac{\partial p}{\partial r} = \frac{\partial p}{\partial z} = 0$, $O(u) = O(v) = O(r) = O(1)$ and $O(w) = O(z) = O(\delta)$ the equations for flow and heat and mass transfer are as follows:

$$\frac{\partial u}{\partial r} + \frac{u}{r} + \frac{\partial w}{\partial z} = 0, \quad (7.1)$$

$$\rho_{nf} \left(u \frac{\partial u}{\partial r} - \frac{v^2}{r} + w \frac{\partial u}{\partial z} \right) = \mu_{nf} \left(\frac{\partial^2 u}{\partial z^2} \right), \quad (7.2)$$

$$\rho_{nf} \left(u \frac{\partial v}{\partial r} + \frac{uv}{r} + w \frac{\partial v}{\partial z} \right) = \mu_{nf} \left(\frac{\partial^2 v}{\partial z^2} \right), \quad (7.3)$$

$$(\rho C_\rho)_{nf} \left(u \frac{\partial T}{\partial r} + w \frac{\partial T}{\partial z} \right) = k_{nf} \left(\frac{\partial^2 T}{\partial z^2} \right), \quad (7.4)$$

$$u \frac{\partial a^*}{\partial r} + w \frac{\partial a^*}{\partial z} = D_A \left(\frac{\partial^2 a^*}{\partial z^2} \right) - K_1 a^* c^{*2}, \quad (7.5)$$

$$u \frac{\partial c^*}{\partial r} + w \frac{\partial c^*}{\partial z} = D_C \left(\frac{\partial^2 c^*}{\partial z^2} \right) + K_1 a^* c^{*2}, \quad (7.6)$$

with boundary conditions

$$\begin{aligned} u = 0, \quad v = r\Omega, \quad w = 0, \quad T = T_w, \quad D_A \frac{\partial a^*}{\partial z} = K_2 a^*, \\ D_C \frac{\partial c^*}{\partial z} = -K_2 a^* \text{ at } z = d \left(\frac{r}{R_0} + 1 \right)^{-p}, \\ u \rightarrow 0, \quad v \rightarrow 0, \quad T \rightarrow T_\infty, \quad a^* \rightarrow a_0, \quad c^* \rightarrow 0 \text{ as } z \rightarrow \infty, \end{aligned} \quad (7.7)$$

In above expressions a_0 the positive dimensional constant.

Using generalized Von Karman transformations can be posited:

$$\begin{aligned} u &= r^* R_0 \Omega \tilde{F}(\eta), \quad v = r^* R_0 \Omega \tilde{G}(\eta), \quad w = R_0 \Omega (1 + r^*)^{-p} \left(\frac{\Omega R_0^2 \rho_f}{\mu_f} \right)^{\frac{-1}{n+1}} \tilde{B}(\eta) \\ \tilde{\Theta} &= \frac{T - T_\infty}{T_w - T_\infty}, \quad \tilde{J}(\eta) = \frac{a^*}{a_0}, \quad \tilde{S}(\eta) = \frac{c^*}{a_0}, \quad \eta = \frac{z}{R_0} (1 + r^*)^p \left(\frac{\Omega R_0^2 \rho_f}{\mu_f} \right)^{\frac{1}{n+1}}, \end{aligned} \quad (7.8)$$

one has

$$2\tilde{F} + \tilde{B}' + \eta \epsilon p \tilde{F}' = 0, \quad (7.9)$$

$$\left(\frac{1}{(1 - \phi)^{2.5} (1 - \phi + \phi \frac{\rho_s}{\rho_f})} \right) \tilde{F}'' (\text{Re})^{\frac{1-n}{1+n}} (1 + r^*)^{2p} - \tilde{F}^2 + \tilde{G}^2 - \tilde{B}\tilde{F}' - \tilde{F}\tilde{F}' p \eta \epsilon = 0, \quad (7.10)$$

$$\left(\frac{1}{(1 - \phi)^{2.5} (1 - \phi + \phi \frac{\rho_s}{\rho_f})} \right) \tilde{G}'' (\text{Re})^{\frac{1-n}{1+n}} (1 + r^*)^{2p} - 2\tilde{F}\tilde{G} - \tilde{B}\tilde{G}' - \tilde{F}\tilde{G}' p \eta \epsilon = 0, \quad (7.11)$$

$$\left(\frac{1}{1 - \phi + \phi \frac{(\rho C_\rho)_s}{(\rho C_\rho)_f}} \right) \left(\frac{k_{nf}}{k_f} \right) \left(\frac{1}{\text{Pr}} \right) (\text{Re})^{\frac{1-n}{1+n}} (1 + r^*)^{2p} \tilde{\Theta}'' - \tilde{F}\tilde{\Theta}' p \eta \epsilon - \tilde{B}\tilde{\Theta}' = 0, \quad (7.12)$$

$$\left(\frac{1}{Sc} \right) (\text{Re})^{\frac{1-n}{1+n}} (1 + r^*)^{2p} \tilde{J}'' - K_r \tilde{L} \tilde{S}^2 - \tilde{F}\tilde{J}' p \eta \epsilon - \tilde{B}\tilde{J}' = 0, \quad (7.13)$$

$$\left(\frac{\delta}{Sc} \right) (\text{Re})^{\frac{1-n}{1+n}} (1 + r^*)^{2p} \tilde{S}'' + K_r \tilde{L} \tilde{S}^2 - \tilde{F}\tilde{S}' p \eta \epsilon - \tilde{B}\tilde{S}' = 0 \quad (7.14)$$

with boundary conditions

$$\begin{aligned}\tilde{B}(\alpha) &= 0, \tilde{F}(\alpha) = 0, \tilde{F}(\infty) \rightarrow 0, \tilde{G}(\alpha) = 1, \tilde{G}(\infty) \rightarrow 0, \tilde{\Theta}(\alpha) = 1, \tilde{\Theta}(\infty) \rightarrow 0, \\ \tilde{J}'(\alpha) &= K_s \tilde{J}(\alpha), \delta \tilde{S}'(\alpha) = -K_s \tilde{S}(\alpha), \tilde{J}(\infty) \rightarrow 1, \tilde{S}(\infty) \rightarrow 0.\end{aligned}\quad (7.15)$$

The diffusion coefficients of chemical species A and C are of comparable size. This leads to assumption that the diffusion coefficient D_A and D_C are equal, i.e. $\delta = 1$. Hence

$$\tilde{J}(\eta) + \tilde{S}(\eta) = 1. \quad (7.16)$$

Eqs. (7.13)-(7.14) yield

$$\left(\frac{1}{Sc}\right) (\text{Re})^{\frac{1-n}{1+n}} (1+r^*)^{2p} \tilde{J}'' - K_r \tilde{J} (1-\tilde{J})^2 - \tilde{F} \tilde{J}' p \eta \epsilon - \tilde{B} \tilde{J}' = 0 \quad (7.17)$$

with the boundary condition

$$\tilde{J}'(\alpha) = K_s \tilde{J}(\alpha), \tilde{J}(\infty) \rightarrow 1. \quad (7.18)$$

The parameters involved in above equations are defined as $\text{Re} = \frac{\Omega R_0^2}{\nu_f}$ the Reynolds number, $r^* = \frac{r}{R_0}$ the dimensionless radius, $\epsilon = \frac{r^*}{R_0 + r^*}$ the dimensionless constant number, $\text{Pr} = \frac{\nu_f (\rho C_p)_f}{k_f}$ the Prandtl number, $\delta = \frac{D_C}{D_A}$ the ratio of diffusion coefficients, $Sc = \frac{\nu_f}{D_A}$ the Schmidt number, $K_r = \frac{K_1 a_0^2}{\Omega}$ homogeneous reaction parameter, $K_s = \frac{K_2 R_0}{\Omega (1+r^*)^p \left(\frac{\Omega R_0^2 \rho_f}{\mu_f}\right)^{\frac{-1}{n+1}}}$ the heterogeneous reaction parameter and $\alpha = \frac{d}{R_0} \left(\frac{\Omega R_0^2 \rho_f}{\mu_f}\right)^{\frac{-1}{n+1}}$ the disk thickness coefficient number.

We introduce [37]

$$\begin{aligned}\tilde{B} &= \tilde{b}(\eta - \alpha) = \tilde{b}(\xi), \tilde{F} = \tilde{f}(\eta - \alpha) = \tilde{f}(\xi), \tilde{G} = \tilde{g}(\eta - \alpha) = \tilde{g}(\xi), \\ \tilde{\Theta} &= \tilde{\theta}(\eta - \alpha) = \tilde{\theta}(\xi), \tilde{J} = \tilde{j}(\eta - \alpha) = \tilde{j}(\xi).\end{aligned}\quad (7.19)$$

and reduce (Eqs. (7.9)-(7.12)) and (7.17) with boundary conditions (7.15) and (7.18) in the forms:

$$2\tilde{f} + \tilde{b}' + (\xi + \alpha)\epsilon p \tilde{f}' = 0, \quad (7.20)$$

$$\left(\frac{1}{(1-\phi)^{2.5}(1-\phi+\phi\frac{\rho_s}{\rho_f})} \right) (\text{Re})^{\frac{1-n}{1+n}} (1+r^*)^{2p} \tilde{f}'' - \tilde{f}^2 + \tilde{g}^2 - \tilde{b}\tilde{f}' - \tilde{f}\tilde{f}'p(\xi+\alpha)\epsilon = 0, \quad (7.21)$$

$$\left(\frac{1}{(1-\phi)^{2.5}(1-\phi+\phi\frac{\rho_s}{\rho_f})} \right) (\text{Re})^{\frac{1-n}{1+n}} (1+r^*)^{2p} \tilde{g}'' - 2\tilde{f}\tilde{g} - \tilde{b}\tilde{g}' - \tilde{f}\tilde{g}'p(\xi+\alpha)\epsilon = 0, \quad (7.22)$$

$$\left(\frac{1}{1-\phi+\phi\frac{(\rho C_p)_s}{(\rho C_p)_f}} \right) \left(\frac{k_{nf}}{k_f} \right) \frac{1}{\text{Pr}} (\text{Re})^{\frac{1-n}{1+n}} (1+r^*)^{2p} \tilde{\theta}'' - \tilde{f}\tilde{\theta}'p(\xi+\alpha)\epsilon - \tilde{b}\tilde{\theta}' = 0, \quad (7.23)$$

$$\frac{1}{S_c} (\text{Re})^{\frac{1-n}{1+n}} (1+r^*)^{2p} \tilde{j}'' - K_r \tilde{j}(1-\tilde{j})^2 - \tilde{f}\tilde{j}'p(\xi+\alpha)\epsilon - \tilde{b}\tilde{j}' = 0, \quad (7.24)$$

$$\tilde{b}(0) = 0, \quad \tilde{f}(0) = 0, \quad \tilde{f}(\infty) \rightarrow 0,$$

$$\tilde{g}(0) = 1, \quad \tilde{g}(\infty) \rightarrow 0,$$

$$\tilde{\theta}(0) = 1, \quad \tilde{\theta}(\infty) \rightarrow 0,$$

$$\tilde{j}(0) = K_s \tilde{j}(0), \quad \tilde{j}(\infty) \rightarrow 1. \quad (7.25)$$

7.1.1 Physical quantities

Skin friction coefficient characterizes the surface drag. At disk the shear stresses τ_{zr} and $\tau_{z\theta}$ in radial and tangential directions are given by

$$\tau_{zr} = \mu_{nf} \left. \frac{\partial u}{\partial z} \right|_{z=0}, \quad \tau_{z\theta} = \mu_{nf} \left. \frac{\partial v}{\partial z} \right|_{z=0}. \quad (7.26)$$

Skin-friction coefficient \tilde{C}_{sf} which is identified by

$$\tilde{C}_{sf} = \frac{\sqrt{\tau_{zr}^2 + \tau_{z\theta}^2}}{\rho_f (r^* \Omega)^2}. \quad (7.27)$$

In dimensionless form one obtains

$$\tilde{C}_{sf} (\text{Re})^{\frac{n-1}{n+1}} = \frac{1}{(1-\phi)^{2.5} r^*} (1+r^*)^p \left(\sqrt{(\tilde{f}'(0))^2 + (\tilde{g}'(0))^2} \right). \quad (7.28)$$

At disk the heat flux q_w is

$$q_w = -k_{nf} \left. \frac{\partial T}{\partial z} \right|_{z=0}, \quad (7.29)$$

Nusselt number \tilde{N}_u is identified by

$$\tilde{N}_u = \left. \frac{R_0 q_w}{k_f (T_w - T_\infty)} \right|_{z=0}, \quad (7.30)$$

Dimensionless form is

$$\tilde{N}_u (\text{Re})^{\frac{-1}{n+1}} = -\frac{k_{nf}}{k_f} (1 + r^*)^p \hat{\theta}'(0). \quad (7.31)$$

7.2 Homotopy procedure

Initial approximations $(\tilde{b}_0, \tilde{f}_0, \tilde{g}_0, \tilde{\theta}_0$ and $\tilde{j}_0)$ with auxiliary linear operators $(\mathcal{L}_{\tilde{b}}, \mathcal{L}_{\tilde{f}}, \mathcal{L}_{\tilde{g}}, \mathcal{L}_{\tilde{\theta}}$ and $\mathcal{L}_{\tilde{j}}$) are given as

$$\tilde{b}_0(\xi) = 0, \quad (7.32)$$

$$\hat{f}_0(\xi) = 0, \quad (7.33)$$

$$\tilde{g}_0(\xi) = \exp(-\xi), \quad (7.34)$$

$$\tilde{\theta}_0(\xi) = \exp(-\xi), \quad (7.35)$$

$$\tilde{j}_0(\xi) = 1 - \frac{1}{2} \exp(-K_s \xi), \quad (7.36)$$

$$\mathcal{L}_{\tilde{b}} = \tilde{b}', \quad \mathcal{L}_{\tilde{f}} = \tilde{f}'' - \tilde{f}, \quad \mathcal{L}_{\tilde{g}} = \tilde{g}'' - \tilde{g}, \quad \mathcal{L}_{\tilde{\theta}} = \tilde{\theta}'' - \tilde{\theta}, \quad \mathcal{L}_{\tilde{j}} = \tilde{j}'' - \tilde{j}. \quad (7.37)$$

satisfying the properties

$$\begin{aligned}
 \mathcal{L}_{\tilde{b}}[C_1] &= 0, \\
 \mathcal{L}_{\tilde{f}}[C_2e^\xi + C_3e^{-\xi}] &= 0, \\
 \mathcal{L}_{\tilde{g}}[C_4e^\xi + C_5e^{-\xi}] &= 0, \\
 \mathcal{L}_{\tilde{\theta}}[C_6e^\xi + C_7e^{-\xi}] &= 0, \\
 \mathcal{L}_{\tilde{j}}[C_8e^\xi + C_9e^{-\xi}] &= 0.
 \end{aligned} \tag{7.38}$$

where C_i ($i = 1 - 9$) are the constants.

7.3 Convergence

Homotopy analysis method (HAM) is performed for convergence of developed solutions. Convergence region is adjusted with the help of auxiliary parameters $\tilde{h}_{\tilde{b}}$, $\tilde{h}_{\tilde{f}}$, $\tilde{h}_{\tilde{g}}$, $\tilde{h}_{\tilde{\theta}}$ and $\tilde{h}_{\tilde{j}}$ for the functions \tilde{b} , \tilde{f} , \tilde{g} , $\tilde{\theta}$ and \tilde{j} respectively. Valid ranges of such variables are attained by plotting the \tilde{h} -curves (see Figures (7.2) and (7.3)). Admissible values for $\tilde{h}_{\tilde{b}}$, $\tilde{h}_{\tilde{f}}$, $\tilde{h}_{\tilde{g}}$, $\tilde{h}_{\tilde{\theta}}$ and $\tilde{h}_{\tilde{j}}$ are described as $-1.1 \leq \tilde{h}_{\tilde{b}} \leq -0.3$, $-1.1 \leq \tilde{h}_{\tilde{f}} \leq -0.5$, $-0.9 \leq \tilde{h}_{\tilde{g}} \leq -0.35$, $-1.5 \leq \tilde{h}_{\tilde{\theta}} \leq -0.8$ and $-1.2 \leq \tilde{h}_{\tilde{j}} \leq -0.4$. The homptopic solutions for whole region of ξ ($0 \leq \xi \leq \infty$) when $\tilde{h}_{\tilde{b}} = -0.7$, $\tilde{h}_{\tilde{f}} = -0.7$, $\tilde{h}_{\tilde{g}} = -0.4$, $\tilde{h}_{\tilde{\theta}} = -0.6$ and $\tilde{h}_{\tilde{j}} = -0.8$. Numerical values of specific heat, density and thermal conductivity of silver and water are presented in Table (7.1). Table (7.2) is prepared to check the convergence of obtained HAM solutions. It is obvious from the table that 12th and 20th order of approximations are suitable for the convergence of $\tilde{f}'(0)$, $\tilde{\theta}'(0)$ and $\tilde{g}'(0)$ while 14th order of approximations are appropriate for $\tilde{b}''(0)$ and $\tilde{j}'(0)$.

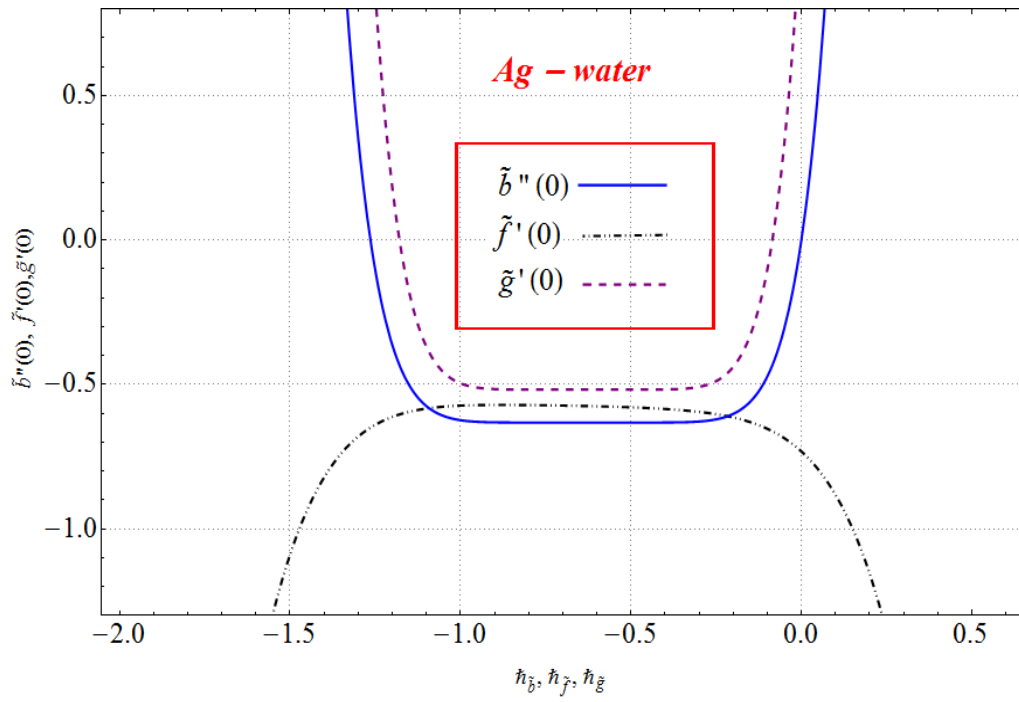


Figure 7.2: h -curves of $\tilde{b}''(0)$, $\tilde{f}'(0)$ and $\tilde{g}'(0)$ for *Ag - water*.

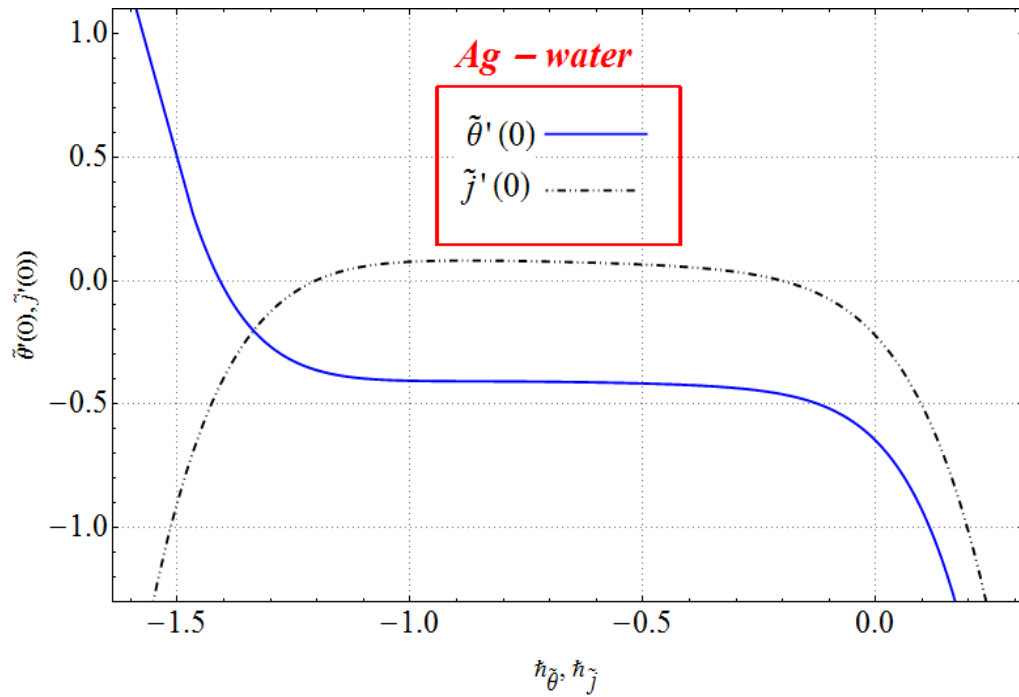


Figure 7.3: h -curves of $\tilde{\theta}'(0)$ and $\tilde{j}'(0)$ for *Ag - water*.

Table 7.1: Thermophysical properties of silver nanoparticles and water

—	$k(W/m.k)$	$\rho(kg/m^3)$	$\sigma(Um)^{-1}$	$C_p(j/kgk)$	$\beta \times 10^5(1/K)$
Ag(Silver)	429	10500	3.6×10^7	235	1.89
H ₂ O(Pure Water)	0.613	997.1	0.05	4179	21

Table 7.2: Convergence of series solutions when $p = Sc = n = 1.0, \epsilon = \alpha = 0.4, Re = 0.9, r^* = 0.3, \phi = 0.01, K_r = K_r = 0.7$ and $Pr = 6.2$.

Order of approximations	$-\tilde{b}''(0)$	$-\tilde{f}'(0)$	$-\tilde{g}'(0)$	$-\tilde{\theta}'(0)$	$-\tilde{j}'(0)$
1	0.000	0.488	0.377	0.224	0.019
5	0.602	0.527	0.392	0.367	0.024
9	0.610	0.551	0.435	0.401	0.031
12	0.612	0.558	0.455	0.406	0.038
14	0.614	0.558	0.499	0.406	0.044
20	0.614	0.558	0.508	0.406	0.044
25	0.614	0.558	0.508	0.406	0.044

7.4 Results and discussion

This segment is organized to reveal the significant features of pertinent variables versus velocity components, temperature and concentration and skin friction coefficient and Nusselt number.

7.4.1 Axial velocity

Figure (7.4) depict the impact of disk thickness power-law index ($p = 0.1, 0.5, 0.8, 1.0$) on axial velocity $\tilde{b}(\xi)$. It is clear that negative values of $\tilde{b}(\xi)$ indicate the flow in downward direction. An increase in disk thickness power-law index (p) reduces the magnitude of axial velocity. Effect of dimensionless constant number ($\epsilon = 0.0, 0.2, 0.4, 0.6$) on axial velocity $\tilde{b}(\xi)$ is portrayed in Figure (7.5). One can easily examine that the magnitude of axial velocity decays for higher (ϵ). Figure (7.6) explores the variation of disk thickness coefficient ($\alpha = 0.1, 0.2, 0.3, 0.4$) on axial velocity $\tilde{b}(\xi)$. It is worth mentioning that magnitude of axial velocity reduces via greater (α). Physically for small R_0 the less particles are in contact with the surface of disk and consequently the velocity decays.

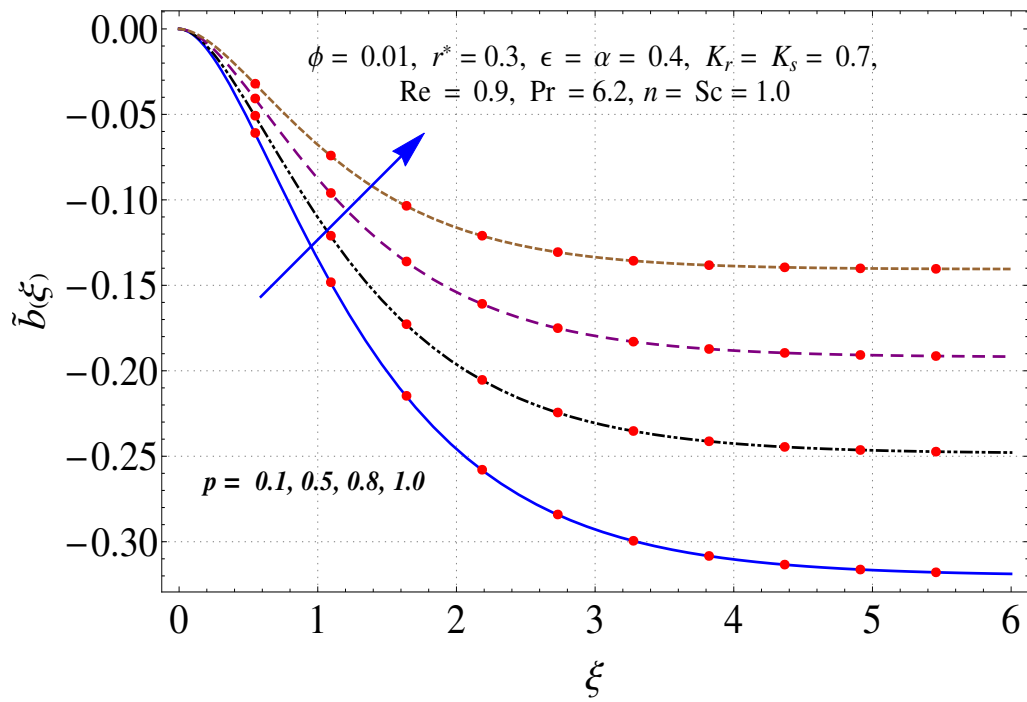


Figure 7.4: Variation of p on $\tilde{b}(\xi)$.

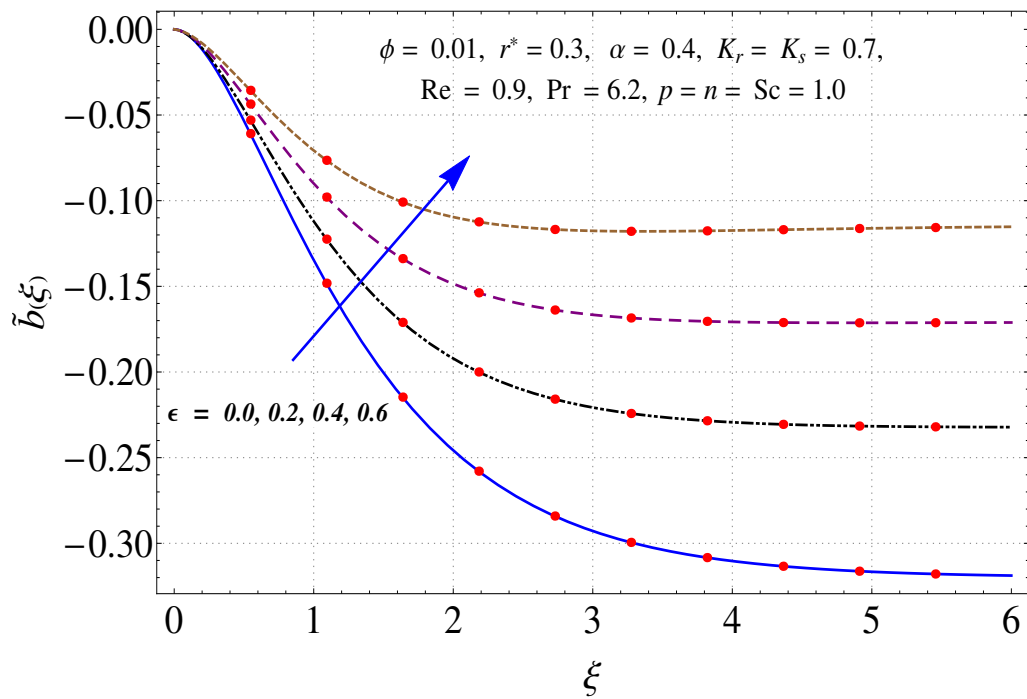
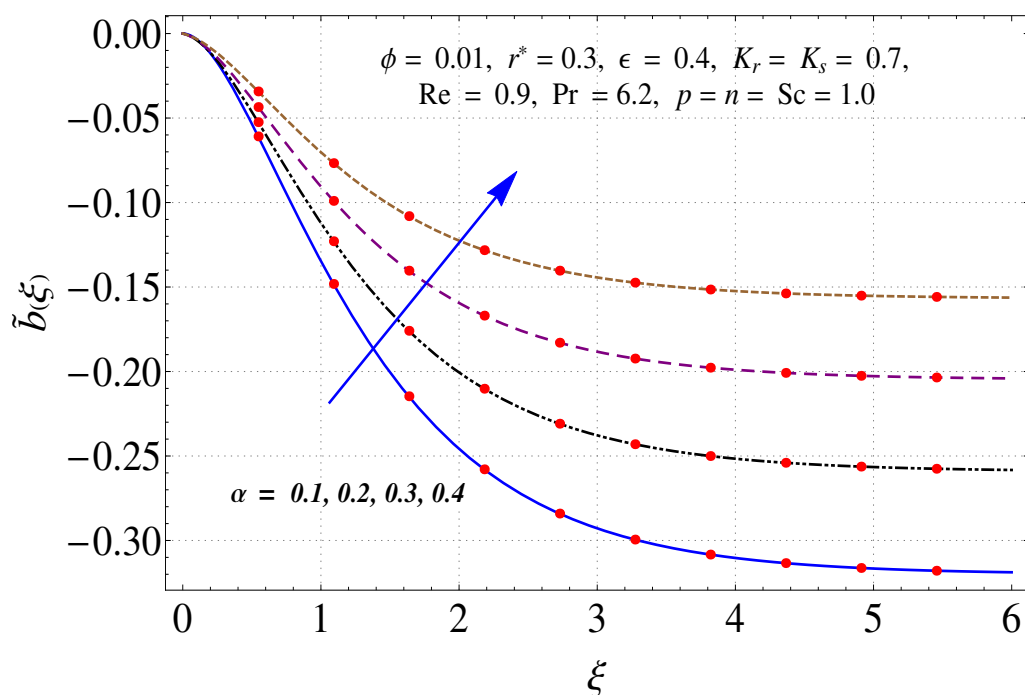


Figure 7.5: Variation of ϵ on $\tilde{b}(\xi)$.


 Figure 7.6: Variation of α on $\tilde{b}(\xi)$.

7.4.2 Radial and Azimuthal velocity components

Behavior of nanomaterial volume fraction ($\phi = 0.01, 0.03, 0.04, 0.05$) on radial $\tilde{f}(\xi)$ and tangential $\tilde{g}(\xi)$ velocity components are presented in Figures (7.7) and (7.8). It is examined that for higher (ϕ) the fluid velocity in both directions decreases. Physically higher volume fraction of silver nanoparticles is a cause of thermal conductivity enhancement and as a result velocities decays. Silent characteristics of disk thickness coefficient ($\alpha = 0.1, 0.2, 0.3, 0.4$) on radial and azimuthal velocities are reported in Figures (7.9) and (7.10). Here velocity in both directions enhances for higher (α). Figures (7.11) and (7.12) are organized to see the outcome of $\tilde{f}(\xi)$ and $\tilde{g}(\xi)$ for increasing values of Reynolds number ($\text{Re} = 0.4, 0.6, 0.7, 0.9$). It is found that both velocities via higher (Re) are increased. In fact Reynolds number (Re) has an inverse relation with viscosity of fluid. For higher (Re) the viscosity of fluid reduces so less resistance is offered to fluid particles and hence radial and azimuthal velocities rise.

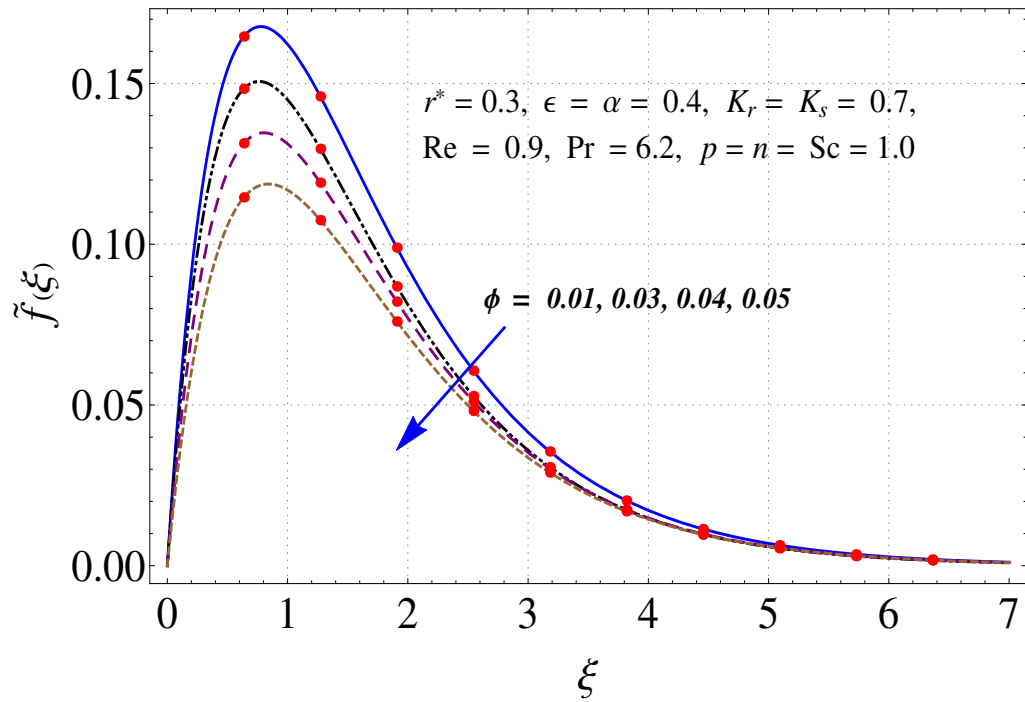


Figure 7.7: Variation of ϕ on $\tilde{f}(\xi)$.

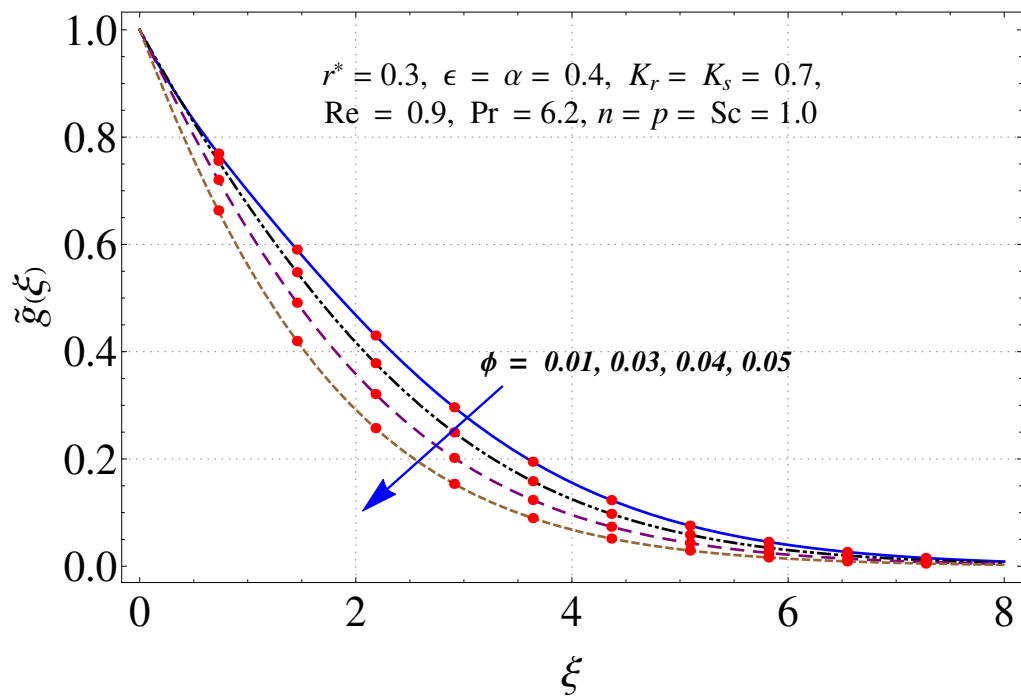


Figure 7.8: Variation of ϕ on $\tilde{g}(\xi)$.

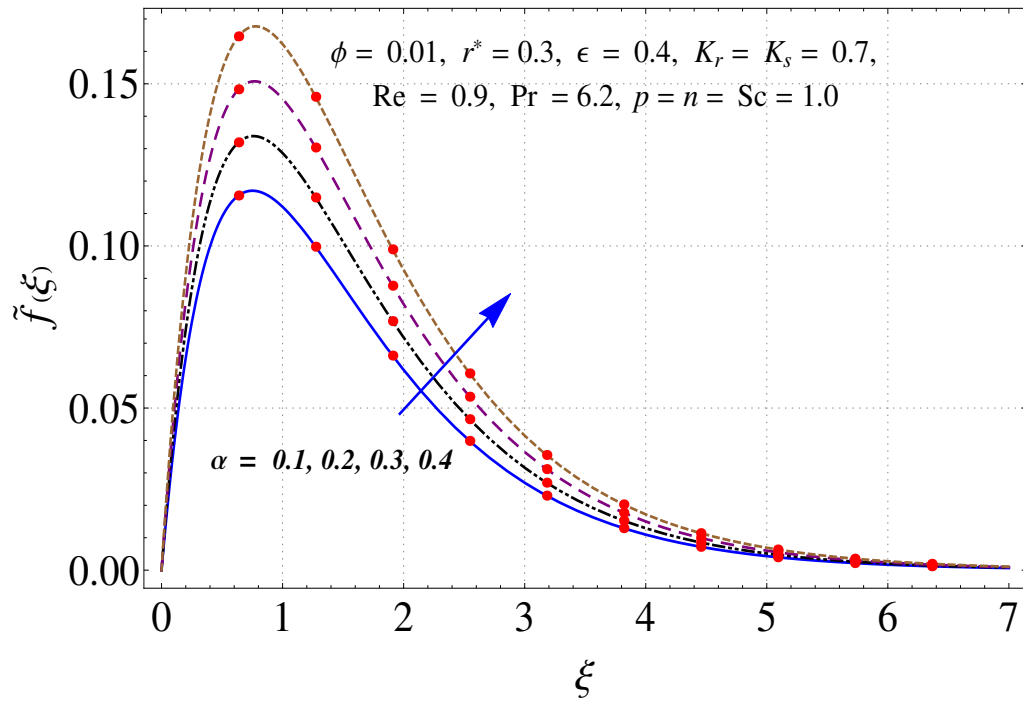


Figure 7.9: Variation of α on $\tilde{f}(\xi)$.

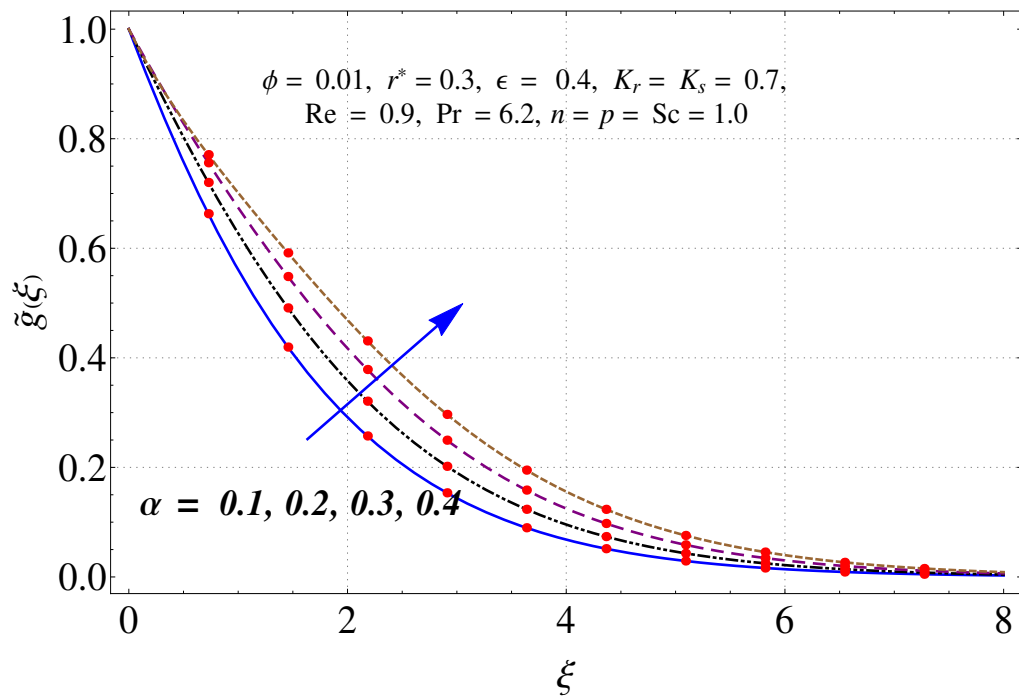


Figure 7.10: Variation of α on $\tilde{g}(\xi)$.

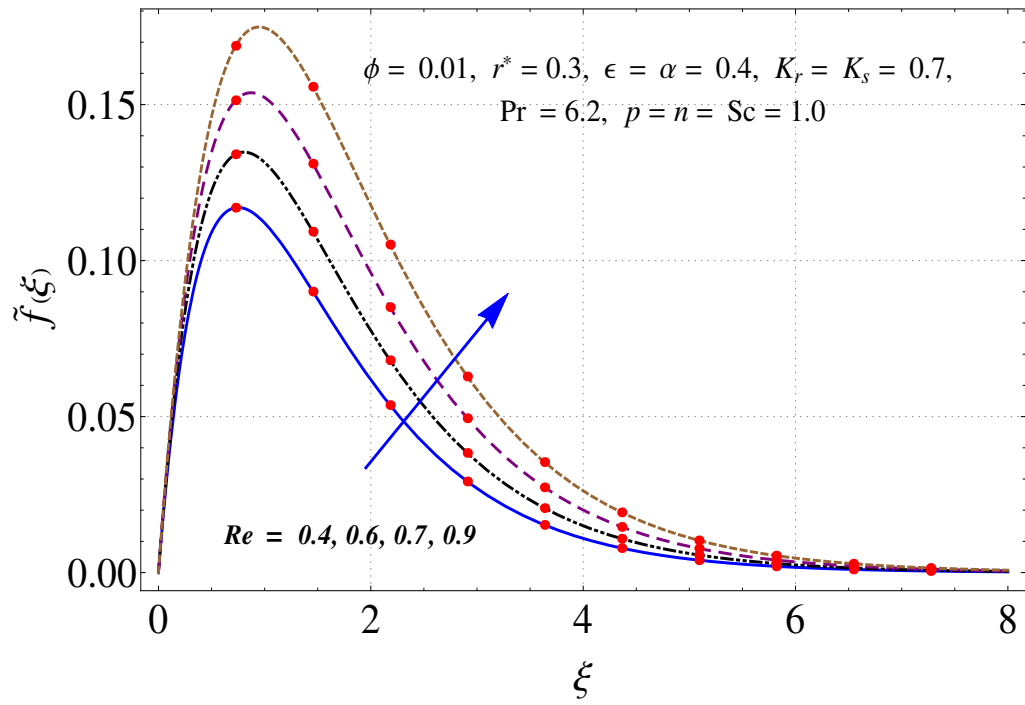


Figure 7.11: Variation of Re on $\tilde{f}(\xi)$.

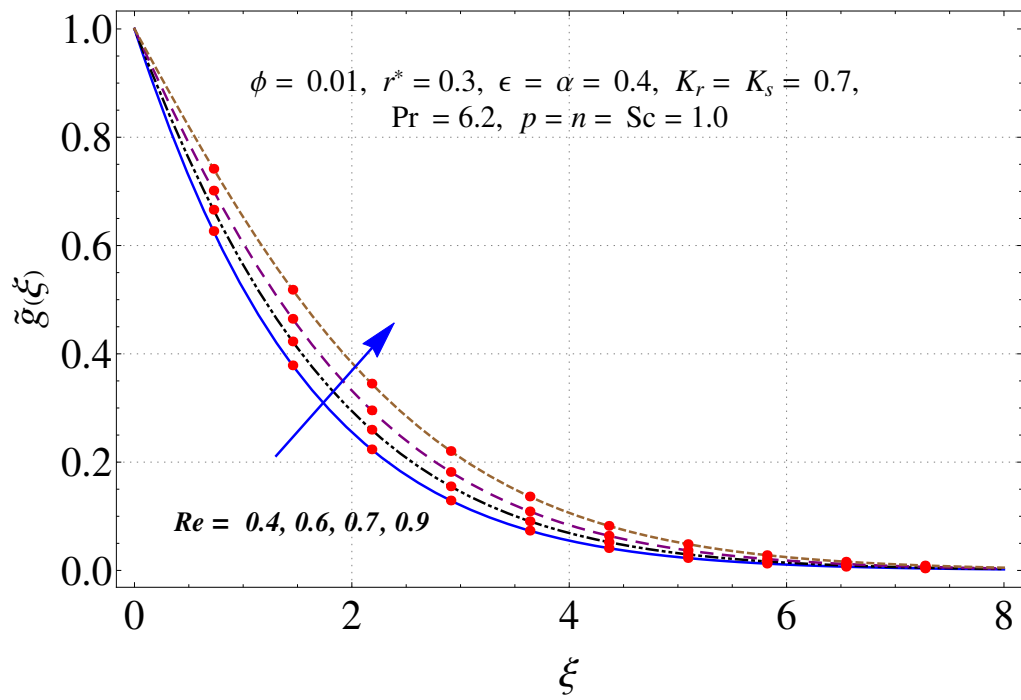


Figure 7.12: Variation of Re on $\tilde{g}(\xi)$.

7.4.3 Temperature

Figure (7.13) illustrates the effect of ($\phi = 0.01, 0.03, 0.04, 0.05$) on temperature $\tilde{\theta}(\xi)$ for silver-water nanofluid. Direct relation is observed between (ϕ) and $\tilde{\theta}(\xi)$. Higher estimations of (ϕ) correspond to more thermal conductivity and thermal layer thickness. Therefore temperature enhances. Impact of Reynolds number ($Re = 0.4, 0.6, 0.7, 0.9$) on temperature $\tilde{\theta}(\xi)$ is shown in Figure (7.14). Here temperature enhances for higher (Re).

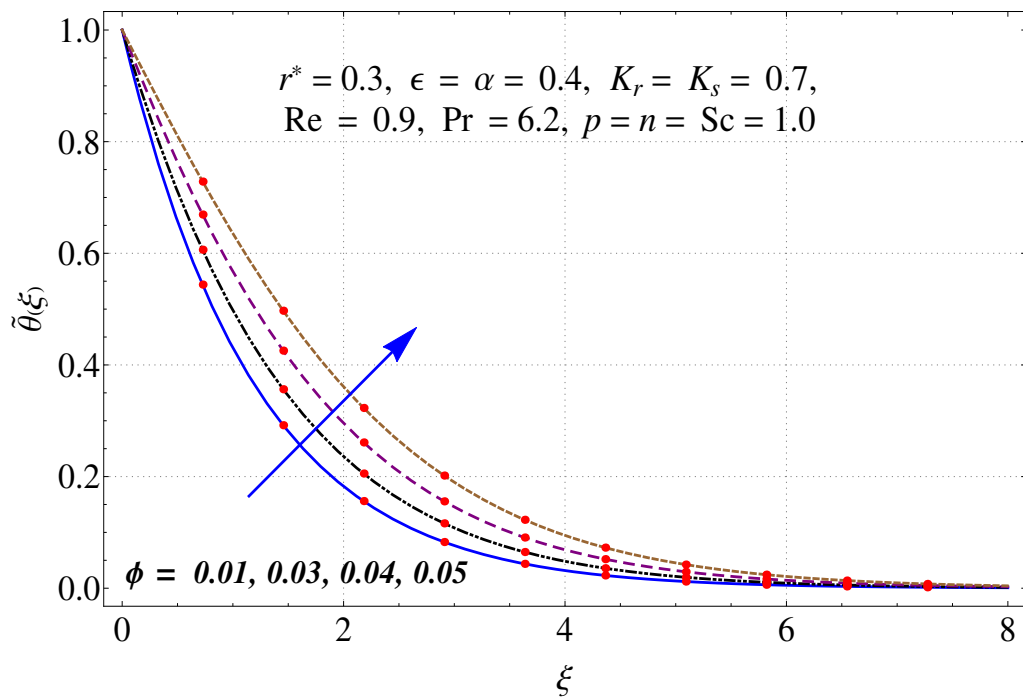


Figure 7.13: Variation of ϕ on $\tilde{\theta}(\xi)$.

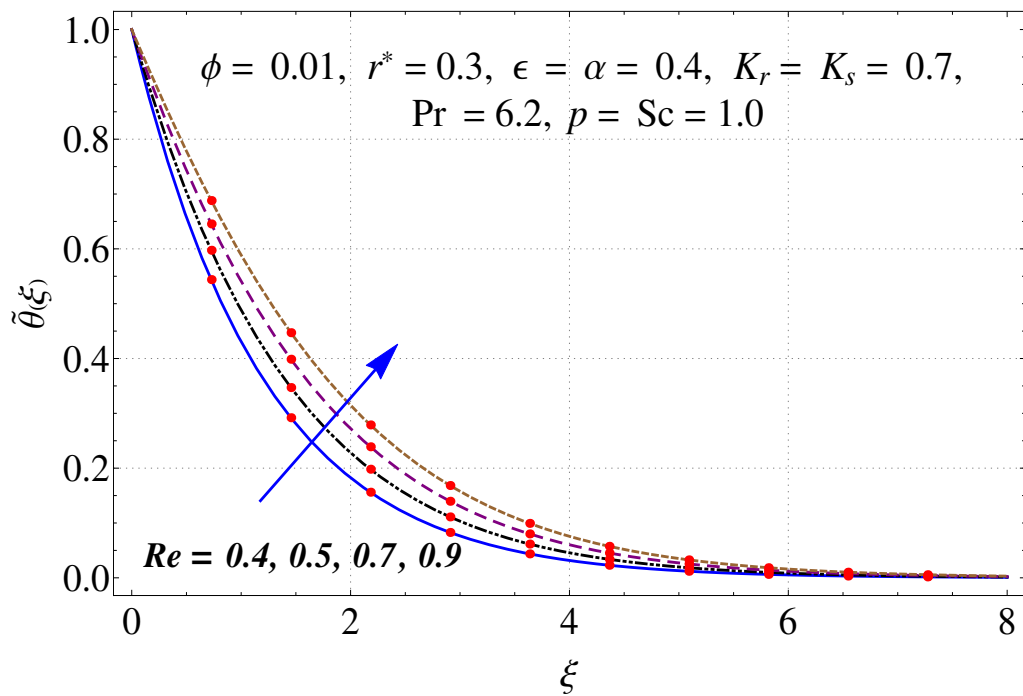


Figure 7.14: Variation of Re on $\tilde{\theta}(\xi)$.

7.4.4 Concentration

Figures (7.15) and (7.16) give variation of homogeneous and heterogeneous reaction parameters on concentration distribution $\tilde{j}(\xi)$. Concentration of nanofluid reduces for higher ($K_r = 0.1, 0.3, 0.7, 0.9$) while opposite behavior is noticed for ($K_s = 0.1, 0.5, 0.8, 1.1$). Chemical reactants are consumed in the case of homogeneous reactions and thus nanoparticles concentration decreases. Higher estimations of (K_s) correspond to diffusion reduction and less diffused nanoparticles enhances the concentration $\tilde{j}(\xi)$. Figure (7.17) is sketched to show effect of Reynolds number ($Re = 0.4, 0.6, 0.7, 0.9$) on concentration $\hat{j}(\xi)$. Reynolds number (Re) significantly favors the concentration $\tilde{j}(\xi)$.

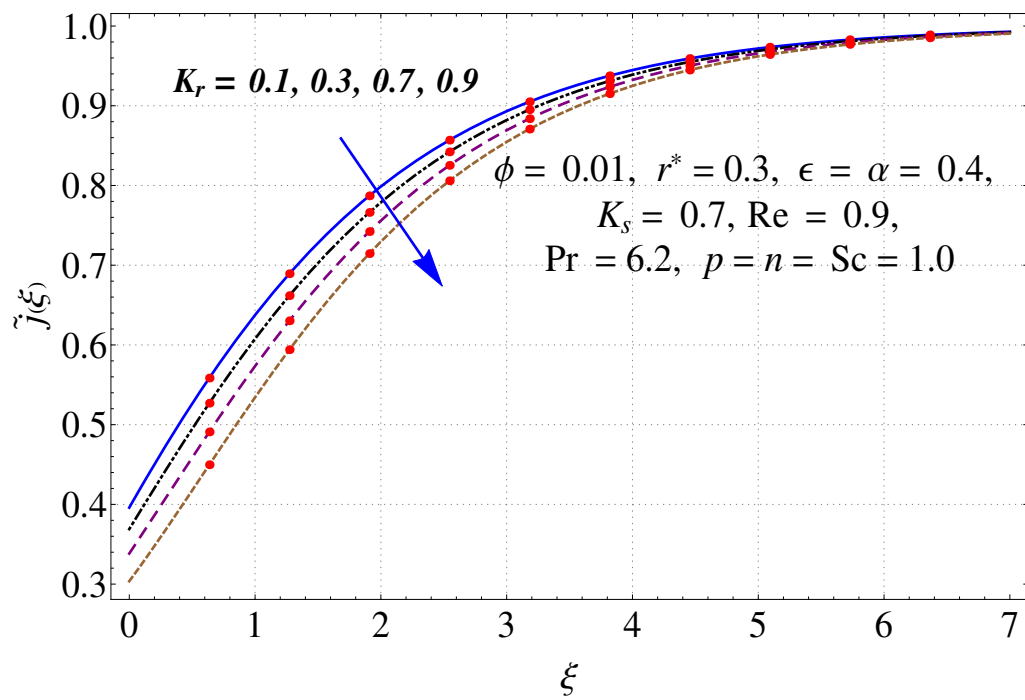


Figure 7.15: Variation of K_r on $\tilde{j}(\xi)$.

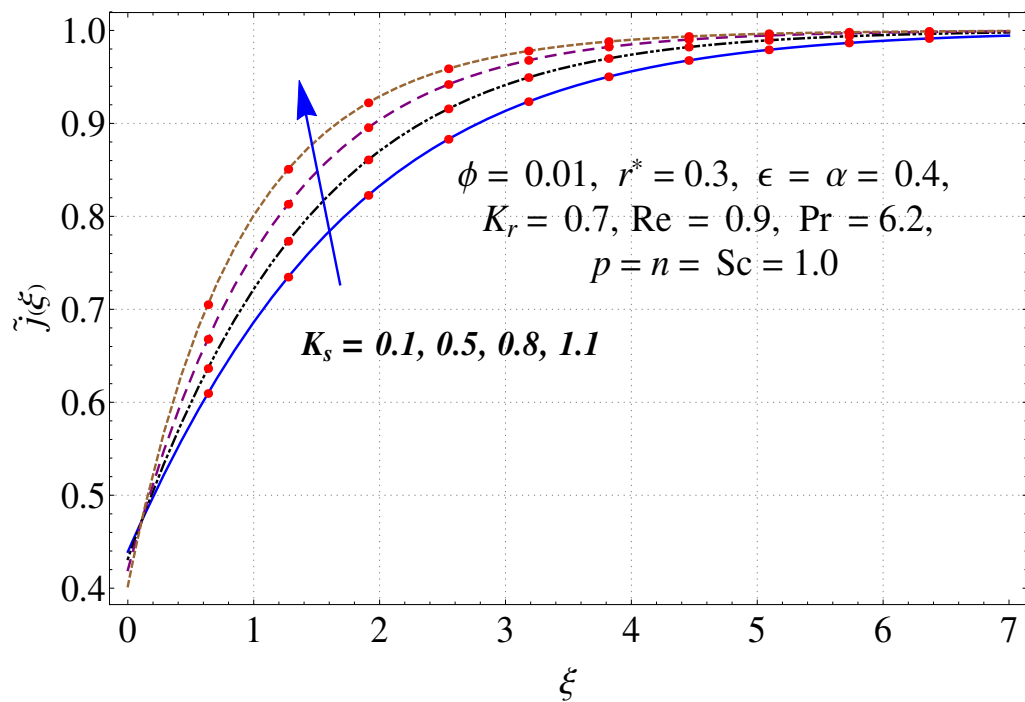
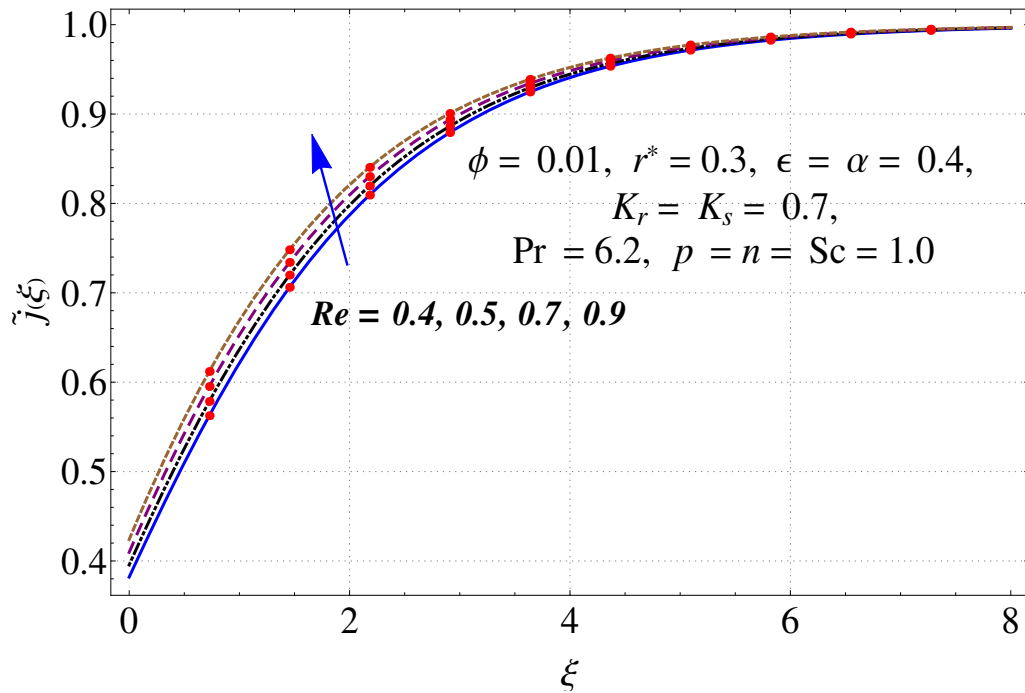


Figure 7.16: Variation of K_s on $\tilde{j}(\xi)$.

Figure 7.17: Variation of Re on $\tilde{j}(\xi)$.

7.4.5 Skin friction coefficient and Nusselt number

Figure (7.18) characterizes the variation of (r^*) on skin friction coefficient $\tilde{C}_{sf}(Re)^{\frac{n-1}{n+1}}$ for specified values of (ϵ) . Results indicate that $\tilde{C}_{sf}(Re)^{\frac{n-1}{n+1}}$ reduces via (r^*) while it has opposite behavior for (ϵ) . Figure (7.19) enlightens the ramifications of $(\phi = 0.01, 0.02, 0.03, 0.05)$ and (Re) on heat transfer rate $\tilde{N}_u(Re)^{\frac{-1}{n+1}}$. Clearly heat transfer rate is an increasing function of (ϕ) and (Re) .

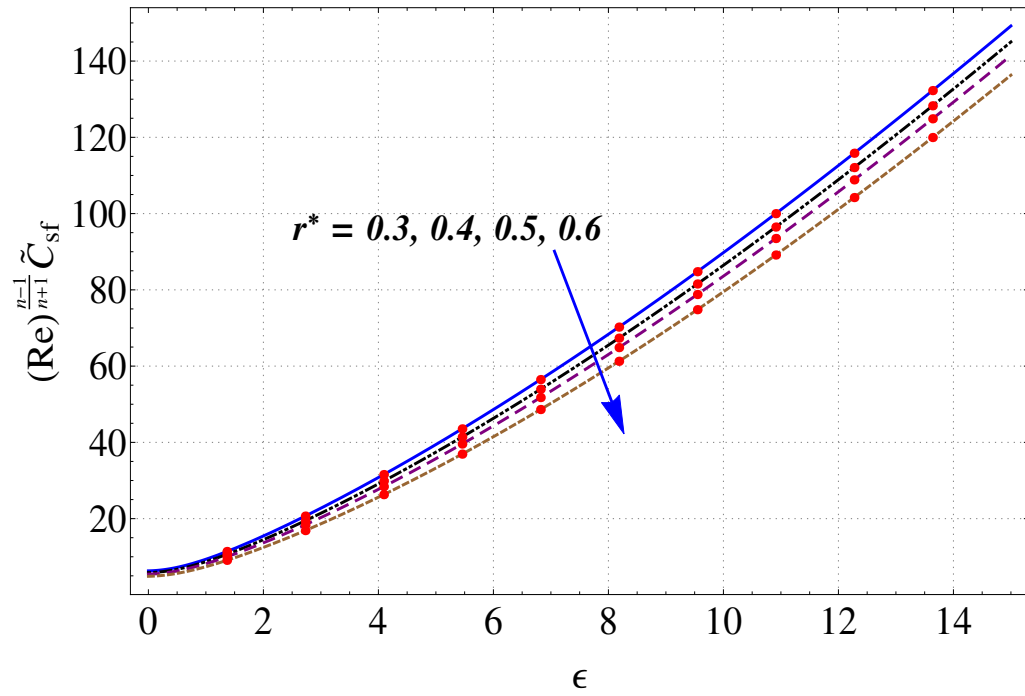


Figure 7.18: Variations of r^* and ϵ on $(\text{Re}_x)^{\frac{n-1}{n+1}} \tilde{C}_{sf}$.

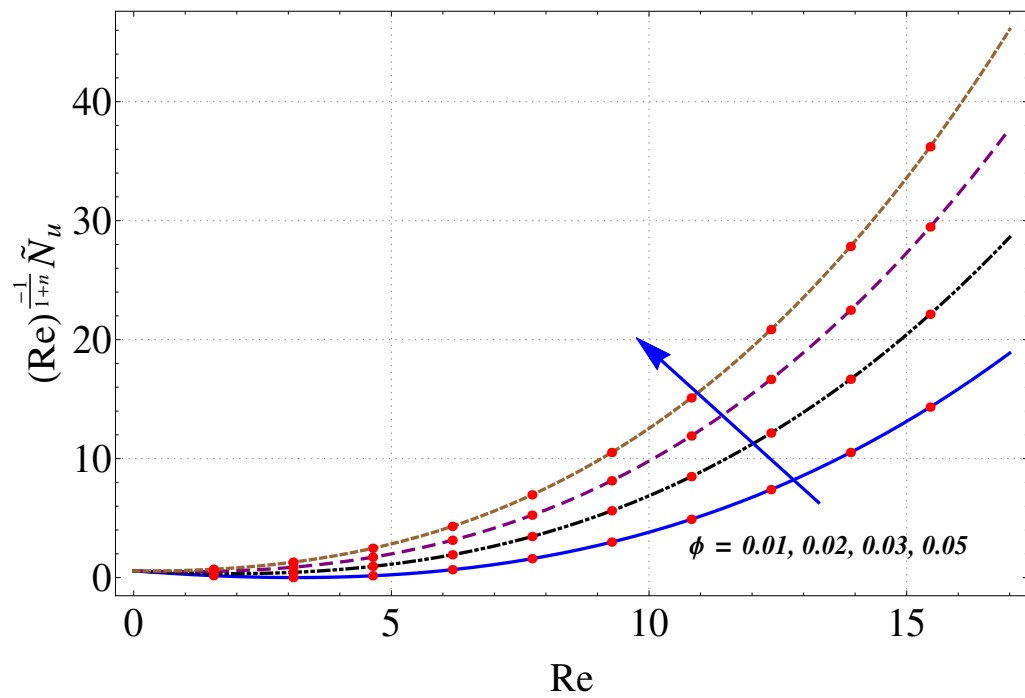


Figure 7.19: Variations of ϕ and Re on $(\text{Re}_x)^{-\frac{1}{n+1}} \tilde{N}_u$.

7.4.6 Comparative study

A comparison between analytical results of the problem and previous literature has been shown in Table (7.3). A good accuracy is obtained between two results.

Table 7.3: Comparison of present results when $p = Pr = n = 1.0, \phi = 0$.

Authors	$-\tilde{f}'(0)$	$-\tilde{g}'(0)$	$-\tilde{\theta}'(0)$
Ming et al. [40]	0.5102	0.6159	0.3963
Xun et al. [44]	0.5102	0.6159	0.3962
Hayat et al. [45]	0.5109	0.6159	0.3959
Present study	0.5130	0.6110	0.3980

7.4.7 Conclusions

Here flow of silver-water nanofluid due to rotating disk is examined. Major findings include the following results:

- Magnitude of axial velocity decays for higher values of dimensionless constant number (ϵ), disk thickness power-law index (p) and disk thickness coefficient (α).
- Higher estimations of Reynolds number (Re) significantly favors both radial and azimuthal velocities while opposite behavior is noticed for silver nanoparticles volume fraction (ϕ).
- Temperature of fluid enhances for higher volume fraction of silver nanoparticles (ϕ).
- Opposite impacts of heterogeneous (K_s) and homogeneous (K_r) reaction parameters are noticed for concentration.
- $\tilde{C}_{sf}(\text{Re})^{\frac{n-1}{n+1}}$ rises for larger estimations of (ϵ) whereas it decays when (r^*) is enhanced.
- $\tilde{N}_u(\text{Re})^{\frac{-1}{n+1}}$ enhances with the increase in (ϕ) and (Re).

Chapter 8

Entropy generation in Darcy-Forchheimer flow of nanofluid due to stretching cylinder

Here we are concerned with optimal homotopy arrangements for two-dimensional flow of magnetite nanofluid. Stretching cylinder with linear velocity creates the flow. Porous space effects are specified by Darcy-Forchheimer model. We have considered silver (Ag), copper (Cu), copper oxide (CuO), Titanium oxide (TiO_2) and aluminium-oxide (Al_2O_3) nanoparticles with water. Energy expression is modeled subject to consideration of non-linear thermal radiation phenomenon and non-uniform heat source/sink. Total entropy generation is calculated by using second law of thermodynamics. Uniformly valid convergent arrangement expressions are established by optimal homotopy technique (OHAM). Fluid flow and temperature behavior for physical variables are examined graphically. Coefficient of skin friction and Nusselt number are calculated and analyzed numerically.

8.1 Mathematical description

We explore the incompressible water-based nanofluid flow by stretching cylinder is studied. Nanofluids are suspensions of nanoparticles such as Copper oxide (CuO), Silver (Ag), Titanium oxide (TiO_2), Copper (Cu) and Aluminium-oxide (Al_2O_3) in water. Cylindri-

cal coordinates (x, r) are used to construct relevant equations. Cylinder with velocity $u_w = u_0 \left(\frac{x}{L}\right)$ is stretched in the axial direction. An incompressible fluid saturates the porous space specifying Darcy-Forchheimer relation. Characteristics of heat transfer is performed through nonlinear radiative heat flux and non-uniform heat source/sink.

Equations for flow and heat transfer are

$$\frac{\partial u}{\partial r} + \frac{u}{r} + \frac{\partial w}{\partial x} = 0, \quad (8.1)$$

$$\left(u \frac{\partial u}{\partial x} + w \frac{\partial u}{\partial r}\right) = \nu_{nf} \left(\frac{\partial^2 u}{\partial r^2} + \frac{1}{r} \frac{\partial u}{\partial r}\right) - \frac{\nu_{nf}}{\kappa_p} u - F_e u^2, \quad (8.2)$$

$$\begin{aligned} (\rho C_p)_{nf} \left(u \frac{\partial T}{\partial x} + w \frac{\partial T}{\partial r}\right) &= k_{nf} \left(\frac{\partial^2 T}{\partial r^2} + \frac{1}{r} \frac{\partial T}{\partial r}\right) + \frac{16\sigma^* T^3}{3k^*} \left(\frac{\partial^2 T}{\partial r^2} + \frac{1}{r} \frac{\partial T}{\partial r}\right) \\ &+ \frac{16\sigma^* 3T^2}{3k^*} \left(\frac{\partial T}{\partial r}\right)^2 + \mu_{nf} \left(\frac{\partial u}{\partial y}\right)^2 + q''', \end{aligned} \quad (8.3)$$

$$\begin{aligned} u = u_w = u_0 \left(\frac{x}{L}\right), \quad v = 0, \quad -k_{nf} \frac{\partial T}{\partial r} &= h_f (T_f - T) \text{ at } r = R, \\ u \rightarrow 0, \quad T \rightarrow T_\infty \text{ when } r \rightarrow \infty, \end{aligned} \quad (8.4)$$

where u and w represents velocity components and L the characteristic length of cylinder.

Non-uniform heat source/sink is defined as

$$q''' = \left(\frac{k_{nf} u_w(r)}{x \nu_f}\right) \left[I_1 * (T_f - T_\infty) \tilde{f}'(\xi) + I_2 (T - T_\infty) \right], \quad (8.5)$$

where generation/absorption coefficients are I_1 and I_2 .

Introducing the suitable transformations

$$u = u_0 \left(\frac{x}{L}\right) \tilde{f}'(\xi), \quad v = -\frac{R}{r} \left(\frac{\nu_f u_0}{L}\right)^{1/2} \tilde{f}(\xi), \quad \tilde{\theta}(\xi) = \frac{T - T_\infty}{T_f - T_\infty}, \quad \xi = \frac{r^2 - R^2}{2R} \sqrt{\frac{u_0}{L \nu_f}}, \quad (8.6)$$

Eqs. (8.2)-(8.4) take the form

$$\left(\frac{1}{(1 - \phi + \phi \frac{\rho_s}{\rho_f})(1 - \phi)^{2.5}}\right) \left[(1 + 2\gamma\xi) \tilde{f}'''' + 2\gamma \tilde{f}'' - \lambda \tilde{f}' \right] - F_r \tilde{f}'^2 + \tilde{f} \tilde{f}'' = 0, \quad (8.7)$$

$$\left(\frac{1}{1 - \phi + \phi \frac{(\rho C_p)_s}{(\rho C_p)_f}} \right) \left(\frac{1}{\text{Pr}} \right) \left[\begin{array}{l} \left(\frac{k_{nf}}{k_f} \right) (1 + 2\gamma\xi) \tilde{\theta}'' + 2\gamma\tilde{\theta}' + I_1\tilde{f}' + I_1\tilde{\theta} + Ec \frac{(1+2\gamma\xi)}{(1-\phi)^{2.5}} \tilde{f}''^2 \\ R_D \left(\tilde{\theta}(\theta_f - 1) + 1 \right)^2 \left(\begin{array}{l} 3\tilde{\theta}^2 (1 + 2\gamma\xi) (\theta_f - 1) \\ + \tilde{\theta}'' (1 + 2\gamma\xi) (\tilde{\theta}(\theta_f - 1) + 1) \\ + 2\gamma\tilde{\theta}'(\tilde{\theta}(\theta_f - 1) + 1) \end{array} \right) \end{array} \right] + \tilde{f}\tilde{\theta}' = 0, \quad (8.8)$$

$$\tilde{f}(0) = 0, \quad \tilde{f}'(0) = 1, \quad \tilde{f}'(\infty) \rightarrow 0, \quad \tilde{\theta}'(0) = -\frac{k_f}{k_{nf}} B_T \left(1 - \tilde{\theta}(0) \right), \quad \tilde{\theta}(\infty) \rightarrow 0. \quad (8.9)$$

where $\lambda = \frac{L\nu_f}{\kappa_p u_0 \rho_f}$ depicts the permeability parameter, $F_r = \frac{F_c}{\sqrt{\kappa_p}}$ the Forchheimer number, $\text{Pr} = \frac{(\mu C_p)_f}{k_f}$ the Prandtl number, $R_D = \frac{16\sigma^* T_\infty^3}{k^* k_f}$ the radiation parameter, $\theta_f = \frac{T_f}{T_\infty}$ the temperature ratio variable, $Ec = \frac{u_0^2 x^2}{(T_f - T_\infty)(C_p)_f L^2}$ the Eckert number, $Bi = \frac{h}{k_f \sqrt{\frac{u_0}{L\nu_f}}}$ the thermal Biot number $B_T = \frac{h_f}{k_f \sqrt{\frac{u_0}{L\nu_f}}}$ and the curvature parameter $\gamma = \sqrt{\frac{L\nu_f}{u_0 R^2}}$.

8.1.1 Physical quantities of curiosity

Surface drag force and heat transfer rate are

$$\tilde{C}_{sf} = \frac{\tau_w}{\rho_{nf} u_w^2}, \quad \tilde{N}_u = \frac{x q_w}{k_f (T_f - T_\infty)}, \quad (8.10)$$

\tilde{C}_{sf} and \tilde{N}_u in dimensionless form

$$\begin{aligned} (\text{Re}_x)^{0.5} \tilde{C}_{sf} &= \frac{1}{(1 - \phi)^{2.5}} \tilde{f}''(0), \\ (\text{Re}_x)^{-0.5} \tilde{N}_u &= - \left(\frac{k_{nf}}{k_f} + R_D (1 + (\theta_f - 1) \tilde{\theta}(0))^3 \right) \tilde{\theta}'(0), \end{aligned} \quad (8.11)$$

in which $\text{Re}_x = u_0 x^2 / L\nu_f$ denotes the local Reynolds number.

8.2 Entropy generation

The entropy generation consists of three factors namely

- (i) Heat transfer Irreversibility (*HTI*),
- (ii) Fluid Friction Irreversibility (*FFI*)

(iii) Porosity Permeability Irreversibility (*PPI*)

Thus

$$E_g = \frac{k_f}{T_\infty^2} \left[\frac{k_{nf}}{k_f} \left(\frac{\partial T}{\partial r} \right)^2 + \frac{16\sigma^* 3T^2}{3k^* k_f} \left(\frac{\partial T}{\partial r} \right)^2 \right] + \frac{\mu_{nf}}{T_\infty} \left[\left(\frac{\partial u}{\partial r} \right)^2 \right] + \frac{\mu_{nf}}{\kappa_p T_\infty} u^2. \quad (8.12)$$

Characteristic entropy generation is defined by

$$E_0 = \frac{L\nu_f T_\infty E_g}{u_0 k_f \Delta T}. \quad (8.13)$$

Characteristic entropy generation rate are written as

$$N_g = \frac{E_g}{E_0} = \left(\frac{k_{nf}}{k_f} + R_D \left(\tilde{\theta} (\theta_f - 1) + 1 \right)^3 \right) (1 + 2\gamma\xi) \alpha_T \tilde{\theta}'^2 + \left. \begin{array}{l} \\ Br \frac{\lambda}{(1-\phi)^{2.5}} f'^2 + \frac{Br(1+2\gamma\xi)}{(1-\phi)^{2.5}} f''^2 \end{array} \right\}, \quad (8.14)$$

where $Br = \frac{\mu_f u_0 x^2}{L^2 k_f \Delta T}$ represents the Brinkman number and $\alpha_T = \frac{T_f - T_\infty}{T_\infty} = \frac{\Delta T}{T_\infty}$ the dimensionless temperature difference.

Bejan number (Be) is

$$Be = \frac{\text{Entropy generation due to heat and mass transfer}}{\text{Total entropy generation}} \quad (8.15)$$

or

$$Be = \frac{\left(\frac{k_{nf}}{k_f} + R_D \left(\tilde{\theta} (\theta_w - 1) + 1 \right)^3 \right) (1 + 2\gamma\xi) \alpha_T \tilde{\theta}'^2}{\left(\frac{k_{nf}}{k_f} + R_D \left(\tilde{\theta} (\theta_f - 1) + 1 \right)^3 \right) (1 + 2\gamma\xi) \alpha_T \tilde{\theta}'^2 + Br \frac{\lambda}{(1-\phi)^{2.5}} f'^2 + \frac{Br(1+2\gamma\xi)}{(1-\phi)^{2.5}} f''^2}. \quad (8.16)$$

8.3 OHAM Solutions

The optimal series solutions are established. We choose

$$\tilde{f}_0(\xi) = (1 - \exp(-\xi)), \quad \tilde{\theta}_0(\xi) = \frac{B_T}{\left(\frac{k_{nf}}{k_f} + B_T \right)} \exp(-\xi), \quad (8.17)$$

with

$$\mathcal{L}_{\tilde{f}} = \tilde{f}''' - \tilde{f}', \quad \mathcal{L}_{\tilde{\theta}} = \tilde{\theta}'' - \tilde{\theta}, \quad (8.18)$$

and

$$\begin{aligned}\mathcal{L}_{\tilde{f}}[C_1 + C_2 \exp(\xi) + C_3 \exp(-\xi)] &= 0, \\ \mathcal{L}_{\tilde{\theta}}[C_4 \exp(\xi) + C_5 \exp(-\xi)] &= 0,\end{aligned}\tag{8.19}$$

in which C_i ($i = 1 - 5$) are arbitrary constants. In homotopy solutions the non-zero auxiliary variables \tilde{h}_f and \tilde{h}_{θ} regulate the convergence zone and also homotopic solutions rate. To obtain the ideal optimal values of \tilde{h}_f and \tilde{h}_{θ} , idea of minimization concept is employed by taking averaged squared residual errors as:

$$\varrho_m^{\tilde{f}} = \frac{1}{k+1} \sum_{l=0}^k \left[\mathcal{N}_{\tilde{f}} \left(\sum_{i=0}^m \tilde{f}(\xi) \right)_{\xi=l\delta^*\xi} \right]^2,\tag{8.20}$$

$$\varrho_m^{\tilde{\theta}} = \frac{1}{k+1} \sum_{l=0}^k \left[\mathcal{N}_{\tilde{\theta}} \left(\sum_{i=0}^m \tilde{f}(\xi), \sum_{i=0}^m \tilde{\theta}(\xi) \right)_{\xi=l\delta^*\xi} \right]^2,\tag{30}$$

Following:

$$\varrho_m^t = \varrho_m^{\tilde{f}} + \varrho_m^{\tilde{\theta}},\tag{32}$$

where ϱ_m^t stands for total squared residual error, $\delta^*\xi = 0.5$ and $k = 20$. The optimal data of convergence control parameter for *Ag*-water are $\tilde{h}_f = -0.504674$ and $\tilde{h}_{\theta} = -0.680152$ with $\varrho_m^t = 0.0265543$. Optimal values of auxiliary variables for *Cu*-water are $\tilde{h}_f = -0.535421$ and $\tilde{h}_{\theta} = -0.692151$ and error $\varrho_m^t = 0.0276802$. The optimal data of convergence control parameter for *CuO*-water are $\tilde{h}_f = -0.643143$ and $\tilde{h}_{\theta} = -0.762613$ with $\varrho_m^t = 0.0275201$. Optimal values of auxiliary variables for *TiO₂*-water are $\tilde{h}_f = -0.726765$ and $\tilde{h}_{\theta} = -0.838434$ with total averaged residual error $\varrho_m^t = 0.0256793$. The optimal values of convergence control parameter for *Al₂O₃*-water are $\tilde{h}_f = -0.688264$ and $\tilde{h}_{\theta} = -0.787352$ with total averaged residual error $\varrho_m^t = 0.0286444$. Curves of residual errors are plotted for all nanofluids (see Figures (8.1)-(8.5)). Table (8.1) presents the thermophysical properties of water and nanoparticles. Table (8.2)-(8.6) show residual errors of all nanofluids.

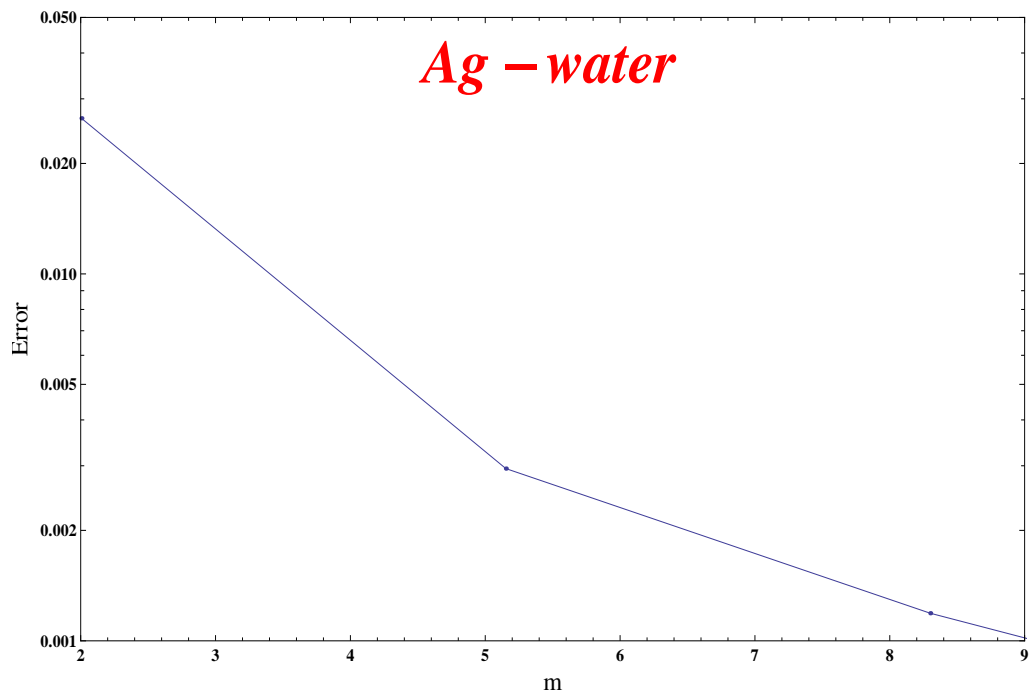


Figure 8.1: Residual error for *Ag*-water nanofluid.

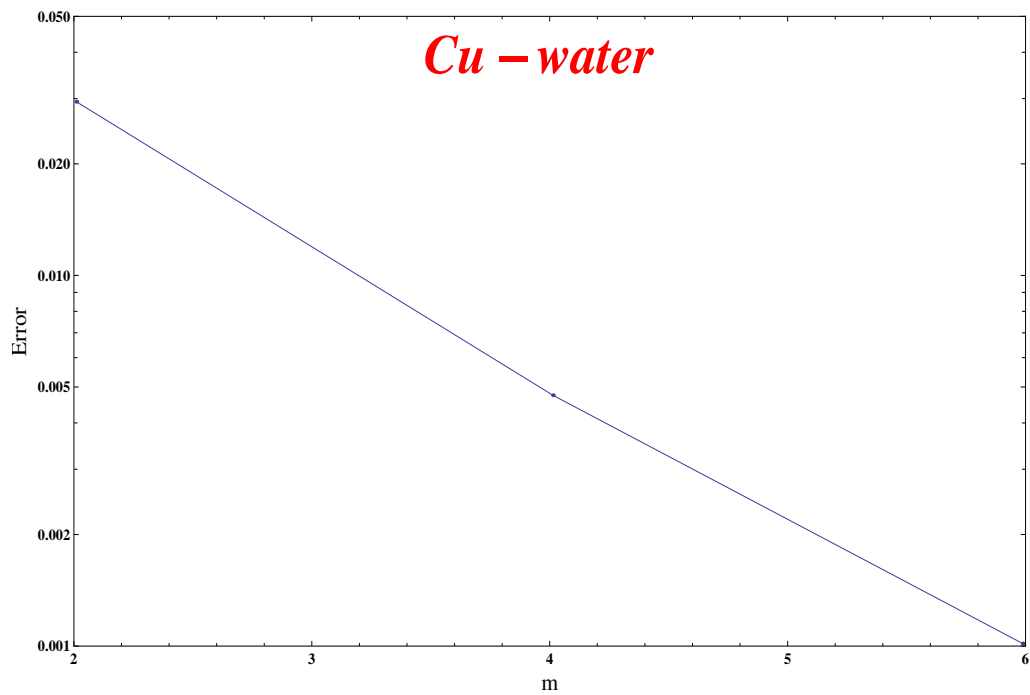


Figure 8.2: Residual error for *Cu*-water nanofluid.

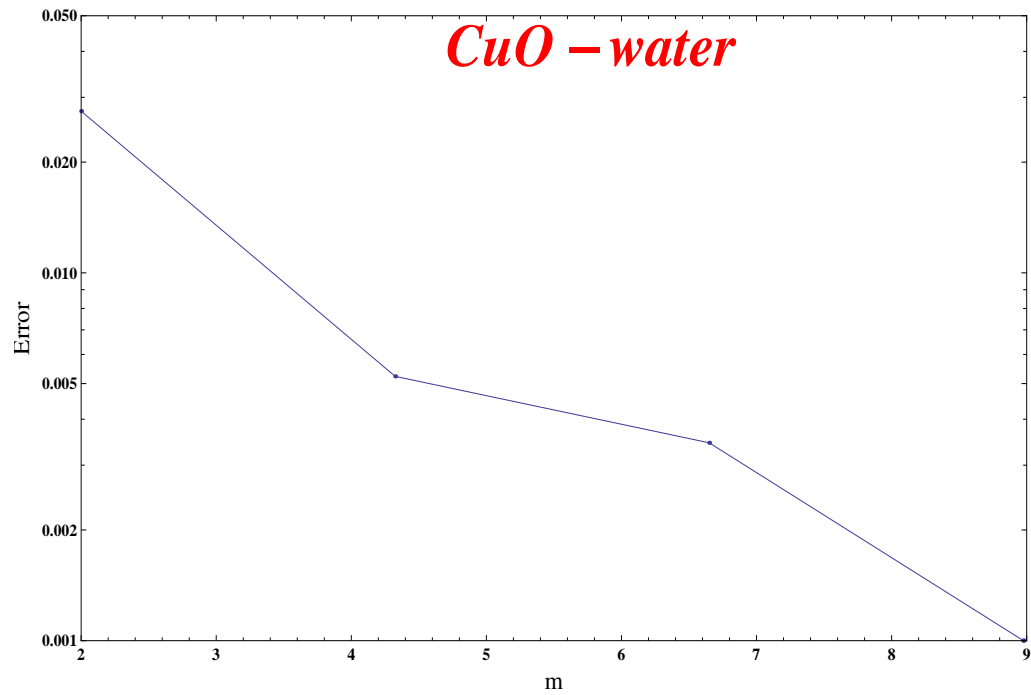


Figure 8.3: Residual error for *CuO*-water nanofluid.

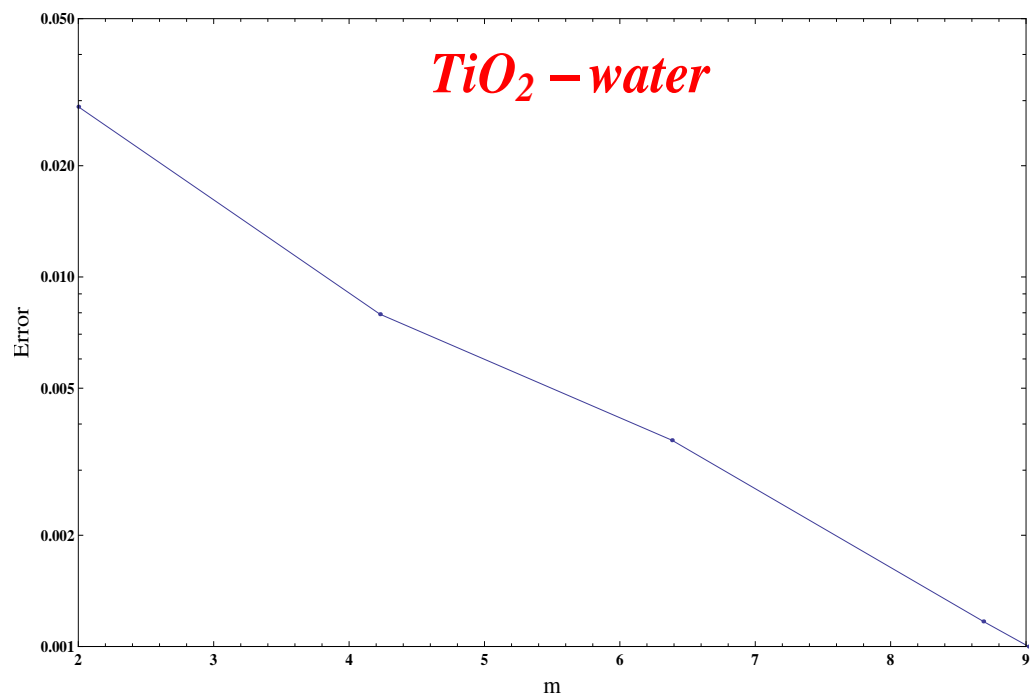


Figure 8.4: Residual error for *TiO₂*-water nanofluid.

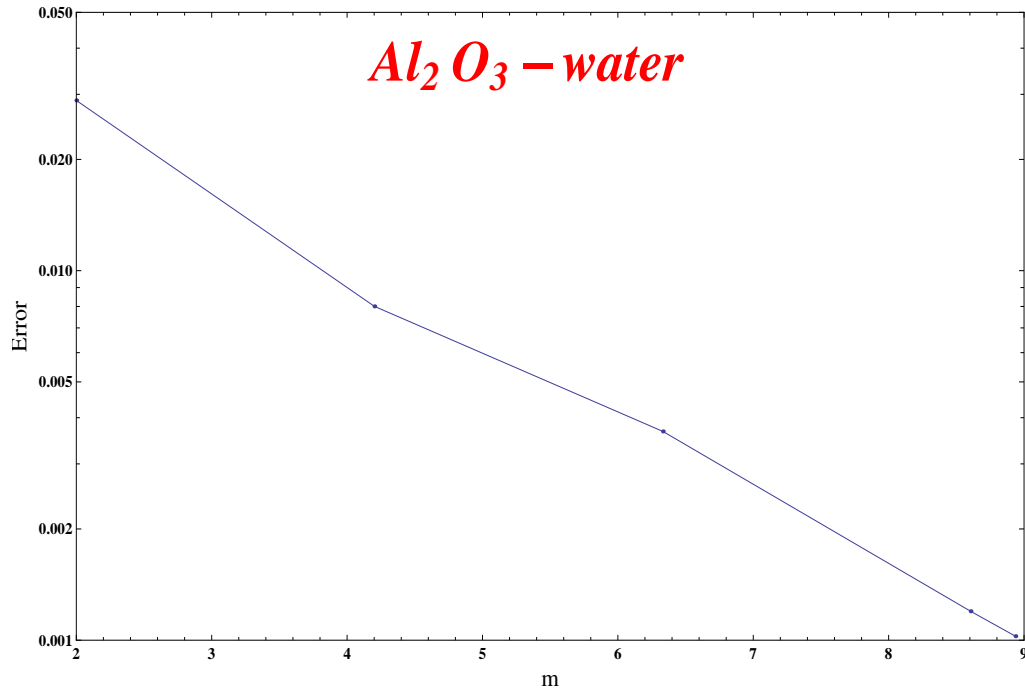
Figure 8.5: Residual error for Al_2O_3 -water nanofluid.

Table 8.1: Characteristics of nanoparticles and water

—	$k(W/mk)$	$\rho(kg/m^3)$	$\sigma(Um)^{-1}$	$C_p(j/m^3)$
Copper(Cu)	401	8933	5.96×10^7	385
Silver(Cu)	429	10500	3.6×10^7	235
Copper Oxide(CuO)	76.1	6320	2.7×10^{-8}	531.8
Alumina(Al_2O_3)	40	3970	$1 \times 10^{7-10}$	765
Titanium Oxide(TiO_2)	8.9538	4250	1×10^{-12}	686.2
H ₂ O(Pure Water)	0.613	997.1	0.05	4179

Table 8.2: Individual average residual errors for *Ag*-water nanofluid.

<i>Ag – water</i>		
m	$\varepsilon_m^{\tilde{f}}$	$\varepsilon_m^{\tilde{\theta}}$
2	3.26765×10^{-3}	2.32866×10^{-2}
4	1.12094×10^{-3}	1.82634×10^{-3}
6	4.64313×10^{-4}	7.24801×10^{-4}
8	2.25327×10^{-4}	3.67716×10^{-4}
10	1.24747×10^{-4}	1.20815×10^{-4}
12	7.71813×10^{-5}	4.48858×10^{-5}
14	5.24467×10^{-5}	2.31161×10^{-5}
16	3.85137×10^{-5}	1.36508×10^{-5}
18	3.00996×10^{-5}	8.03119×10^{-6}
20	2.46948×10^{-5}	4.66100×10^{-6}

 Table 8.3: Individual average residual errors for *Cu*-water nanofluid.

<i>Cu – water</i>		
m	$\varepsilon_m^{\tilde{f}}$	$\varepsilon_m^{\tilde{\theta}}$
2	3.52588×10^{-3}	2.41543×10^{-2}
4	1.17509×10^{-3}	2.00740×10^{-3}
6	5.00180×10^{-4}	1.07170×10^{-3}
8	2.56175×10^{-4}	5.01717×10^{-4}
10	1.51005×10^{-4}	1.50434×10^{-4}
12	9.92802×10^{-5}	5.35087×10^{-5}
14	9.92802×10^{-5}	5.35087×10^{-5}
16	5.43861×10^{-5}	1.62122×10^{-5}
18	4.37754×10^{-5}	9.46327×10^{-6}
20	3.66237×10^{-5}	5.45314×10^{-6}

Table 8.4: Individual average residual errors for CuO -water nanofluid.

$CuO - water$		
m	$\varepsilon_m^{\tilde{f}}$	$\varepsilon_m^{\tilde{\theta}}$
2	3.41411×10^{-3}	2.41060×10^{-2}
4	1.08771×10^{-3}	4.14403×10^{-3}
6	4.97279×10^{-4}	2.95399×10^{-3}
8	2.81586×10^{-4}	7.19484×10^{-4}
10	1.83343×10^{-4}	1.40087×10^{-4}
12	1.31457×10^{-4}	5.32527×10^{-5}
14	1.00931×10^{-4}	3.13949×10^{-5}
16	8.14252×10^{-5}	1.67787×10^{-5}
18	6.81239×10^{-5}	7.35824×10^{-6}
20	5.85695×10^{-5}	3.62701×10^{-6}

Table 8.5: Individual average residual errors for TiO_2 -water nanofluid.

$TiO_2 - water$		
m	$\varepsilon_m^{\tilde{f}}$	$\varepsilon_m^{\tilde{\theta}}$
2	3.40734×10^{-3}	2.22720×10^{-2}
4	1.14445×10^{-3}	9.74970×10^{-3}
6	5.68582×10^{-4}	4.26139×10^{-3}
8	3.46269×10^{-4}	3.94865×10^{-4}
10	2.38774×10^{-4}	8.27567×10^{-5}
12	1.78712×10^{-4}	4.32835×10^{-5}
14	1.41553×10^{-4}	3.46839×10^{-5}
16	1.16756×10^{-4}	1.05392×10^{-5}
18	9.92210×10^{-5}	2.86704×10^{-6}
20	8.62438×10^{-5}	2.15518×10^{-6}

Table 8.6: Individual average residual errors for Al_2O_3 -water nanofluid

$Al_2O_3 - water$		
m	$\varepsilon_m^{\tilde{f}}$	$\varepsilon_m^{\tilde{\theta}}$
2	3.89764×10^{-3}	2.47468×10^{-2}
4	1.33607×10^{-3}	6.55269×10^{-3}
6	6.68945×10^{-4}	4.23514×10^{-3}
10	2.81166×10^{-4}	1.32792×10^{-4}
12	2.09896×10^{-4}	5.79818×10^{-5}
14	1.65735×10^{-4}	4.02838×10^{-5}
16	1.36272×10^{-4}	1.98703×10^{-5}
18	1.15465×10^{-4}	7.34830×10^{-6}
20	1.00097×10^{-4}	3.72899×10^{-6}

8.4 Results and discussion

Primary goal here is to explore the characteristics of several sundry variables for velocity, temperature, entropy rate and Bejan number. This goal is achieved here by plotting the (8.6)-(8.19). Numerical data of skin friction and Nusselt number is also computed.

8.4.1 Velocity

Figure (8.6) presents the variation of curvature parameter ($\gamma = 0.1, 0.2, 0.3, 0.4$) on velocity $\tilde{f}'(\xi)$ for CuO , TiO_2 , Cu , Ag and Al_2O_3 -water nanofluids. It is observed that velocity is more for larger (γ). By increasing values of curvature parameter the radius of cylinder gradually reduces. Thus less surface of cylinder is in contact with fluid particles which provides a small resistance to fluid particles. Therefore velocity enhances. It is observed that velocity of CuO , Al_2O_3 and TiO_2 - water nanofluids dominant over Ag and Cu -water nanofluids. Because Ag and Cu nanoparticles are more dense than the rest of nanoparticles. Influence of volume fraction of nanoparticles ($\phi = 0.01, 0.02, 0.03, 0.05$) on velocity $\tilde{f}'(\xi)$ for all nanofluids is captured in Figure (8.7). An increment in (ϕ) yields reduction in $\tilde{f}'(\xi)$. Velocity of Cu and Ag -water nanofluids is less than CuO , TiO_2 and Al_2O_3 - water nanofluids because of their higher densities. Salient characteristics of permeability parameter ($\lambda = 0.3, 0.4, 0.5, 0.6$) on $\tilde{f}'(\xi)$ is plotted in Figure (8.8). Here $\tilde{f}'(\xi)$

decays for higher (λ). It is because of the fact for higher (λ) mean lead to more kinematic viscosity. A small permeability causes the production of resistive force to the fluid flow which is responsible of reduction in $\tilde{f}'(\xi)$. Figure (8.9) reports the impact of Forchheimer number ($F_r = 0.2, 0.3, 0.4, 0.5$) on $\tilde{f}'(\xi)$. Higher Forchheimer number (F_r) cause reduction in $\tilde{f}'(\xi)$. Physically drag force has significant association with Forchheimer number (F_r). Higher Forchheimer number (F_r) enhance drag force which has tendency to reduce the velocity. Similar results are obtained for all nanofluids.

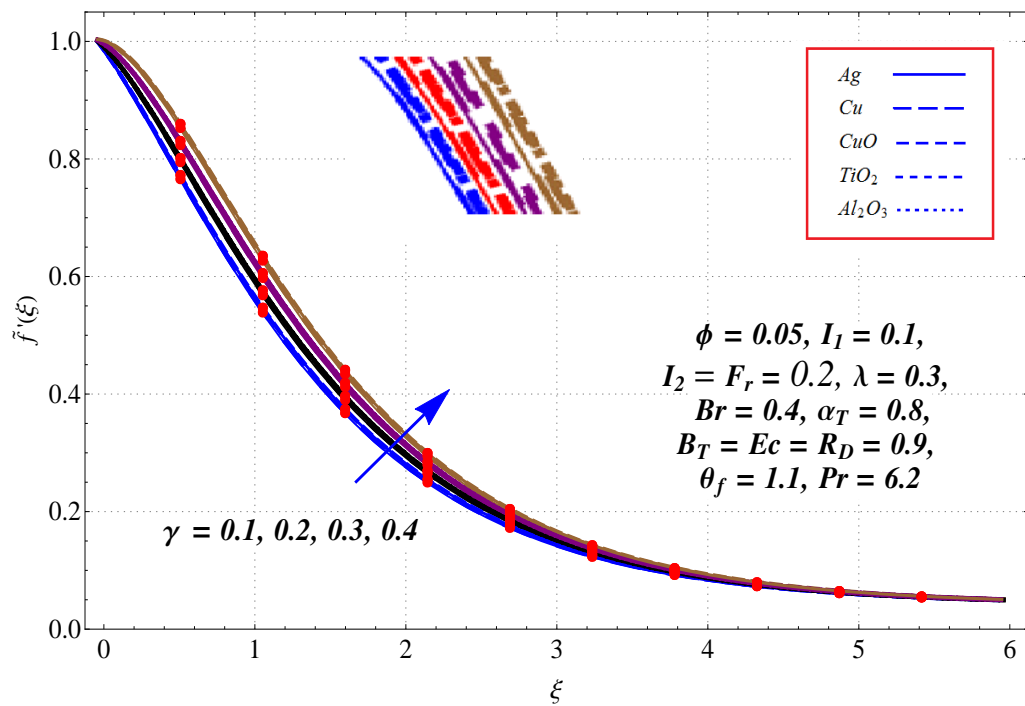


Figure 8.6: Variation of γ on $\tilde{f}'(\xi)$.

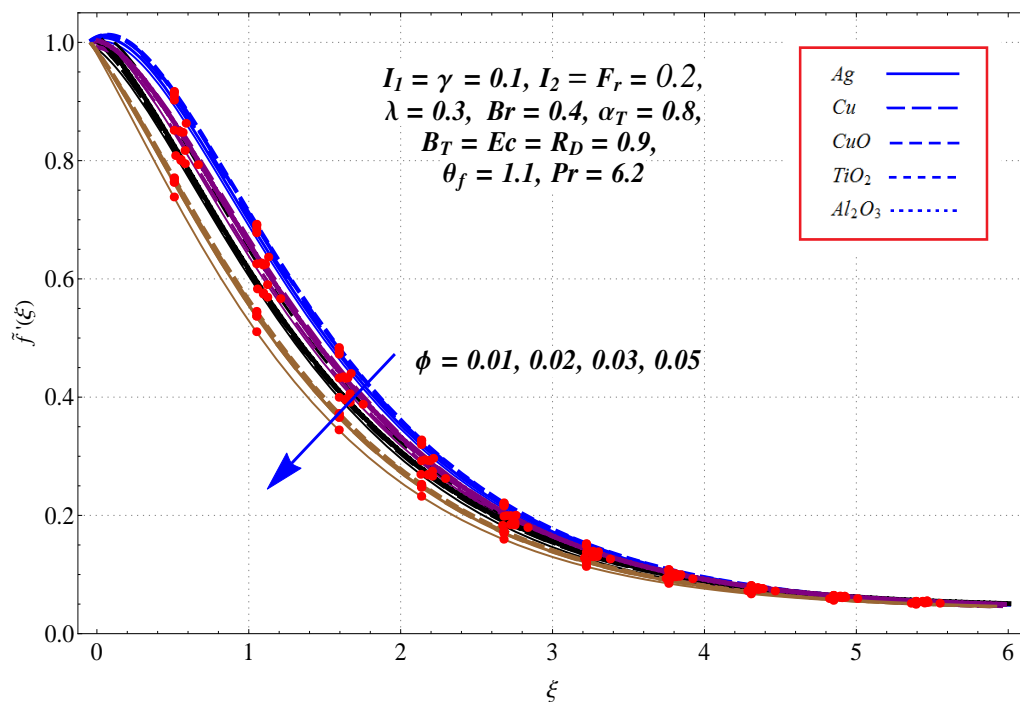


Figure 8.7: Variation of ϕ on $\tilde{f}'(\xi)$.

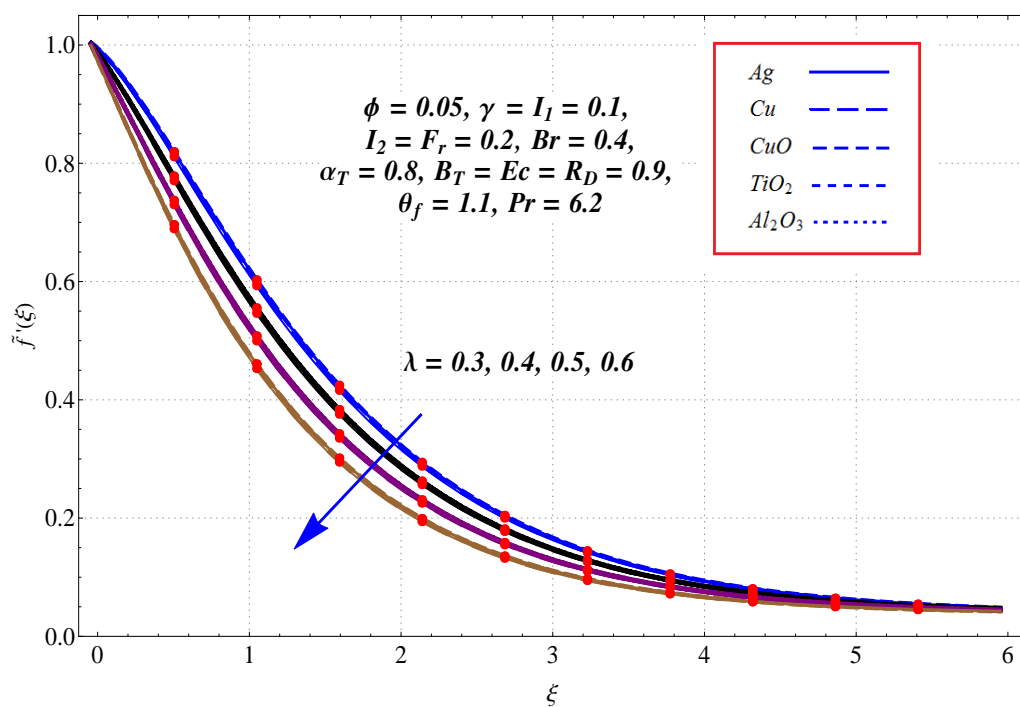
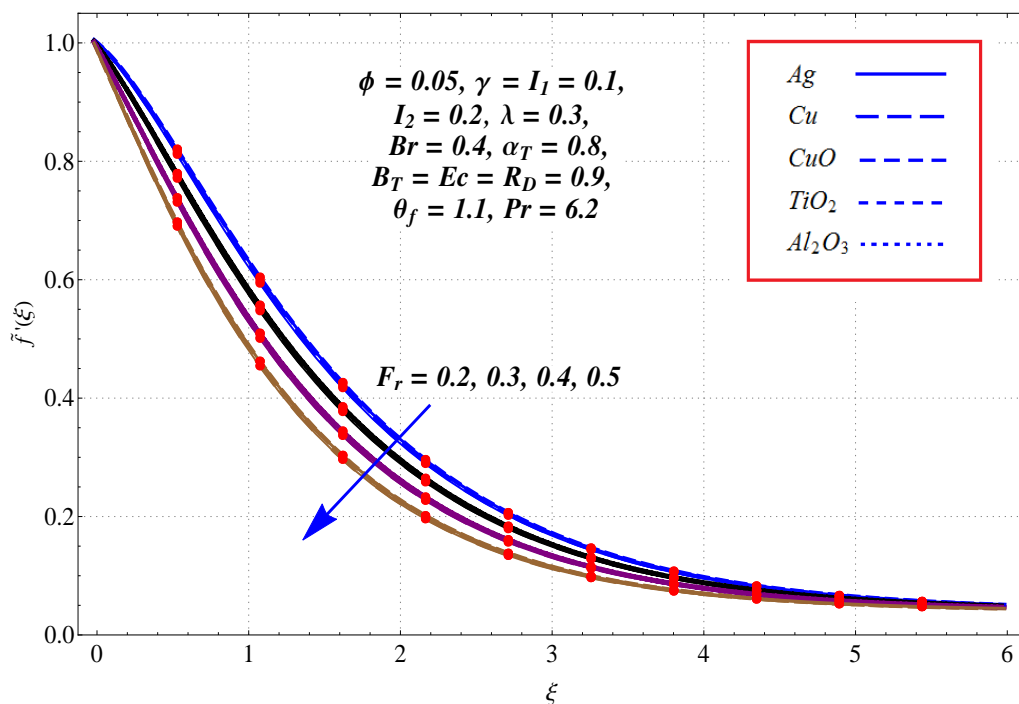


Figure 8.8: Variation of λ on $\tilde{f}'(\xi)$.

Figure 8.9: Variation of F_r on $\tilde{f}'(\xi)$.

8.4.2 Temperature

Figure (8.10) present the outcome of ($\phi = 0.01, 0.03, 0.04, 0.05$) on temperature for CuO , Al_2O_3 , TiO_2 , Ag and Cu -water nanofluids. As expected higher (ϕ) estimations yield an increment in temperature. The sensitivity of associated thermal layer to nanoparticles volume fraction has relationship with an enhancement of nanofluid's thermal conductivity which uplifts the nanofluid temperature. It is worth mentioning that temperature are slightly higher for Ag -water nanofluid rather than Cu , TiO_2 , Al_2O_3 - and CuO -water nanofluids due to its high thermal conductivity. An enhancement in $\tilde{\theta}(\xi)$ and thermal layer thickness via ($\gamma = 0.1, 0.2, 0.3, 0.4$) is noted in Figure (8.11). Greater values of (γ) shrinks the surface area of cylinder. High heat transfer rate by convection is created due to minimum particles are attached on the surface. Thus temperature enhances. Figure (8.12) interprets the impact of Eckert number ($Ec = 0.1, 0.4, 0.7, 0.9$) on temperature. Higher (Ec) boosts temperature of fluid. It occurs due to friction of molecules where mechanical energy is converted into thermal energy. Hence temperature

enhances. Thermal Biot number ($B_T = 0.1, .4, 0.7, 0.9$) for all nanofluids on temperature $\tilde{\theta}(\xi)$ is plotted in Figure (8.13). It is observed that $\tilde{\theta}(\xi)$ rises when (B_T) is augmented.

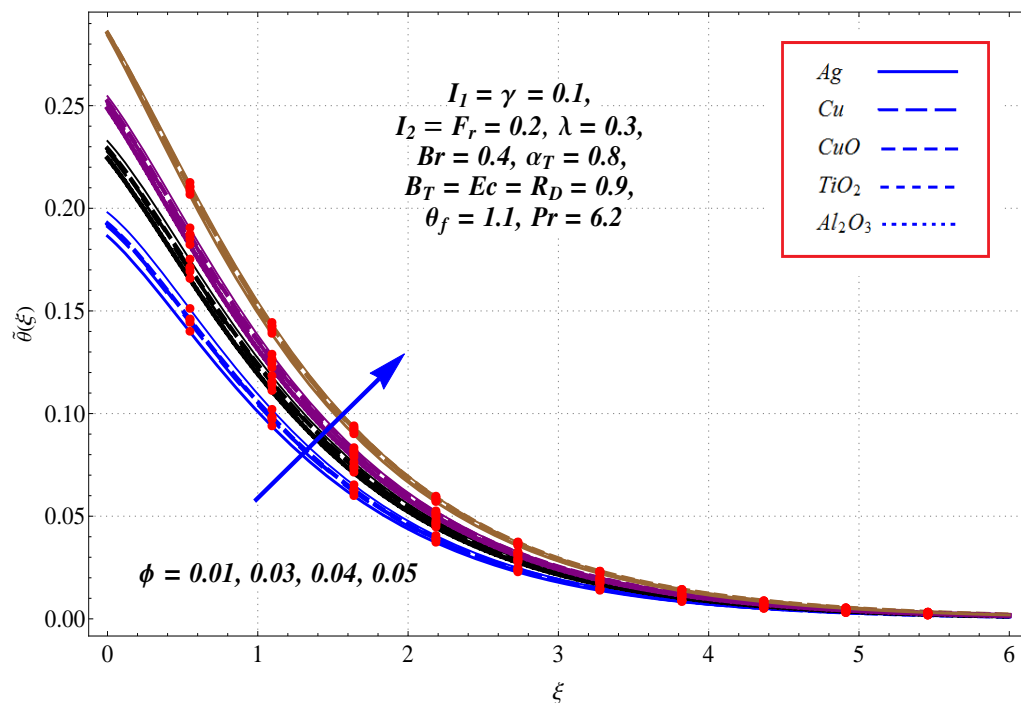


Figure 8.10: Variation of ϕ on $\tilde{\theta}(\xi)$.

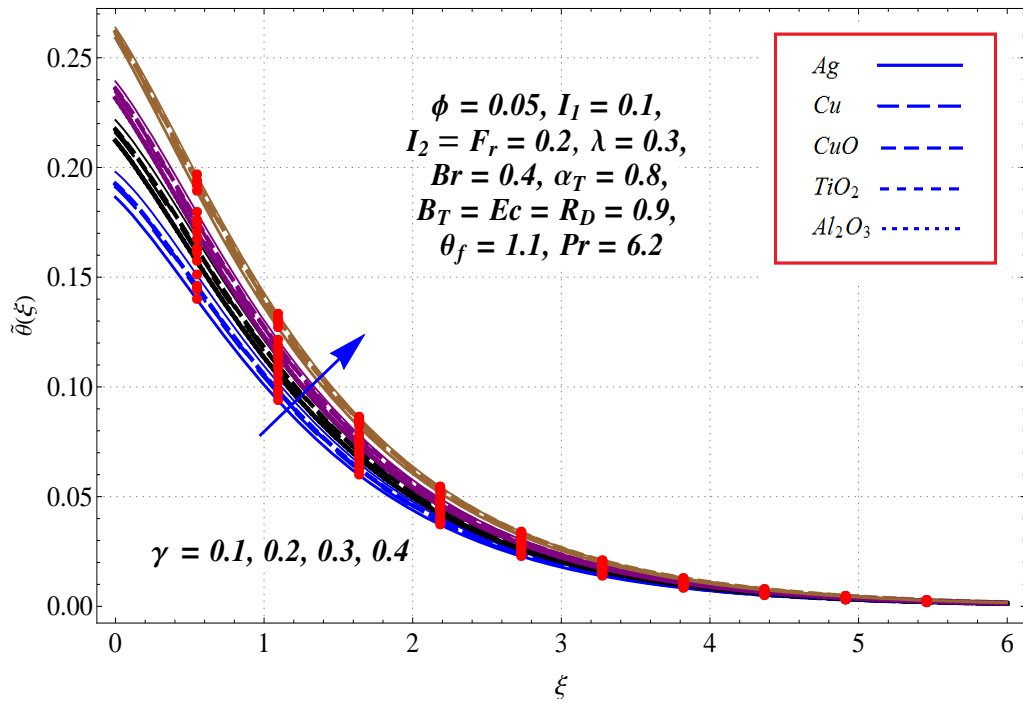


Figure 8.11: Variation of γ on $\tilde{\theta}(\xi)$.

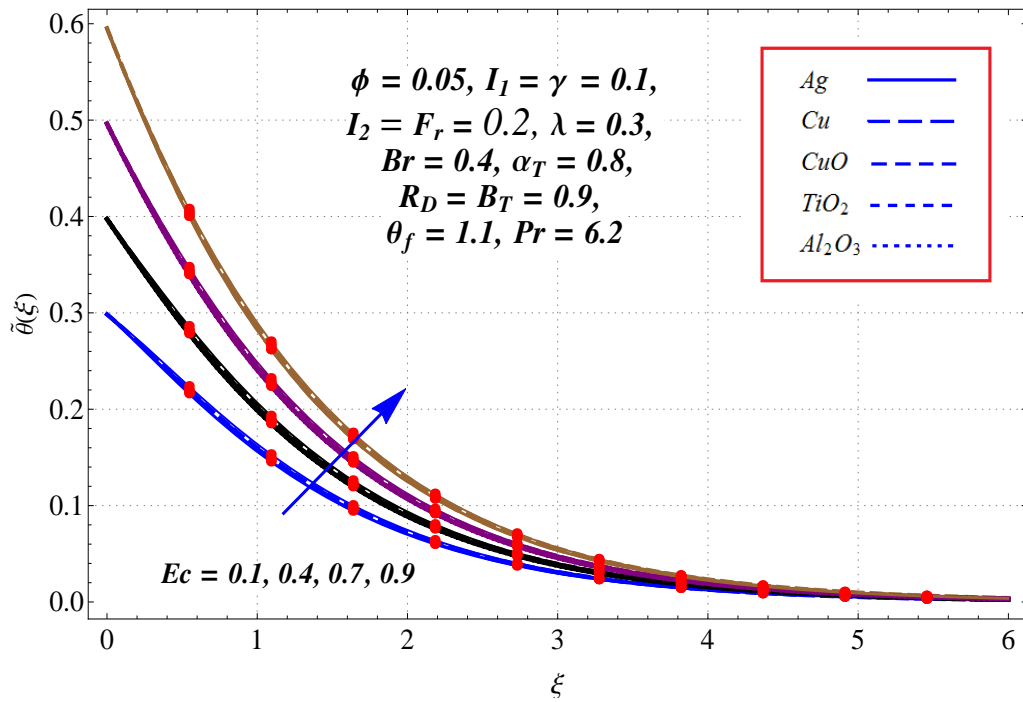
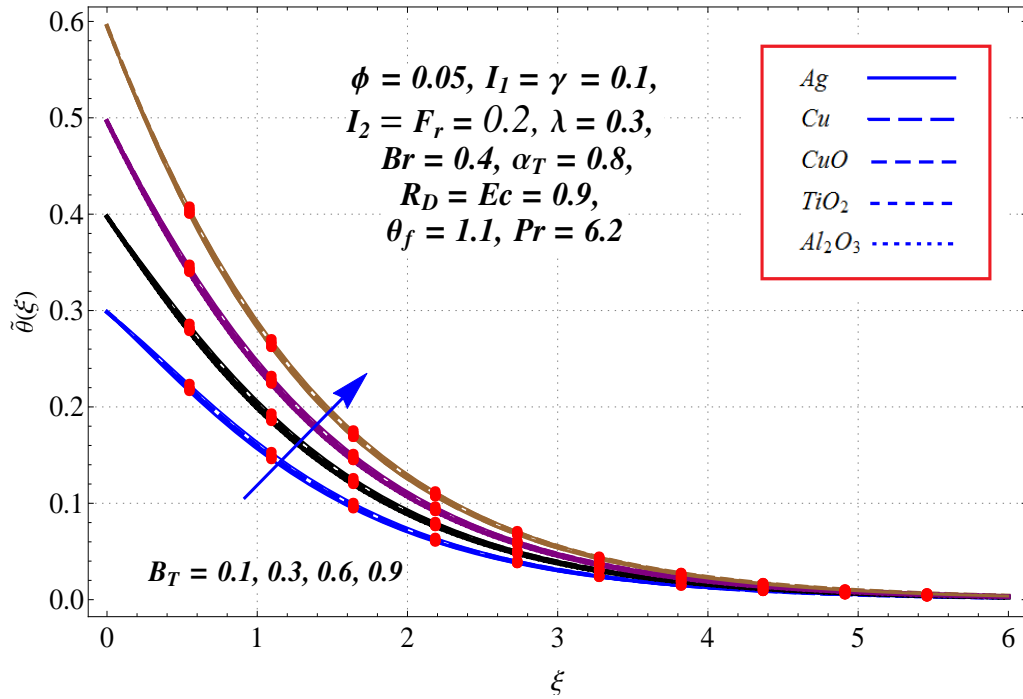


Figure 8.12: Variation of Ec on $\tilde{\theta}(\xi)$.


 Figure 8.13: Variation of B_T on $\tilde{\theta}(\xi)$.

8.4.3 Entropy generation and Bejan number

Figures (8.14) and (8.15) shows the outcome of Brinkman number ($Br = 0.2, 0.3, 0.4, 0.5$) on $N_g(\xi)$ and Bejan number Be . Higher values of Brinkman number (Br) enhance viscous dissipation irreversibilities and thus entropy rate boosts while Bejan number decreases for low thermal conductivity. Plots for temperature ratio parameter ($\alpha_T = 0.8, 0.9, 1.0, 1.2$) on $N_g(\xi)$ and (Be) are displayed in Figures (8.16) and (8.17). Disorderliness in the system and Bejan number are enhanced for higher (α_T). It is noted that $N_g \rightarrow 0$ away from surface. For larger (α_T) the heat transfer effects are prominent than fluid friction. That is why (Be) is increases. It is found that Ag -water nanofluid have more prominent effects than rest of the nanofluids for (Be) due to its higher heat conductive ability. Effect of Forchheimer number ($F_r = 0.2, 0.3, 0.4, 0.5$) on entropy generation $N_g(\xi)$ and Bejan number (Be) are plotted in Figures (8.18) and (8.19). Here $N_g(\xi)$ and (Be) are enhanced for higher (F_r) in all nanofluids. Physically disorderliness of system increases for higher Forchheimer number F_r . Therefore $N_g(\xi)$ and (Be) rise.

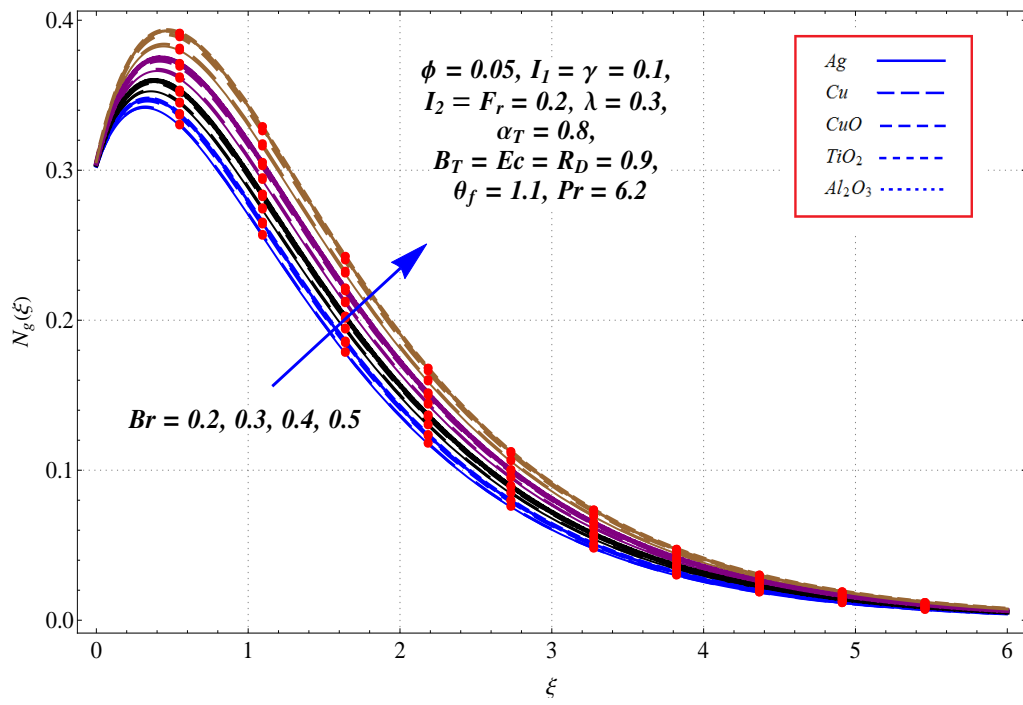


Figure 8.14: Variation of Br on $N_g(\xi)$.

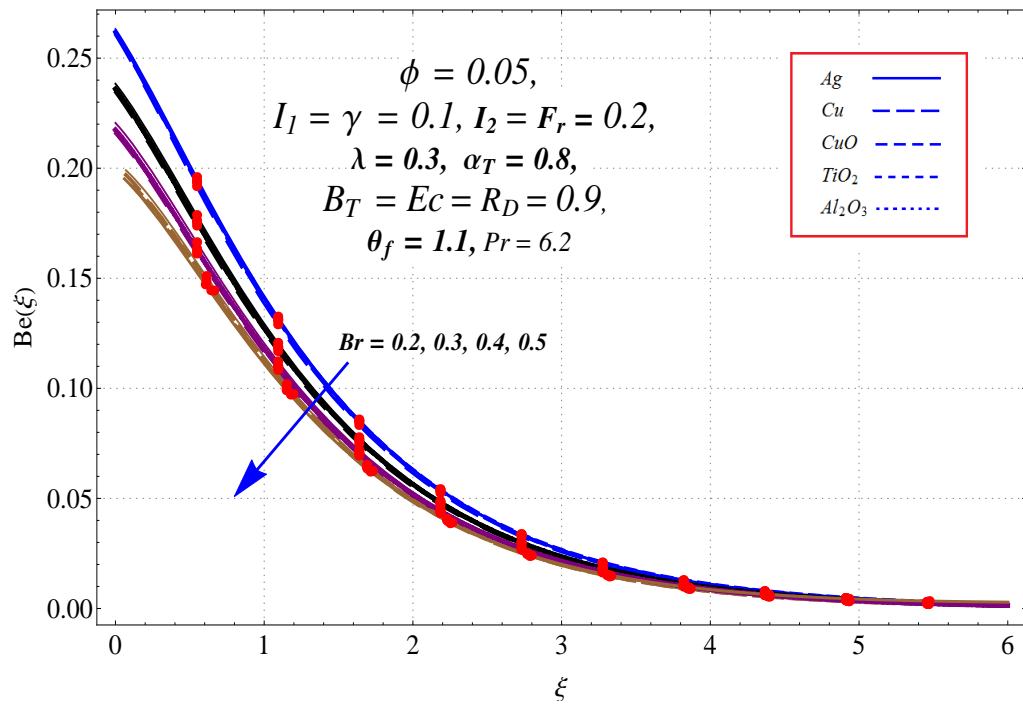
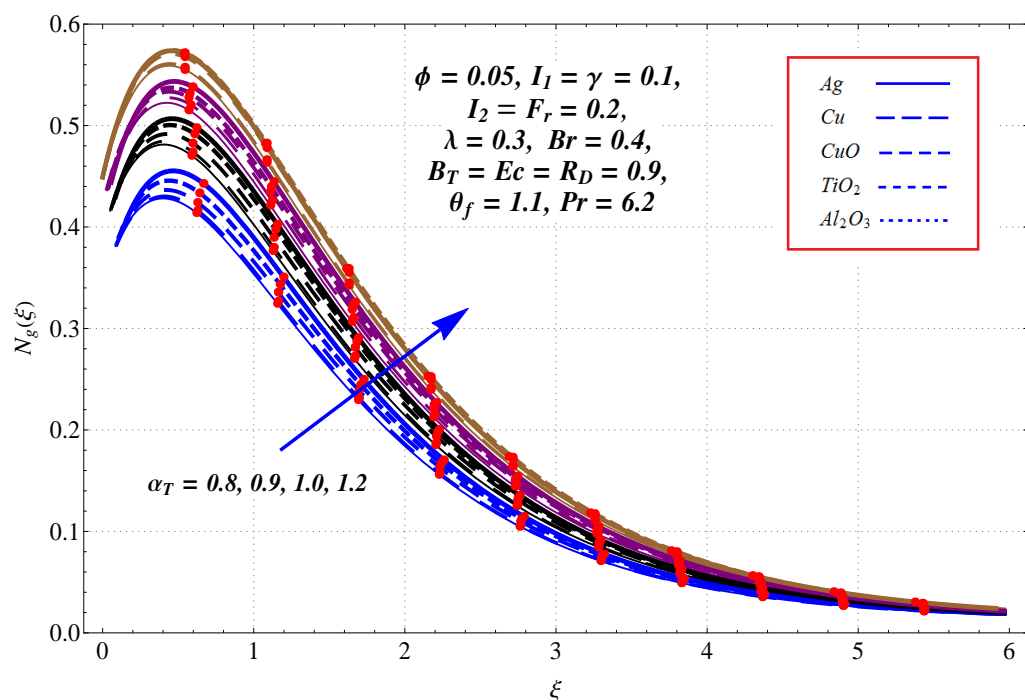
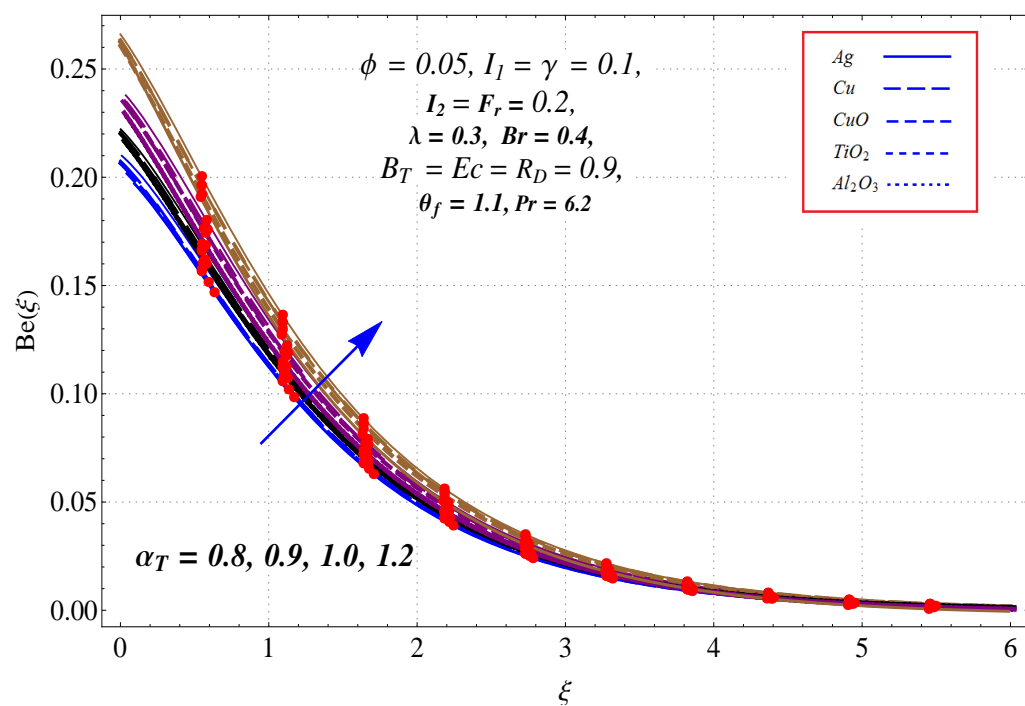


Figure 8.15: Variation of Br on Be .


 Figure 8.16: Variation of α_T on $N_g(\xi)$.

 Figure 8.17: Variation of α_T on Be .

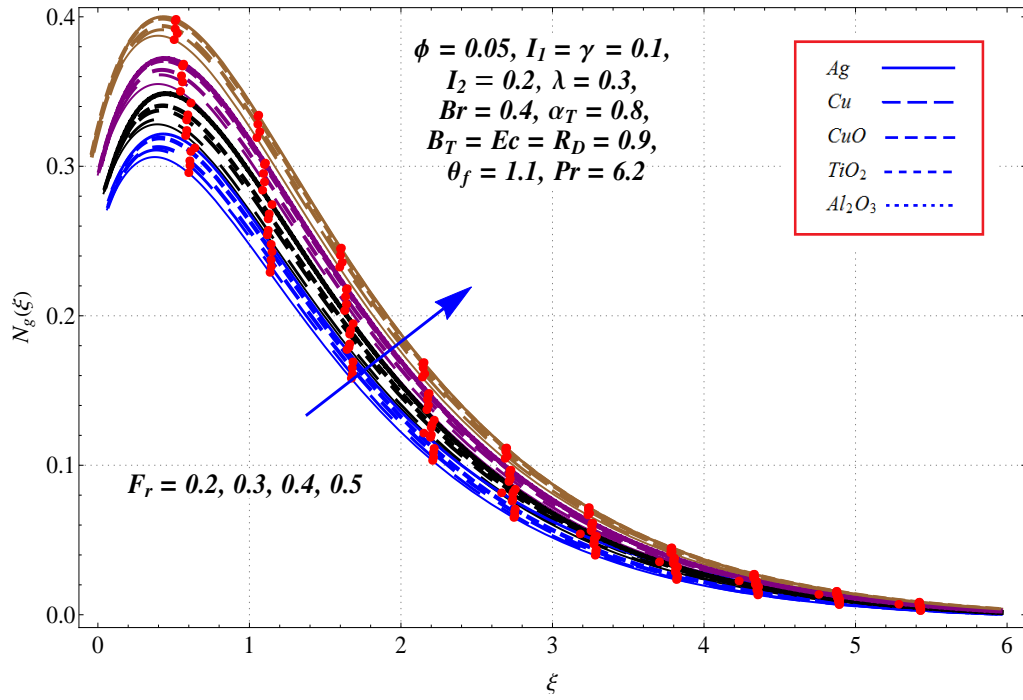


Figure 8.18: Variation of F_r on $N_g(\xi)$.

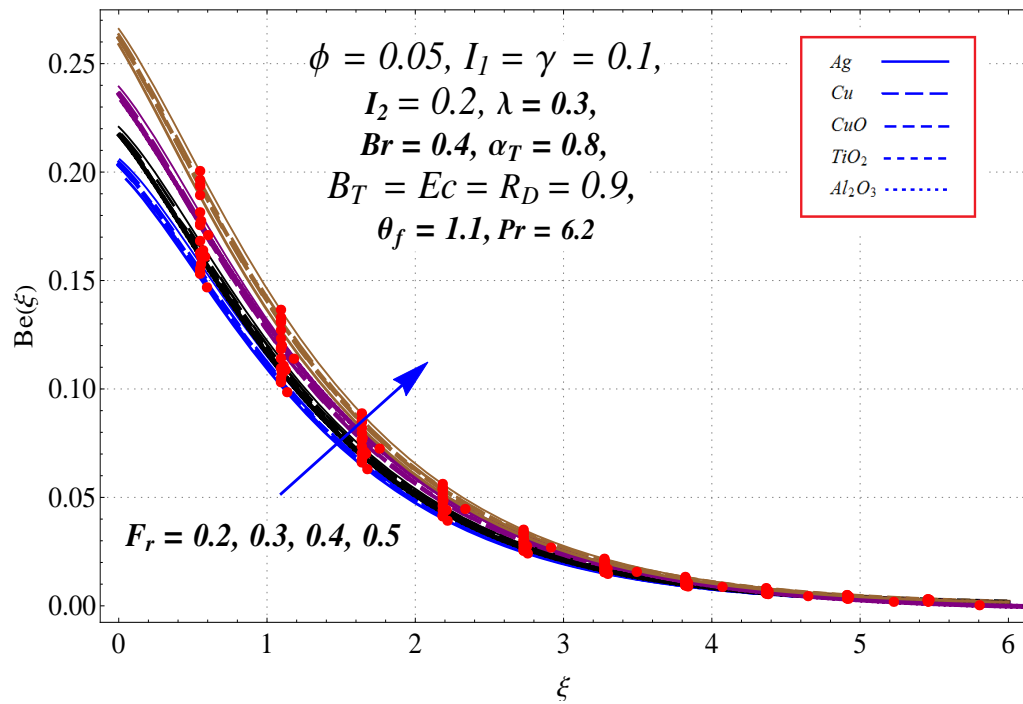


Figure 8.19: Variation of F_r on Be .

8.4.4 Skin friction coefficient and heat transfer rate

Influence of nanoparticles volume fraction (ϕ) on skin friction coefficient and heat transfer rate for five different types of nanofluids are elaborated through Tables (8.7)-(8.8). Magnitude of skin friction coefficient and heat transfer rate enhanced for higher ϕ .

Table 8.7: Behavior of ϕ on skin friction coefficient for all nanofluids.

ϕ	<i>Ag</i>	<i>Cu</i>	<i>CuO</i>	<i>TiO₂</i>	<i>Al₂O₃</i>
0.01	-0.9747	-0.9704	-0.9631	-0.9566	-0.9574
0.03	-1.0616	-1.0490	-1.0278	-1.0080	-1.0106
0.05	-1.1501	-1.1297	-1.0949	-1.0626	-1.0665

Table 8.8: Behavior of ϕ on heat transfer rate for all nanofluids.

ϕ	<i>Ag</i>	<i>Cu</i>	<i>CuO</i>	<i>TiO₂</i>	<i>Al₂O₃</i>
0.01	-1.005	-1.004	-1.004	-1.003	-1.001
0.03	-1.066	-1.066	-1.064	-1.062	-1.049
0.05	-1.129	-1.129	-1.125	-1.123	-1.101

8.5 Concluding remarks

Darcy-Forchheimer flow of nanofluid due to stretching cylinder with entropy generation is studied. Main observations are:

- Rise in nanoparticles volume fraction has tendency to retard the velocity and enhance the temperature.
- A reduction in velocity is observed for higher values of permeability and Forchheimer variables.
- For higher Eckert number the temperature of fluid enhances and impact of silver-water nanofluid dominates when compared with rest of nanofluids.

- ❑ Temperature of fluid increases for thermal Biot number.
- ❑ Entropy generation enhances for higher estimations of temperature difference variable, Forchheimer number and Brinkman number while Bejan number reduces for Brinkman number.
- ❑ Magnitude of skin friction coefficient is an increasing function of volume fraction of nanoparticles.
- ❑ An enhancement in local Nusselt number occurs for volume fraction of nanoparticles.

Chapter 9

Chemically reactive flow of Maxwell nanofluid due to stretching cylinder with thermal radiation

This chapter investigates the non-linear mixed convective flow of Maxwell nanofluid due to stretching cylinder. Electrically conducting fluid is considered. Silent features of Joule heating, thermal radiation and first order chemical reaction are attended. Concentration and energy expressions consist of Brownian motion and thermophoresis phenomena. Heat and mass transfer are described by convective conditions associated with cylinder. Strong non-linear systems are solved for convergent homotopy solutions. Salient characteristics of magnetic parameter, Deborah number, curvature parameter, Biot number, Prandtl number, thermophoresis parameter, Eckert number and Schmidt number on the velocity, temperature, nanoparticles concentration, Nusselt and Sherwood numbers are reported via graphs.

9.1 Problem statement

Non-linear mixed convective flow of Maxwell nanofluid towards stretching cylinder is modeled. Fluid is conducted electrically through \tilde{B}_0^* applied along radial direction. Also, the magnetic Reynolds number is assumed small and the characteristics of induced magnetic field are not considered. Electric field is absent. Cylinder with velocity $w_w = w_0 \left(\frac{z}{L}\right)$ is stretching in the axial direction. Thermal radiation, Joule heating and convective heating

effects are considered in the heat transfer process. Brownian motion and thermophoresis attributes are considered. Viscous dissipation is absent. Chemically reacted species model are accounted. The relevant problems satisfy:

$$\frac{\partial u}{\partial r} + \frac{u}{r} + \frac{\partial w}{\partial z} = 0, \quad (9.1)$$

$$\begin{aligned} u \frac{\partial w}{\partial r} + w \frac{\partial w}{\partial z} + \lambda_1 \left(w^2 \frac{\partial^2 w}{\partial z^2} + u^2 \frac{\partial^2 w}{\partial r^2} + 2uw \frac{\partial^2 w}{\partial r \partial z} \right) \\ = \nu_f \left(\frac{\partial^2 w}{\partial r^2} + \frac{1}{r} \frac{\partial w}{\partial r} \right) - \frac{\sigma_f B_0^{*2}}{\rho_f} \left(w - \lambda_1 u \frac{\partial w}{\partial r} \right) \\ + g(\epsilon_1 (T - T_\infty) + \epsilon_2 (T - T_\infty)(T - T_\infty)) \\ + g(\epsilon_3 (C - C_\infty) + \epsilon_4 (C - C_\infty)(C - C_\infty)), \end{aligned} \quad (9.2)$$

$$\begin{aligned} \left(u \frac{\partial T}{\partial r} + w \frac{\partial T}{\partial z} \right) = \alpha_f \left(\frac{\partial^2 T}{\partial r^2} + \frac{1}{r} \frac{\partial T}{\partial r} \right) + \tau \left(D_B \frac{\partial C}{\partial r} \frac{\partial T}{\partial r} + \frac{D_T}{T_\infty} \left(\frac{\partial T}{\partial r} \right)^2 \right) \\ + \frac{16\sigma^* T_\infty^3}{3k^*(\rho C_p)_f} \left(\frac{\partial^2 T}{\partial r^2} + \frac{1}{r} \frac{\partial T}{\partial r} \right) + \frac{\sigma B_0^2}{(\rho C_p)_f} w^2. \end{aligned} \quad (9.3)$$

$$\left(u \frac{\partial C}{\partial r} + w \frac{\partial C}{\partial z} \right) = D_B \left(\frac{\partial^2 C}{\partial r^2} + \frac{1}{r} \frac{\partial C}{\partial r} \right) + \frac{D_T}{T_\infty} \left(\frac{\partial^2 T}{\partial r^2} + \frac{1}{r} \frac{\partial T}{\partial r} \right) - K_c (C - C_\infty), \quad (9.4)$$

$$\begin{aligned} u = 0, \quad v = 0, \quad w = w_w = \frac{zw_0}{L}, \quad -k_f \frac{\partial T}{\partial r} = h_f (T_f - T), \\ -D_m \frac{\partial C}{\partial r} = k_m (C_f - C) \text{ at } r = R, \\ w \rightarrow 0, \quad T \rightarrow T_\infty, \quad C \rightarrow C_\infty \text{ as } r \rightarrow \infty. \end{aligned} \quad (9.5)$$

in which (u, w) are the velocity components in (r, z) directions, λ_1 the relaxation time, C the nanoparticles volume fraction, $\tau = \frac{(\rho C_p)_p}{(\rho C_p)_f}$ the heat capacity ratio, $\alpha_f = \frac{k_f}{(\rho C_p)_f}$ the thermal diffusivity, g the gravitational acceleration, ϵ_1 and ϵ_2 the linear and nonlinear thermal expansion coefficients, ϵ_3 and ϵ_4 the linear and nonlinear concentration expansion coefficients, K_c the reaction rate of solute, D_T thermophoresis diffusion coefficient and D_B the Brownian diffusion coefficient.

Considering

$$u = -\frac{R}{r} \sqrt{\frac{\nu_f w_0}{L}} \tilde{f}(\xi), \quad w = \frac{z w_0}{L} \tilde{f}'(\xi), \quad \tilde{\theta}(\xi) = \frac{T - T_\infty}{T_f - T_\infty},$$

$$\tilde{\phi}(\xi) = \frac{C - \check{C}_\infty}{C_f - C_\infty}, \quad \xi = \frac{r^2 - R^2}{2R} \sqrt{\frac{w_0}{L \nu_f}}, \quad (9.6)$$

we have

$$\begin{aligned} \left((1 + 2\gamma\xi) \tilde{f}''' + 2\gamma\tilde{f}'' \right) - \beta \left[2\tilde{f}\tilde{f}'\tilde{f}'' - \tilde{f}^2\tilde{f}''' - \frac{\gamma}{(1 + 2\gamma\xi)} \tilde{f}^2\tilde{f}'' \right] \\ - M \left(\tilde{f}' - \beta f f'' \right) + N_1 \tilde{\theta} (1 + \varsigma_T \theta) \\ + N_1 N_2 \tilde{j} (1 + \varsigma_C j) + \tilde{f}\tilde{f}'' - \tilde{f}'^2 = 0, \end{aligned} \quad (9.7)$$

$$\begin{aligned} \left(\frac{1}{\text{Pr}} \right) (1 + R_D) \left((1 + 2\gamma\xi) \tilde{\theta}'' + 2\gamma\tilde{\theta}' \right) + N_B (1 + 2\gamma\xi) \tilde{\theta}'\tilde{j}' \\ + N_T (1 + 2\gamma\xi) \tilde{\theta}'^2 + \tilde{f}\tilde{\theta}' + M E_C \tilde{f}''^2 = 0, \end{aligned} \quad (9.8)$$

$$\left((1 + 2\gamma\xi) \tilde{j}'' + 2\gamma\tilde{j}' \right) + \frac{N_T}{N_B} \left((1 + 2\gamma\xi) \tilde{\theta}'' + 2\gamma\tilde{\theta}' \right) - S_C \tilde{f}\tilde{j}' - L_C S_C \tilde{j} = 0, \quad (9.9)$$

$$\begin{aligned} \tilde{f}(0) = 0, \quad \tilde{f}'(0) = 1, \quad \tilde{f}'(\infty) \rightarrow 0, \quad \tilde{\theta}'(0) = -B_T(1 - \tilde{\theta}(0)), \quad \tilde{\theta}(\infty) \rightarrow 0, \\ \tilde{j}'(0) = -B_C(1 - \tilde{j}(0)), \quad \tilde{j}(\infty) \rightarrow 0, \end{aligned} \quad (9.10)$$

Here incompressibility condition (9.1) is trivially verified, $M = \frac{L\sigma_f B_0^{*2}}{\rho_f w_0}$ the magnetic parameter, $\beta = \frac{w_0 \lambda_1}{L}$ the Deborah number, $N_1 = \frac{z^3 g \epsilon_1 (T_w - T_\infty)}{\text{Re}^2 \nu_f^2}$ the mixed convection parameter, $N_2 = \frac{z^3 g \epsilon_2 (C_w - C_\infty)}{\text{Re}^2 \nu_f^2}$ the ratio of concentration to thermal buoyancy forces $\varsigma_T = \frac{A_2 (T_f - T_\infty)}{A_1}$ and $\varsigma_C = \frac{A_4 (C_f - C_\infty)}{A_3}$ the non-linear convection parameter due to temperature and concentration, $Gr = \frac{g A_1 (T_f - T_\infty) z^3}{\nu_f^2}$ the Grashof number for temperature, $Gr^* = \frac{g A_3 (C_f - C_\infty) z^3}{\nu_f^2}$, the Grashof number for concentration, $\text{Pr} = \frac{(\mu C_p)_f}{k_f}$ the Prandtl number, $E_C = \frac{w_w^2}{(C_p)_f (T_f - T_\infty)}$ the Eckert number, $R_D = \frac{16\sigma^* T_\infty^3}{3k^* k_f}$ the radiation parameter, $N_B = \frac{\tau (C_f - C_\infty) D_B}{\nu_f}$ the Brownian motion parameter, $N_T = \frac{\tau (T_f - T_\infty) D_T}{T_\infty \nu_f}$ the thermophoresis parameter, $L_C = \frac{L K_c}{\dot{w}_0}$ the reaction-rate parameter, $B_T = \frac{h_f}{k_f \sqrt{\frac{w_0}{\nu_f L}}}$ the thermal Biot number, $B_C = \frac{k_m}{D_m \sqrt{\frac{w_0}{\nu_f L}}}$ the concentration Biot number, $Sc = \frac{\nu_f}{D_B}$ the Schmidt number and $\gamma = \sqrt{\frac{L \nu_f}{w_0 R^2}}$ the curvature parameter.

9.1.1 Local Nusselt number

It is the ratio of heat transferred through convection (fluid motion) to the heat transferred through conduction (if the fluid is stagnant). Mathematically we have

$$\tilde{N}_u = \frac{zq_z}{k_f(T_f - T_\infty)}, \quad (9.11)$$

with

$$q_w = - \left[k_f \left(1 + \frac{16\sigma^* T_\infty^3}{3k_f k^*} \right) \left(\frac{\partial T}{\partial r} \right) \right]_{r=R}. \quad (9.12)$$

Now

$$\text{Re}^{-0.5} \tilde{N}_u = - (1 + R_D) \tilde{\theta}'(0), \quad (9.13)$$

9.1.2 Sherwood number

It portrays the ratio of convective mass transfer to diffusive mass transport rate i.e.

$$\tilde{S}_h = \frac{j_w}{D_B(C_f - C_\infty)}, \quad (9.14)$$

$$j_w = -D_B \left(\frac{\partial C}{\partial r} \right)_{r=R}. \quad (9.15)$$

Dimensionless version of \tilde{S}_h is

$$\text{Re}^{-0.5} \tilde{S}_h = -\tilde{j}'(0), \quad (9.16)$$

in which $\text{Re} = \frac{w_0 z^2}{\nu}$ denotes the local Reynolds number.

9.2 Solution Methodology

For solutions we choose

$$\tilde{f}_0(\xi) = 1 - \exp(-\xi), \quad \tilde{\theta}_0(\xi) = \frac{B_T}{1 + B_T} \exp(-\xi), \quad \tilde{j}_0(\xi) = \frac{B_C}{1 + B_C} \exp(-\xi), \quad (9.17)$$

with

$$\mathcal{L}_1(\tilde{f}) = \tilde{f}''' - \tilde{f}', \quad \mathcal{L}_2(\tilde{\theta}) = \tilde{\theta}'' - \tilde{\theta}, \quad \mathcal{L}_3(\tilde{j}) = \tilde{j}'' - \tilde{j}, \quad (9.18)$$

and

$$\begin{aligned}
 \mathcal{L}_{\bar{f}} [C_1 + C_2 \exp(-\xi) + C_3 \exp(\xi)] &= 0, \\
 \mathcal{L}_{\bar{\theta}} [C_4 \exp(\xi) + C_5 \exp(-\xi)] &= 0, \\
 \mathcal{L}_{\bar{j}} [C_6 \exp(\xi) + C_7 \exp(-\xi)] &= 0,
 \end{aligned} \tag{9.19}$$

9.3 Convergence analysis

It is quite obvious that convergence controlling parameters $\bar{h}_{\bar{f}}$, $\bar{h}_{\bar{\theta}}$ and $\bar{h}_{\bar{j}}$ are involved in the developed HAM solutions. For determination of suitable values of these parameter controlling convergence of series solutions, the Figure (9.1) is sketched. The valid regions of $\bar{h}_{\bar{f}}$, $\bar{h}_{\bar{\theta}}$ and $\bar{h}_{\bar{j}}$ are found $-0.9 \leq \bar{h}_{\bar{f}} \leq -0.3$, $-7.9 \leq \bar{h}_{\bar{\theta}} \leq -0.41$ and $-1.1 \leq \bar{h}_{\bar{j}} \leq -0.5$. When $\bar{h}_{\bar{f}} = -0.7$, $\bar{h}_{\bar{\theta}} = -0.5$ and $\bar{h}_{\bar{j}} = -0.7$. The convergence of series solutions upto four decimal places for $\tilde{f}''(0)$, $\tilde{\theta}'(0)$ and $\tilde{j}'(0)$ is found in Table (9.1). It is clear that $\tilde{f}''(0)$ and $\tilde{\theta}'(0)$ converge at 13th order of approximations while for $\tilde{j}'(0)$ the 15th order of approximations is required.

Residual errors are sketched in Figures (9.2)-(9.4). The residual errors are calculated for velocity, energy and concentration equations through the expressions:

$$\begin{aligned}
 \Delta_m^{\bar{f}} &= \int_0^1 \left[\mathcal{R}_m^{\bar{f}}(\xi, \bar{h}_{\bar{f}}) \right]^2 d\xi, \\
 \Delta_m^{\bar{\theta}} &= \int_0^1 \left[\mathcal{R}_m^{\bar{\theta}}(\xi, \bar{h}_{\bar{\theta}}) \right]^2 d\xi, \\
 \Delta_m^{\bar{j}} &= \int_0^1 \left[\mathcal{R}_m^{\bar{j}}(\xi, \bar{h}_{\bar{j}}) \right]^2 d\xi.
 \end{aligned} \tag{9.20}$$

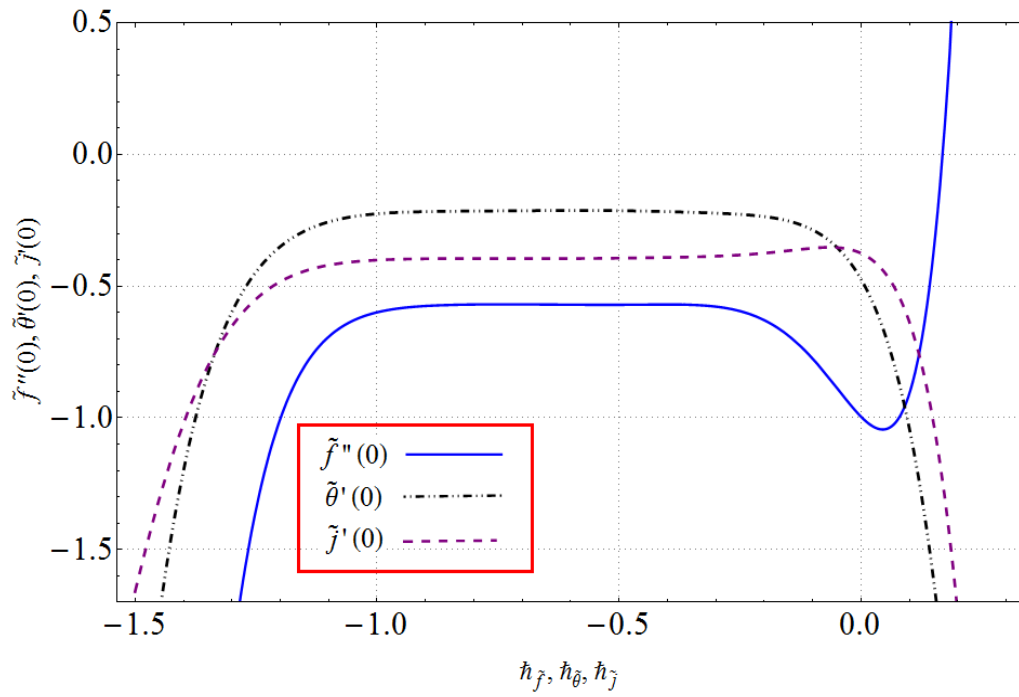


Figure 9.1: h -curves for velocity, temperature and concentration fields.

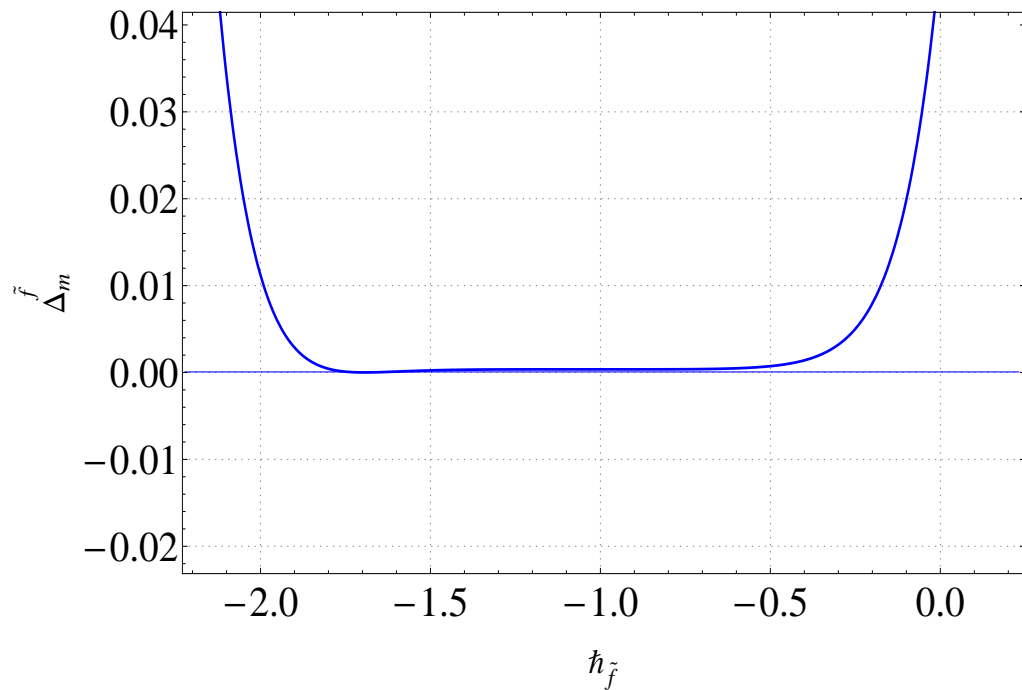


Figure 9.2: $h_{\tilde{f}}$ -curve for the residual error $\Delta_m^{\tilde{f}}$.

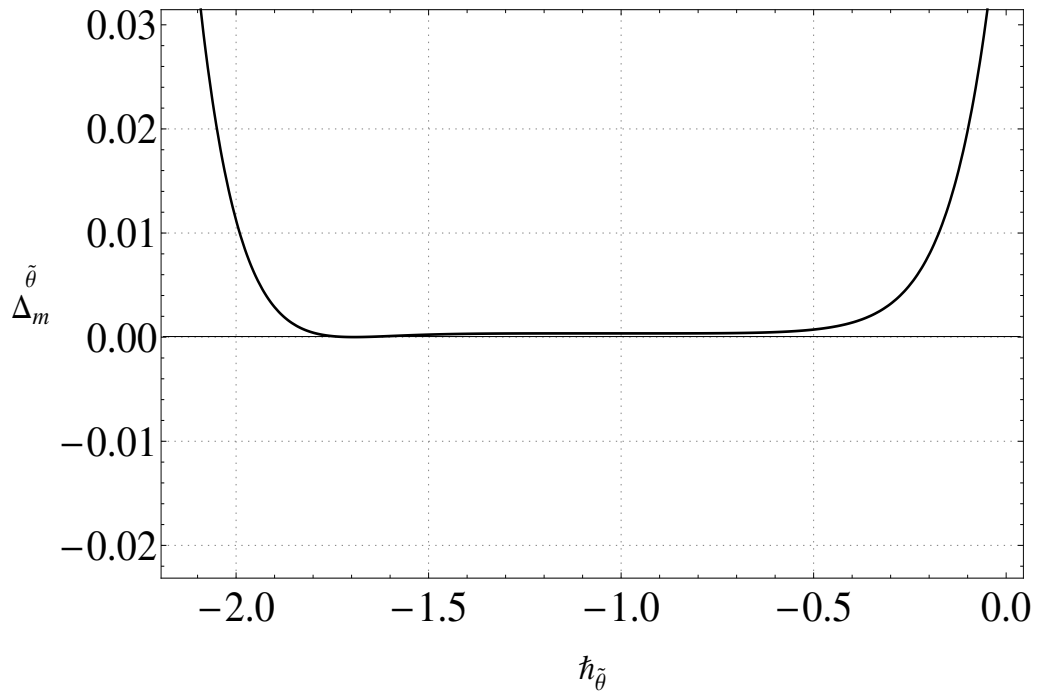


Figure 9.3: $h_{\tilde{\theta}}$ -curve for the residual error $\Delta_m^{\tilde{\theta}}$.

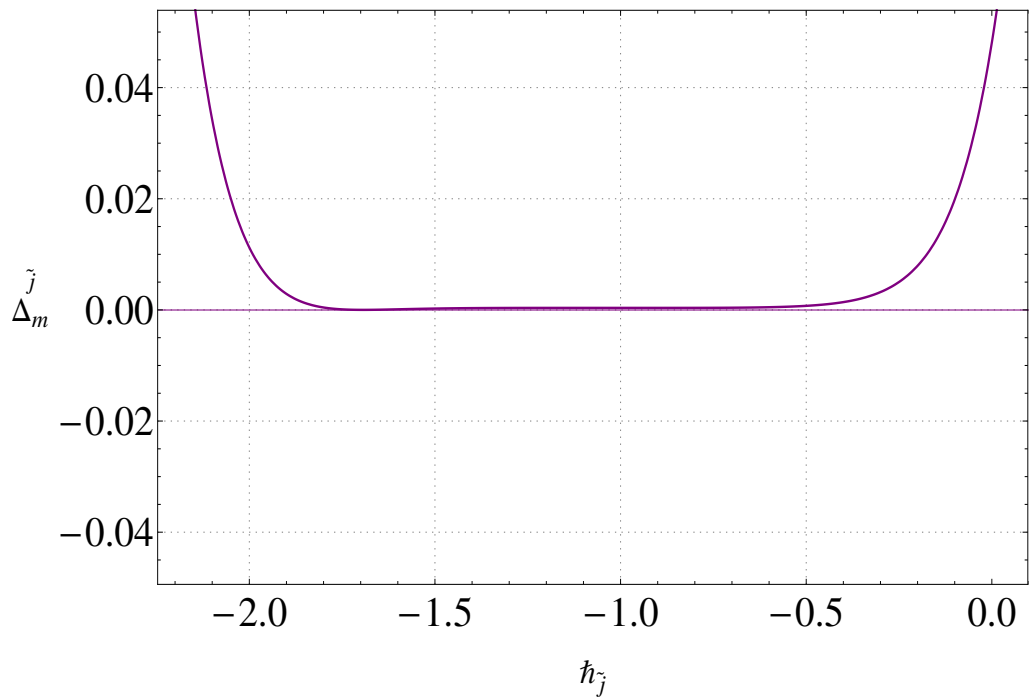


Figure 9.4: $h_{\tilde{j}}$ -curve for the residual error $\Delta_m^{\tilde{j}}$.

Table 9.1: HAM solutions convergence when $\gamma = 0.1, \beta = 0.2, Ec = 0.4, \varsigma_T = M = N_B = N_T = 0.5, B_C = \varsigma_C = 0.6, R_D = 0.7, N_1 = N_2 = 0.8, B_T = 0.9, L_C = Sc = 1.1$ and $Pr = 1.3$.

Order of approximation	$-\tilde{f}''(0)$	$-\tilde{\theta}'(0)$	$-\tilde{j}'(0)$
1	0.9676	0.3534	0.3163
3	0.7236	0.2744	0.3602
7	0.6738	0.2403	0.3819
13	0.6654	0.2353	0.3847
15	0.6654	0.2353	0.3848
20	0.6654	0.2353	0.3848
25	0.6654	0.2353	0.3848
30	0.6654	0.2353	0.3848
35	0.6654	0.2353	0.3848

9.4 Interpretation

This portion presents the dimensionless parameters for 2D Maxwell fluid flow past a stretching cylinder. Figures (9.5)-(9.15) are sketched for velocity, temperature and concentration.

9.4.1 Velocity

Figure (9.5) interprets the impact of Deborah number ($\beta = 0.2, 0.3, 0.4, 0.5$) on $\tilde{f}'(\xi)$. Here velocity decays via higher Deborah number (β). Physically fluid relaxation time enlarges with increasing values of Deborah number (β). Hence velocity decays. Figure (9.6) portrays the characteristics of curvature parameter ($\gamma = 0.1, 0.2, 0.4, 0.5$) on $\tilde{f}'(\xi)$. Clearly $\tilde{f}'(\xi)$ increments for (γ). Radius of cylinder reduces due to an increment in curvature parameter. Hence less resistance is offered towards fluid motion and fluid velocity increases. Behavior of magnetic parameter ($M=0.0, 0.2, 0.4, 0.6$) for velocity $f'(\xi)$ is portrayed in Figure (9.7). Velocity retards for higher (M). As magnetic parameter has association with resistive Lorentz force. Lorentz force enhances through higher values of (M) which resists the fluid velocity. Thus velocity decays.

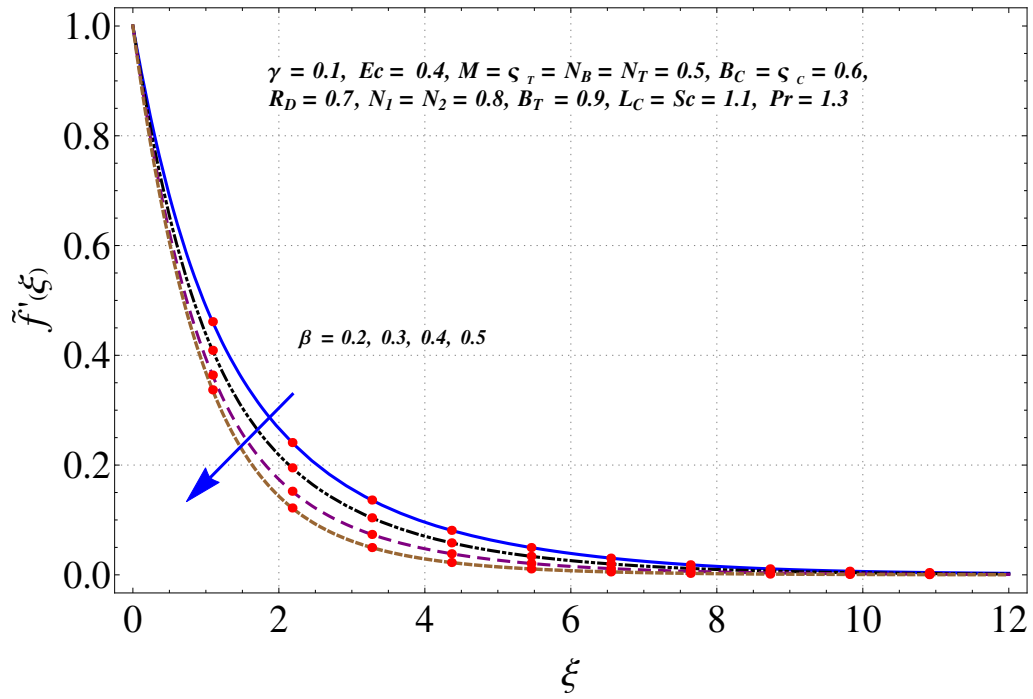


Figure 9.5: Variation of β on $\tilde{f}'(\xi)$.

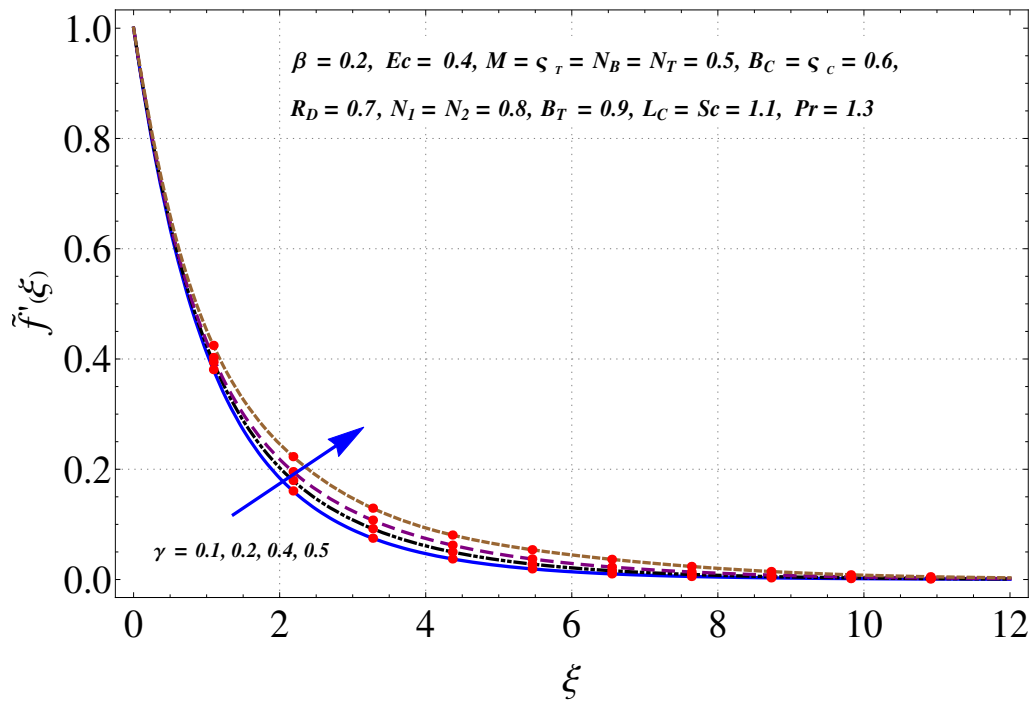
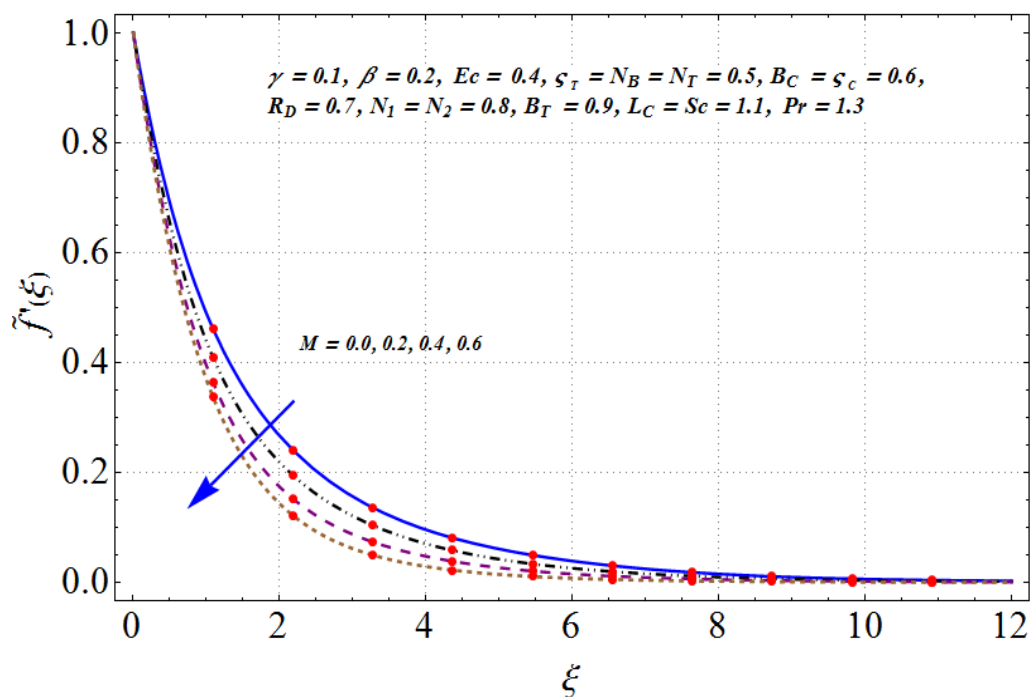


Figure 9.6: Variation of γ on $\tilde{f}'(\xi)$.

Figure 9.7: Variation of M on $\tilde{f}'(\xi)$.

9.4.2 Temperature

Figure (9.8) elaborates the characteristics of curvature parameter ($\gamma = 0.1, 0.2, 0.4, 0.5$) on $\tilde{\theta}(\xi)$. Temperature enhances for larger (γ). Behavior of Eckert number ($Ec = 0.1, 0.2, 0.4, 0.5$) on temperature $\tilde{\theta}(\xi)$ is captured in Figure (9.9). Temperature $\tilde{\theta}(\xi)$ rises via higher (Ec). Physically the mechanical energy is converted into thermal energy for internal friction of molecules. That is why thermal field rises. Figure (9.10) is plotted to show the combined effects of Brownian motion ($N_B = 0.2, 0.4, 0.5, 0.6$) and thermophoresis parameter ($N_T = 0.2, 0.4, 0.5, 0.6$) on temperature. Here temperature of nanofluid is more for thermophoresis and Brownian motion parameter (N_B and N_T). Due to presence of thermophoresis phenomenon the temperature of fluid increases in which heated particles are pulled away from hot region to cold surface. It is noted that higher Brownian motion parameter N_B rises the temperature of fluid. It is physically expected because Brownian motion parameter N_B describes the movement of nanoparticles in fluid. Figure (9.11) indicates temperature variation for ($Pr = 1.1, 1.2, 1.3, 1.4$). There is a reduction

in temperature for higher (Pr). In fact thermal conductivity reduces for higher (Pr) and consequently the temperature decays. Figure (9.12) graphed to indicate the behavior of thermal Biot number on temperature. Positive values of ($B_T=0.1,0.3,0.5,0.9$) offer more heat transfer resistance inside a fluid when compared with cylinder and thus temperature enhances.

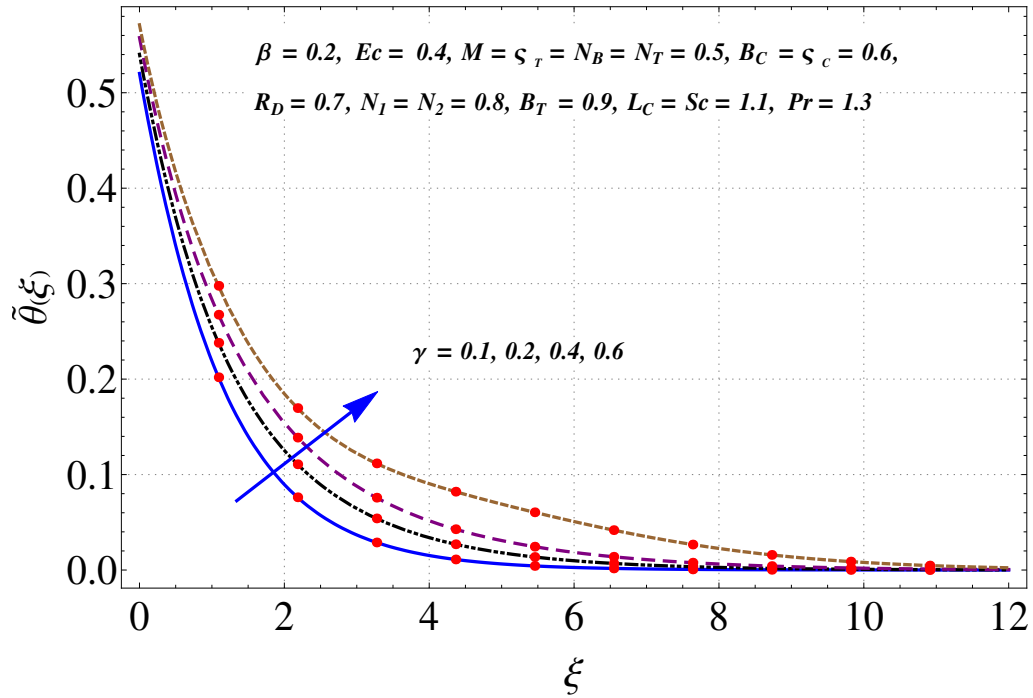


Figure 9.8: Variation of γ on $\tilde{\theta}(\xi)$.

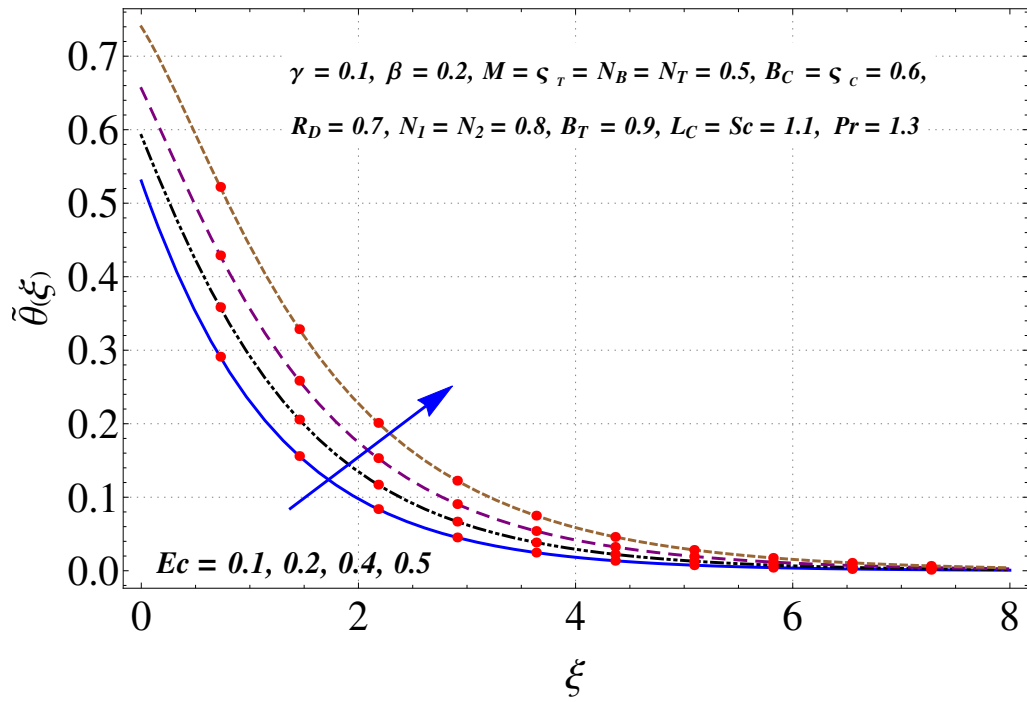


Figure 9.9: Variation of Ec on $\tilde{\theta}(\xi)$.

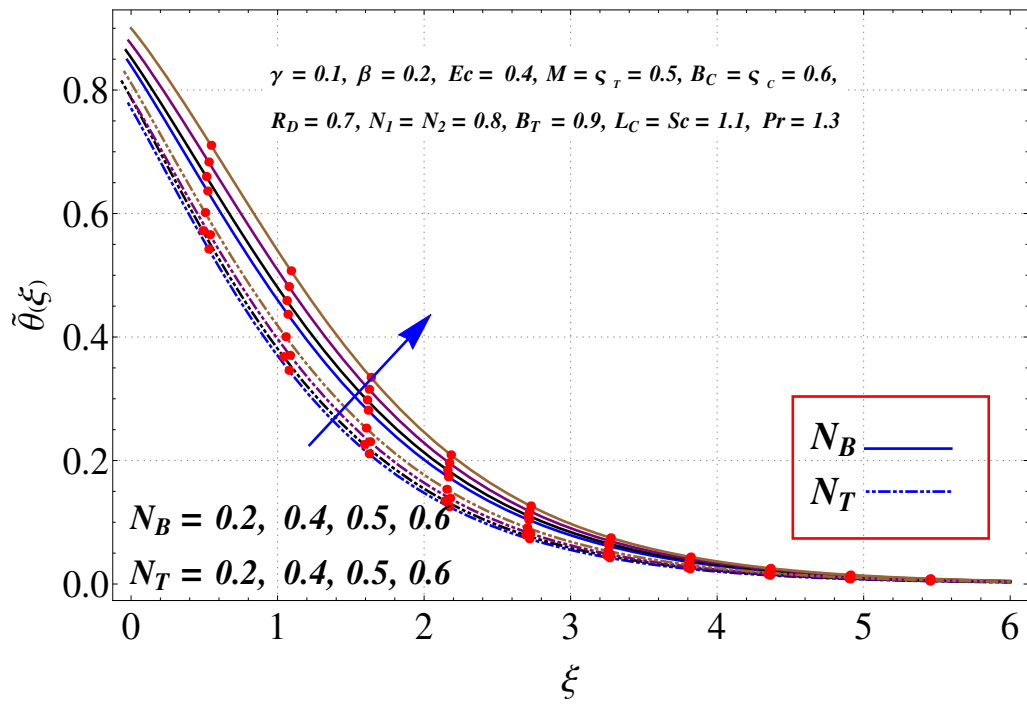


Figure 9.10: Variations of N_B and N_T on $\tilde{\theta}(\xi)$.

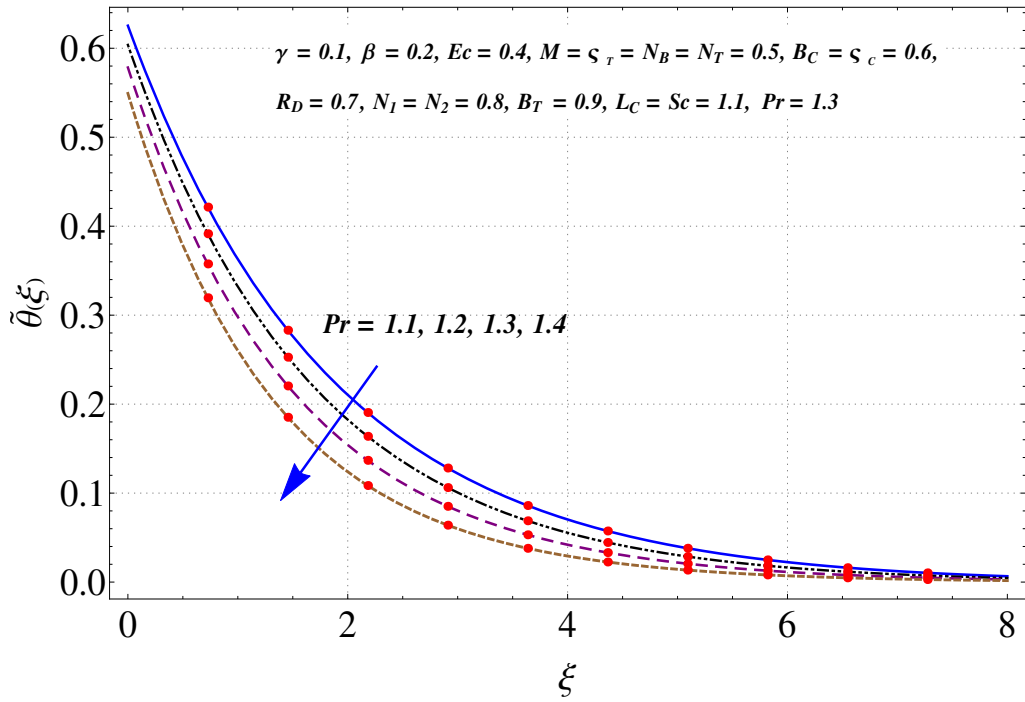


Figure 9.11: Variation of Pr on $\tilde{\theta}(\xi)$.

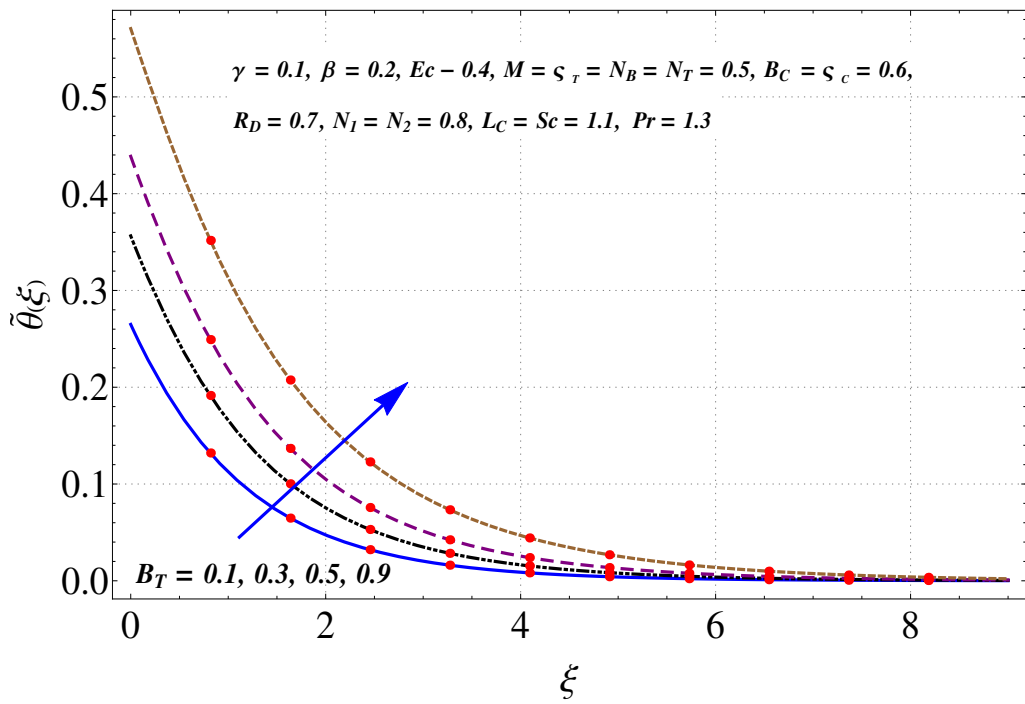


Figure 9.12: Variation of B_T on $\tilde{\theta}(\xi)$.

9.4.3 Concentration

Figure (9.13) presents impact of curvature parameter ($\gamma = 0.1, 0.2, 0.4, 0.5$) for concentration $\tilde{j}(\xi)$. There is an enhancement in concentration $\tilde{j}(\xi)$ for larger (γ). Brownian motion parameter ($N_B = 0.2, 0.4, 0.6, 0.8$) and thermophoresis parameter ($N_T = 0.2, 0.4, 0.6, 0.8$) have opposite effect on concentration $\tilde{j}(\xi)$ (see Figure (9.14)). Action of destructive chemical reaction ($L_C > 0$) and generative chemical reaction ($L_C < 0$) on concentration $\tilde{j}(\xi)$ is graphed in Figure (9.15). It is noted that concentration $\tilde{j}(\xi)$ enhances for generative chemical reaction parameter ($L_C < 0$) while reverse response is noticed for destructive chemical reaction parameter ($L_C > 0$). During destructive chemical reaction ($L_C > 0$) rate of species decreases and concentration decays.

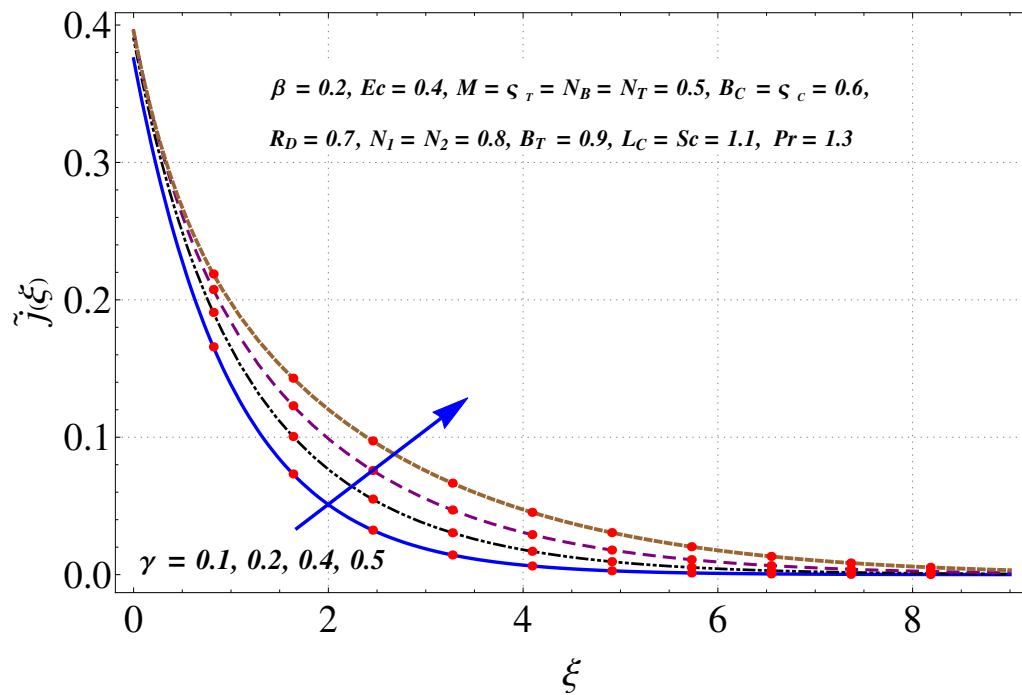


Figure 9.13: Variation of γ on $\tilde{j}(\xi)$.

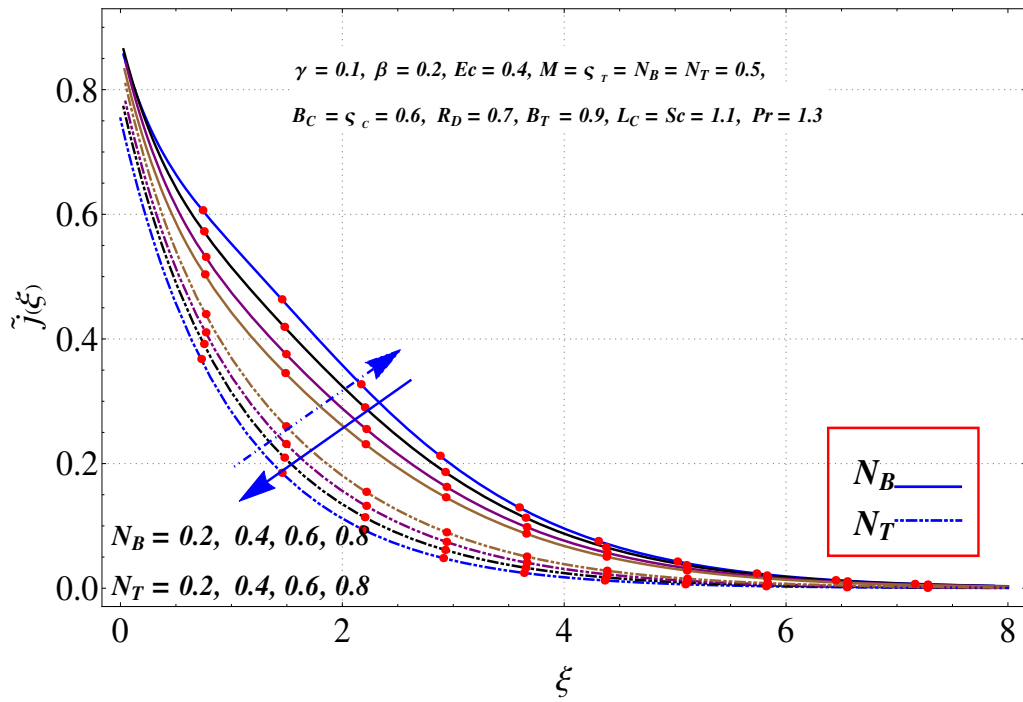


Figure 9.14: Variations of N_B and N_T on $\tilde{j}(\xi)$.

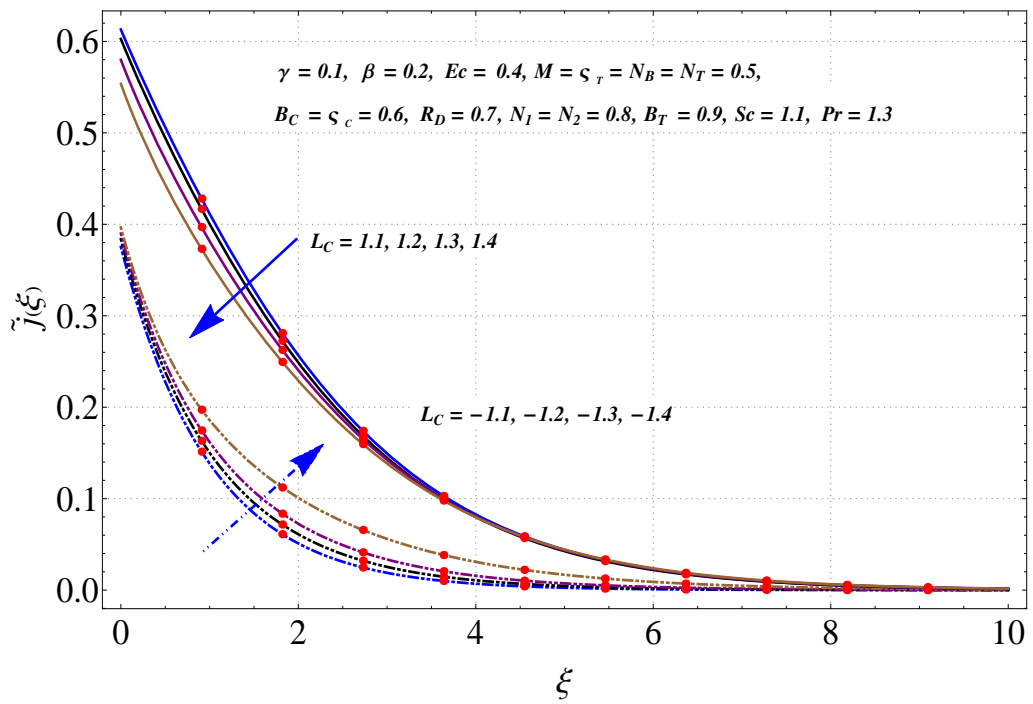


Figure 9.15: Variation of $(L_C < 0)$ and $(L_C > 0)$ on $\tilde{j}(\xi)$.

9.4.4 Heat and mass transfer rates

Figures (9.16)-(9.19) show the variations of heat and mass transfer rates for different physical variables. Behavior of thermal Biot number on local Nusselt number $(\text{Re}_z)^{-0.5} \tilde{N}_u$ is plotted in Figure (9.16). Clearly heat transfer rate for thermal Biot number is increased. Figure (9.17) illustrates the variation of curvature parameter (γ) on Nusselt number $(\text{Re}_z)^{-0.5} \tilde{N}_u$. It is noted that local Nusselt number is reduces via (γ). Figure (9.18) reflects less magnitude of the mass transfer rate for chemical reaction parameter L_C . Figure (9.19) depicts decreasing behavior of Sherwood number when γ enhances.

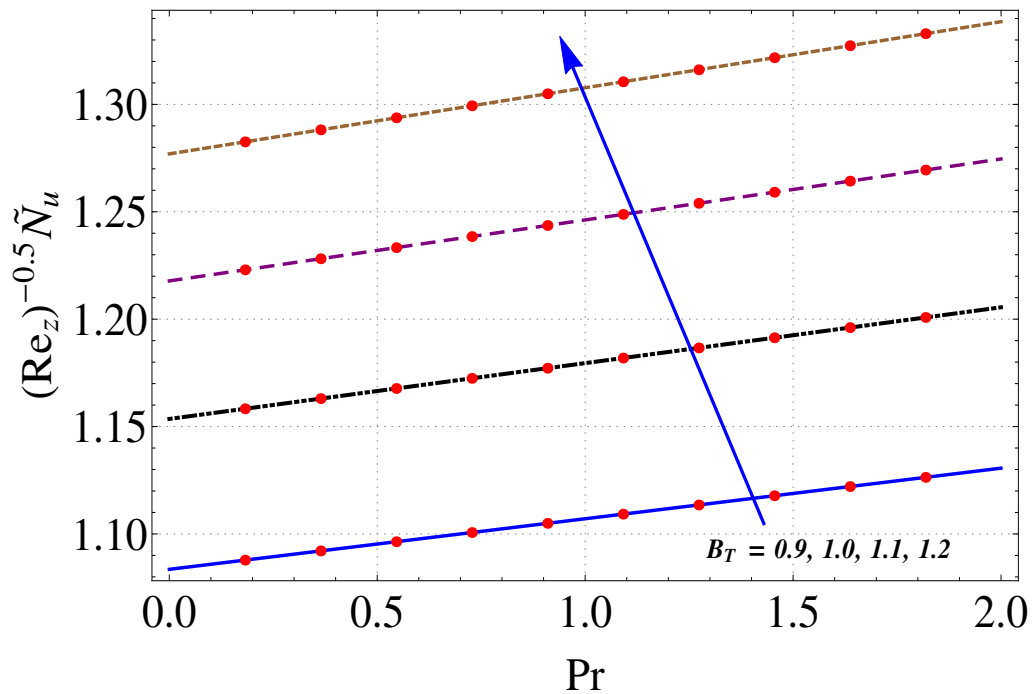


Figure 9.16: Variation of B_T on $(\text{Re}_z)^{-0.5} \tilde{N}_u$.

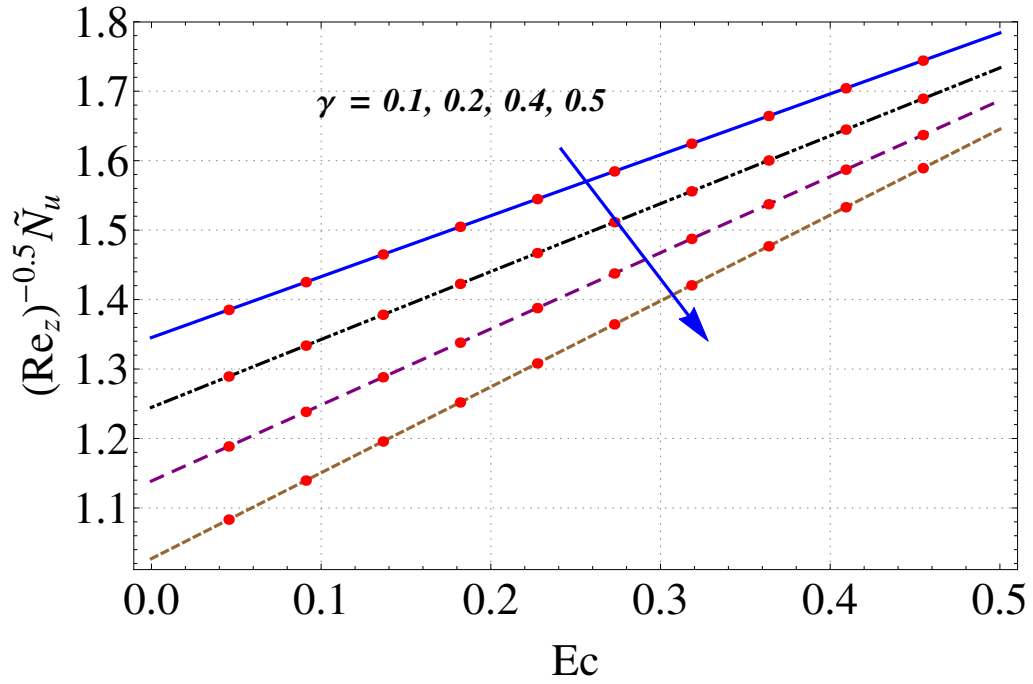


Figure 9.17: Variation of γ on $(\text{Re}_z)^{-0.5} \tilde{N}_u$.

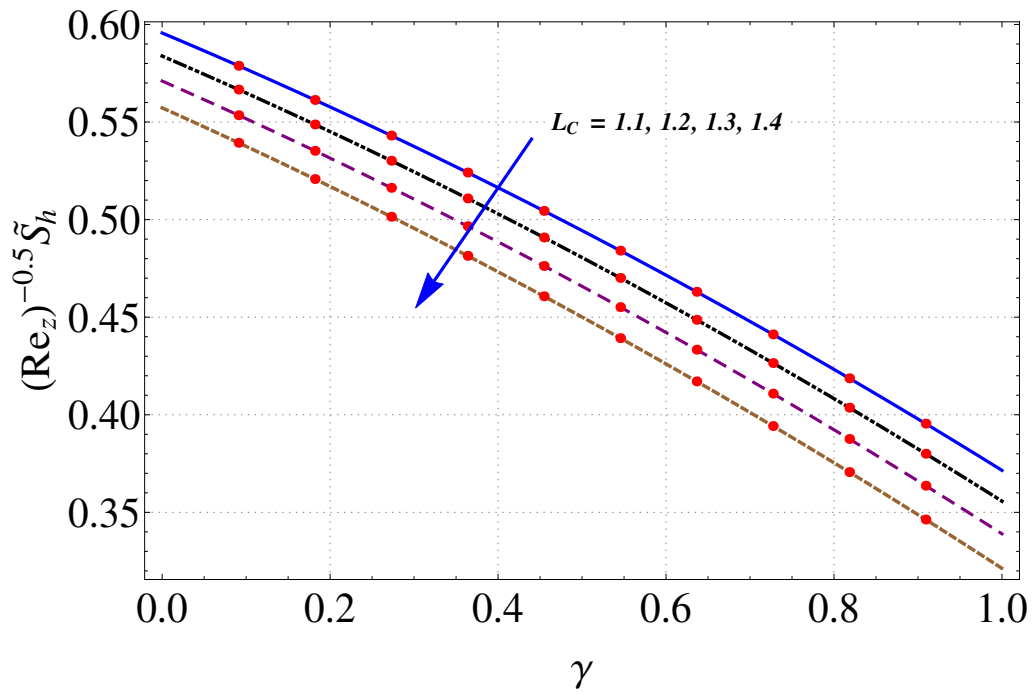


Figure 9.18: Variation of L_C on $(\text{Re}_z)^{-0.5} \tilde{S}_h$.

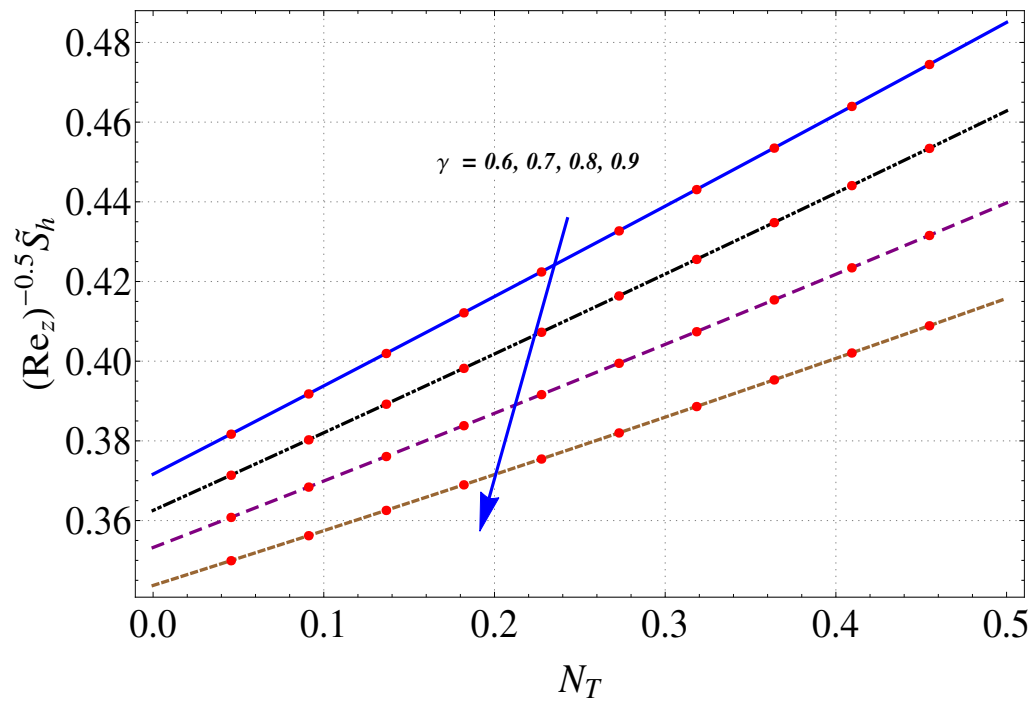


Figure 9.19: Variation of γ on $(\text{Re}_z)^{-0.5} \tilde{S}_h$.

9.5 Major findings

We have following observations.

- Curvature parameter has tendency to rise fluid velocity, temperature and concentration.
- Brownian motion for temperature and concentration has reverse response.
- Concentration is reduced for destructive chemical reaction whereas it enhances for generative chemical reaction.
- Influence of thermal Biot number on Nusselt number is opposite when compared with curvature parameter.
- Sherwood number is reduced for the curvature and chemical reaction parameters.

Chapter 10

Chemically reactive flow of Maxwell nanofluid due to stretching cylinder with activation energy

This chapter discussed the radiative flow of Maxwell nanofluid over a stretching cylinder. Modeling of heat transfer is made with thermal radiation, convective conditions and heat generation/absorption effects. A modified Arrhenius function is analyzed in order to investigate activation energy. Mass transfer is examined by considering the activation energy along with binary chemical reaction, thermophoresis and Brownian diffusion. Mass, energy, momentum and concentration laws give rise to nonlinear differential systems. Homotopic algorithm is adopted to derived the convergent series solutions. Five quantities namely the velocity, temperature, concentration and local Nusselt and Sherwood numbers are discussed. Clearly concentration of nanoparticles enhances for activation energy while it reduces for chemical reaction parameter.

10.1 Modeling

Here two-dimensional flow of Maxwell nanomaterial past a stretching cylinder is modeled. Cylinder has constant concentration C_f of nanoparticles whereas (T_∞, C_∞) are fluid's ambient concentration and temperature respectively when $z \rightarrow \infty$. The Brownian diffusion and thermophoresis properties are accounted. Let the cylinder with velocity $w_w = w_0 \left(\frac{z}{L}\right)$ is stretched in axial direction. Fluid is electrically conducting. Moreover influence of ac-

tivation energy with binary chemical reaction is stated to debate mass transfer rate. A phenomenon of thermal radiation with heat generation/absorption effects is reviewed. Viscous dissipation and Joule heating effects are taken absent. The governing problems under the aforementioned assumptions become:

$$\frac{\partial u}{\partial r} + \frac{u}{r} + \frac{\partial w}{\partial z} = 0, \quad (10.1)$$

$$\begin{aligned} u \frac{\partial w}{\partial r} + w \frac{\partial w}{\partial z} + \lambda_1 \left(w^2 \frac{\partial^2 w}{\partial z^2} + u^2 \frac{\partial^2 w}{\partial r^2} + 2uw \frac{\partial^2 w}{\partial r \partial z} \right) \\ = \nu_f \left(\frac{\partial^2 w}{\partial r^2} + \frac{1}{r} \frac{\partial w}{\partial r} \right) - \frac{\sigma_f B_0^{*2}}{\rho_f} \left(w - \lambda_1 u \frac{\partial w}{\partial r} \right), \end{aligned} \quad (10.2)$$

$$\begin{aligned} \left(u \frac{\partial T}{\partial r} + w \frac{\partial T}{\partial z} \right) = \alpha_f \left(\frac{\partial^2 T}{\partial r^2} + \frac{1}{r} \frac{\partial T}{\partial r} \right) + \tau \left(D_B \frac{\partial C}{\partial r} \frac{\partial T}{\partial r} + \frac{D_T}{T_\infty} \left(\frac{\partial T}{\partial r} \right)^2 \right) \\ + \frac{16\sigma^* T_\infty^3}{3k^*(\rho C_p)_f} \left(\frac{\partial^2 T}{\partial r^2} + \frac{1}{r} \frac{\partial T}{\partial r} \right). \end{aligned} \quad (10.3)$$

$$\begin{aligned} \left(u \frac{\partial C}{\partial r} + w \frac{\partial C}{\partial z} \right) = D_B \left(\frac{\partial^2 C}{\partial r^2} + \frac{1}{r} \frac{\partial C}{\partial r} \right) + \frac{D_T}{T_\infty} \left(\frac{\partial^2 T}{\partial r^2} + \frac{1}{r} \frac{\partial T}{\partial r} \right) \\ - K_c^2 (C - C_\infty) \left[\frac{T}{T_\infty} \right]^n \exp \left[\frac{-E_a}{k_1 T} \right], \end{aligned} \quad (10.4)$$

$$\begin{aligned} u = 0, \quad v = 0, \quad w = w_w, \quad -k_f \frac{\partial T}{\partial r} = h_f (T_f - T), \quad C = C_f \text{ at } r = R, \\ w \rightarrow 0, \quad T \rightarrow T_\infty, \quad C \rightarrow C_\infty \text{ as } r \rightarrow \infty, \end{aligned} \quad (10.5)$$

where (u, w) are velocity components in (r, z) directions. The term $\left[\frac{T}{T_\infty} \right]^n \exp \left[\frac{E_a}{k_1 T} \right]$ is referred as the modified Arrhenius function. Here $k_1 = 8.61 \times 10^{-5} \text{ eV/K}$ represents the Boltzmann constant, n is the dimensionless constant or rate constant having the range $-1 < n < 1$ and E_a the activation energy.

Considering

$$\begin{aligned} u = -\frac{R}{r} \sqrt{\frac{\nu_f w_0}{L}} \tilde{f}(\xi), \quad w = \frac{z w_0}{L} \tilde{f}'(\xi), \quad \tilde{\theta}(\xi) = \frac{T - T_\infty}{T_f - T_\infty}, \\ \tilde{j}(\xi) = \frac{C - C_\infty}{C_f - C_\infty}, \quad \xi = \frac{r^2 - R^2}{2R} \sqrt{\frac{w_0}{L \nu_f}} \end{aligned} \quad (10.6)$$

we have

$$\begin{aligned} & \left[(1 + 2\gamma\xi) \tilde{f}''' + 2\gamma\tilde{f}'' \right] - \beta \left[2\tilde{f}\tilde{f}'\tilde{f}'' - \tilde{f}^2\tilde{f}''' - \frac{\gamma}{(1 + 2\gamma\xi)} \tilde{f}^2\tilde{f}'' \right] \\ & - M \left(\tilde{f}' - \beta f f'' \right) + N_1\tilde{\theta} + N_2\tilde{j} + \tilde{f}\tilde{f}'' - \tilde{f}'^2 = 0, \end{aligned} \quad (10.7)$$

$$\begin{aligned} & \left(\frac{1}{\text{Pr}} \right) (1 + R_D) \left((1 + 2\gamma\xi) \tilde{\theta}'' + 2\gamma\tilde{\theta}' \right) + N_B (1 + 2\gamma\xi) \tilde{\theta}'\tilde{j}' \\ & + N_T (1 + 2\gamma\xi) \tilde{\theta}'^2 + \tilde{f}\tilde{\theta}' + Q\tilde{\theta} = 0, \end{aligned} \quad (10.8)$$

$$\begin{aligned} & ((1 + 2\gamma\xi) \tilde{j}'' + 2\gamma\tilde{j}') + \frac{N_T}{N_B} \left((1 + 2\gamma\xi) \tilde{\theta}'' + 2\gamma\tilde{\theta}' \right) - Sc\tilde{f}\tilde{j}' \\ & - L_C Sc [1 + \alpha_T\theta]^n \exp \left(\frac{-E^*}{1 + \alpha_T\theta} \right) \tilde{j} = 0, \end{aligned} \quad (10.9)$$

$$\begin{aligned} & \tilde{f}(0) = 0, \quad \tilde{f}'(0) = 1, \quad \tilde{f}'(\infty) \rightarrow 0, \quad \tilde{\theta}'(0) = -B_T[1 - \tilde{\theta}(0)], \\ & \tilde{\theta}(\infty) \rightarrow 0, \quad \tilde{j}(0) = 1, \quad \tilde{j}(\infty) \rightarrow 0. \end{aligned} \quad (10.10)$$

in which $M = \frac{L\sigma_f B_0^{*2}}{\rho_f w_0}$ depicts magnetic parameter, $\beta = \frac{\lambda_1 w_0}{L}$ the Deborah number, $R_D = \frac{16\sigma^* T_\infty^3}{3k^* k_f}$ the radiation parameter, $\text{Pr} = \frac{(\mu C_p)_f}{k_f}$ the Prandtl number, $N_B = \frac{\tau(C_w - C_\infty) D_B}{\nu_f}$ the Brownian motion parameter, $N_T = \frac{\tau(T_f - T_\infty) D_T}{T_\infty \nu_f}$ the thermophoresis parameter, $Q = \frac{Q_0 L}{w_0 (\rho C_p)_f}$ the heat generation/absorption parameter, $\alpha_T = \frac{T_f - T_\infty}{T_\infty}$ the temperature difference parameter, $L_C = \frac{LK_c^2}{w_0}$ the reaction-rate parameter, $E^* = \frac{E_a}{k_1 T_\infty}$ the non-dimensional activation energy, $Sc = \frac{\nu_f}{D_B}$ the Schmidt number and $\gamma = \sqrt{\frac{L\nu_f}{w_0 R^2}}$ the curvature parameter.

10.1.1 Quantities of interest

Mathematically

$$\tilde{N}_u = \frac{z q_w}{k_f (T_f - T_\infty)}, \quad (10.11)$$

with

$$q_w = - \left[k_f \left(1 + \frac{16\sigma^* T_\infty^3}{3k_f k^*} \right) \left(\frac{\partial T}{\partial r} \right) \right]_{r=R}. \quad (10.12)$$

Now

$$(\text{Re}_z)^{-0.5} \tilde{N}_u = - (1 + R_D) \tilde{\theta}'(0), \quad (10.13)$$

Sherwood number

$$\tilde{S}_h = \frac{j_m}{D_B (\check{C}_f - \check{C}_\infty)}, \quad (10.14)$$

$$j_m = -D_B \left(\frac{\partial \check{C}}{\partial r} \right)_{r=R}. \quad (10.15)$$

Dimensionless version of \tilde{S}_h is

$$(\text{Re}_z)^{-0.5} \tilde{S}_h = -\tilde{j}'(0), \quad (10.16)$$

in which $\text{Re} = \frac{w_0 z^2}{L\nu_f}$ denotes the local Reynolds number.

10.2 Homotopy procedure

For solutions we choose

$$\tilde{f}_0(\xi) = 1 - \exp(-\xi), \quad \tilde{\theta}_0(\xi) = \frac{B_T}{1 + B_T} \exp(-\xi), \quad \tilde{j}_0(\xi) = \exp(-\xi), \quad (10.17)$$

with

$$\mathcal{L}_1(\tilde{f}) = \tilde{f}''' - \tilde{f}', \quad \mathcal{L}_2(\tilde{\theta}) = \tilde{\theta}'' - \tilde{\theta}, \quad \mathcal{L}_3(\tilde{\phi}) = \tilde{j}'' - \tilde{j}, \quad (10.18)$$

and

$$\begin{aligned} \mathcal{L}_1 [C_1 + C_2 \exp(-\xi) + C_3 \exp(\xi)] &= 0, \\ \mathcal{L}_2 [C_4 \exp(\xi) + C_5 \exp(-\xi)] &= 0, \\ \mathcal{L}_3 [C_6 \exp(\xi) + C_7 \exp(-\xi)] &= 0, \end{aligned} \quad (10.19)$$

10.3 Convergence analysis

Auxiliary parameters $\tilde{h}_{\tilde{f}}$, $\tilde{h}_{\tilde{\theta}}$ and $\tilde{h}_{\tilde{j}}$ gave us opportunity to adjust convergence region for solutions of highly nonlinear system. \tilde{h} curves are plotted in Figure (10.1) for the velocity, temperature and concentration. Permissible values of $\tilde{h}_{\tilde{f}}$, $\tilde{h}_{\tilde{\theta}}$ and $\tilde{h}_{\tilde{j}}$ are adjusted in the ranges $-1.05 \leq \tilde{h}_{\tilde{f}} \leq -0.2$, at 13th, $-1.4 \leq \tilde{h}_{\tilde{\theta}} \leq -0.65$, at 15th and $-1.6 \leq \tilde{h}_{\tilde{j}} \leq -0.2$, at 18th order of approximations. When $\tilde{h}_{\tilde{f}} = -0.4$, $\tilde{h}_{\tilde{\theta}} = -1.1$ and $\tilde{h}_{\tilde{j}} = -0.7$ the series solutions converges in whole region of ξ ($0 < \xi < \infty$). Table (10.1) is also constructed to guarantee convergence.

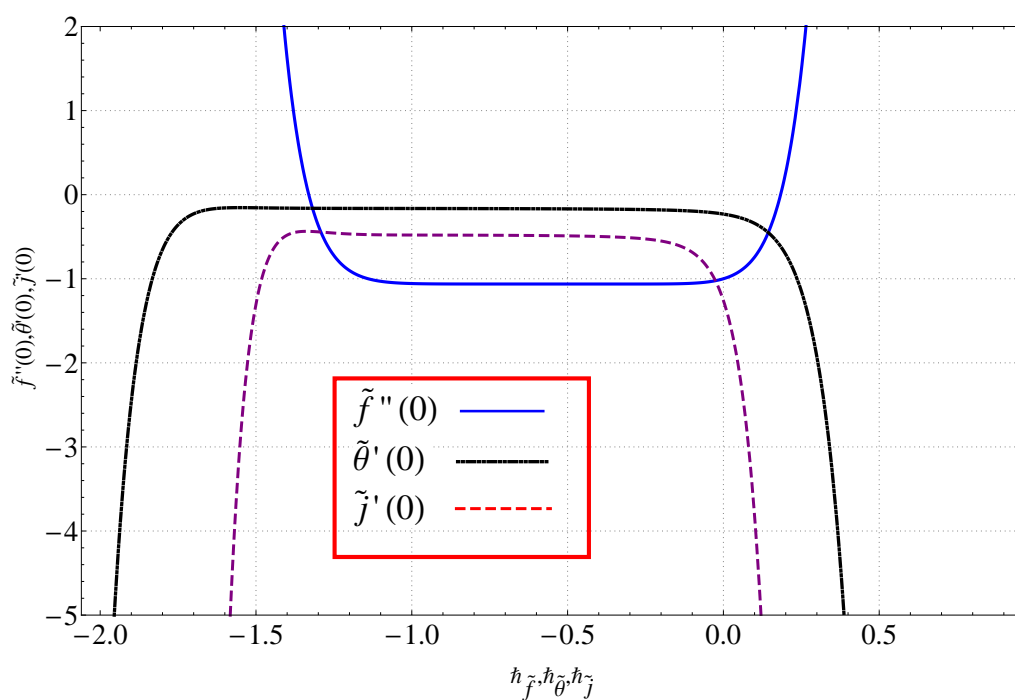


Figure 10.1: \tilde{h} -curves for velocity, temperature and concentration.

Table 10.1: Convergence of series solutions when $\gamma = R_D = Q = 0.1, \beta = N_B = 0.2, B_T = \alpha_T = 0.3, M = Sc = 0.5, E^* = 0.6, N_T = 0.8, n = 0.9, L_C = 1.1$ and $Pr = 1.5$.

Order of approximation	$-\tilde{f}''(0)$	$-\tilde{\theta}'(0)$	$-\tilde{j}'(0)$
1	1.0323	0.2000	0.5575
5	1.0797	0.1811	0.5454
8	1.0862	0.1787	0.5367
11	1.0878	0.1779	0.5321
13	1.0879	0.1777	0.5296
15	1.0879	0.1776	0.5290
18	1.0879	0.1776	0.5275
25	1.0879	0.1776	0.5275
35	1.0879	0.1776	0.5275
50	1.0879	0.1776	0.5275

10.4 Discussions

This section is developed to scrutinized the behavior of physical variables on temperature, concentration and velocity. Moreover heat and mass transfer rates are presented in tabular form.

10.4.1 Velocity

Figure (10.2) is prepared to examine velocity of nanofluid for higher Deborah number ($\beta=0.1,0.2,0.3,0.4$). Velocity gradually reduces for larger values of (β). Physically Deborah number (β) is a ratio of fluid relaxation time to its characteristic time scale. when shear stress is applied on fluid, then the time in which fluid attain its equilibrium position is called relaxation time. This time becomes larger for those fluids having higher viscosity. Thus an increment in (β) enhances the viscosity of fluid. As a result viscosity of fluid reduces. Note that if (β) fluid behave like a Newtonian fluid. Figure (10.3) is plotted to investigate the behavior of magnetic parameter ($M = 0.0, 0.2, 0.4, 0.6$) on velocity $f'(\xi)$. Clearly velocity reduces when (M) is increased. Larger (M) give rise to more Lorentz force . As a result velocity is reduced. A resisting force is induced with application of magnetic field which slows down the fluid flow. Contribution of curvature parameter on

velocity is captured in Figure (10.4). As expected velocity of fluid near the cylinder is increased. It is observed that the radius of cylinder will decrease with the increase of curvature parameter (γ). As a result less surface of cylinder is in contact with fluid particles which produce a small resistance towards fluid particles. Hence velocity enhances.

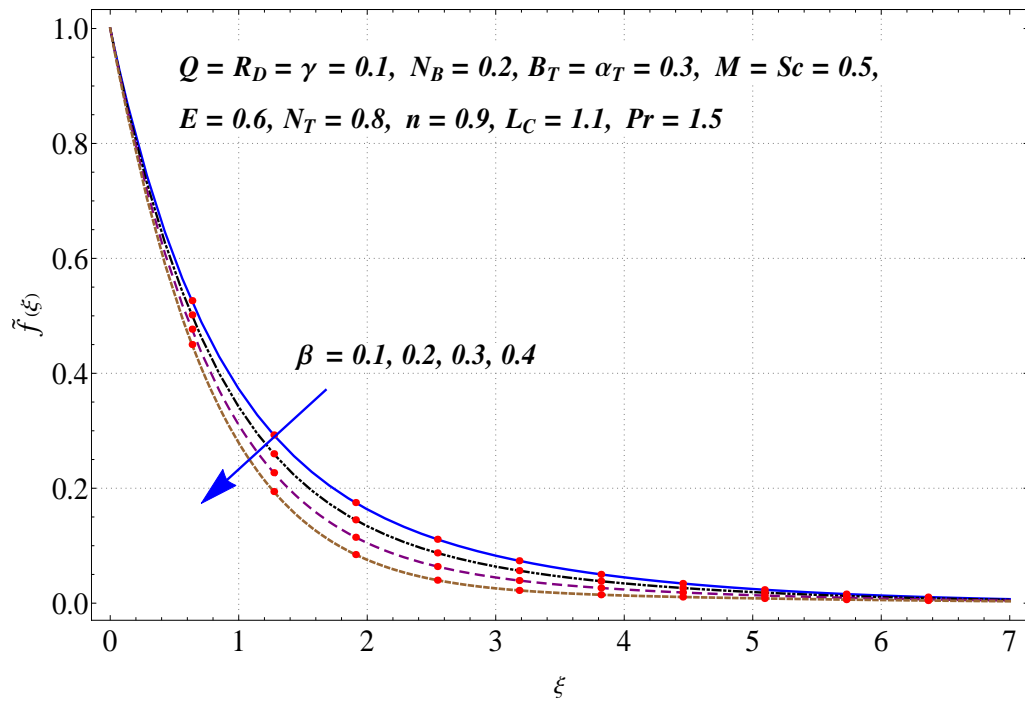


Figure 10.2: Variation of β on $\tilde{f}'(\xi)$.

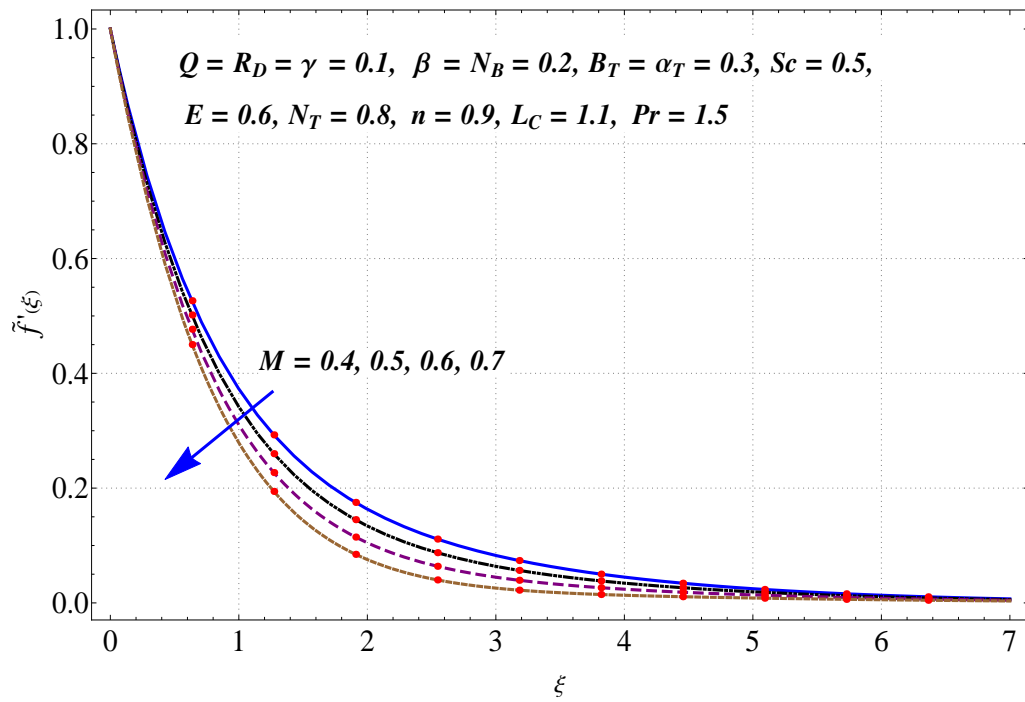


Figure 10.3: Variation of M on $\tilde{f}'(\xi)$.

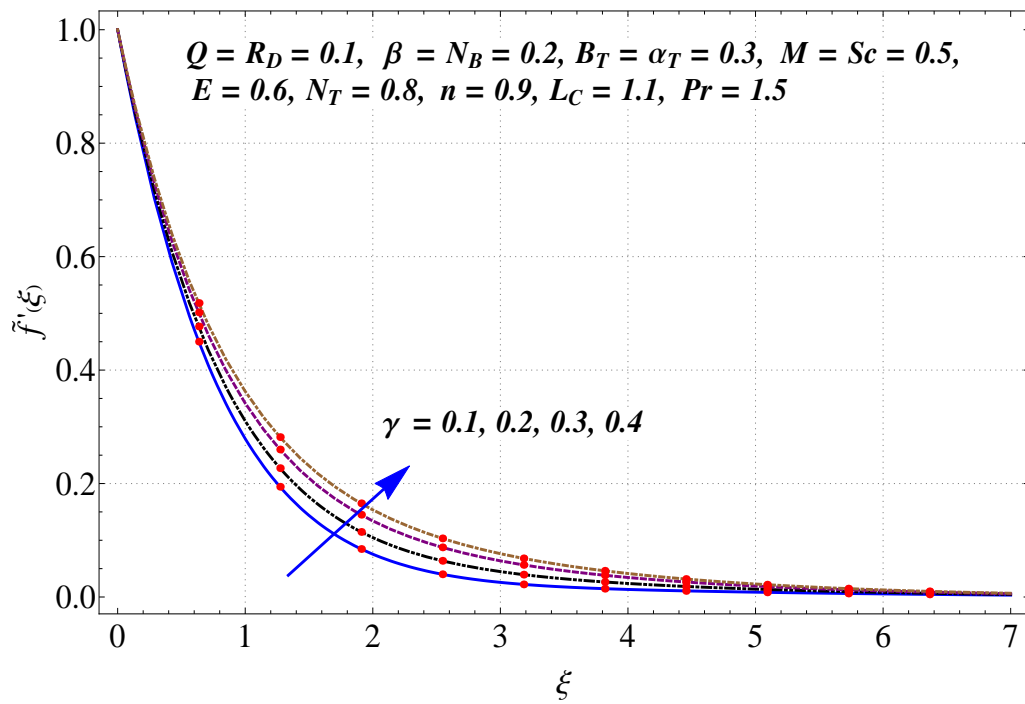


Figure 10.4: Variation of γ on $\tilde{f}'(\xi)$.

10.4.2 Temperature

Figure (10.5) displayed the influence of heat generation parameter ($Q > 0$) on temperature $\tilde{\theta}(\xi)$. Here temperature of fluid rises subject to higher estimations of heat generation parameter ($Q > 0$). Physically nanomaterial has the property to improve the temperature of fluid. Thus heat generation present in system boosts the temperature. Temperature $\tilde{\theta}(\xi)$ for ($R_D = 0.2, 0.3, 0.4, 0.5$) is increased (see Figure (10.6)). Note that the mean absorption coefficient becomes less for (R_D) and thus temperature enhances.

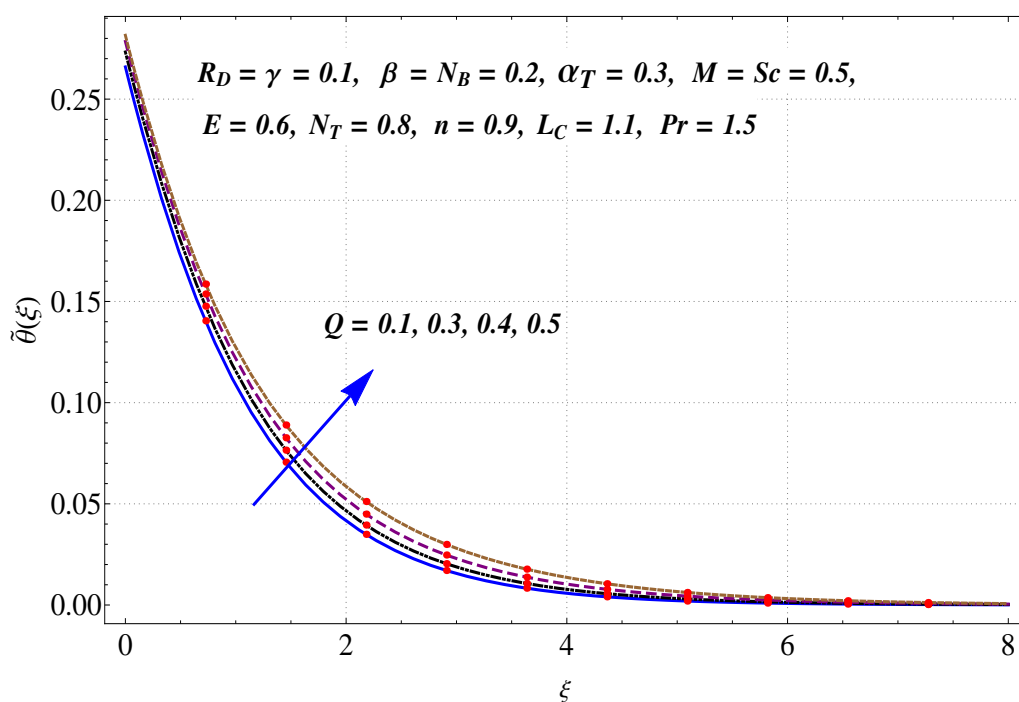


Figure 10.5: Variation of Q on $\tilde{\theta}(\xi)$.

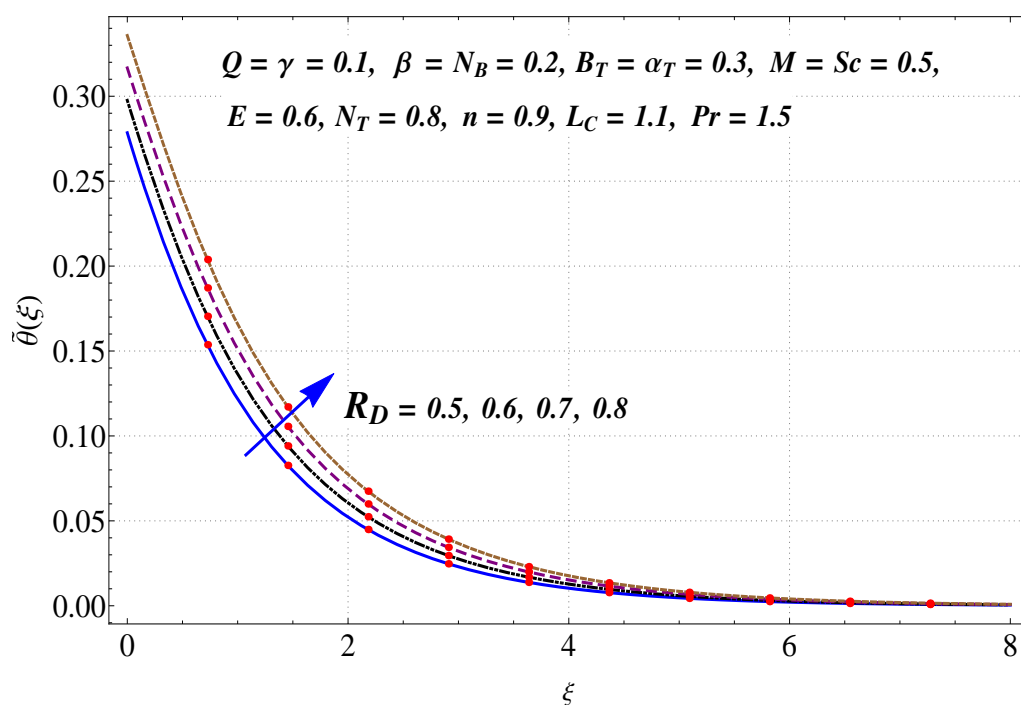


Figure 10.6: Variation of R_D on $\tilde{\theta}(\xi)$.

10.4.3 Concentration

Exploration of dimensionless activation energy ($E^* = 0.2, 0.4, 0.7, 0.9$) on nanoparticles concentration is reflected in Figure (10.7). A rise in concentration is observed. Since activation energy is small amount of energy to activate molecules in a system to start chemical reaction. Therefore if activation energy is very high then rate of reaction reduces and thus concentration enhances. The influence of temperature difference parameter (α_T) on concentration is noted in Figure (10.8). It is observed that $\tilde{j}(\xi)$ is decreasing function of (α_T). Figure (10.9) clarifies the influence of non-dimensional chemical reaction parameter ($L_C = 0.5, 0.6, 0.7, 0.8$) on concentration of nanoparticles. Decay in nanoparticle's concentration is noticed with an increase in (L_C).

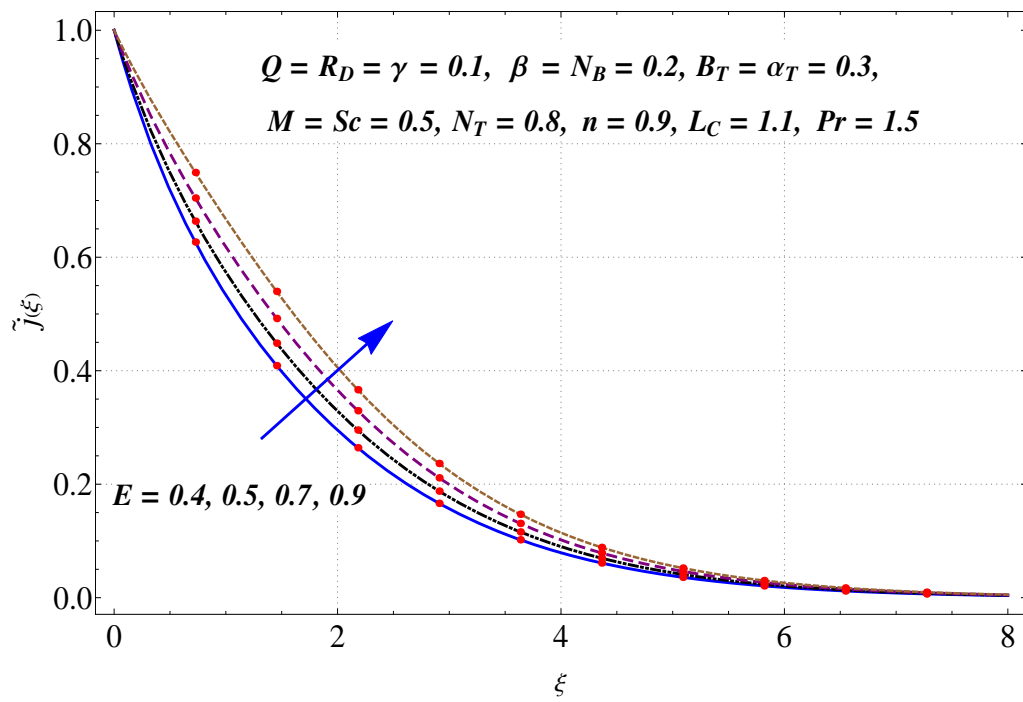


Figure 10.7: Variation of E^* on $\tilde{j}(\xi)$.

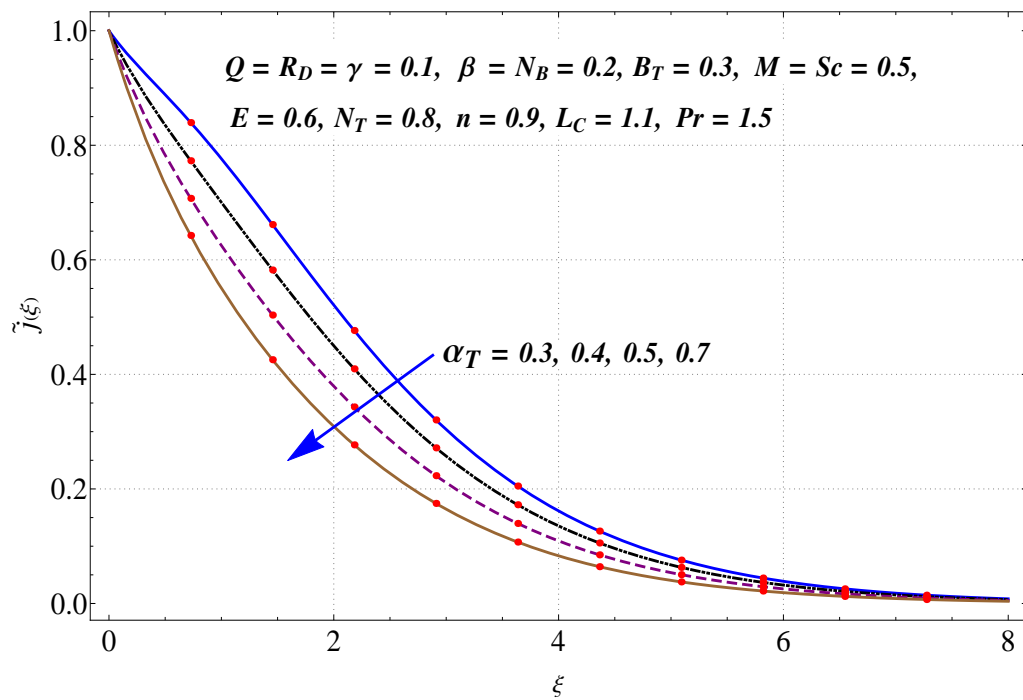


Figure 10.8: Variation of α_T on $\tilde{j}(\xi)$.

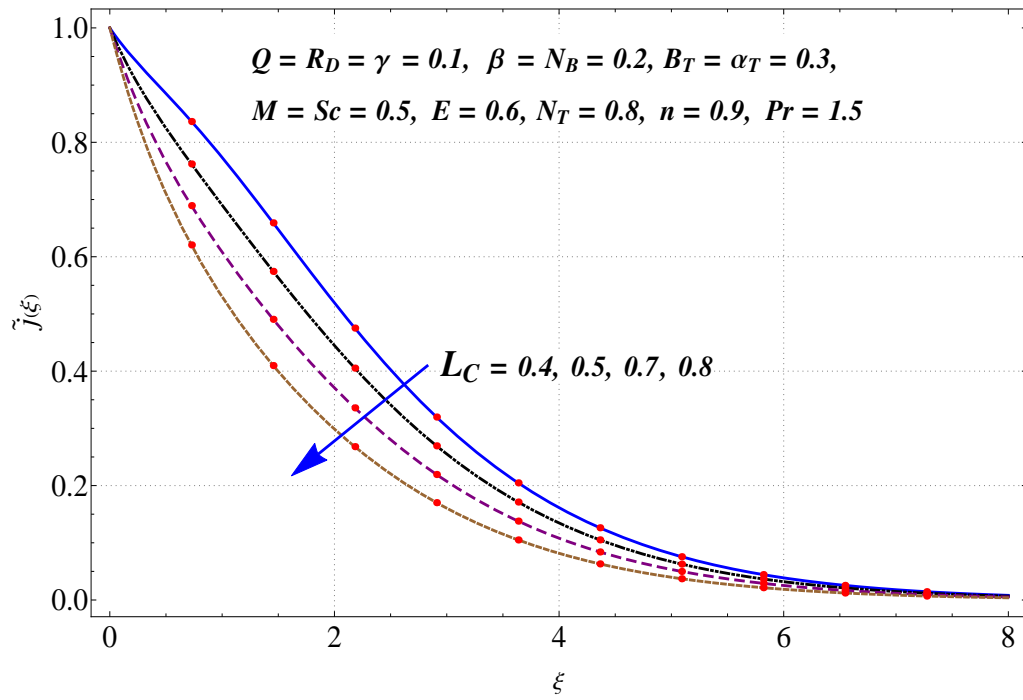


Figure 10.9: Variation of $L_c > 0$ on $\tilde{j}(\xi)$.

10.4.4 Heat and mass transfer rates

Impact of emerging variables on $(Re_x)^{-0.5} \tilde{N}_u$ and $(Re_x)^{-0.5} \tilde{S}_h$ is calculated in Table (10.2). It is noted that heat transfer rate enhances for non-dimensional activation energy parameter while it reduces for Brownian motion and thermophoresis. Clearly mass transfer rate enhances for Brownian motion and Thermophoresis and decreased for non-dimensional activation energy parameter.

Table 10.2: Numerical Values of heat transfer and mass transfer rates when $\gamma = R_D = Q = 0.1, \beta = 0.2, B_T = \alpha_T = 0.3, M = Sc = 0.5, n = 0.9, L_C = 1.1$ and $Pr = 1.5$ are fixed.

N_B	N_T	E^*	$(Re_x)^{-0.5} \tilde{N}_u$	$(Re_x)^{-0.5} \tilde{S}_h$
0.2	0.8	0.6	0.1964	0.5301
0.3	—	—	0.1894	0.5640
0.4	—	—	0.1831	0.5851
0.5	—	—	0.1762	0.5980
—	0.5	—	0.2018	0.4995
—	0.6	—	0.1997	0.5041
—	0.7	—	0.1975	0.5142
—	0.8	—	0.1907	0.9288
—	—	0.2	0.1911	0.8198
—	—	0.4	0.1931	0.6888

10.4.5 Comparison results

Table (2.3) presents the comparison of $-\tilde{f}''(0)$ for different values of Maxwell parameter in limiting case. The results are found in good agreement.

Table 10.3: Comparison values of β for Newtonian case i.e., $M = 0$.

β	$-\tilde{f}''(0)$		
	Abel et al. [78]	Megahed [79]	Present outcomes
0.0	1.000000	0.999978	1.00000
0.2	1.051948	1.051945	1.051889
0.4	1.101850	1.101848	1.101903
0.6	1.150163	1.150160	1.150137
0.8	1.196692	1.196690	1.196711
1.2	1.285257	1.285253	1.285362
1.6	1.368641	1.368641	1.368757
2.0	1.447617	1.447616	1.447650

10.5 Conclusions

We summarize the major findings as follows:

- Velocity of fluid enhances via curvature parameter while it reduces for magnetic parameter.
- Temperature of fluid increases for radiation and heat generation parameters.
- Concentration is reduced for destructive chemical reaction whereas as it enhances for temperature difference number.
- Concentration of nanofluid enhances for non-dimensional energy.
- Brownian motion and thermophoresis reduces for heat transfer rate while it enhances for mass transfer rate.

Chapter 11

Magnetohydrodynamic flow of thixotropic nanofluid with Soret and Dufour. . .

This chapter addresses magnetohydrodynamic (MHD) flow of thixotropic nanofluid. Stagnation point flow due to nonlinear stretching sheet of variable thickness is elaborated. Heat and mass transfer features are discussed using Soret and Dufour effects. Convective conditions are also imposed. Nonlinear systems are solved by homotopy algorithm. Convergence of derived solutions is ensured explicitly. Velocity, temperature, concentration, skin friction coefficient and local Sherwood and Nusselt numbers are examined for influential parameters.

11.1 Formulation

Let us model stagnation point flow of thixotropic nanofluid due to stretching surface of variable thickness. Flow caused by nonlinear stretching surface is restricted in domain $y > 0$. Behaviors of Brownian movements and thermophoresis are studied. Stretching velocity of sheet is $u_w(x) = u_0(x + b)^n$ (n being power-law index). A magnetic field of constant strength \tilde{B}_0^* is applied. Omission of electric and induced magnetic fields is ensured. The related problem satisfy:

$$\frac{\partial u}{\partial x} + \frac{\partial v}{\partial y} = 0, \quad (11.1)$$

$$\rho_f \left(u \frac{\partial u}{\partial x} + v \frac{\partial u}{\partial y} \right) = u_e \frac{du_e}{dx} - \sigma_f B_0^{*2} (u_e - u) + \mu_f \left(\frac{\partial^2 u}{\partial y^2} \right) - 6R_a \left(\frac{\partial u}{\partial y} \right)^2 \frac{\partial^2 u}{\partial y^2} \left. \vphantom{\rho_f} \right\} \quad (11.2)$$

$$+ 4R_b \left[\begin{array}{l} \left(\frac{\partial u}{\partial y} \right) \left(\frac{\partial^2 u}{\partial y^2} \right) \left(u \frac{\partial^2 u}{\partial x \partial y} + v \frac{\partial^2 u}{\partial y^2} \right) \\ + \left(\frac{\partial u}{\partial y} \right)^2 \left(u \frac{\partial^3 u}{\partial x \partial y^2} + v \frac{\partial^3 u}{\partial y^3} + \frac{\partial u}{\partial y} \frac{\partial^2 u}{\partial x \partial y} + \frac{\partial v}{\partial y} \frac{\partial^2 u}{\partial y^2} \right) \end{array} \right],$$

$$u \frac{\partial T}{\partial x} + v \frac{\partial T}{\partial y} = \alpha_f \left(\frac{\partial^2 T}{\partial y^2} \right) + \tau \left[D_B \left(\frac{\partial C}{\partial y} \frac{\partial T}{\partial y} \right) + \frac{D_T}{T_\infty} \left(\frac{\partial T}{\partial y} \right)^2 \right] \left. \vphantom{u} \right\} \quad (11.3)$$

$$+ \frac{1}{(\rho C_p)_f} \frac{16\sigma^*}{3k^*} \frac{\partial}{\partial y} \left(T^3 \frac{\partial T}{\partial y} \right) + \frac{D_B K_T}{(C_p)_f C_s} \frac{\partial^2 C}{\partial y^2}.$$

$$\left(u \frac{\partial C}{\partial r} + w \frac{\partial C}{\partial z} \right) = D_B \left(\frac{\partial^2 C}{\partial y^2} \right) + \frac{D_T}{T_\infty} \left(\frac{\partial^2 T}{\partial y^2} \right) + \frac{D_B K_T}{T_\infty} \frac{\partial^2 T}{\partial y^2}, \quad (11.4)$$

$$\left. \begin{array}{l} u = u_w = u_0 (x+b)^n, \quad v = 0, \quad -k_f \frac{\partial T}{\partial y} = h_f (T_f - T), \\ -D_m \frac{\partial C}{\partial y} = k_m (C_f - C) \quad \text{at } y = d(x+b)^{\frac{1-n}{2}}, \\ u = u_e = v_0 (x+b)^n, \quad T \rightarrow T_\infty, \quad C \rightarrow C_\infty \quad \text{as } y \rightarrow \infty, \end{array} \right\} \quad (11.5)$$

where components of velocity in (x, y) directions are (u, v) and R_a and R_b the material constants.

Considering:

$$\left. \begin{array}{l} u = u_0 (x+b)^n \tilde{F}'(\eta), \quad v = -\sqrt{\left(\frac{n+1}{2}\right)} \nu_f u_0 (x+b)^{n-1} \left[\tilde{F}(\eta) + \frac{n-1}{n+1} \eta \tilde{F}'(\eta) \right], \\ \eta = y \sqrt{\left(\frac{n+1}{2}\right)} \frac{u_0}{\nu_f} (x+b)^{n-1}, \quad \tilde{\Theta}(\eta) = \frac{T-T_\infty}{T_f-T_\infty}, \quad \tilde{J}(\eta) = \frac{C-C_\infty}{C_f-C_\infty}, \end{array} \right\} \quad (11.6)$$

Eq. (11.1) is trivially satisfied while Eqs. (11.2)-(11.5) give

$$\left. \begin{array}{l} \tilde{F}'''' - \frac{2n}{n+1} \tilde{F}'^2 + \tilde{F} \tilde{F}'' + K_a(x) \left[\frac{n+1}{2} \tilde{F}''^2 \tilde{F}'''' \right] - \frac{2}{n+1} M \tilde{F}' + \frac{2n}{n+1} \Psi^2 + \frac{2}{n+1} \Psi M \\ + K_b(x) \left[-\left(\frac{n+1}{2}\right)^2 \tilde{F} \tilde{F}'' \tilde{F}'''' + \frac{5n^2+2n-3}{2} \tilde{F}' \tilde{F}''^2 \tilde{F}'''' \right] = 0, \end{array} \right\} \quad (11.7)$$

$$\left. \begin{array}{l} \frac{1}{Pr} (1 + R_D) \tilde{\Theta}'' + R_D \left[\begin{array}{l} (\tilde{\Theta} - 1)^3 \left(3\tilde{\Theta}^2 (\tilde{\Theta}')^2 + \tilde{\Theta}^3 \tilde{\Theta}' \right) \\ + 3(\tilde{\Theta} - 1)^3 \left(2\tilde{\Theta} (\tilde{\Theta}')^2 + \tilde{\Theta}^2 \tilde{\Theta}'' \right) \\ + 3(\tilde{\Theta} - 1) \left((\tilde{\Theta}')^2 + \tilde{\Theta} \tilde{\Theta}'' \right) \end{array} \right] \\ + N_B \tilde{\Theta}' \tilde{J}' + N_T \tilde{\Theta}^2 + \tilde{F} \tilde{\Theta}' + D_f \tilde{J}'' = 0, \end{array} \right\} \quad (11.8)$$

$$\tilde{\varphi}'' + \left(\frac{N_T}{N_B} + SrSc \right) \tilde{\Theta}'' + Sc \tilde{F} \tilde{J}' = 0, \quad (11.9)$$

$$\left. \begin{aligned} \tilde{F}(\alpha) &= \alpha^{\frac{1-n}{1+n}}, \tilde{F}'(\alpha) = 1, \tilde{F}'(\infty) \rightarrow \Psi, \\ \tilde{\Theta}'(\alpha) &= -B_T[1 - \tilde{\Theta}(\alpha)], \tilde{\Theta}(\infty) \rightarrow 0, \\ \tilde{J}'(\alpha) &= -B_C[1 - \tilde{J}(\alpha)], \tilde{J}(\infty) \rightarrow 0. \end{aligned} \right\} \quad (11.10)$$

Letting

$$\tilde{F}(\xi) = \tilde{f}(\eta - \alpha) = \tilde{f}(\xi), \tilde{\Theta} = \tilde{\theta}(\eta - \alpha) = \tilde{\theta}(\xi), \tilde{J} = \tilde{j}(\eta - \alpha) = \tilde{j}(\xi) \quad (11.11)$$

one can write

$$\left. \begin{aligned} \tilde{f}''' - \frac{2n}{n+1}\tilde{f}'^2 + \tilde{f}\tilde{f}'' + K_a(x) \left[\frac{n+1}{2}\tilde{f}''^2\tilde{f}''' \right] - \frac{2}{n+1}M\tilde{f}' + \frac{2n}{n+1}\Psi^2 + \frac{2}{n+1}\Psi M \\ + K_b(x) \left[-\left(\frac{n+1}{2}\right)^2\tilde{f}\tilde{f}''\tilde{f}'''^2 + \frac{5n^2+2n-3}{2}\tilde{f}'\tilde{f}''^2\tilde{f}''' \right] = 0, \end{aligned} \right\} \quad (11.12)$$

$$\left. \begin{aligned} \frac{1}{\text{Pr}}(1 + R_D)\tilde{\theta}'' + R_D \left[\begin{aligned} &(\tilde{\theta}_w - 1)^3 \left(3\tilde{\theta}^2(\tilde{\theta}')^2 + \tilde{\theta}'\tilde{\theta}^3 \right) \\ &+ 3(\tilde{\theta}_w - 1)^2 \left(2\tilde{\theta}(\tilde{\theta}')^2 + \tilde{\theta}^2\tilde{\theta}'' \right) \\ &+ 3(\tilde{\theta}_w - 1) \left((\tilde{\theta}')^2 + \tilde{\theta}\tilde{\theta}'' \right) \end{aligned} \right] \\ + N_B\tilde{\theta}'\tilde{j}' + N_T\tilde{\theta}''^2 + \tilde{F}\tilde{\theta}' + D_f\tilde{j}'' = 0, \end{aligned} \right\} \quad (11.13)$$

$$\tilde{j}'' + \left(\frac{N_T}{N_B} + SrSc \right) \tilde{\theta}'' + Scf\tilde{j}' = 0, \quad (11.14)$$

$$\left. \begin{aligned} \tilde{f}(0) &= \alpha^{\frac{1-n}{1+n}}, \tilde{f}'(0) = 1, \tilde{f}'(\infty) \rightarrow \Psi, \\ \tilde{\theta}'(0) &= -B_T[1 - \tilde{\theta}(0)], \tilde{\theta}(\infty) \rightarrow 0, \\ \tilde{j}'(0) &= -B_C[1 - \tilde{j}(0)], \tilde{j}(\infty) \rightarrow 0. \end{aligned} \right\} \quad (11.15)$$

Here $K_a = \frac{6u_0^3 R_a(x+b)^{3n-1}}{\rho_f \nu_f^2}$, $K_b = \frac{-4u_0^4 R_b(x+b)^{4n-2}}{\rho_f \nu_f^2}$ are the non-Newtonian parameters, $B_T = \frac{h_f}{k_f \sqrt{\left(\frac{n+1}{2}\right) \frac{u_0}{\nu_f} (x+b)^{n-1}}}$ the thermal Biot number, $B_C = \frac{k_m}{D_m \sqrt{\left(\frac{n+1}{2}\right) \frac{u_0}{\nu} (x+b)^{n-1}}}$ the concentration Biot number, $\text{Pr} = \frac{(\mu C_p)_f}{k_f}$ the Prandtl number, $M = \frac{\sigma_f B_0^{*2}}{\rho_f u_0}$ the magnetic parameter, $\Psi = \frac{v_0}{u_0}$ the velocity ratio parameter, $Sc = \frac{\nu_f}{D_B}$ the Schmidt number, $R_D = \frac{16\sigma^* T_\infty^3}{3k_f k^*}$ the radiation parameter, $\theta_f = \frac{T_f}{T_\infty}$ the temperature ratio parameter, $N_B = \frac{\tau D_B (C_f - C_\infty)}{\nu}$ the Brownian motion parameter, $N_T = \frac{\tau D_T (T_f - T_\infty)}{\nu T_\infty}$ the thermophoresis parameter, $D_f = \frac{D_B K_T (C_f - C_\infty)}{\nu_f (C_p)_f C_s (T_f - T_\infty)}$ the Dufour number and $Sr = \frac{D_B K_T (T_f - T_\infty)}{\nu_f T_\infty (C_f - C_\infty)}$ the Soret number.

11.1.1 Physical quantities of curiosity

Mathematically, skin friction coefficient is defined as

$$\tilde{C}_{sf} = \frac{\tau_w}{\rho u_w^2}, \quad (11.16)$$

where wall shear stress (τ_w) is expressed as

$$\tau_w = \left[\left(\mu_f - 2R_a \left(\frac{\partial u}{\partial y} \right)^2 \right) \frac{\partial u}{\partial y} \right]_{y=d(x+b)^{\frac{1-n}{2}}}. \quad (11.17)$$

In dimensionless form

$$(\text{Re}_x)^{0.5} \tilde{C}_{sf} = \left(\frac{n+1}{2} \right)^{0.5} \left[\tilde{f}''(0) + \left(\frac{n+1}{2} \right) \frac{K_a}{3} \left(\tilde{f}''(0) \right)^3 \right]. \quad (11.18)$$

Mathematically, Nusselt number is defined as

$$\tilde{N}_u = \frac{(x+b) q_w}{k_f (T_f - T_\infty)}, \quad (11.19)$$

where wall heat flux (q_w) satisfies

$$q_w = -k_f \left(1 + \frac{16\sigma^* T_\infty^3}{3k_f k^*} \right) \left(\frac{\partial T}{\partial y} \right)_{y=d(x+b)^{\frac{1-n}{2}}} \quad (11.20)$$

or

$$(\text{Re}_x)^{-0.5} \tilde{N}_u = - \left(\frac{n+1}{2} \right)^{0.5} \left(1 + R_D (1 + (\theta_f - 1)) \tilde{\theta}(0) \right)^3 \tilde{\theta}'(0). \quad (11.21)$$

Mathematically, Sherwood number is defined as

$$\tilde{S}_h = \frac{(x+b) q_m}{D_B (C_f - C_\infty)}, \quad (11.22)$$

where the mass flux (q_m) obeys

$$q_m = -D_B \left(\frac{\partial C}{\partial y} \right)_{y=d(x+b)^{\frac{1-n}{2}}} \quad (11.23)$$

or

$$(\text{Re}_x)^{-0.5} \tilde{S}_h = - \left(\frac{n+1}{2} \right)^{0.5} \tilde{j}'(0). \quad (11.24)$$

In the above expressions $\text{Re}_x (= \tilde{u}_0 (x+b)^{n+1} / \nu_f)$ the local Reynolds number.

11.2 HAM Solutions

We take for solutions here as

$$\left. \begin{aligned} \tilde{f}_0(\xi) &= \Psi(\xi) + (1 - \Psi)(1 - \exp(-\xi)) + \alpha \left(\frac{1-n}{1+n} \right), \\ \tilde{\theta}_0(\xi) &= \frac{B_T}{1+B_T} \exp(-\xi), \\ \tilde{j}_0(\xi) &= \frac{B_C}{1+B_C} \exp(-\xi), \end{aligned} \right\} \quad (11.25)$$

with

$$\left. \begin{aligned} \mathcal{L}_{\tilde{f}}(\tilde{f}) &= \tilde{f}''' - \tilde{f}', \\ \mathcal{L}_{\tilde{\theta}}(\tilde{\theta}) &= \tilde{\theta}'' - \tilde{\theta}, \\ \mathcal{L}_{\tilde{j}}(\tilde{j}) &= \tilde{j}'' - \tilde{j}, \end{aligned} \right\} \quad (11.26)$$

and

$$\left. \begin{aligned} \mathcal{L}_{\tilde{f}}[C_1 + C_2 \exp(\xi) + C_3 \exp(-\xi)] &= 0, \\ \mathcal{L}_{\tilde{\theta}}[C_4 \exp(\xi) + C_5 \exp(-\xi)] &= 0, \\ \mathcal{L}_{\tilde{j}}[C_6 \exp(\xi) + C_7 \exp(-\xi)] &= 0, \end{aligned} \right\} \quad (11.27)$$

11.3 Convergence

Convergence region is adjusted with the help of auxiliary parameters $\hbar_{\tilde{f}}$, $\hbar_{\tilde{\theta}}$ and $\hbar_{\tilde{j}}$ in homotopy analysis method. Thus we have inspected and plotted the \hbar -curves (see Figure (11.1)). Ranges of admissible values for \hbar are $-1.1 \leq \hbar_{\tilde{f}} \leq -0.68$, $-1.86 \leq \hbar_{\tilde{\theta}} \leq -0.98$ and $-2.12 \leq \hbar_{\tilde{j}} \leq -0.6$. Solutions converge in whole region of ξ ($0 \leq \xi \leq \infty$) when $\hbar_{\tilde{f}} = -1.0$, $\hbar_{\tilde{\theta}} = -1.4$ and $\hbar_{\tilde{j}} = -1.6$. Series solutions convergence can be seen from Table (11.1). $\tilde{f}''(0)$ and $\tilde{\theta}'(0)$ converge at 20th order of approximations and $\tilde{j}'(0)$ converges at 17th order of approximations.

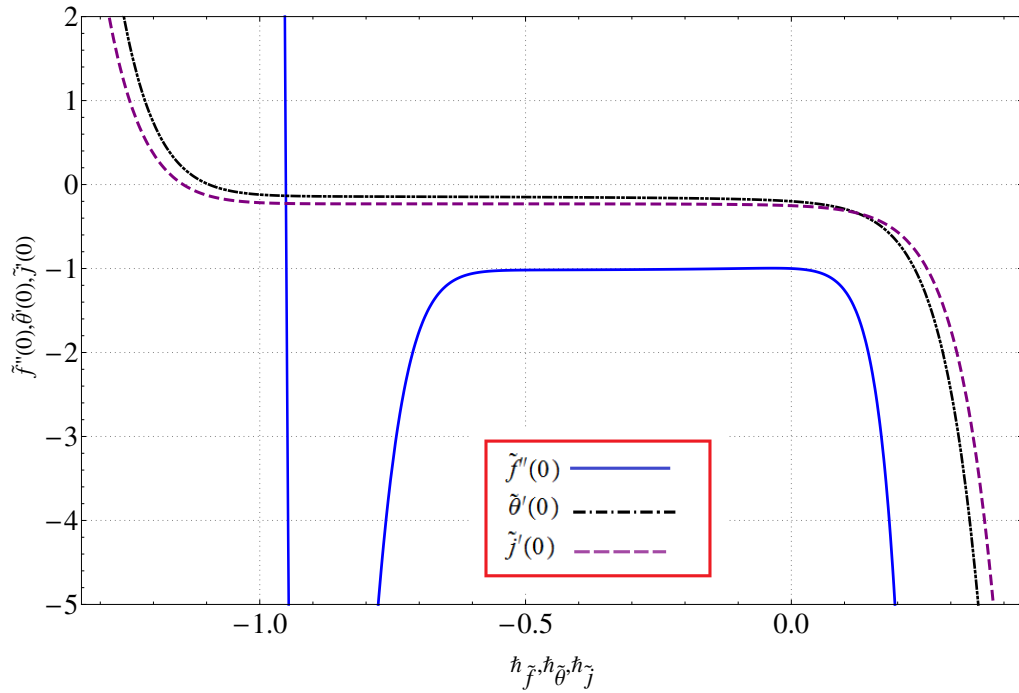


Figure 11.1: h -curves for velocity, temperature and concentration.

Table 11.1: Series solution convergence when $\Psi = 0.1, K_a = K_b = 0.2, B_T = B_C = 0.3, R_D = D_f = M = S_r = N_T = N_B = 0.5, \theta_w = 1.3, n = 1.1, Pr = 1.3$ and $Sc = 1.7$.

Order of approximations	$-\tilde{f}'(0)$	$-\tilde{\theta}'(0)$	$-\tilde{j}'(0)$
1	0.9943	0.2192	0.2223
5	0.9997	0.2001	0.2104
10	1.0074	0.1950	0.2068
15	1.0120	0.1850	0.2058
17	1.0133	0.1833	0.2056
20	1.0149	0.1818	0.2056
23	1.0149	0.1818	0.2056
30	1.0149	0.1818	0.2056
40	1.0149	0.1818	0.2056
45	1.0149	0.1818	0.2056
50	1.0149	0.1818	0.2056
60	1.0149	0.1818	0.2056
70	1.0149	0.1818	0.2056
80	1.0149	0.1818	0.2056

11.4 Analysis

This section highlights the behaviors of velocity, temperature, concentration, surface drag force and heat and mass transfer rates for different involved parameters.

11.4.1 Dimensionless velocity field

Figures (11.2) and (11.3) are plotted to investigate influences of thixotropic parameters ($K_a = 0.2, 0.4, 0.6, 0.7$) and ($K_b = 0.2, 0.4, 0.6, 0.7$) on velocity $\tilde{f}'(\xi)$. It is noted that velocity field enhances for thixotropic parameters (K_a) and (K_b). Physically it is verified that (K_a) and (K_b) lead to shear thinning case which demonstrates viscosity change due to time. Hence larger values of thixotropic parameters (K_a) and (K_b) correspond to longer the fluid experiences shear stress which causes reduction in fluid viscosity. Hence velocity of fluid enhances.

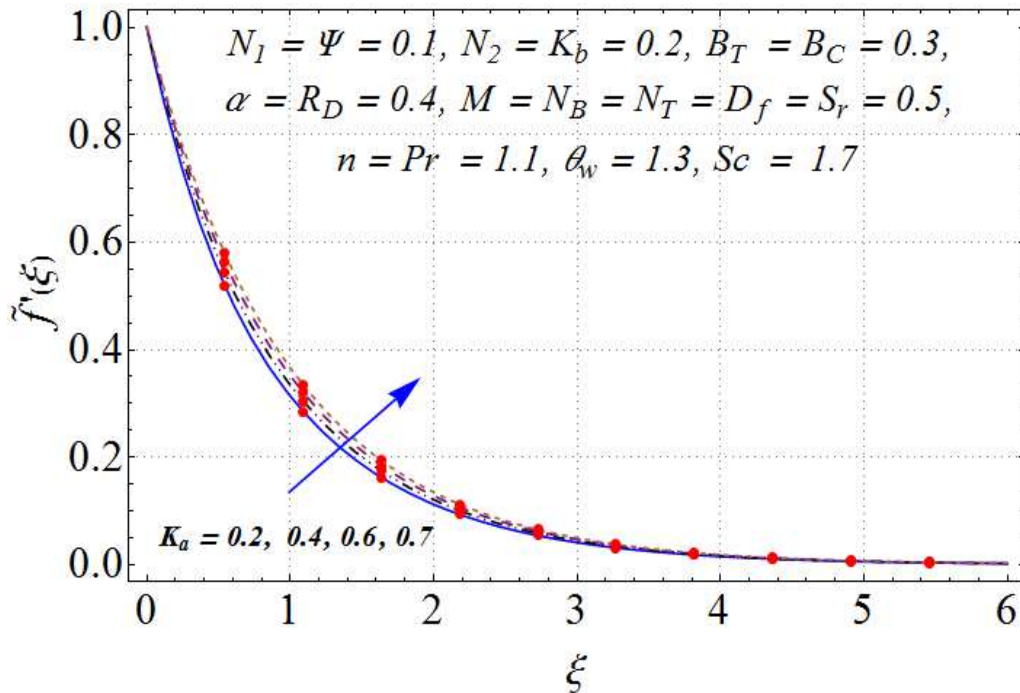
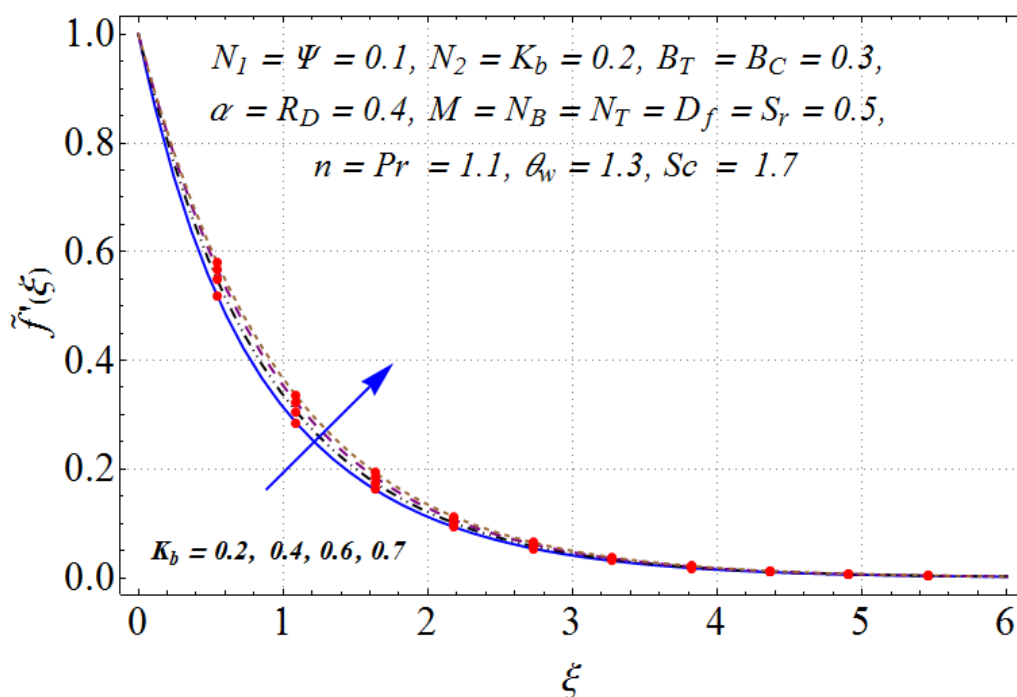


Figure 11.2: Variation of K_a on $\tilde{f}'(\xi)$.

Figure 11.3: Variation of K_b on $\tilde{f}'(\xi)$.

11.4.2 Temperature

Combined effects of Brownian motion ($N_B = 0.2, 0.4, 0.5, 0.6$) and thermophoresis ($N_T = 0.2, 0.4, 0.5, 0.6$) on $\tilde{\theta}(\xi)$ are displayed in Figure (11.4). Increasing behavior of temperature and thermal layer thickness is noted for Brownian motion (N_B) and thermophoresis (N_T). Impact of Dufour number ($D_f = 0.2, 0.3, 0.5, 0.7$) on temperature $\tilde{\theta}(\xi)$ is portrayed in Figure (11.5). Results indicate that temperature $\tilde{\theta}(\xi)$ is an increasing function of Dufour number (D_f). Effect of Prandtl number ($Pr = 1.1, 1.2, 1.3, 1.4$) on temperature is shown in Figure (11.6). There is a reduction in temperature for higher (Pr). In fact thermal conductivity reduces for higher (Pr) and consequently the temperature decays. Figure (11.7) is plotted to study the impact of thermal Biot number on temperature. Higher ($B_T = 0.3, 0.4, 0.5, 0.6$) offer more heat transfer resistance inside a fluid when compared with stretching sheet and thus temperature enhances.

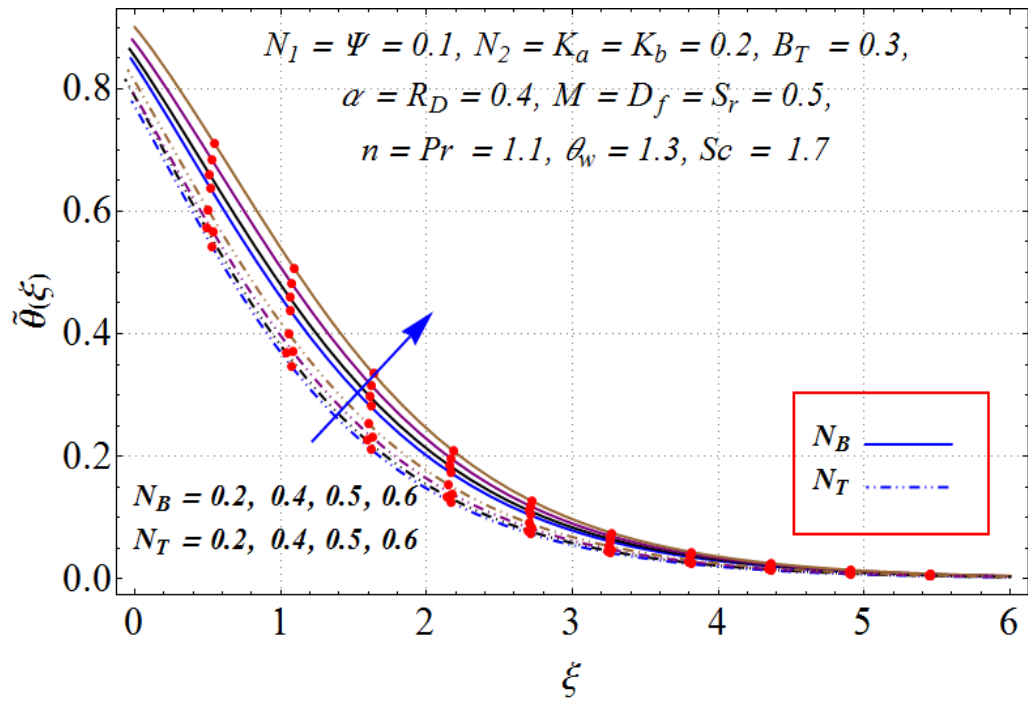


Figure 11.4: Variations of N_B and N_T on $\tilde{\theta}(\xi)$.

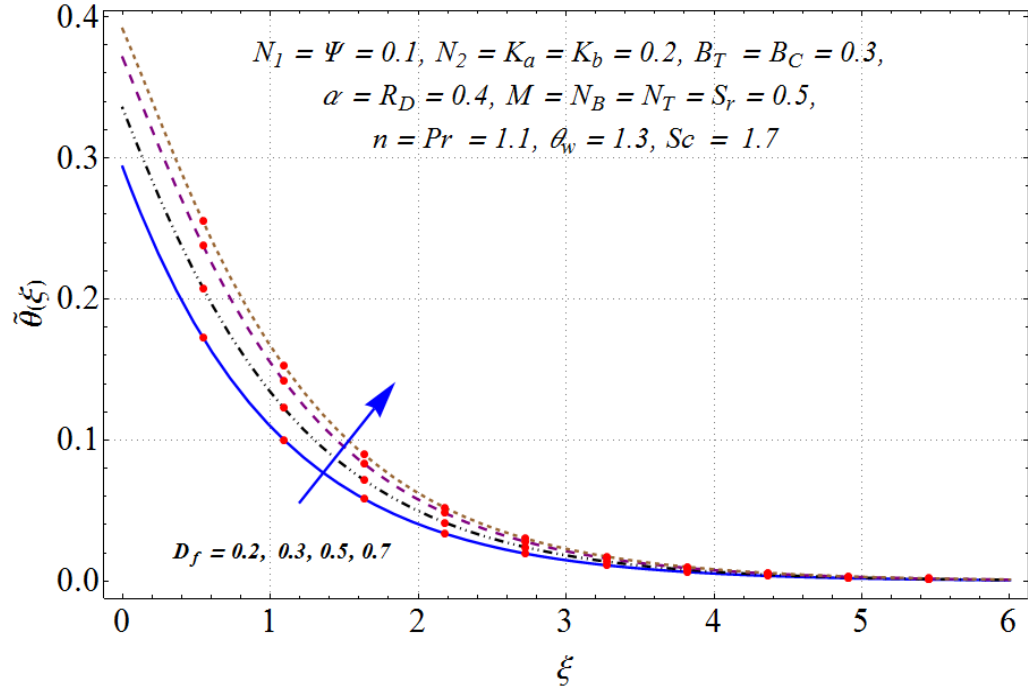


Figure 11.5: Variation of D_f on $\tilde{\theta}(\xi)$.

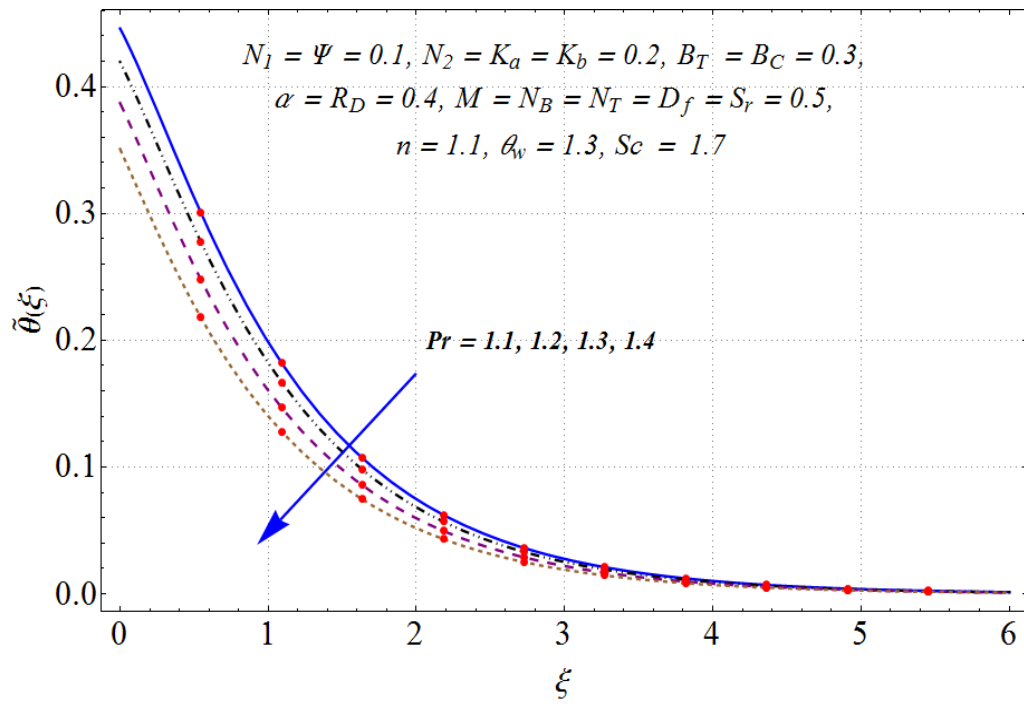


Figure 11.6: Variation of Pr on $\tilde{\theta}(\xi)$.

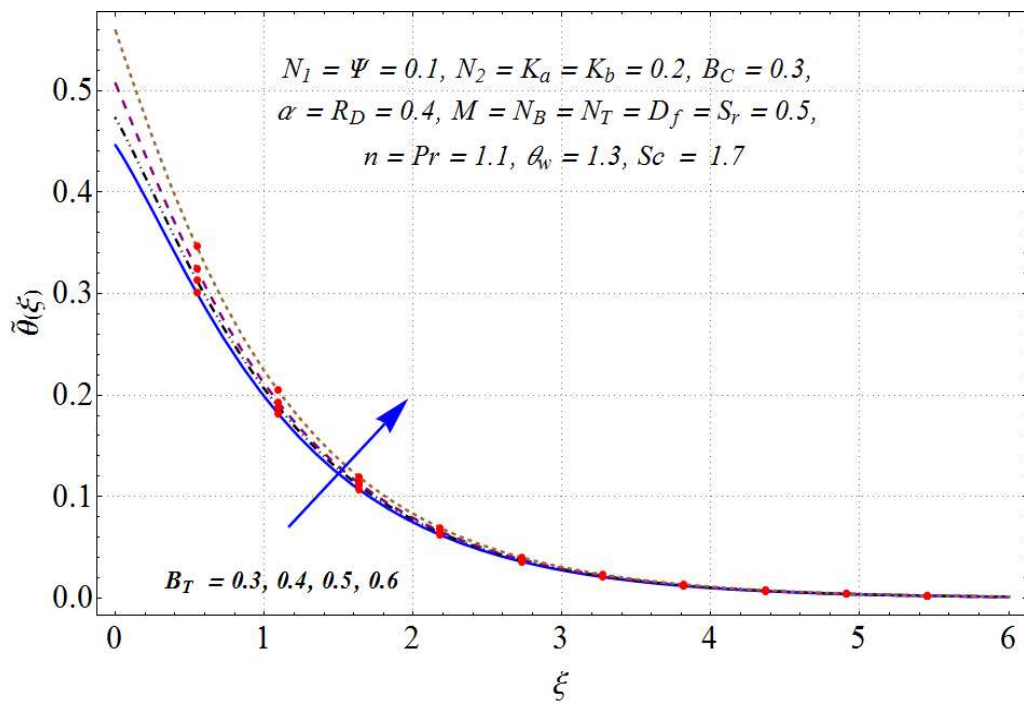


Figure 11.7: Variation of B_T on $\tilde{\theta}(\xi)$.

11.4.3 Concentration

We can see from Figure (11.8) that an increase in thermophoresis parameter (N_T) yields an enhancement of concentration $\tilde{j}(\xi)$. No doubt thermal conductivity increases in presence of nanoparticles. Higher values of (N_T) correspond to an increase in fluid thermal conductivity. Larger thermal conductivity lead to more concentration. Mean while concentration of nanoparticles reduces through N_B . Physically for larger (N_B) the collision among the fluid particles increases and the corresponding concentration decreases. Higher values of ($S_r = 0.2, 0.3, 0.5, 0.7$) on concentration $\tilde{j}(\xi)$ is depicted in Figure (11.9). Clearly concentration is an increasing function of (S_r). Figure (11.10) is plotted to study variation of concentration $\tilde{j}(\xi)$ for larger (B_C). Concentration $\tilde{j}(\xi)$ of fluid enhances for larger solutal Biot number (B_C). It is due to the fact that coefficient of mass transfer enhances via higher (B_C).

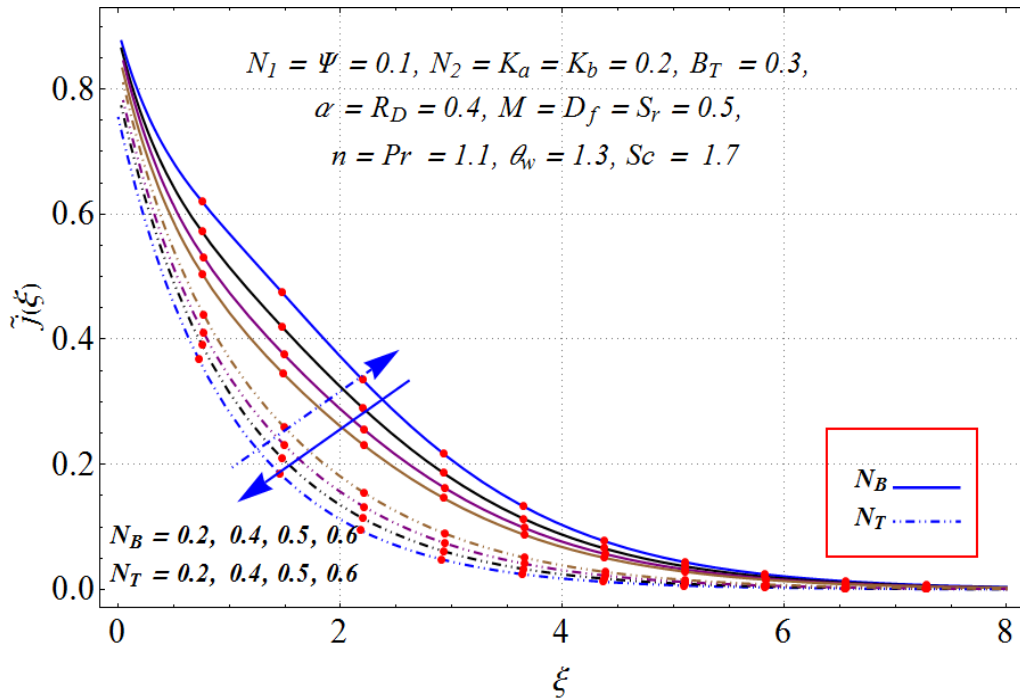


Figure 11.8: Variation of N_T and N_B on $\tilde{j}(\xi)$.

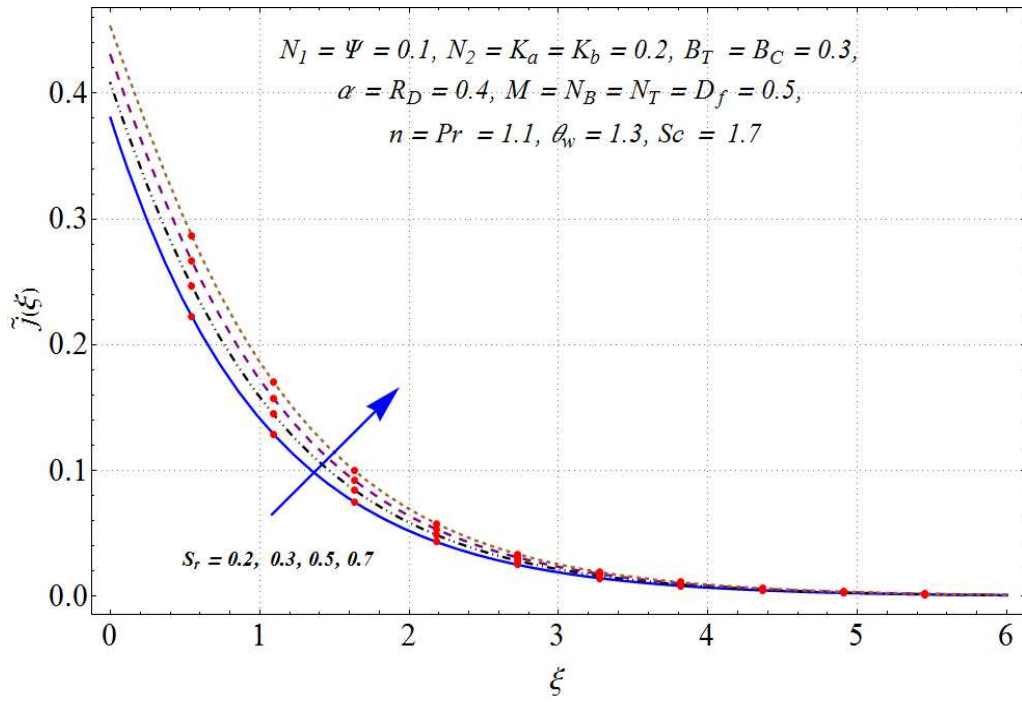


Figure 11.9: Variation of S_r on $\tilde{j}(\xi)$.

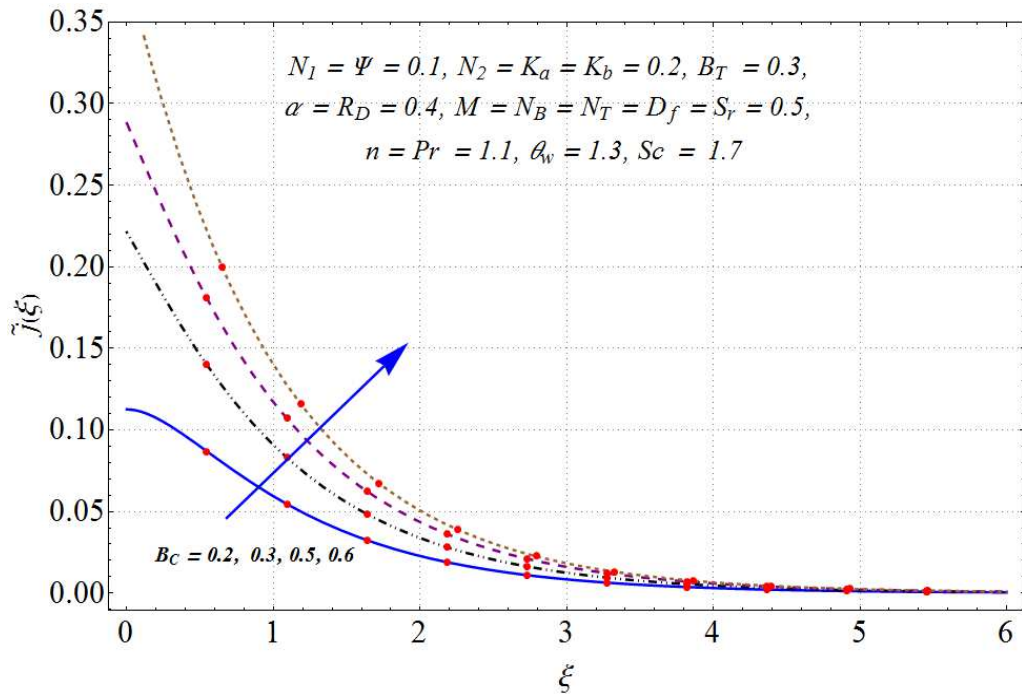


Figure 11.10: Variation of B_C on $\tilde{j}(\xi)$.

11.4.4 Skin friction coefficient and local Nusselt and Sherwood numbers

Figure (11.11) depicts impacts of K_a and M on skin friction coefficient. Magnitude of skin friction coefficient enhances for larger K_a . Heat transfer rate reduces for N_T (see Figure (11.12)). For higher n the local Sherwood number enhances (see Figure (11.13)). Figure (11.14) shows that Sherwood number reduces for larger N_T .

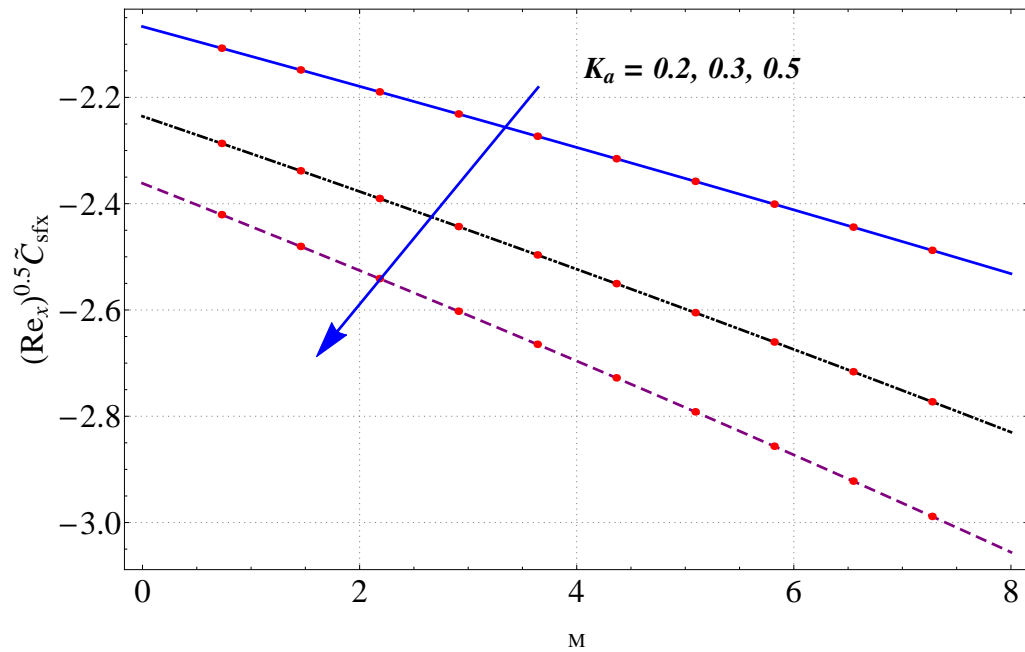


Figure 11.11: Variation of K_a on $(Re_x)^{0.5} \tilde{C}_{sf}$.

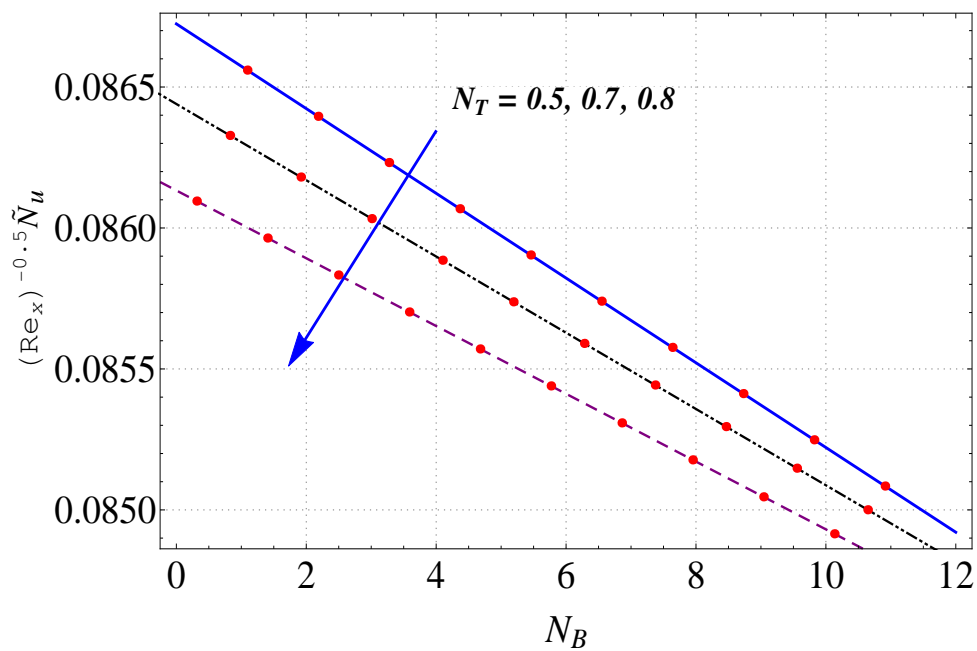


Figure 11.12: Variation of N_T on $(\text{Re}_x)^{-0.5} \tilde{N}_u$.

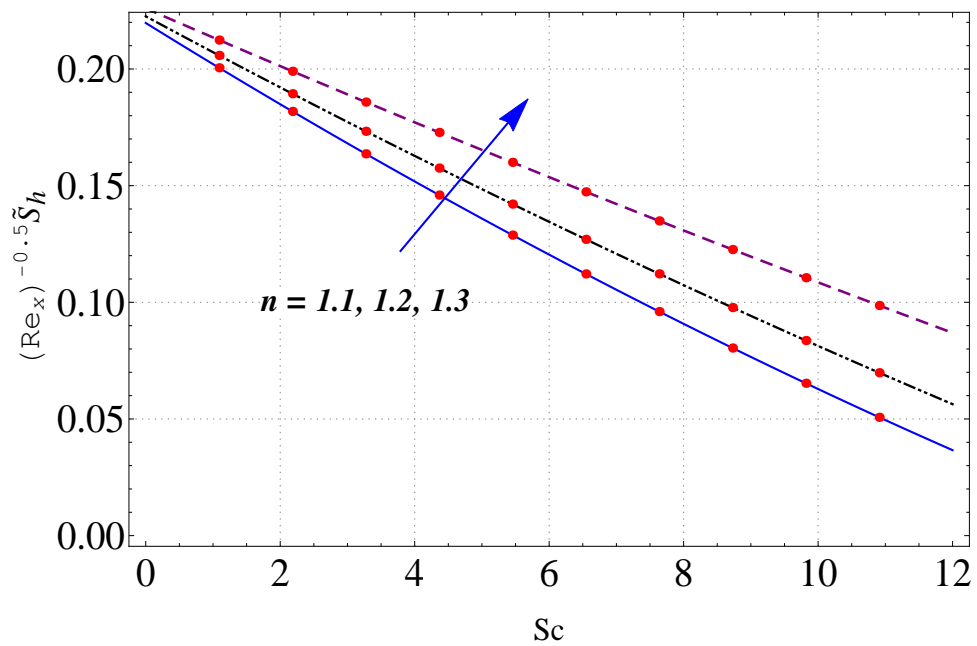
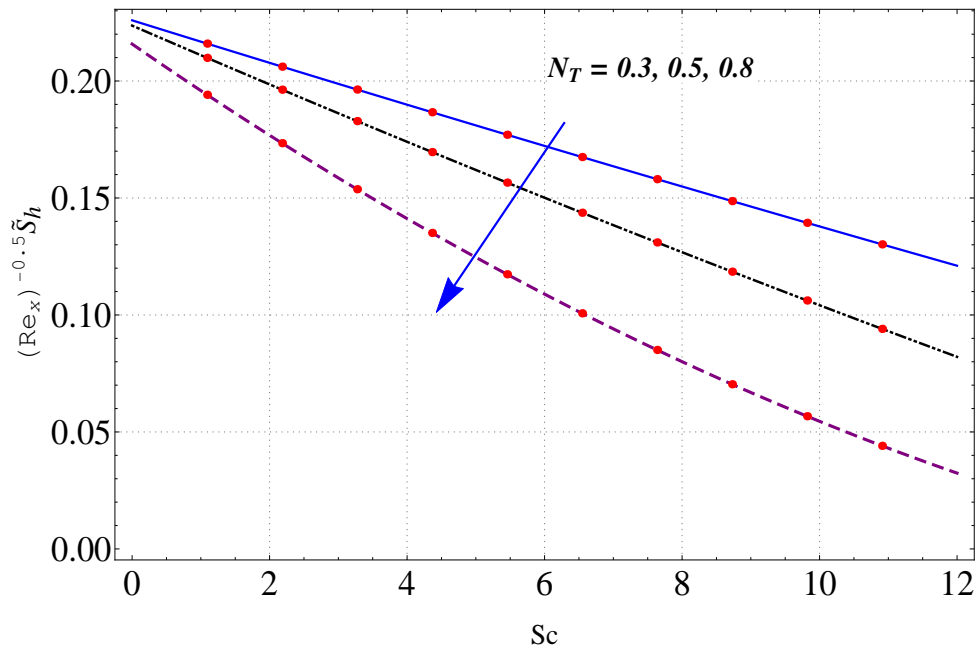


Figure 11.13: Variation of n on $(\text{Re}_x)^{-0.5} \tilde{S}_h$.


 Figure 11.14: Variation of N_T on $(\text{Re}_x)^{-0.5} \tilde{S}_h$.

11.5 Closing remarks

Nonlinear radiation in flow of thixotropic nanofluid is studied in presence of Soret and Dufour effects. The following points are worth mentioning:

- ❑ Velocity is an increasing function of material parameters (K_a, K_b) of thixotropic liquids.
- ❑ Temperature of fluid enhances for higher Brownian motion, thermophoresis parameter, thermal Biot number and Dufour number.
- ❑ Concentration of nanofluid strongly depends upon the Soret number and solutal Biot number.
- ❑ Magnitude of Skin friction coefficient rises for material variable (K_a).
- ❑ Thermophoresis parameter reduces for heat and mass transfer rates.

Bibliography

- [1] S.U.S Choi and J.A. Eastman, Enhancing thermal conductivity of fluids with nanoparticles, ASME Int. Mech. Eng. Cong. Expo., 66 (1995) 99-105.
- [2] Y. Xuan and Q. Li, Heat transfer enhancement of nanofluids, Int. J. Heat Fluid Flow, 21 (2000) 58-64.
- [3] S.U.S Choi, Z.G. Zhang, W.Y.F.E. Lockwoow and E.A. Grulke, Anomalous thermal conductivities enhancement on nanotube suspensions, Appl. Phys. Lett., 79 (2001) 2252-2254.
- [4] W. Daungthongsuk and S. Wongwises, A critical review of convective heat transfer nanofluids, Rene. Sust. Energy Rev., 11 (2007) 797-817.
- [5] V. Trisaksri and S. Wongwises, Critical review of heat transfer characteristics of nanofluids, Rene. Sust. Energy Rev., 11 (2007) 512-523.
- [6] Q. Wang and A.S. Mujumadar, Heat transfer characteristics of nanofluids: A review, Int. J. Therm. Sci., 46 (2007) 1-16.
- [7] Q. Wang and A.S. Mujumadar, A review on nanofluids-Part I:Theoretical and numerical investigations, Braz. J. Chem. Eng., 25 (2008) 613-630.
- [8] Q. Wang and A.S. Mujumadar, A review on nanofluids-Part II:Experiments and applications, Braz. J. Chem. Eng. 25 (2008) 631-648.
- [9] S. Kakac and A. Pramuanjaroenkij, Review of convective heat transfer enhancement with nanofluids, Int. J. Heat and Mass Transf., 52 (2009) 3187-3196.

-
- [10] M. Sheikholeslami and D.D. Ganji, Influence of magnetic field on CuO–H₂O nanofluid flow considering Marangoni boundary layer, *Int. J. Hydrogen Energy.*, 42 (2017) 2748-2755.
- [11] A.K. Pandey and M. Kumar, Boundary layer flow and heat transfer analysis on Cu–water nanofluid flow over a stretching cylinder with slip, *Alex. Eng. J.*, 56 (2017) 671-677.
- [12] P.D. Prasad, R.V.M.S.S.K. Kumar and S.V.K. Varma, Heat and mass transfer analysis for the MHD flow of nanofluid with radiation absorption, *Ain Shams Eng. J.*, (2018) 801-813.
- [13] E.H. Aly, Dual exact solutions of Graphene water nanofluid flow over stretching/shrinking sheet with suction/injection and heat source/sink: Critical values and regions with stability, *Powder Tech.*, 342 (2019) 528-544.
- [14] J. Buongiorno, Convective transport in nanofluids, *ASME J. Heat Tranf.*, 128 (2006) 240-250.
- [15] J. Buongiorno et al., A benchmark study on the thermal conductivity of nanofluids, *J. Appl. Phy.*, 106 (2009), 094312.
- [16] T. Hayat, M. Rashid, M. Imtiaz and A. Alsaedi, Magnetohydrodynamic (MHD) stretched flow of nanofluid with power-law velocity and chemical reaction, *AIP Advances*, 5 (2015) 117121.
- [17] S.H. Pourhoseini, N. Naghizadeh and H. Hoseinzadeh, Effect of silver-water nanofluid on heat transfer performance of a plate exchanger: An experimental and theoretical study, *Powder Tech.*, 332 (2018) 279-286.
- [18] S. Jahan, H. Sakidin, R. Nazar and I. Pop, Analysis of heat transfer in nanofluid past a convectively heated permeable stretching/shrinking sheet with regression and stability analysis, *Results Phy.*, 10 (2018) 395-405.

- [19] J.V.R. Reddy, V. Sugunamma and N. Sandeep, Thermophoresis and Brownian motion effects on unsteady MHD nanofluid flow over a slendering stretching surface with slip effects, *Alex. Eng. J.*, 57 (2018) 2465-2473.
- [20] W.C. Tan, W. Pan and M.Y. Xu, A note on unsteady flow of Maxwell model between two parallel plates, *Int. J. Nonlinear Mech.*, 38 (2003) 645-650.
- [21] S. Sadeqi, N. Khabazi and K. Sadeghy, Blasius flow of thixotropic fluids: A numerical study, *Comm. Nonlinear Sci. and Num. Sim.*, 16 (2011) 711-721.
- [22] H.P.A. Deus and G.S.P. Dupim, On behavior of the thixotropic fluids, *Phys. Lett. A*, 377 (2013) 478-485.
- [23] M. Zubair, M. Waqas, T. Hayat, M. Ayub and A. Alsaedi, Simulation of nonlinear convective thixotropic liquid with Cattaneo-Christov heat flux, *Results Phys.*, 8 (2018) 1023-1027.
- [24] M. Bilal, M. Sagheer and S. Hussain, Three dimensional MHD upper-convected Maxwell nanofluid flow with nonlinear radiative heat flux, *Alex. Eng. J.*, 57 (2018) 1917-1925.
- [25] G. Lebon and H. Machrafi, A thermodynamic model of nanofluid viscosity based on a generalized Maxwell-type constitutive equation, *J. Non-Newtonian Fluid Mech.*, 253 (2018) 1-6.
- [26] L. Crane, Flow past a stretching plate, (*ZAMP*) *J. Appl. Math. and Phys.*, 21 (1970) 645-647.
- [27] P.S. Gupta and A.S. Gupta, Heat and mass transfer on a stretching sheet with suction and blowing, *Can. J. Chem. Eng.*, 55 (1977) 744-746.

-
- [28] J.A. Khan, M. Mustafa, T.Hayat and A. Alsaedi, Three dimensional flow of nanofluid over a nonlinear stretching sheet : An application to solar energy, *Int. J. Heat Mass Transf.*, 86 (2015) 158-164.
- [29] B. Mahanthesh, B.J. Gireesha and R.S.R Gorla, Nonlinear radiative heat transfer in MHD three dimensional flow over a nonlinearly stretching sheet with convective boundary condition, *J. Nig. Math Soc.*, 35 (2016) 178-198.
- [30] M. Sajid, N. Ali, T. Javed and Z. Abbas, Stretching a curved surface in a viscous fluid, *Chin. Phys. Lett.*, 27 (2010) 024703.
- [31] M. Naveed, Z. Abbas and M. Sajid, MHD flow of a micropolar fluid due to curved stretching surface with thermal radiation, *J. Appl. Fluid. Mech.*, 9 (2016) 131-138.
- [32] T. Hayat, M. Rashid, M. Imtiaz and A. Alsaedi, MHD convective flow due to a curved surface with thermal radiation and chemical reaction, *J. Mol. Liq.*, 225 (2017) 482-489.
- [33] K.M. Sanni, S. Asghar, M. Jalil and N.F. Okechi, Flow of viscous fluid along a nonlinearly stretching curved surface, *Results Phys.*, 7 (2017) 1-4.
- [34] T. Hayat, M. Rashid and A. Alsaedi, MHD convective flow of magnetite-Fe₃O₄ nanoparticles by curved stretching sheet, *Results phy.*, 7 (2017) 3107-3115.
- [35] J.V.R. Reddy, V Sugunamma and N. Sandeep, Dual solutions for nanofluid flow past a curved surface with nonlinear radiation, Soret and Dufour effects, *J. Physics: Conf. Series*, 1000 (2018) 012152.
- [36] T. Hayat, M. Rashid, A. Alsaedi and B. Ahmad, Flow of nanofluid by nonlinear stretching velocity, *Results in Phy.*, 8 (2018) 1104-1109.
- [37] T.V. Karman, Classical problem of rotating disk, *Transf.*, ASME 61 (1939) 705.

- [38] K. Stewartson, On the flow between two rotating coaxial disks, *Proc. Camb. Phil. Soc.*, 49 (1953) 333-341.
- [39] G.L. Mellor, P.J. Chapple and V.K. Stokes, On the flow between a rotating and a stationary disk, *J. Fluid Mech.*, 31 (1968) 95-112.
- [40] C.Y. Ming, L.C. Zheng and X.X. Zhang, Steady flow and heat transfer of the power-law fluid over rotating disk, *Int. Commun. Heat Mass Transf.*, (2011) 280-284.
- [41] T. Hayat, M. Rashid, M. Imtiaz and A. Alsaedi, Magnetohydrodynamic (MHD) flow of Cu-water nanofluid due to a rotating disk with partial slip, *AIP Advances*, 5 (2015) 067169.
- [42] T. Fang, J. Zhang and Y. Zhong, Boundary layer flow over a stretching sheet with variable thickness, *Appl. Math. Comp.*, 218 (2012) 7241-7252.
- [43] S.V. Subhashini, R. Sumathi and I. Pop, Dual solutions in a thermal diffusive flow over a stretching sheet with variable thickness, *Int. Commun. Heat Mass Transf.*, 48 (2013) 61-66.
- [44] S. Xun, J. Zhao, L. Zheng, X.Cheng and X. Zhang, Flow and heat transfer of Ostwald-de- fluid over a variable thickness rotating disk with index decreasing, *Int. Heat Mass Transf.*, 103 (2016) 1214-1224.
- [45] T. Hayat, S. Qayyum, M. Imtiaz and Ahmed Alsaedi, Radiative flow due to stretchable rotating disk with variable thickness, *Results Phys.*, 7 (2017) 156-165.
- [46] T. Hayat, M. Rashid, M.I. Khan and Ahmed Alsaedi, Melting heat transfer and induced magnetic field effects on flow of water based nanofluid over a rotating disk with variable thickness, *Results Phys.*, 9(2018) 1618-1630.

-
- [47] Y.S. Daniel, Z.A. Aziz, Z. Ismail and F. Salah, Impact of thermal radiation on electrical MHD flow of nanofluid over nonlinear stretching sheet with variable thickness, *Alex. Eng. J.*, 57 (2018) 2187-2197.
- [48] H. Darcy, *Les Fontaines Publiques De La Ville De Dijon*, Victor Dalmont, Paris (1856).
- [49] P. Forchheimer, *Wasserbewegung durch boden*, *Zeitschrift Ver. D. Ing.*, 45 (1901) 1782-1788.
- [50] M. Muskat, *The Flow of Homogeneous Fluids through Porous Media*, Edwards, MI., (1946).
- [51] M.A. Seddeek, Influence of viscous dissipation and thermophoresis on Darcy–Forchheimer mixed convection in a fluid saturated porous media, *J. Colloid Interface Sci.*, 293 (2006) 137-142.
- [52] A. K. Singh, R. Kumar, U. Singh, N.P. Singh and A.K. Singh, Unsteady hydro-magnetic convective flow in a vertical channel using Darcy-Brinkman-Forchheimer extended model with heat generation/absorption: Analysis with asymmetric heating/cooling of the channel walls, *Int. J. Heat Mass Transf.*, 54 (2011) 5633-5642.
- [53] D. Pal and H. Mondal, Hydromagnetic convective diffusion of species in Darcy–Forchheimer porous medium with non-uniform heat source/sink and variable viscosity, *Int. Commun. Heat Mass Transf.*, 39 (2012) 913-917.
- [54] T. Hayat, K. Rafique, T. Muhammad, A. Alsaedi and M. Ayub, Carbon nanotubes significance in Darcy Forchheimer flow, *Results Phys.*, 8(2018) 26-33.
- [55] N.V. Ganesh, A.K.A. Hakeem and B. Ganga, Darcy–Forchheimer flow of hydromagnetic nanofluid over a stretching/shrinking sheet in a thermally stratified porous medium with second order slip, viscous and Ohmic dissipations effects, *Ain Shams Eng.J.*, 9 (2018) 939-951.

- [56] A. Bejan, *Entropy Generation Through Heat and Fluid Flow*, Wiley, New York (1982).
- [57] A. Bejan, *Entropy Generation Minimization*, CRC Press, New York (1995).
- [58] M.H. Abolbashari, N. Freidoonimehr, F. Nazari and M.M. Rashidi, Analytical modeling of entropy generation for Casson nano-fluid flow induced by a stretching surface, *Adv. Powder Technol.*, 26 (2015) 542-552.
- [59] M. Khan, T. Khan, S. Qayyum, T. Hayat, M. Khan and A. Alsaedi, Entropy generation optimization and activation energy in nonlinear mixed convection flow of tangent hyperbolic nanofluid, *Eur. Phys. J. Plus.*, 133 (2018) 329.
- [60] H. Sithole, H. Mondal and P. Sibanda, Entropy Generation in a second grade magnetohydrodynamic nanofluid flow over a convectively heated stretching sheet with nonlinear thermal radiation and viscous dissipation, *Results in Phys.*, 9 (2018) 1077–1085.
- [61] M.I. Khan, S. Qayyum, T. Hayat, A. Alsaedi and M.I. Khan, Investigation of Sisko fluid through entropy generation, *J. Mol. Liq.*, 257 (2018) 155–163.
- [62] M.I. Khan, S. Ullah, T. Hayat, M. Waqas, M.I. Khan and A. Alsaedi, Salient aspects of entropy generation optimization in mixed convection nanomaterial flow, *Int. J. Heat Mass Transf.*, 126 (2018) 1337-1346.
- [63] S. P. Goqo, S. D. Olonijju, H. Mondal, P. Sibanda and S. S. Motsa, Entropy generation in MHD radiative viscous nanofluid flow over a porous wedge using the bivariate spectral quasi-linearization method, *Case Stud. Ther. Eng.*, 12 (2018) 774-788.
- [64] M.E. Bahmanyar and S. Talebi, A performance analysis of vertical steam generator using an entropy generation method, *Annals of Nuclear Energy*, 125 (2019) 212-221.

-
- [65] M. Rashid, M.I. Khan, T. Hayat, M.I. Khan and A. Alsaedi, Entropy generation in flow of ferromagnetic liquid with nonlinear radiation and slip condition, *J. Mol. Liq.*, 276 (2019) 441–452.
- [66] M.A. Chaudhary and J.H. Merkin, A simple isothermal model for homogeneous-heterogeneous reactions in boundary-layer flow. II Different diffusivities for reactant and autocatalyst, *Fluid Dynam. Res.*, 16 (1995) 335–359
- [67] J.H. Merkin, A model for isothermal homogeneous-heterogeneous reactions in boundary-layer flow, *Math. Comput. Model.*, 24 (1996) 125-136.
- [68] T. Hayat, M. Rashid, M. Imtiaz and A. Alsaedi, Nanofluid flow due to rotating disk with variable thickness and homogeneous-heterogeneous reactions, *Int. J. Heat Mass Transf.*, 113 (2017) 96-105.
- [69] A. Raees, R.Z. Wang and H. Xu, A homogeneous-heterogeneous model for mixed convection in gravity-driven film flow of nanofluids, *International Comm. Heat and Mass Transf.*, 95 (2018) 19-24.
- [70] Y. Wang, W. Yang, J. Zhou, H. Yang and K. Cen, Heterogeneous reaction characteristics and their effects on homogeneous combustion of methane/air mixture in micro channels, *Fuel*, 234 (2018) 20-29.
- [71] A.K. Alzahrani, Darcy-Forchheimer 3D flow of carbon nanotubes with homogeneous and heterogeneous reactions, *Phy. Lett. A*, 382 (2018) 2787-2793.
- [72] T. Hayat, M. Rashid, and Ahmed Alsaedi, Three dimensional radiative flow of magnetite-nanofluid with homogeneous-heterogeneous reactions, *Results Phys.*, 8 (2018) 268-275.
- [73] H.C. Brinkman, The viscosity of concentrated suspensions and solutions, *J. Chem. Phys.*, 20 (1952) 571-581.

- [74] R.K. Tiwari and M.K. Das, Heat transfer augmentation in a two-sided lid-driven differentially heated square cavity utilizing nanofluids, *Int. J. Heat Mass Transf.*, 50 (2007) 2002-2018.
- [75] J.C. Maxwell, *A Treatise on Electricity and Magnetism*, Cambridge Oxford University Press, (1904).
- [76] T. Cebeci and P. Bradshaw, *Physical and Computational Aspects of Convective Heat Transfer*, Springer-Verlag, Newyork (1998).
- [77] S.J. Liao, On the homotopy analysis method for nonlinear problems, *App. Math. and Comput.*, 147(2004) 499-513.
- [78] M.S. Abel, J. V. Twade and M.M Nandeppanavar, MHD flow and heat transfer for the upper-convected Maxwell fluid over a stretching sheet, *Meccanica*, 47 (2012) 385-393.
- [79] A.M. Megahed, Variable fluid properties and variable heat flux effects on the flow and heat transfer in a non-Newtonian Maxwell fluid over an unsteady stretching sheet with slip velocity, *Chin. Phys. B*, 22 (2013) 094701.
- [80] S. Abbasbandy, M. Yurusoy, and H. Gulluce, Analytical solutions of non-linear equations of power-law fluids of second grade over an infinite porous plate, *Math. Comput. App.*, 19 (2014) 124-133.
- [81] S. A. Shehzad, T. Hayat, A. Alsaedi and B. Chen, A useful model for solar radiation, *Energ. Ecol. Environ.*, 1 (2016) 30-38.
- [82] M. Imtiaz, T. Hayat, A. Alsaedi and S. Asghar, Slip flow by a variable thickness rotating disk subject to magnetohydrodynamics, *Results Phy.*, 7 (2017) 503-509.

-
- [83] M.Awais, S. Ehsan, A. Khalid, I.Zuhaib, A. Khan, M.A.Z. Raja, Hydromagnetic mixed convective flow over a wall with variable thickness and Cattaneo-Christov heat flux model: OHAM analysis, *Results Phys.*, 8 (2018) 621-627.
- [84] T. Hayat, A. Aziz, T. Muhammad and A. Alsaedi, An optimal analysis for Darcy–Forchheimer 3D flow of nanofluid with convective condition and homogeneous–heterogeneous reactions, *Phy. Lett. A*, 382 (2018) 2846-2855.

Turnitin Turnitin Originality Report

Modeling an analysis for nonlinear problems involving nanofluid. by Madiha Rashid .

From DRSM (DRSML)

- Processed on 24-Sep-2019 09:00 PKT
- ID: 1178834227
- Word Count: 35066

Similarity Index
17%
Similarity by Source

Internet Sources:
5%
Publications:
10%
Student Papers:
11%

sources:
1

PROFESSOR
Department of Mathematics
Quaid-i-Azam University
Islamabad

Handwritten signature and date: 24/09/2019
Focal Person (Turnitin)
Quaid-i-Azam University
Islamabad

1% match (Internet from 18-Sep-2019)

<https://link.springer.com/article/10.1007%2Fs40430-019-1576-3>

2

1% match (Internet from 28-Apr-2019)

<https://www.unilab.eu/articles/technical-articles/thermodynamic-engineering-articles/nanofluids/>

3

1% match (publications)

Tasawar Hayat, Madiha Rashid, Ahmed Alsaedi. "Three dimensional radiative flow of magnetite-nanofluid with homogeneous-heterogeneous reactions". Results in Physics, 2018

4

1% match (student papers from 09-Aug-2016)

Submitted to Higher Education Commission Pakistan on 2016-08-09

5

1% match (student papers from 30-Apr-2019)

Submitted to Higher Education Commission Pakistan on 2019-04-30

6

1% match (publications)